NUMERICAL SOLUTIONS TO THE NAVIER-STOKES EQUATIONS IN TWO AND THREE DIMENSIONS

A thesis submitted to the University of Manchester
for the degree of Doctor of Philosophy
in the Faculty of Engineering and Physical Sceince

2013

By
Badr Alkahtani
Mathematics

Contents

List of Tables

List of Figures

Abstract

In this thesis the solutions of the two-dimensional ($2D$) and three-dimensional ($3D$) lid-driven cavity problem are obtained by solving the steady Navier-Stokes equations at high Reynolds numbers. In $2D$, we use the streamfunction-vorticity $(\psi) - (\omega)$ formulation to solve the problem in a square domain. A numerical method is employed to discretize the problem in the x and y directions with a spectral collocation method. The problem is coded in the MATLAB programming environment. Solutions at high Reynolds numbers are obtained up to $Re = 25000$ on a fine grid of 131×131.

The same method is also used to obtain the numerical solutions for the steady separated corner flow at high Reynolds numbers are generated using a for various domain sizes, at various Reynolds number which are much higher than those obtained by other researchers.

Finally, the numerical solutions for the three-dimensional lid-driven cavity problem are obtained by solving the velocity-vorticity formulation of the Navier-Stokes equations for various Reynolds numbers. A spectral collocation method is employed to discretize the y and z directions and finite difference method is used to discretize the x direction. Numerical solutions are obtained for Reynolds number up to 200.

Declaration

No portion of the work referred to in this thesis has been submitted in support of an application for another degree or qualification of this or any other university or other institute of learning.

Copyright

and commercialisation of this thesis, the Copyright and any Intellectual Property and/or Reproductions described in it may take place is available in the University IP Policy (see `http://www.campus.manchester.ac.uk/medialibrary/policies/intellectual-property.pdf`), in any relevant Thesis restriction declarations deposited in the University Library, The University Library's regulations (see `http://www.manchester.ac.uk/library/aboutus/regulations`) and in The University's policy on presentation of Theses

Acknowledgements

Firstly, I would like to give thanks and sincere gratitude to my supervisor, Prof. Jitesh Gajjar, for his advice, help and guidance, and for giving me a lot of his precious time throughout my research. Also, I would like to thank him for allowing me to use some of his codes and subroutines.

I would like to thank my beloved parents and brothers in my home country for supporting me all of the time. Thanks to my great wife for her support, patience and for keeping our family going. Thanks to our three little sons for their patience when I have missed some their childhood for me.

I would like to thank the IT service in the University of Manchester for permitting me to use the cs machines to run my codes. Thanks also to the School of Mathematics and to my colleagues and friends for creating a nice environment.

Chapter 1

Introduction

The Navier-Stokes equations are the governing equations for fluid flow. They are a system of nonlinear partial differential equations. There are very few exact solutions of the equations, and even for simple geometries, the equations have to be solved numerically. With increasing the Reynolds number, the accurate solution of the equations becomes more difficult, see Ghia *et al.* (1982), Azzam (2003), Erturk *et al.* (2005), Boppana & Gajjar (2010) and others. A number of techniques and algorithms have been developed to obtain an accurate solution of the equation for high Reynolds numbers.

The lid-driven cavity problem is used typically to test new methods and codes. The lid-driven cavity can be introduced as a fluid contained in a square or rectangular domain with stationary rigid walls and a moving wall, see Figure (1.1). The literature review of the two-dimensional and three-dimensional lid-driven cavity reveals that both problems are challenging at a high Reynolds number. Despite the simplicity of the geometry, difficulties arise from many complex flow features, such as the recirculating regions in the corner. This motivates us to obtain the numerical solution to the two-dimensional and three-dimensional lid-driven cavity

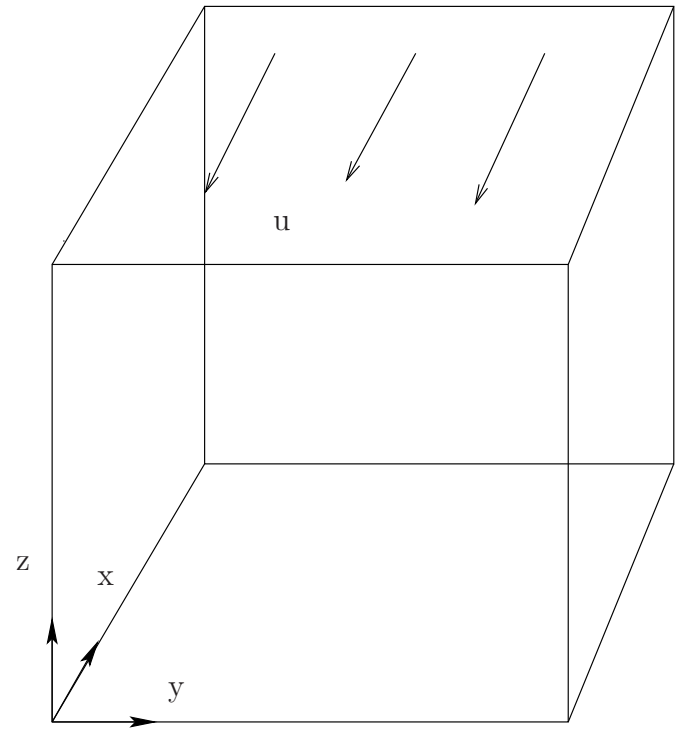

Figure 1.1: The lid-driven cavity problem geometry.

at a high Reynolds number using techniques based on the Chebyshev collocation in two directions to exploit the accuracy it offers.

The solution of the two-dimensional Navier-Stokes equations for the lid-driven cavity is presented in many papers. Burggraf (1966) was one of the earliest who studied the problem, using a second order finite difference approximation to solve the equations. Burggraf presented results for Reynolds numbers up to 1000, which in itself was impressive given the computational facilities available at that time.

A singular behaviour is exhibited in a lot of realistic two dimensional domains which contain sharp corners. The singularities are observed when solving the lid driven cavity problem in the vicinity of the two corners of the sliding wall. Moffatt (1964) give detailed information of the mathematical and physical properties of

what is expected near the corners of the lid driven cavity problem. Usually, when a numerical solution is considered for such flows the singularity is ignored with assumption that the flow is only affected in a small region of the singularity, Logue (2005).

Gupta *et al.* (1981) used a semi-analytic technique for solving the lid driven cavity problem to examine the effect of the singularity in the vicinity of the two singular corners of the moving wall. They found a good agreement for the vorticity on the sliding wall and poor agreement for the vorticity on the side walls. They refer the poor agreement to the fact that the "vorticity values on the stationary walls were very sensitive to the inaccuracy inherent in the numerical solution". Another technique has been used by Peyret & Taylor (1984) to smooth the velocity profile. They defined the velocity on $y = 1$ boundary as $u(x) = -16x^2(1-x)^2$ rather than $u(x) = 1$. This leads to a good solution and remove the singularity but this modification changed the problem significantly. Botella & Peyret (1998) presented a numerical solution for the two-dimensional lid-driven cavity flow using the Chebyshev collocation method, and the accuracy of the results is achieved by using the leading term of the asymptotic expansion of the solution in the vicinity of the corner where there is a discontinuity of velocity. Extensive results at $Re = 1000$ are presented and demonstrate the accuracy by comparing the results with other investigators. They mentioned that the maximum error of the numerical result is 0.02 percent, while in Ghia *et al.* (1982) it is 4 percent. In our work, we use $\psi_y(x) = u(x) = 1 - e^{500x(1-x)}$ and this modification does not change the problem as it will been observed through this thesis.

Ghia *et al.* (1982) were among the first to provide detailed solutions for Reynolds numbers up to 10000. They used an implicit multigrid method with

meshes consisting of as many as 257×257 points. The fine grid enables the method to resolve the secondary vortices with a good accuracy. Our results are compared with the Ghia *et al.* (1982) work for Reynolds numbers up to 10000. Schreiber & Keller (1983) gave an accurate numerical solution of the two-dimensional lid-driven cavity at Reynolds numbers up to 10000 on a 180×180 grid. They were one of the first to use Richardson extrapolation to obtain fourth order accuracy for solving the Navier-Stokes equations. Their technique combines a linear system solver and the Newton method for the nonlinear system, and employing the continuation procedure to obtain solutions for high Reynolds numbers. A numerical solution of the lid-driven cavity has been presented by Bruneau & Jouron (1990). They employed combined multigrid-relaxation scheme to achieve good convergence on fine grids and obtain results up to $Re = 15000$. The results agreed with other published results. The lattice Boltzmann method was used by Miller (1995) to solve the lid-driven cavity in two dimensions. The primitive variables formulation was considered in a geometry with Dirichlet boundary conditions. Results were presented for varying aspect ratio on various grid sizes for Reynolds numbers up to 1000. Jackson (1996) used the multigrid method, combined with iterative techniques, to obtain accurate two-dimensional solutions up to $Re = 10750$ on a 605×605 fine grid. The computations were carried out on massively parallel computers. Chiang *et al.* (1996) conducted a numerical simulation for a two-dimensional rectangular cavity with spanwise aspect ratio of $3 : 1$, using the finite volume method. The problem is defined by the square cross-section. They chose Reynolds number at 1500 to be investigated and provided physical insight to the spanwise flow motion. Chiang *et al.* (1998) applied the finite volume method to obtain the two-dimensional solution of the incompressible Navier-Stokes equations in a lid-driven cavity. On staggered grids, solutions were

presented for a depth-to-width aspect ratio of 1 : 1 and a span-to-width aspect ratio of 3 : 1. They state the critical Reynolds number where the instability is generated.

More recently, Azzam (2003),Erturk *et al.* (2005) have obtained numerical solutions for the lid driven cavity for $Re = 20000$. Azzam (2003) employed a high order finite difference method in the x direction with a spectral Chebychev collocation method in the y direction and used direct methods to obtain numerical solutions for Reynolds numbers up to $Re = 20000$. Her result showed a good agreement with Ghia *et al.* (1982) up to $Re = 10000$. Although her results presented new data for $Re = 20000$, finer grids are needed to resolve some high Reynolds number features. Two years later, the two-dimensional steady incompressible lid-driven cavity problem has been solved by Erturk *et al.* (2005), who used the streamfunction-vorticity formulation with a uniform grid of 601×601 points. A finite difference formulation was used to obtain the numerical solution. Results have been presented at Reynolds numbers up to 21000. Their results showed good agreement with Azzam (2003) results and they suggested finer grid should be used to obtain higher Reynolds number solutions. An implicit finite volume method is used to obtain the solution of the Navier-Stokes equations by Sahin & Owens (2003). The finite volume method was applied to the resulting formulation to obtain the two-dimensional solution for the lid-driven cavity at Reynolds numbers up to 10000. Sahin & Owens (2003) show excellent agreement with previous literature results. Simulation of the two-dimensional lid-driven cavity has been performed by Bruneau & Saad (2004). A 512×512 grid size was used to generate results for a wide range of Reynolds number. They found a Hopf bifurcation firstly at $Re = 8000$, and a periodic solution was obtained at $Re = 10000$. The finite element method has been used to solve the isothermal

flow in two dimensional lid driven cavity by Sun *et al.* (2006). Where comparison was possible, there was very good agreement with published results. They mentioned that the study results are relevant to devices, such as a scraped surface heat exchanger. Kumar *et al.* (2009) used the multigrid method to present the solution of the incompressible Navier-Stokes equations in two dimensions. A square lid-driven cavity with a moving upper wall was considered. A fine uniform grid of 513×513 was used to obtain the solution for the steady flow for $Re \leq 10000$. Boppana & Gajjar (2010) used a hybrid scheme with spectral collocation and high order finite differences to study the global stability in a square lid-driven cavity. Their aim was to find the critical parameters that lead to the loss of stability for aspect ratios of 1.5 and 2, and they found a reasonable agreement with the previous studies. A new paradigm of compact finite difference approximation, named Five Points Constant Coefficient Second Order Compact (5PCC-SOC) scheme, is proposed by Tian & Yu (2011) for the two-dimensional streamfunction-vorticity formulation. Numerical results were obtained and compared with literature up to $Re = 7500$ using various grids and showed good agreement.

In fluid mechanics, the desire to obtain the proper asymptotic description of the flow at a high Reynolds number has attracted many researchers to study various flow problems. One of the problems that has remained unsolved at high Reynolds number is the the steady flow past a finite plate attached normally to an unbounded wall, see Figure (1.2). A sketch of the flow problem is shown in Figure (1.2) where the left-hand sketch is the entire plane and one on the right is the local geometry that we solve. This flow has been of interest to researchers because it is simpler than the other flows that have been studied whilst simultaneously retaining many features of interest, such as separating boundary

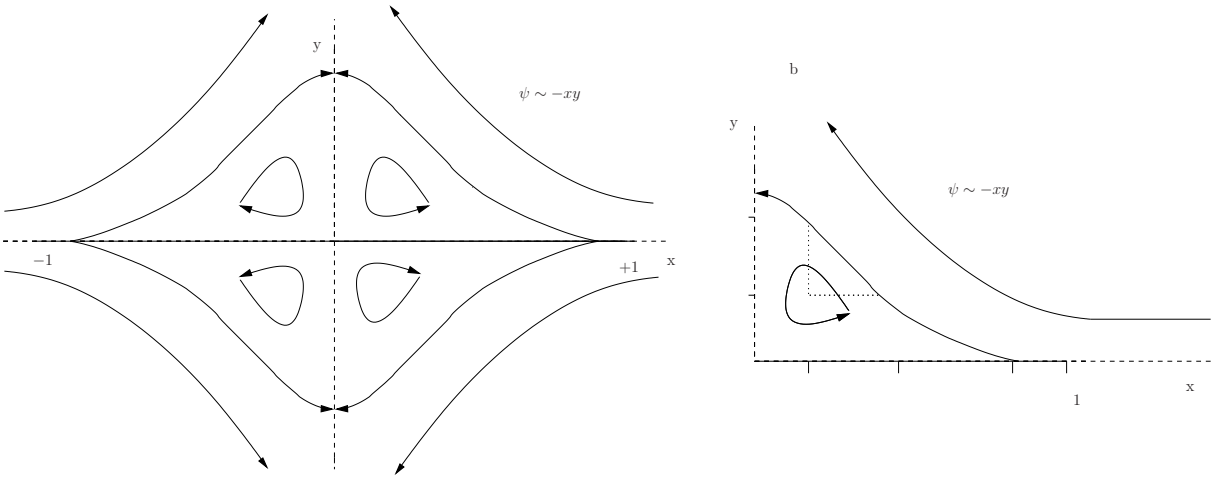

Figure 1.2: Corner flow geometry : (a) entire flow geometry, (b) local geometry .

layers, reattaching shear layer and eddies, see Mclachlan (1990). Also, it can be amenable to accurate simulation because the eddies sizes seem not to grow significantly when Re is increased; hence, the problem can be solved in a smaller domain. Another reason is that a simple conformal mapping can be applied to the geometry so that the grid points concentrate on places where the separation takes place, see Mclachlan (1990).

At the beginning of the twentieth century, Prandtl (1905) presented his pioneering work on boundary layers. He was the first to have an explanation of the separation at high Reynolds numbers being associated with the separation of boundary layers. His work became the basis of the further study of the separation phenomena. Goldstein (1948) considered the singularities in the solution of the boundary layer equations at the point of separation. Singularities occur when the velocity distribution outside the boundary layers decrease, giving rise to an adverse pressure gradient. In that case, the boundary layers equations cease to be valid at, and near, the separation on the upstream and downstream sides. Leal (1973) has used numerical methods to describe the separated flow over a finite

flat plate placed on the x axis between $x = -1$ and 1. In the absence of the plate at large distances, the flow is given by the stream function $\psi = -xy$. Leal (1973) presented the numerical solution with Reynolds numbers ranging from 10 to 800. Three-point backward differences and the Runge-Kutta method were employed for the simulations. Leal (1973) reported that the separation point position displaced slightly further away from the leading edge. The same formulation of the problem has been discussed and solved by Suh & Liu (1990). Numerical methods have been employed to obtain the numerical solutions at Reynolds numbers up to $Re = 2800$. Suh & Liu (1990) applied Newton's method to the full Navier-Stokes equations in order to obtain the solution, and they observed the recirculating region around the corner. Pauley *et al.* (1990) studied the boundary layer separation under a sudden adverse pressure gradient in two dimensions. The problem was studied by obtaining the numerical solution of the Navier-Stokes equations. They found that the periodic vortex is created by an adverse pressure gradient. A comparison of the numerical results with Gaster (1967) experiments were made and good agreement was found. Mclachlan (1991) studied the case of corner flow as a separated flow example in an infinite domain. Mclachlan (1991) used the multigrid to exploit the rapid convergence and obtain the numerical solution at a high Reynolds number. The Navier-Stokes equations were discretized and solved at Reynolds numbers up to 5000. Mclachlan (1991) concluded that the multigrid method is a practical and economical method and can be used instead of Newton's method.

Because of the limitations of computers time and memory, the majority of attention for the solution of Navier-Stokes equations has been devoted to two-dimensional problems, see Chiang *et al.* (1996). With an increase in computer power, it has been possible to simulate the three dimensional problems.

In Speziale (1987), it has been addressed that the three dimensional velocity-vorticity formulation has advantages when it is used for solving problems as it is more suited to a description of incompressible flow. With the primitive variables formulation, problems have been faced in the accuracy and stability of the pressure boundary conditions. However, the velocity-vorticity formulation in three dimensions has a disadvantage in that one has to solve for more unknowns, i.e. three velocity and three vorticity components. In this work, a novel formulation used by Davies & Carpenter (2001) has been employed to overcome this disadvantage. One of our aims is to obtain an accurate numerical solution of the three-dimensional incompressible Navier-Stokes equations using this novel formulation. There are various methods to solve such equations. In this work, we use a hybrid spectral method with, in particular, the Chebychev collocation method and the finite difference method. Our main motivation is to extend methods developed by Azzam (2003), Gajjar & Azzam (2004) and Boppana & Gajjar (2010).

The primitive variable formulation has been used to obtain the numerical solution by Takami & Kuwahara (1974), Ku *et al.* (1987), Perng & Street (1989), Albensoeder & Kuhlmann (2005) and Albensoeder & Kuhlmann (2006). Takami & Kuwahara (1974) obtained three dimensional numerical solutions up to $Re = 400$ employing a marker and cell (MAC) approach. Chebychev pseudo-spectral technique has been used by Ku *et al.* (1987) to obtain the solution up to $Re = 1000$. Perng & Street (1989) used MAC strategy to obtain the solution at $Re = 3200$ using an explicit and implicit MAC scheme. A numerical method for three dimensional lid-driven cavity is presented in Albensoeder & Kuhlmann (2005), using the Chebyshev collocation method for $Re = 1000$ with different spanwise aspect ratio (SAR). The collocation method has been employed for the rigid boundary

in spanwise z direction, and the mixed Chebyshev-collocation-fourier method for periodic boundary conditions in z direction. Albensoeder & Kuhlmann (2006) investigated numerically the three-dimensional flow in a lid-driven cavity in cubic geometry. The simulation was conducted by translating the three-dimensional flow as a number of two-dimensional problems parallel to the third direction. The problem was descretized using pseudospectral Chebyshev collocation method. The singularity near the corner was avoided by using an analytical asymptotic solution for accuracy.

Solutions to the three-dimensional lid-driven cavity using velocity-vorticity have been obtained Jackson (1996), Yeckel *et al.* (1997), Young *et al.* (2000) and Zunic *et al.* (2006). Using the multigrid method Jackson (1996) has obtained numerical solutions for the three-dimensional lid driven cavity up to $Re = 3200$. His results agreed well with the literature for moderate Reynolds number up to $Re = 2000$ but differences were observed for higher Reynolds number. Yeckel *et al.* (1997) use parallel computers to study the steady flow in the three-dimensional lid-driven cavity at moderate Reynolds numbers. They used finite elements and a GMRES method with diagonal preconditioning to solve the resulting linear system. Solutions at Re up to 500 were obtained. They failed to obtain the solution at Re greater than 500. Young *et al.* (2000) used a combined boundary element method - finite element method to show the accuracy of this combination in solving the three-dimensional Navier-Stokes equations. They have given results of the velocity-vorticity formulation at moderate Re numbers up to 1000 in a typical cubic cavity. The approach to solve three-dimensional Navier-Stokes equations in velocity-vorticity formulation has been carried out by Zunic *et al.* (2006). A boundary element method was employed to calculate the boundary vorticity while

the finite element method was used for the transport equations. For the computation of velocity, finite element discretization was used. Parallelization has been performed to speed up the implementation, and the three-dimensional lid-driven cavity solution was obtained at $Re = 100$ and $Re = 1000$ to show an agreement with the Young *et al.* (2000) result.

A mixture of experimental and simulation works have been obtained by several researchers. Davis & Mallinson (1974) used central finite differences to obtain solutions for the two-dimensional lid-driven cavity solution at various Reynolds numbers. The same method was employed to gain a three-dimensional numerical solution of the lid-riven cavity at $Re = 100$ of spanwise aspect ratio (SAR) $1 : 1 : 3$, and compared with experimental data. Their results suggest that all two-dimensional results for the flow in lid-driven cavity at Re greater than 500 are in error when compared with physical experiments because the two-dimensional model overestimates the strength of the motion. Koseff *et al.* (1983) mentioned that the general features of the flow can be obtained. Experimental data have been compared with numerical simulation generated by two codes; one using a finite difference method and the second employing the finite element method. The code failed to resolve some precise features, such as Taylor-Gortler like longitudinal vortices, because of the limitation of the computing facilities at that time. An experimental study was conducted by Koseff & Street (1984), in which they investigated the influence of spanwise aspect ratio on the size of downstream eddies. They obtained results based on the experiments of square cross-section ($B = D = 150$mm), where B is the cavity width and D is the cavity depth, of the cavity at various spanwise aspect ratios (SAR) of $1 : 1, 2 : 1$ and $3 : 1$, where $SAR = L/B$ where L is the cavity length. The experiments were conducted with Re varying from $Re = 1000$ to $Re = 10000$. They found that, when

$SAR = 3 : 1$, the downstream eddies increase in their size as Re increases. Unlikely, for $SAR = 1 : 1$ and $SAR = 2 : 1$, the downstream eddies decrease in their size as Re increases. A successful simulation of the three-dimensional lid-driven cavity has been achieved by Freita *et al.* (1985) by using an improved finite difference code. Results at $Re = 3200$ were obtained, and experimental results validate the simulation results. Guermond *et al.* (2002) provided a comparison between experimental results and numerical simulation results at $Re = 1000$, and of spanwise aspect ratio (SAR) $1 : 1 : 2$ in a rectangular lid-driven cavity. The study observed the evolution of the flow up to $t = 12$, and it found that both experimental and simulation results are sensitive to the boundary perturbation. Very small changes to the boundary geometry have been applied in order to observe the sensitivity. They indicated that, for three-dimensional bounded region, controlling the shape of the boundary and the value of boundary conditions are more important than in two dimensions.

Although we solve the steady Navier-Stokes equations, it is important to review some literature of the time dependent Navier-Stokes equations for the lid driven cavity. A study of the hydrodynamic stability of flows such as the lid driven cavity flow is complicated by the fact that the steady flow depends on two variables and is non parallel. The linear stability of the flow leads to a two dimensional edge value problems as described by Boppana & Gajjar (2010). They identified the critical parameters which lead to loss of stability for the lid driven cavity problems for various aspect ratio $A = 1, 1.5$ and $A = 2$ by solving linearized unsteady equations. It is found that their results reasonably agreed with literature for the square cavity and there were a discrepancy with the literature for the other two aspect ratios. An alternative to solving eigenvalue problem is the direct simulation of the flow. This approach was employed, for

example, by Gustafson & Halasi (1986*b*) and Gustafson & Halasi (1986*a*) to study driven cavity flow. The direct simulation is expensive in computer time especially when the flow parameters are close to the critical values. But on the positive side, it makes the flow accessible after the first Hopf bifurcation Auteri *et al.* (2002). By a simulation, a numerical solutions of regularized unsteady lid driven cavity have been obtained by Shen (1991) using a Chebyshev-Tau approximation. A Hopf bifurcation is observed between $Re = 10500, 15000$ and periodic solutions for the same interval. Cortes & Miller (1994) obtained numerical solutions of the steady unit lid driven cavity and with aspect ratio two of $Re = 5000$ using a spectral difference method. Their result for the aspect ratio two contradict those obtained by Goodrich *et al.* (1990) who observed a periodic solutions for $Re = 5000$ and Hopf bifurcation for $2000 \leq Re \leq 5000$.

Poliashenko & Aidun (1995) identified the critical parameter Re for the lid driven cavity and with aspect ratio $0.8, 1.5$. They found that the square lid driven cavity is stable with increasing Reynolds number. A similar comment is mentioned by Fortin *et al.* (1997) who studied the Hopf bifurcation of the unit lid driven cavity. These two references results are consistent with Shen (1991). The stability of unsteady lid driven cavity was studied by Auteri *et al.* (2002) using spectral method to discrtize the primitive variable formulation of the Navier-Stokes equations. Their simulation determined the critical value of Re between $Re = 8017.6$ and 8018.8. Tiesinga *et al.* (2002) studied the transition of the steady to the periodic flow in the lid driven cavity using the Tau-method for time and finite volume method of second order for variables. Their work predict the first Hopf bifurcation at $Re = 8375$.

The literature review has revealed that obtaining the solution of Navier-Stokes equations at high Reynolds number is challenging. This provides motivation to

solve the lid-driven cavity problem in two and three dimensions as the literature review reveals the shortage of results at Reynolds numbers greater than 20000. Moreover, the literature review indicates that solving the steady separated corner flow at high Reynolds number is challenging, thereby motivating us to solve this problem, since it is rich in flow features, such as circulations and eddies.

1.1 Thesis Outline

In the following chapter, we review the numerical methods used to obtain the numerical solution for the three problems; two and three-dimensional lid-driven cavity problems and steady separated corner flow. In Chapter 3, a two-dimensional test problem is used to test our method. In fact, in this thesis, a number of test problems are chosen, as described in the later chapters, which are such that they provide exact solutions to the governing equations provided suitable forcing functions added. These provide a mean to test code solving equations as close as possible to the real problems under consideration. Once the forcing functions are removed, the equations revert in the most cases to the full $2D$ and $3D$ Navier-Stokes equations that we wish to solve. the "exact solutions" give a measure of the errors involved and convergence properties. This is especially important when developing complicated codes to make sure that any mistakes are minimized as much as possible. The problem is coded in MATLAB and the numerical solution is compared with the exact solution. Two-dimensional lid-driven cavity in streamfunction-vorticity formulation is solved at high Reynolds number using the Chebyshev collocation method in the x and y directions, and we compare our results with those available in the literature. Numerical solutions are obtained at Reynolds numbers up to 25000.

In Chapter 4, the two-dimensional steady separated corner flow in streamfunction-vorticity formulation is solved using the same technique as detailed in the preceding chapter. Solutions are obtained for increasing domain sizes for various Reynolds numbers up to 14000.

In Chapter 5, the three-dimensional lid-driven cavity in velocity-vorticity formulation is considered using the Chebyshev collocation method to discretize the equations in the y and z directions, and a finite difference method in the x direction. Results for various Reynolds numbers are obtained and compared with the available literature. Finally, conclusions are provided in Chapter 6.

Chapter 2

Employed Methods

2.1 Finite Difference Method

In applied mathematics, many problems can be modelled in terms of partial differential equations. These equations can be solved by numerical methods using many different approaches. The finite difference method replaces each derivative in the differential equation with appropriate approximation, based on nodal values. The local approximations can be derived by low order Taylor series expansions. First, we concentrate on how to approximate the derivative of a known function by a finite difference formula based only on values of the function itself at discrete points.

2.1.1 Basic Approximation

Let $\psi(x)$ be a function of one variable that is assumed to be smooth, meaning that the function can be differentiated several times. Furthermore, each derivative is well defined and bounded over the interval, which contains the point of our

interest x. Using Taylor's series expansion, we have

$$\psi(x+h) \approx \psi(x) + h\psi'(x) + \frac{h^2}{2!}\psi''(x) + \frac{h^3}{3!}\psi'''(x) + ... \tag{2.1}$$

and

$$\psi(x-h) \approx \psi(x) - h\psi'(x) + \frac{h^2}{2!}\psi''(x) - \frac{h^3}{3!}\psi'''(x) + ... \tag{2.2}$$

for the small value of h. The simplest way to approximate the first derivative of the function ϕ at the point x is by subtracting equations (2.1) and (2.2), which gives the following finite difference approximation

$$\psi'(x) \approx \frac{\psi(x+h) - \psi(x-h)}{2h} + O(h^2). \tag{2.3}$$

In an analogous manner, the finite difference approximation to the second derivative can be obtained by adding equations (2.1) and (2.2) to have the following form

$$\psi''(x) \approx \frac{\psi(x+h) - 2\psi(x) + \psi(x-h)}{h^2} + O(h^2). \tag{2.4}$$

2.1.2 Finite Difference Scheme For The Laplacean Operator

Assuming that the function $\psi = \psi(x, y)$, we divide the $x - y$ plane in a mesh with spacing $\Delta x = h$ and $\Delta y = k$, as shown below in Figure (2.1). The node (x_i, y_j) is given by

$$x_i = x_0 + ih \quad i = 0, ..., N \qquad , \qquad y_j = y_0 + jk \quad j = 0, ..., M.$$

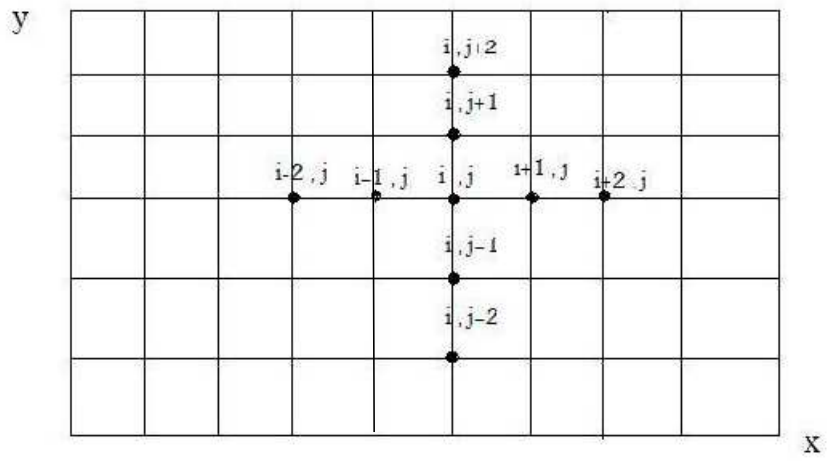

Figure 2.1: Divided plane in finite difference mesh.

At each point x_i, y_j we try to approximate the derivative of the function $\psi_{i,j} = \psi(x_i, y_j)$ in the x direction. Therefore, using (2.3) and (2.4), the approximation for the derivatives in x are

$$\left(\frac{\partial \psi}{\partial x}\right)_{i,j} = \frac{\psi_{i+1,j} - \psi_{i-1,j}}{2h} + O(h^2), \tag{2.5}$$

$$\left(\frac{\partial^2 \psi}{\partial x^2}\right)_{i,j} = \frac{\psi_{i+1,j} - 2\psi_{i,j} + \psi_{i-1,j}}{h^2} + O(h^2). \tag{2.6}$$

These two approximations are centered at each point (x_i, y_j) and, therefore, are called centered difference approximations. For the y direction, we follow the same idea to obtain the first and second derivative respectively as follows:

$$\left(\frac{\partial \psi}{\partial y}\right)_{i,j} = \frac{\psi_{i,j+1} - \psi_{i,j-1}}{2k} + O(k^2), \tag{2.7}$$

$$\left(\frac{\partial^2\psi}{\partial y^2}\right)_{i,j} = \frac{\psi_{i,j+1} - 2\psi_{i,j} + \psi_{i,j-1}}{k^2} + O(k^2). \tag{2.8}$$

2.1.3 Fourth-Order Accurate Formulation

Another approximation to the derivatives is the five point formula of fourth-order accuracy. The derivatives in this case, in x direction, are approximated by

$$\left(\frac{\partial\psi}{\partial x}\right)_{i,j} = \frac{\psi_{i-2,j} - 8\psi_{i-1,j} + 8\psi_{i+1,j} - \psi_{i+2,j}}{12h} + O(h^4), \tag{2.9}$$

and

$$\left(\frac{\partial^2\psi}{\partial x^2}\right)_{i,j} = \frac{-\psi_{i-2,j} + 16\psi_{i-1,j} - 30\psi_{i,j} + 16\psi_{i+1,j} - \psi_{i+2,j}}{12h^2} + O(h^4). \tag{2.10}$$

For y direction, the derivatives can be approximated by

$$\left(\frac{\partial\psi}{\partial y}\right)_{i,j} = \frac{\psi_{i,j-2} - 8\psi_{i,j-1} + 8\psi_{i,j+1} - \psi_{i,j+2}}{12k} + O(k^4), \tag{2.11}$$

and

$$\left(\frac{\partial^2\psi}{\partial y^2}\right)_{i,j} = \frac{-\psi_{i,j-2} + 16\psi_{i,j-1} - 30\psi_{i,j} + 16\psi_{i,j+1} - \psi_{i,j+2}}{12k^2} + O(k^4), \tag{2.12}$$

see Azzam (2003).

2.1.4 Type Of Resulting Matrix Associated with Finite Difference Discretization

For 1-D Problem

Consider the one-dimensional Poisson equation,

$$-\psi''(x) = f(x) \qquad \text{for} \quad x \quad \in \quad (0,1) \tag{2.13}$$

$$\psi(0) = \psi(1) = 0. \tag{2.14}$$

The domain [0,1] can be discretized spaced with $N+1$ points, such that

$$x_i = i \times h, \quad i = 0, ...N$$

where $h = 1/N$. The value of $\psi(x_0)$ and $\psi(x_N)$ are known from the boundary conditions. At every point, we seek an approximation ψ_i to the exact solution $\psi_(x_i)$, where $1 \leq i \leq N-1$. If the centered difference approximation (2.10) is used, then by the equation (2.13) the unknowns $\psi_i, \psi_{i-1}, \psi_{i+1}, \psi_{i-2}, \psi_{i+2}$ satisfy the relation

$$-\psi_{i-2} + 16\psi_{i-1} - 30\psi_i + 16\psi_{i+1} - \psi_{i+2} = 12h^2 f_i,$$

in which $f_i = f(x_i)$. Notice that, for the boundaries $i = 0$ and $i = N$, the equation will involve ψ_0 and ψ_N, which are equal to zero in this case. Since the points are at $i = 1$ and $i = N-1$, we need points outside the domain to be associated with the calculation, we apply the second-order finite difference, rather than the fourth-order, to overcome this problem, which can be seen in the

resulting matrix. Thus, for $n = 5$, the linear system obtained is of the form

$$A\psi = f \tag{2.15}$$

where

$$A = \frac{1}{h^2}\begin{pmatrix} 1 & & & & & \\ -1 & 2 & -1 & & & \\ 1 & -16 & 30 & -16 & 1 & \\ & 1 & -16 & 30 & -16 & 1 \\ & & & -1 & 2 & -1 \\ & & & & & 1 \end{pmatrix}. \tag{2.16}$$

see Saad (1998).

It can be observed that the resulting matrix is a pentadiagonal matrix for the fourth-order formulation, which will be the focus of this work. By solving (2.15), one can obtain ψ at the nodal points.

For 2-D Problem

Similar to the previous case, consider the simple problem,

$$\begin{aligned} -\left(\frac{\partial^2\psi}{\partial x^2} + \frac{\partial^2\psi}{\partial y^2}\right) &= f(x,y) \qquad \text{in} \quad \Omega \\ \psi &= 0 \qquad \text{on} \quad \Gamma, \end{aligned} \tag{2.17}$$

where Ω is now the rectangle $(0, l_1) \times (0, l_2)$ and Γ its boundary. The domain can be discretized by taking $N + 1$ points in x direction and $M + 1$ in y direction;

$$x_i = i \times h, \quad i = 0, ..., N \qquad y_j = j \times k, \quad j = 0, ..., M$$

where

$$h = \frac{l_1}{N}, k = \frac{l_2}{M}.$$

We number only the interior points, which are those (x_i, y_j) with $0 < i < N$ and $0 < j < M$, since the boundary values are known. Again, since the derivative approximations at $i = 1$, $i = N - 1$, $j = 1$and $j = M - 1$ need points outside the domain to be associated with the calculation, we apply the second-order finite difference, rather than the fourth-order, to overcome this problem. Now, by (2.18), $\psi_{i,j}, \psi_{i-1,j}, \psi_{i+1,j}, \psi_{i-2,j}, \psi_{i+2,j}$ satisfies the relation

$$\begin{aligned} - & \left(\frac{-\psi_{i-2,j} + 16\psi_{i-1,j} - 30\psi_{i,j} + 16\psi_{i+1,j} - \psi_{i+2,j}}{12h^2} \right) \\ - & \left(\frac{-\psi_{i,j-2} + 16\psi_{i,j-1} - 30\psi_{i,j} + 16\psi_{i,j+1} - \psi_{i,j+2}}{12k^2} \right) = f(x_i, y_j), \end{aligned}$$

see Saad (1998).

In our work, we are interested in the type of matrix resulting from the finite difference discretization. Figure (2.2) shows the pattern of the matrix before imposing the boundary conditions corresponding to the above equation when $N = 9$ and $M = 7$. The matrix pattern depends on how the unknowns are ordered; Hence, to obtain a pentadiagonal pattern, the components of the unknowns vector

ψ in (2.15) have to be in order, as they are indexed such that

$$\psi = \begin{pmatrix} \psi_{1,1} \\ \psi_{1,2} \\ \vdots \\ \psi_{N+1,1} \\ \psi_{1,2} \\ \vdots \\ \psi_{N+1,2} \\ \psi_{1,3} \\ \vdots \\ \psi_{N+1,M+1} \end{pmatrix}. \tag{2.18}$$

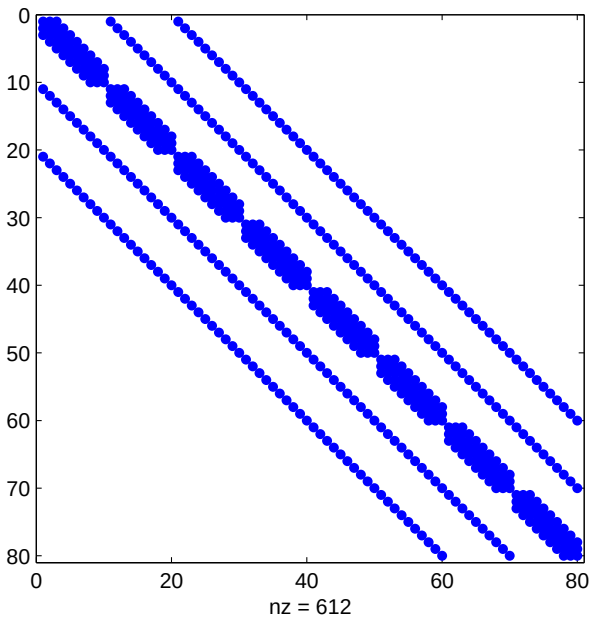

Figure 2.2: The pattern of the two-dimensional matrix resulting from finite difference discretization when $N = 9$ and $M = 7$.

For 3-D Problem

From the discussion above, one can see that the pattern corresponding to the finite difference discretization tends to be a banded and highly sparse matrix. The same pattern of matrix resulting from discretization arises when we deal with the three-dimensional problem. Figure (2.3) shows the pattern of the matrix arising when solving the three dimensional Poisson equation using similar finite difference approximation.

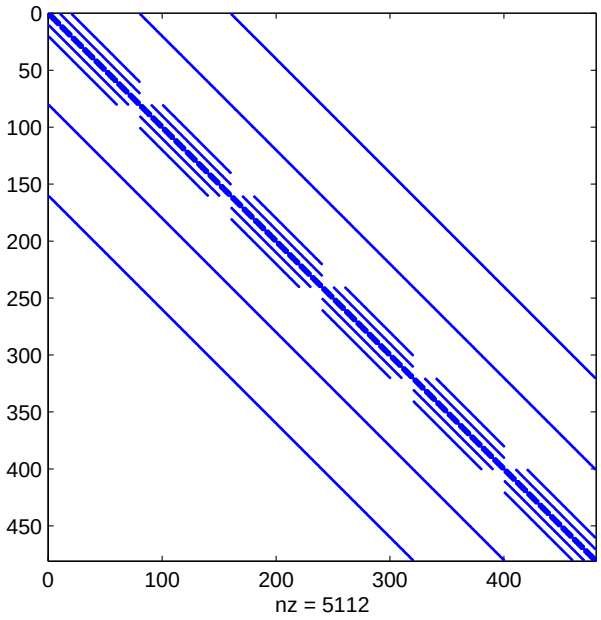

Figure 2.3: The pattern of matrix resulting from fourth-order finite difference discretization for the three-dimensional Poisson problem.

The fourth-order accurate formula is preferable for use in association with Chebyshev discretization in order to give a more accurate solution.

2.2 Chebyshev Collocation Method

Definition *The Chebyshev polynomial $T_n(x)$ of the first kind is a polynomial in x of degree n, defined by the relation*

$$T_n(x) = \cos n\theta \qquad \text{where} \quad x = \cos\theta,$$

which implies

$$T_n(x) = \cos(n \arccos x), \qquad \text{for} \quad n \geq 0 \qquad \text{and} \qquad x \in [-1, 1]. \tag{2.19}$$

It can be seen that the variable θ can be taken as $[0, \pi]$, and we know that $\cos n\theta$ is a polynomial of degree n in $\cos\theta$; therefore one can think of a recurrence relation. Now, the elementary formulas for Chebyshev polynomials are as follow

$$\cos 0\theta = 1, \quad \cos 1\theta = \cos\theta, \quad \cos 2\theta = 2\cos^2\theta - 1,$$

$$\cos 3\theta = 4\cos^3 -3\cos\theta, \quad \cos 4\theta = 8\cos^4\theta - 8\cos^2\theta + 1, ...$$

From (2.19), by $x = \cos\theta$, it can be deduced that the first few Chebyshev polynomials are

$$\begin{aligned} T_0(x) = 1, \quad T_1(x) = x, \quad T_2(x) = 2x^2 - 1, \\ T_3(x) = 4x^3 - 3x, \quad T_4(x) = 8x^4 - 8x^2 + 1, ... \end{aligned} \tag{2.20}$$

In general, we obtain the recurrence relation

$$T_n(x) = 2xT_{n-1}(x) - T_{n-2}(x), \qquad n = 2, 3, ... \tag{2.21}$$

with

$$T_0(x) = 1, \quad T_1(x) = x. \tag{2.22}$$

The recurrence relation defined by (2.21) shows that the Chebyshev polynomial is a polynomial of degree n with leading coefficient 2^{n-1} Mason & Handscomb (2002).

2.2.1 The Chebyshev Expansion

The Gauss Lobatto collocation points are given by

$$x_j = \cos\left(\frac{j\pi}{N}\right) \qquad j = 0, ..., N, \tag{2.23}$$

where $N+1$ is the number of points, and a set of grid points in the domain $[-1, 1]$ that are $(\frac{2}{\pi})^d$ times as dense in the middle as an equally-spaced grid, where d is the dimensions of the problem; i.e they cluster at boundaries, see Trefthen (2000). Trefthen (2000) mentions that, to visualize these points, one can imagine them as the projections on $[-1, 1]$ of equispaced points on the upper half of the unit circle.

We can calculate a discrete derivative, w_j say, for any smooth continuous function, $f(x_j)$ say, defined on the Chebyshev points. To do that, consider the unique polynomial $p(x)$ of degree $\leq N$ with $p(x_j) = f_j$, and let $w_j = p'(x_j)$; then $w_j = (D_N f)_j$, where D_N is the $(N+1) \times (N+1)$ Chebyshev differentiation matrix. For simplicity, consider the case where $N = 2$. The Chebyshev points will be $1, 0$ and -1; using Lagrange interpolation across these points gives

$$p(x) = \frac{(x-0)}{(1-0)}\frac{(x+1)}{(1+1)}f_0 + \frac{(x-1)}{(0-1)}\frac{(x+1)}{(0+1)}f_1 + \frac{(x-1)}{(-1-1)}\frac{(x-0)}{(-1-0)}f_2 \tag{2.24}$$

and the differentiation of this equation gives

$$p'(x) = (x + \frac{1}{2})f_0 - 2xf_1 + (x - \frac{1}{2})f_2. \tag{2.25}$$

Now, the differentiation matrix can be assembled by evaluating equation (2.25) at the Chebyshev points, with the jth point giving the jth row of the matrix

$$D_2 = \begin{pmatrix} \frac{3}{2} & -2 & \frac{1}{2} \\ \frac{1}{2} & 0 & -\frac{1}{2} \\ -\frac{1}{2} & 2 & -\frac{3}{2} \end{pmatrix}, \tag{2.26}$$

see Trefthen (2000).

Theorem Chebyshev differentiation matrix *For each $N \geq 1$, let the rows and columns of the $(N+1) \times (N+1)$ Chebyshev spectral differentiation matrixD_N be indexed from 0 to N. The entries of this matrix are*, see Canuto *et al.* (1988)

$$(D)_{i,j}(x) = \begin{cases} \frac{c_i(-1)^{i+j}}{c_j(x_i - x_j)}, & i \neq j \\ \frac{-x_j}{2(1-x_j^2)}, & 1 \leq i = j \leq N-1 \\ \frac{2N^2+1}{6}, & i = j = 1 \\ -\frac{2N^2+1}{6}, & i = j = N \end{cases} \tag{2.27}$$

where

$$c_i = \begin{cases} 2, & i = 0 \quad \text{or} \quad N \\ 1, & \text{otherwise.} \end{cases} \tag{2.28}$$

A second-order derivative can also be represented by the Chebyshev expansion, which is the square of the Chebyshev differentiation matrix D_N, see Canuto *et al.*

(1988).

2.2.2 Discretization in 2-D

Consider a two-dimensional problem to be discretized using Chebyshev discretization in the x and y directions. Intuitively, when dealing with a 2-D domain, the differentiation matrix will be larger. To see that, let $\psi_{i,j} = \psi(x_i, y_j)$, where x_i and y_j are the Chebyshev collocation points in the x and y directions respectively. Then, the partial derivative can be written as follows

$$(\frac{\partial \psi}{\partial x})_{i,j} = \sum_{k=0}^{N} (Dx)_{i,k} \psi_{k,j} \tag{2.29}$$

$$(\frac{\partial \psi}{\partial y})_{i,j} = \sum_{k=0}^{M} (Dy)_{j,k} \psi_{i,k}, \tag{2.30}$$

where $N+1$ is the number of points in the x direction, $M+1$ is the number of points in the y direction, Dx is the Chebyshev differentiation matrix related to the x points and Dy is the Chebyshev differentiation matrix related to the y points. Equation (2.29) can be written in the following form,

$$\begin{pmatrix} \frac{\partial \psi}{\partial x}_{0,0} \\ \frac{\partial \psi}{\partial x}_{1,0} \\ \vdots \\ \frac{\partial \psi}{\partial x}_{N,0} \\ \vdots \\ \frac{\partial \psi}{\partial x}_{0,M} \\ \vdots \\ \frac{\partial \psi}{\partial x}_{N,M} \end{pmatrix} = \tag{2.31}$$

$$\begin{pmatrix} (D_x)_{0,0} & (D_x)_{0,1} & \dots & (D_x)_{0,N} & \dots & 0 & \dots & 0 \\ (D_x)_{1,0} & (D_x)_{1,1} & \dots & (D_x)_{1,N} & \dots & 0 & \dots & 0 \\ \vdots & \vdots & \vdots & \vdots & \vdots & \vdots & \vdots & \vdots \\ (D_x)_{N,0} & (D_x)_{N,1} & \dots & (D_x)_{N,N} & \dots & 0 & \dots & 0 \\ \vdots & \vdots & \vdots & \vdots & \vdots & \vdots & \vdots & \vdots \\ 0 & 0 & 0 & 0 & \dots & (D_x)_{0,0} & \dots & (D_x)_{0,N} \\ \vdots & \vdots & \vdots & \vdots & \vdots & \vdots & \vdots & \vdots \\ 0 & 0 & 0 & 0 & \dots & (D_x)_{N,0} & \dots & (D_x)_{N,N} \end{pmatrix} \begin{pmatrix} \psi_{0,0} \\ \psi_{1,0} \\ \vdots \\ \psi_{N,0} \\ \vdots \\ \psi_{0,M} \\ \vdots \\ \psi_{N,M} \end{pmatrix}.$$

Considering $N = 2$, the differential operator matrix for $\frac{\partial}{\partial x}$ will be,

$$\begin{pmatrix} \frac{3}{2} & -2 & \frac{3}{2} & 0 & 0 & 0 & 0 & 0 & 0 \\ \frac{1}{2} & 0 & -\frac{1}{2} & 0 & 0 & 0 & 0 & 0 & 0 \\ -\frac{1}{2} & 2 & -\frac{3}{2} & 0 & 0 & 0 & 0 & 0 & 0 \\ 0 & 0 & 0 & \frac{3}{2} & -2 & \frac{3}{2} & 0 & 0 & 0 \\ 0 & 0 & 0 & \frac{1}{2} & 0 & -\frac{1}{2} & 0 & 0 & 0 \\ 0 & 0 & 0 & -\frac{1}{2} & 2 & -\frac{3}{2} & 0 & 0 & 0 \\ 0 & 0 & 0 & 0 & 0 & 0 & \frac{3}{2} & -2 & \frac{3}{2} \\ 0 & 0 & 0 & 0 & 0 & 0 & \frac{1}{2} & 0 & -\frac{1}{2} \\ 0 & 0 & 0 & 0 & 0 & 0 & -\frac{1}{2} & 2 & -\frac{3}{2} \end{pmatrix}. \tag{2.32}$$

Now, the equation (2.30) can similarly be written in matrix form, as follows

$$\begin{pmatrix} \frac{\partial\psi}{\partial y}_{0,0} \\ \frac{\partial\psi}{\partial y}_{1,0} \\ \vdots \\ \frac{\partial\psi}{\partial y}_{N,0} \\ \vdots \\ \frac{\partial\psi}{\partial y}_{0,M} \\ \vdots \\ \frac{\partial\psi}{\partial y}_{N,M} \end{pmatrix} = \begin{pmatrix} (D_y)_{0,0} & 0 & \dots & 0 & \dots & (D_y)_{0,N} & \dots & 0 \\ 0 & (D_y)_{0,0} & \dots & 0 & \dots & 0 & \ddots & 0 \\ \vdots & \vdots & \vdots & \vdots & \vdots & \vdots & \ddots & \vdots \\ 0 & 0 & \dots & (D_y)_{0,0} & \dots & 0 & \dots & (D_y)_{0,N} \\ \vdots & \vdots & \vdots & \vdots & \vdots & \vdots & \vdots & \vdots \\ (D_y)_{N,0} & 0 & 0 & 0 & \dots & (D_y)_{N,N} & \dots & 0 \\ \vdots & \ddots & \ddots & \vdots & \vdots & \vdots & \vdots & \vdots \\ 0 & 0 & (D_y)_{N,0} & 0 & 0 & 0 & \dots & (D_y)_{N,N} \end{pmatrix} \begin{pmatrix} \psi_{0,0} \\ \psi_{1,0} \\ \vdots \\ \psi_{N,0} \\ \vdots \\ \psi_{0,M} \\ \vdots \\ \psi_{N,M} \end{pmatrix}, \tag{2.33}$$

and let $N = 2$, then the differential operator matrix for $\frac{\partial}{\partial y}$, will be,

$$\begin{pmatrix} \frac{3}{2} & 0 & 0 & -2 & 0 & 0 & \frac{1}{2} & 0 & 0 \\ 0 & \frac{3}{2} & 0 & 0 & -2 & 0 & 0 & \frac{1}{2} & 0 \\ 0 & 0 & \frac{3}{2} & 0 & 0 & -2 & 0 & 0 & \frac{1}{2} \\ \frac{1}{2} & 0 & 0 & 0 & 0 & 0 & -\frac{1}{2} & 0 & 0 \\ 0 & \frac{1}{2} & 0 & 0 & 0 & 0 & 0 & -\frac{1}{2} & 0 \\ 0 & 0 & \frac{1}{2} & 0 & 0 & 0 & 0 & 0 & -\frac{1}{2} \\ -\frac{1}{2} & 0 & 0 & 2 & 0 & 0 & -\frac{3}{2} & 0 & 0 \\ 0 & -\frac{1}{2} & 0 & 0 & 2 & 0 & 0 & -\frac{3}{2} & 0 \\ 0 & 0 & -\frac{1}{2} & 0 & 0 & 2 & 0 & 0 & -\frac{3}{2} \end{pmatrix}. \tag{2.34}$$

When an equation has derivatives with respect to x and y which have to be discretized by Chebyshev methods, the differentiation matrix will contain elements similar to (2.32) and (2.34). This implies that there will be a block of size $(N+1)\times(N+1)$, in the main diagonal, where $N+1$ is the number of Chebyshev points. Figure (2.4) shows the case where $N = 4$ in both directions x and y; the

dots indicate the non-zero entries.

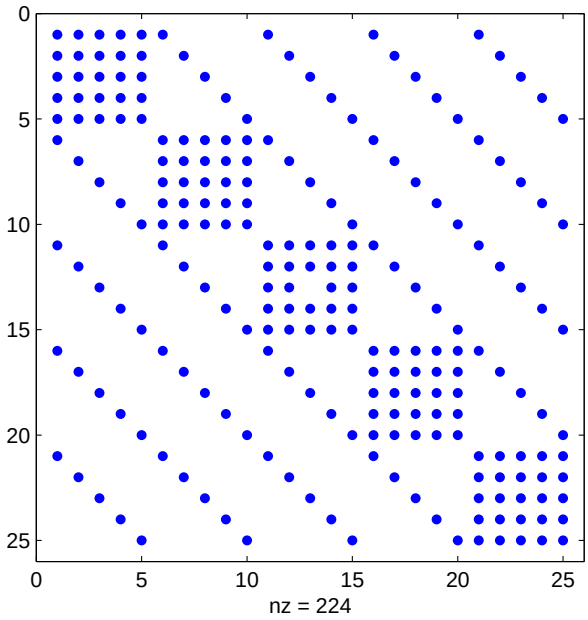

Figure 2.4: The pattern of the two-dimensional differential matrix using $N = 4$.

In some problems we need N to be larger, therefore Figure (2.5) shows what the matrix look like for a realistic value of N. In the Figure, we have $N = 20$ and the shaded lines indicate the non-zero elements. Matrices (2.32) and (2.34) are examples of Chebyshev differentiation matrices discretized on a tensor product spectral grid. The easiest way to generate these matrices is to use the kronecker product, Trefthen (2000). The kronecker product $\bigotimes$ of two matrices, a and b is denoted by $a \otimes b$, and the resulting matrix, C say, is formed by all possible products of elements of a with those of b. If a is a $p \times q$ matrix and b is a $r \times s$, the kronecker product, $C = a \otimes b$, will be a matrix of the size $pr \times qs$ and of the following form

$$C_{k+(i-1)r,m+(j-1)s} = a_{i,j} b_{k,m}$$

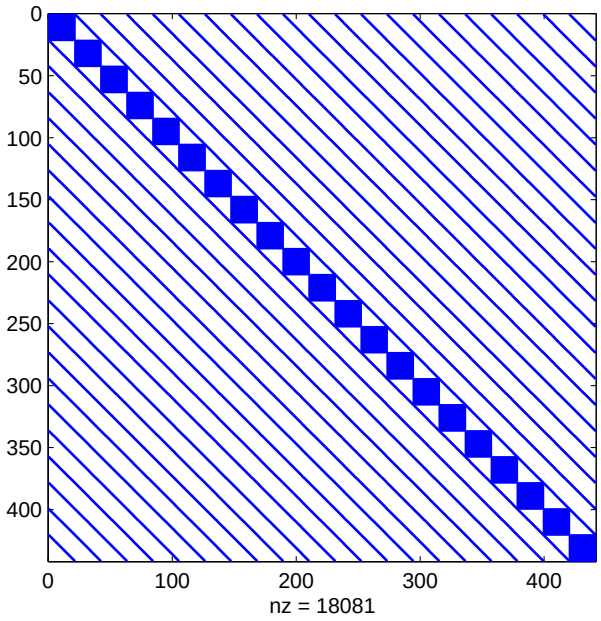

Figure 2.5: The pattern of the two-dimensional differential matrix using $N = 20$.

where $j = 1, 2, ..., q$, $i = 1, 2, ..., p$, $m = 1, 2, ..., s$ and $k = 1, 2, ..., r$. Alternatively, the entries will be assembled in the following way,

$$\begin{pmatrix} a_{1,1} \times b & a_{1,2} \times b & \dots & a_{1,q} \times b \\ a_{2,1} \times b & a_{2,2} \times b & \dots & a_{2,q} \times b \\ \vdots & \vdots & \vdots & \vdots \\ a_{p,1} \times b & a_{p,2} \times b & \dots & a_{p,q} \times b \end{pmatrix}. \tag{2.35}$$

Chapter 3

Solution to the 2-D Navier-Stokes Equations

3.1 Introduction

In this chapter, we consider the steady Navier-Stokes problem to be solved using numerical methods. Firstly, we consider a test problem with a known solution and therefore the results of the numerical simulations can be compared with the exact solution. Secondly, we solve the lid-driven cavity problem, and the results can be compared with previous results. We discretize the problem using Chebyshev discretization in the x and y directions. Because of the non-linearity of the Navier-Stokes equations, Newton linearization is used to work in terms of correction terms. Here, we combine the use of Newton linearization with a direct solver to solve the vorticity-streamfunction formulation. We solve the Navier-Stokes problem exploiting the accuracy of the use of Chebyshev discretization to obtain the numerical solution at high Reynolds number and to recognize the type of resulting matrix. The resulting matrix which arise from the discretization is

usually full and the linear system is solved by a direct solver.

3.2 Test Problem

3.2.1 Problem Formulation

The equations that describe the flow of an incompressible unsteady fluid flow in non-dimensional form are the continuity equation,

$$u_x + v_y = 0, \tag{3.1}$$

and the Navier-Stokes equations,

$$u_t + (u.\nabla)u = -\nabla P + \frac{1}{Re}\nabla^2 u \tag{3.2}$$

$$v_t + (u.\nabla)v = -\nabla P + \frac{1}{Re}\nabla^2 v, \tag{3.3}$$

where (u, v) is the velocity of fluid in the (x, y) directions, P is the fluid pressure and the Reynolds number Re is defined as $\frac{Uw}{\nu}$, where U is the velocity of the lid and w is the cavity width.

An alternative formulation of two-dimensional Navier-Stokes equations is to use the vorticity (ω) and streamfunction (ψ) as dependent variables. Equations (3.1), (3.2) and (3.3) are expressed in terms of streamfunction (ψ where $u = \psi_y$ and $v = -\psi_x$) and vorticity ($\omega = v_x - u_y$), which gives the following formulation,

$$\begin{aligned} \nabla^2\psi &= \omega \\ \text{and} \quad \omega_t + \psi_y\omega_x - \psi_x\omega_y &= \frac{1}{Re}\nabla^2\omega. \end{aligned} \tag{3.4}$$

To test our methods, we first work with a simple modification to the above equations; namely

$$\begin{aligned} \nabla^2\psi &= \omega \\ \text{and} \quad \psi_y\omega_x - \psi_x\omega_y &= \frac{1}{Re}\nabla^2\omega + F(x,y), \end{aligned} \tag{3.5}$$

where

$$F(x,y) = \left((y-1)Re^{\frac{1}{2}}+1\right) Re \quad e^{-Re^{\left(\frac{1}{2}\right)}y}\sin x\cos x - \frac{1}{Re}\sin x\left((Re-1)^2 e^{Re^{\left(\frac{1}{2}\right)}y} + y - 1\right).$$

These equations, together with the boundary conditions, see Figure (3.1)

$$\begin{cases} \psi = 0 \quad \text{and} \quad \omega = 0 \quad , & \text{for} \quad x = 0, \quad 0 \le y \le 1, \\ \psi = 0 \quad \text{and} \quad \omega = 0 \quad , & \text{for} \quad x = \pi, \quad 0 \le y \le 1, \\ \psi = 0 \quad \text{and} \quad \omega = Re\sin x \quad , & \text{for} \quad y = 0, \quad 0 \le x \le \pi, \\ \psi = e^{-\sqrt{Re}}\sin x \quad \text{and} \quad \omega = (Re-1)e^{-\sqrt{Re}y}\sin x \quad , & \text{for} \quad y = 1, \quad 0 \le x \le \pi, \end{cases} \tag{3.6}$$

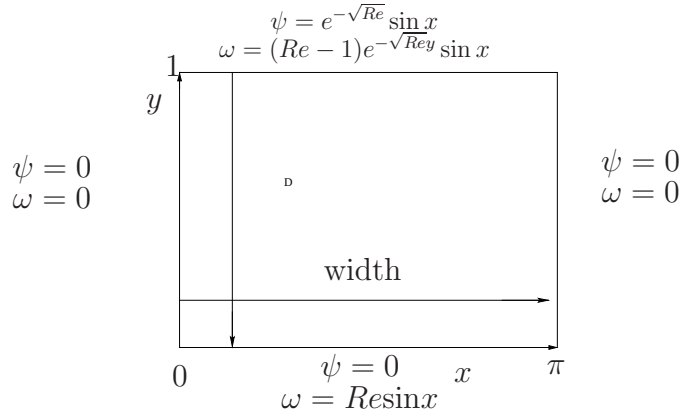

Figure 3.1: Sketch of the lid-driven cavity boundary condition.

have an exact solution given by

$$\psi = (y + e^{-\sqrt{Re}y} - 1)\sin x \tag{3.7}$$

$$\omega = (e^{-\sqrt{Re}y}(Re - 1) - (y - 1))\sin x. \tag{3.8}$$

3.2.2 Discretization in x and y Directions

In the x and y directions, Chebyshev collocation is used, evaluating the function values at the collocation points. As mentioned previously, we use the collocation in both directions for this test problem to see the accuracy of the Chebyshev collocation method and to gain the high resolution which is required to resolve the thin layers at high Reynolds number. The mapping $x \in (0, 1) \rightarrow z \in (-1, 1)$ in Chebyshev space has to be used such that the collocation points are given by

$$z = z_j = \cos(\frac{j\pi}{N}), \qquad j = 0, 1, ..., N, \tag{3.9}$$

and

$$x = x(z_i) = x_i = \frac{\pi}{2}(z_i + 1), \qquad j = 0, 1, ..., N. \tag{3.10}$$

In a similar way, the mapping can be used for the y direction,

$$y = y(z_j) = y_j = \frac{1}{2}(z_j + 1), \qquad j = 0, 1, ..., M. \tag{3.11}$$

The function $\psi_{i,j}$ is defined as $\psi_{i,j} = \psi(x = x_i, y = y_j)$. Then, the derivatives in x and y are given respectively as follows

$$\left(\frac{\partial \psi}{\partial x}\right)_{i,j} = \frac{2}{\pi}\sum_{k=0}^{N} D1_{i,k}\psi_{k,j}, \quad \Rightarrow \left(\frac{\partial^2 \psi}{\partial x^2}\right)_{i,j} = \frac{4}{\pi^2}\sum_{k=0}^{N} D1^2_{i,k}\psi_{k,j} \tag{3.12}$$

$$\left(\frac{\partial\psi}{\partial y}\right)_{i,j} = 2\sum_{k=0}^{M} D2_{j,k}\psi_{i,k}, \quad \Rightarrow \left(\frac{\partial^2\psi}{\partial y^2}\right)_{i,j} = 4\sum_{k=0}^{M} D2^2_{j,k}\psi_{i,k}, \tag{3.13}$$

where $D1$ and $D2$ are the differentiation matrices as described previously and N,M are the number of points in the x and y directions respectively. The second derivative can be obtained simply by squaring the differentiation matrix. Therefore, the discrete forms of the equations are

$$\omega_{i,j} = \frac{4}{\pi^2}\sum_{k=0}^{N} D1^2_{i,k}\psi_{k,j} + 4\sum_{k=0}^{M} D2^2_{j,k}\psi_{i,k}, \tag{3.14}$$

$$\begin{aligned} 2\sum_{k=0}^{M} D2_{j,k}\psi_{i,k}\frac{2}{\pi}\sum_{k=0}^{N} D1_{i,k}\omega_{k,j} \quad &- \quad \frac{2}{\pi}\sum_{k=0}^{N} D1_{i,k}\psi_{k,j}2\sum_{k=0}^{M} D2_{j,k}\omega_{i,k} \\ = \frac{1}{Re}(\frac{4}{\pi^2}\sum_{k=0}^{N} D1^2_{i,k}\psi_{k,j} \quad &+ \quad 4\sum_{k=0}^{M} D2^2_{j,k}\psi_{i,k}). \end{aligned} \tag{3.15}$$

3.2.3 Linearization

One difficulty with the system, (3.14) and (3.16), is the non-linearity. The non-linearity can be overcome by using a Newton-Raphson linearization and working in terms of correction terms. Let Ψ and Ω be the correction terms where

$$\omega_{i,j} = \bar{\omega}_{i,j} + \Omega_{i,j}, \tag{3.16}$$

$$\psi_{i,j} = \bar{\psi}_{i,j} + \Psi_{i,j}, \tag{3.17}$$

such that $|\Psi_{i,j}|,|\Omega_{i,j}| \ll 1$. The overbar quantities denote some initial guesses. Substituting (3.16) and (3.17) in (3.14) and (3.16) leads to

$$\bar{\omega}_{i,j} + \Omega_{i,j} = \frac{4}{\pi^2}\sum_{k=0}^{N} D1_{i,k}^2(\bar{\psi}_{k,j} + \Psi_{k,j}) + 4\sum_{k=0}^{M} D2_{j,k}^2(\bar{\psi}_{i,k} + \Psi_{i,k}), \tag{3.18}$$

and

$$2\sum_{k=0}^{M} D2_{j,k}(\bar{\psi}_{i,k}+\Psi_{i,k})\frac{2}{\pi}\sum_{k=0}^{N} D1_{i,k}(\bar{\omega}_{k,j}+\Omega_{k,j}) - \frac{2}{\pi}\sum_{k=0}^{N} D1_{i,k}(\bar{\psi}_{k,j}+\Psi_{k,j})2\sum_{k=0}^{M} D2_{j,k}(\bar{\omega}_{i,k}+\Omega_{i,k}) = Rh_{i,j} \tag{3.19}$$

where

$$Rh_{i,j} = \frac{4}{\pi^2 Re}\sum_{k=0}^{N} D1_{i,k}^2(\bar{\omega}_{k,j} + \Omega_{k,j}) + \frac{4}{Re}\sum_{k=0}^{M} D2_{j,k}^2(\bar{\omega}_{i,k} + \Omega_{i,k}).$$

The above are linearized equations by neglecting second-order quantities to give

$$\Omega_{i,j} - \frac{4}{\pi^2}\sum_{k=0}^{N} D1_{i,k}^2\Psi_{k,j} - 4\sum_{k=0}^{M} D2_{j,k}^2\Psi_{i,k} = R1_{i,j}, \tag{3.20}$$

where

$$R1_{i,j} = \frac{4}{\pi^2}\sum_{k=0}^{N} D1_{i,k}^2\bar{\psi}_{k,j} + 4\sum_{k=0}^{M} D2_{j,k}^2\bar{\psi}_{i,k} - \bar{\omega}_{i,j},$$

and

$$\begin{aligned} & \left\{\frac{4}{\pi}\sum_{k=0}^{M} D2_{j,k}\bar{\psi}_{i,k}\sum_{k=0}^{N} D1_{i,k} - \frac{4}{\pi}\sum_{k=0}^{N} D1_{i,k}\bar{\psi}_{k,j}\sum_{k=0}^{M} D2_{j,k}\right. \\ - & \left.\frac{4}{\pi^2 Re}\sum_{k=0}^{N} D1_{i,k}^2 - \frac{4}{Re}\sum_{k=0}^{M} D2_{j,k}^2\right\}\Omega_{i,j} \\ + & \left\{\frac{4}{\pi}\sum_{k=0}^{N} D1_{i,k}\bar{\omega}_{k,j}\sum_{k=0}^{M} D2_{j,k} - \frac{4}{\pi}\sum_{k=0}^{M} D2_{j,k}\bar{\omega}_{i,k}\sum_{k=0}^{N} D1_{i,k}\right\}\Psi_{i,j} = R2_{i,j}, \end{aligned} \tag{3.21}$$

where

$$R2_{i,j} = \frac{4}{\pi^2 Re}\sum_{k=0}^{N} D1^2_{i,k}\bar{\omega}_{k,j} + \frac{4}{Re}\sum_{k=0}^{M} D2^2_{j,k}\bar{\omega}_{i,k}$$
$$-\frac{4}{\pi}\sum_{k=0}^{M} D2_{j,k}\bar{\psi}_{i,k}\sum_{k=0}^{N} D1_{i,k}\bar{\omega}_{k,j}$$
$$+\frac{4}{\pi}\sum_{k=0}^{N} D1_{i,k}\bar{\psi}_{k,j}\sum_{k=0}^{M} D2_{j,k}\bar{\omega}_{i,k}.$$

Collecting the discrete equations together gives the following system of the form

$$\begin{pmatrix} A & B \\ C & D \end{pmatrix}\begin{pmatrix} \Omega \\ \Psi \end{pmatrix} = \begin{pmatrix} R1 \\ R2 \end{pmatrix} \tag{3.22}$$

where $A = (A_{i,j})\,, \quad B = (B_{i,j})\,, \quad C = (C_{i,j})\,, \quad D = (D_{i,j})$ and

$$\begin{aligned}
A_{i,j} &= I_{i,j} \\
B_{i,j} &= -\frac{4}{\pi^2}\sum_{k=0}^{N} D1^2_{i,k}\Psi_{k,j} - 4\sum_{k=0}^{M} D2^2_{j,k}\Psi_{i,k} \\
C_{i,j} &= \frac{4}{\pi}\sum_{k=0}^{M} D2_{j,k}\bar{\psi}_{i,k}\sum_{k=0}^{N} D1_{i,k} - \frac{4}{\pi}\sum_{k=0}^{N} D1_{i,k}\bar{\psi}_{k,j}\sum_{k=0}^{M} D2_{j,k} \\
&- \frac{4}{\pi^2 Re}\sum_{k=0}^{N} D1^2_{i,k} - \frac{4}{Re}\sum_{k=0}^{M} D2^2_{j,k} \\
D_{i,j} &= \frac{4}{\pi}\sum_{k=0}^{N} D1_{i,k}\bar{\omega}_{k,j}\sum_{k=0}^{M} D2_{j,k} - \frac{4}{\pi}\sum_{k=0}^{M} D2_{j,k}\bar{\omega}_{i,k}\sum_{k=0}^{N} D1_{i,k}.
\end{aligned}$$

Here, the matrices A, B, C and D are those of size $(N+1)\times(M+1)$, and the vectors $R1$ and $R2$ are those of size $(N+1)(M+1)\times 1$. Recall that the Kronecker operator can be used to give the Chebyshev differentiation matrices.

For example, matrix C can be written as follows

$$\begin{aligned} C &= \frac{4}{\pi}(((D2 \otimes I1)\bar{\psi})) * (I2 \otimes D1)) - \frac{4}{\pi}\text{diag}(((I2 \otimes D1)\bar{\psi})) * ((D2 \otimes I1)) \\ &- (\frac{4}{\pi^2 Re})(I2 \otimes D1^2) - (\frac{4}{Re})(D2^2 \otimes I1), \end{aligned}$$

where $I1$ is the identity matrix of size $(N+1) \times (N+1)$ and $I2$ is the identity matrix of size $(M+1) \times (M+1)$. The vectors $\bar{\psi}, \bar{\omega}, \Psi$ and Ω have to be ordered in a particular way, similar to the way of ordering the vector (2.18). After applying the Newton linearization, the boundary condition becomes

$$\begin{cases} \Psi_{i,j} = -\bar{\psi}_{i,j} \quad \& \quad \Omega_{i,j} = -\bar{\omega}_{i,j} & \text{for}, x = 0, \\ \Psi_{i,j} = -\bar{\psi}_{i,j} \quad \& \quad \Omega_{i,j} = -\bar{\omega}_{i,j} & \text{for}, x = \pi, \\ \Psi_{i,j} = -\bar{\psi}_{i,j} \quad \& \quad \Omega_{i,j} = Re \sin x_i - \bar{\psi}_{i,j} & \text{for}, y = 0, \\ \Psi_{i,j} = e^{-\sqrt{Re}} \sin x_i - \bar{\psi}_{i,j} \quad \& \quad \Omega_{i,j} = (Re-1)e^{-\sqrt{Rey}} \sin x_i - \bar{\omega}_{i,j} & \text{for}, y = 1. \end{cases} \tag{3.23}$$

The linear system (3.22) has been solved after imposing the boundary conditions (3.23) in the MATLAB programming environment, and the obtained results are presented in the next section.

3.2.4 Numerical Results

A direct solver has been used to solve the linear system (3.22) with the boundary conditions (3.23) in order to obtain the streamline function ψ and vorticity ω. The solver combined the Newton iteration with the MATLAB backslash (\) operator to obtain the solution corrected by correction terms Ψ and Ω, as mentioned above. The convergence stopping criteria that halt the Newton iteration when

the desired corrections have been made is as follows,

$$\epsilon = \max\left(R_\Psi, R_\Omega\right) \leq 10^{-6} \tag{3.24}$$

where R_Ψ and R_Ω are the infinite norm of the correction terms vectors Ψ and Ω respectively. In other words, they can be written as $R_\Psi = \|\Psi\|_\infty$ and $R_\Omega = \|\Omega\|_\infty$. In Figure (3.2), we fix the number of points in one direction and vary the number of points in the other direction from 3 to 40 to obtain the numerical solution at $Re = 1$. This shows how the numerical error decreases quickly as the number of points is increased. It is obvious that the numerical solution converges to the exact solution and Table (3.1) emphasize that. The numerical errors of ψ, tabulated in (3.1) on various grids for $Re = 1$, are calculated such that $\|\psi_{exact} - \psi_{numerical}\|_\infty$. Also, the numerical errors of ω listed in the same table are calculated in the same way. Figure (3.3) shows the relation between the numerical error and Re on various grids. It also shows the dependence of the grid size to the accuracy of the solutions. The method maintains the accuracy if the implementation is run on a fine grid as in Figures (3.4). From these figures, one can see that the maximum error occurs near the boundary conditions where the solution changes quickly. Furthermore, it can be observed that the error increases as we increase the Reynolds number, see Figures (3.3,3.4).

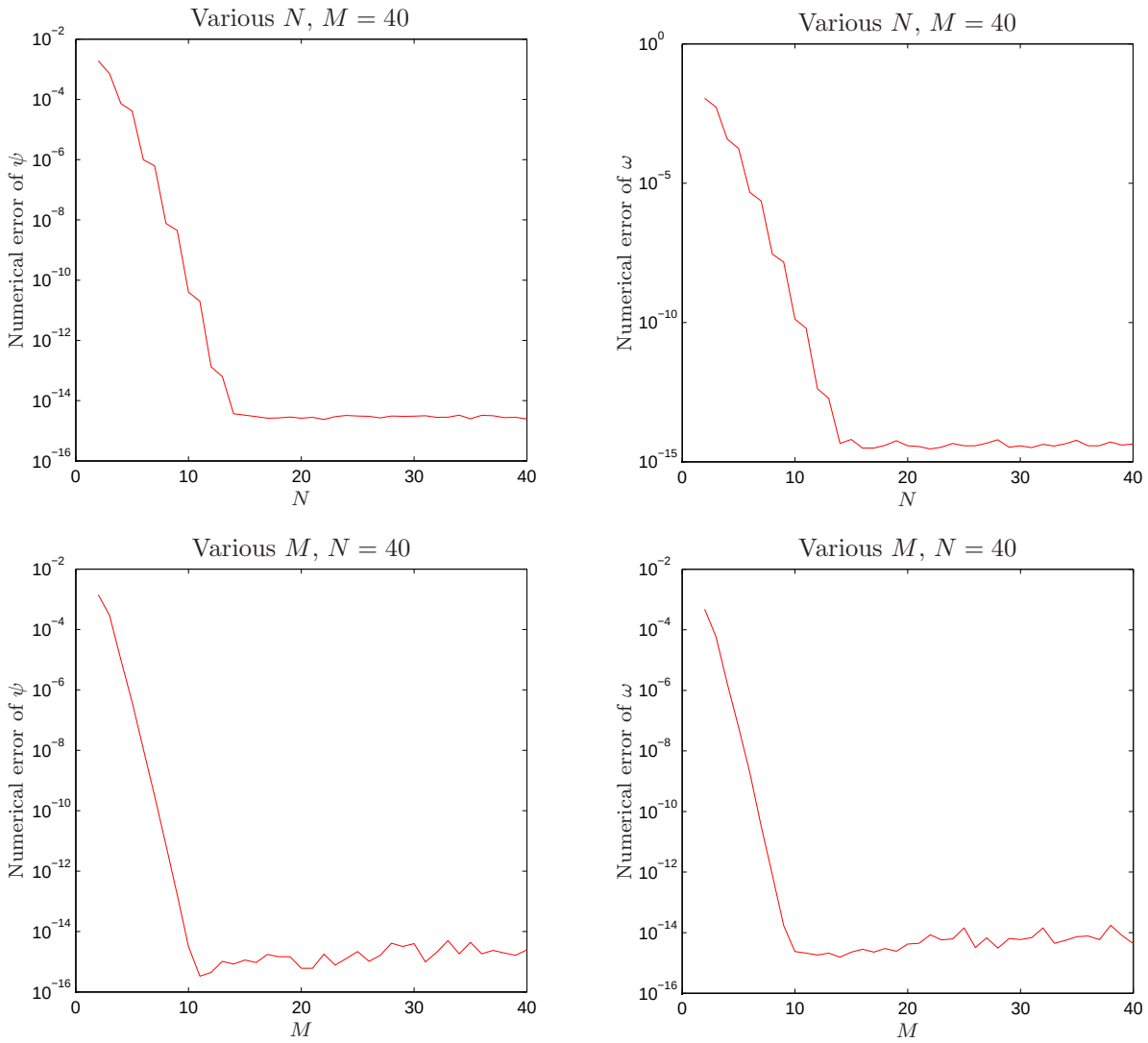

Figure 3.2: Numerical error of ψ (left) and ω (right) at $Re = 1$.

Grid size	Error of ψ	Error of ω
5×5	7.03895E-4	1.12039E-2
10×10	3.97234E-10	6.34623E-9
20×20	3.16414E-15	4.52971E-14
30×30	6.38378E-15	3.97460E-14
40×40	2.77556E-15	5.77316E-14

Table 3.1: Numerical error of ψ and ω at $Re = 1$ on various grids.

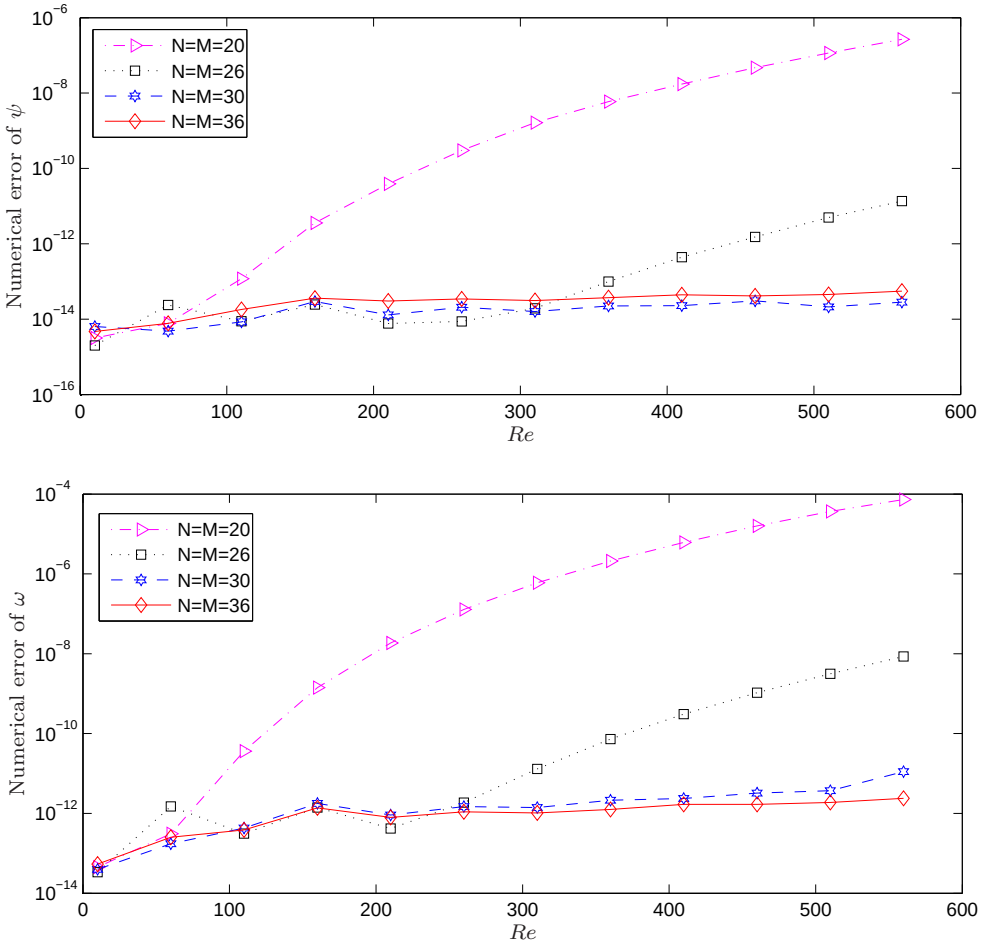

Figure 3.3: Numerical error of various Re on various grids size.

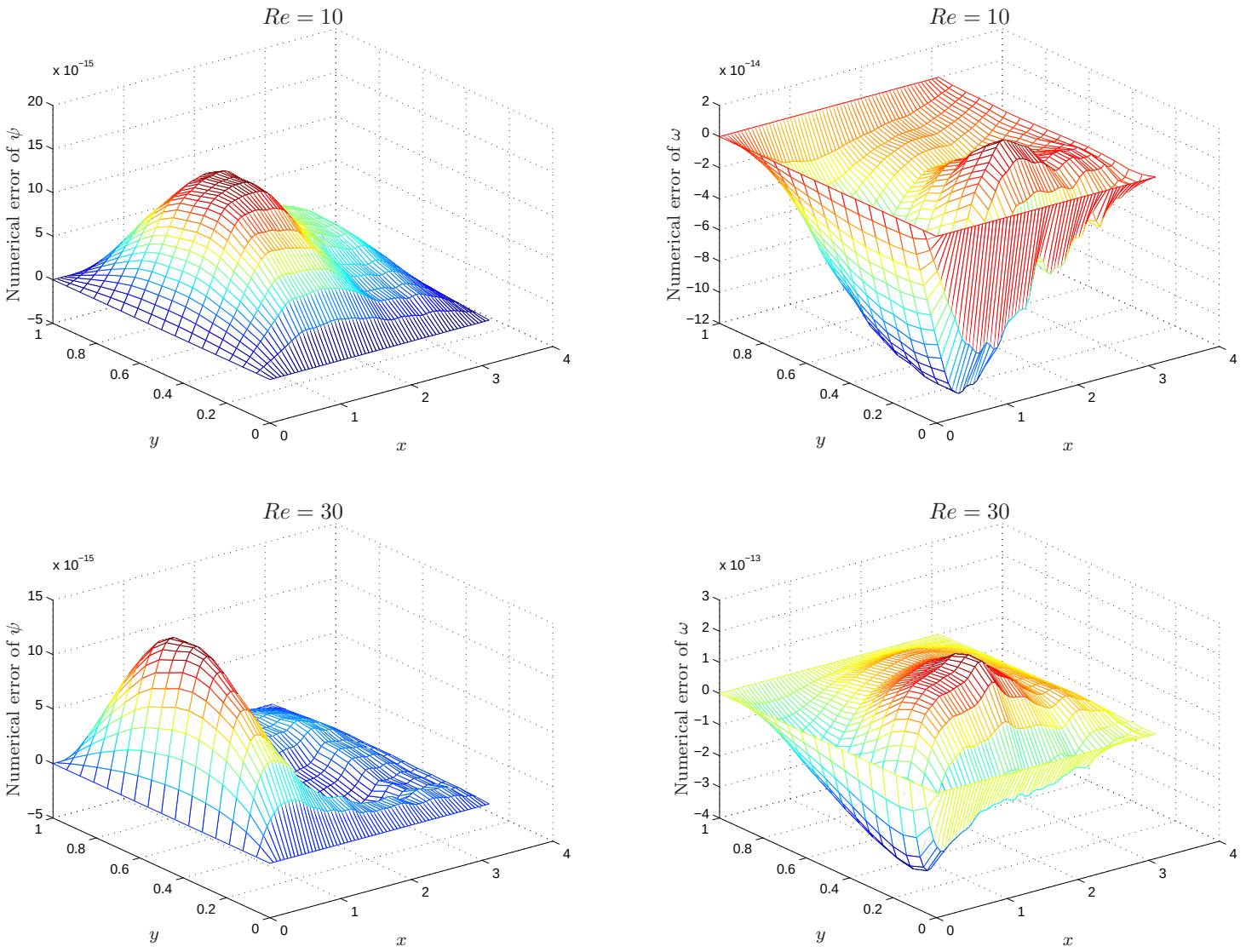

Figure 3.4: Numerical error of ψ (left) and ω (right) at $Re = 10, 30$ on a 51×51 grid.

3.3 Solution to 2-D Lid-Driven Cavity

In this section, we consider the two-dimensional lid-driven cavity to be solved using the same technique that has been used to solve the test problem above. Setting the function F in the system (3.5) to zero with the boundary conditions shown in Figure (3.5) leads to the lid-driven cavity problem.

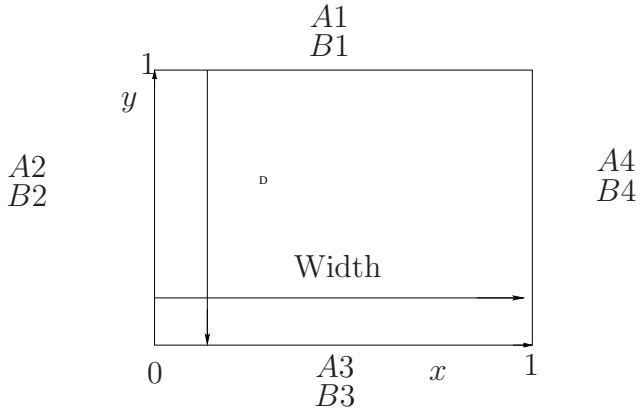

Figure 3.5: Sketch of the lid-driven cavity boundary condition.

In Figure (3.5), the various quantities are given as

$$
\begin{cases}
A1: & \psi = 0, & \text{for} \quad 0 < x < 1, \quad y = 1 \\
B1: & \psi_y = 1, & \text{for} \quad 0 < x < 1, \quad y = 1 \\
A2: & \psi = 0, & \text{for} \quad 0 < y < 1, \quad x = 0 \\
B2: & \int_0^1 \left(\frac{\partial^2 \psi}{\partial y^2} - \omega \right) dx = 0, & \text{for} \quad 0 < y < 1, \quad x = 0 \\
A3: & \psi = 0, & \text{for} \quad 0 < x < 1, \quad y = 0 \\
B3: & \psi_y = 0, & \text{for} \quad 0 < x < 1, \quad y = 0 \\
A4: & \psi = 0, & \text{for} \quad 0 < y < 1, \quad x = 1 \\
B4 & \int_0^1 \left[\int_0^x \left(\frac{\partial^2 \psi}{\partial y^2} - \omega \right) dx \right] dx = 0, & \text{for} \quad 0 < y < 1, \quad x = 1.
\end{cases}
\tag{3.25}
$$

At the corners of $y = 1$, we use a different boundary condition, which is

$$\int_0^1 \left(\frac{\partial^2 \psi}{\partial x^2} - \omega \right) dy = 1,$$

while for the boundary conditions of the corners of $y = 0$, we use

$$\int_0^1 \left[\int_0^y \left(\frac{\partial^2 \psi}{\partial x^2} - \omega \right) dy \right] dy = 0.$$

3.3.1 Derivation and Implementation of Boundary Conditions

After applying the Newton linearization, the boundary conditions become

$$\begin{cases} \Psi = -\bar{\psi}, & \text{for} \quad 0 < x < 1, \quad y = 1 \\ \Psi_y = 1 - \bar{\psi}_y, & \text{for} \quad 0 < x < 1, \quad y = 1 \\ \Psi = -\bar{\psi}, & \text{for} \quad 0 < y < 1, \quad x = 0 \\ \int_0^1 \left(\frac{\partial^2 \Psi}{\partial y^2} - \Omega \right) dx = -\int_0^1 \left(\frac{\partial^2 \bar{\psi}}{\partial y^2} - \bar{\omega} \right) dx, & \text{for} \quad 0 < y < 1, \quad x = 0 \\ \Psi = -\bar{\psi}, & \text{for} \quad 0 < x < 1, \quad y = 0 \\ \Psi_y = \bar{\psi}_y, & \text{for} \quad 0 < x < 1, \quad y = 0 \\ \Psi = -\bar{\psi}, & \text{for} \quad 0 < y < 1, \quad x = 1 \\ \int_0^1 \left[\int_0^x \left(\frac{\partial^2 \Psi}{\partial y^2} - \Omega \right) dy \right] dx = \int_0^1 \left[\int_0^x \left(\frac{\partial^2 \bar{\psi}}{\partial y^2} - \bar{\omega} \right) dx \right] dx & \text{for} \quad 0 < y < 1, \quad x = 1. \end{cases}$$

For the corners of $y = 1$, the boundary conditions become

$$\int_0^1 \left(\frac{\partial^2 \Psi}{\partial x^2} - \Omega \right) dy = -1 - \int_0^1 \left(\frac{\partial^2 \bar{\psi}}{\partial x^2} - \bar{\omega} \right) dy,$$

and for the boundary conditions of the corners of $y = 0$, the boundary conditions become

$$\int_0^1 \left[\int_0^y \left(\frac{\partial^2 \Psi}{\partial x^2} - \Omega \right) dy \right] dy = - \int_0^1 \left[\int_0^y \left(\frac{\partial^2 \bar{\psi}}{\partial x^2} - \bar{\omega} \right) dy \right] dy.$$

One difficulty arises when using the vorticity-streamfunction formulation is the implementation of the no-slip boundary condition on the domain. Here, a technique similar to one used by Davies & Carpenter (1997), Azzam (2003), Gajjar & Azzam (2004) and Davies & Carpenter (2001) is employed, where some integral constraints are used instead. These integral relations are derived from the Navier-Stokes equations by integration, which leads to the compatibility constraints on the vorticity. Consider the Navier Stokes equations (3.4) in the domain $0 \leq x \leq 1$ and $0 \leq y \leq 1$, with the boundary condition (3.25). These constraints conditions are found by integrating the first equation of (3.4) system with respect to y to obtain

$$\int_0^y \left(\frac{\partial^2 \psi}{\partial x^2} + \frac{\partial^2 \psi}{\partial y^2} - \omega \right) dy = 0, \tag{3.26}$$

which gives

$$[\psi_y]_0^y + \int_0^y \left(\frac{\partial^2 \psi}{\partial x^2} - \omega \right) dy = 0. \tag{3.27}$$

By evaluating this at $y = 1$ and making use of conditions on ψ_y, we obtain

$$1 + \int_0^1 \left(\frac{\partial^2 \psi}{\partial x^2} - \omega \right) dy = 0. \tag{3.28}$$

Putting $\omega_{i,j} = \bar{\omega}_{i,j} + \Omega_{i,j}, \psi_{i,j} = \bar{\psi}_{i,j} + \Psi_{i,j}$ gives

$$\int_0^1 \left(\frac{\partial^2 \Psi}{\partial x^2} - \Omega \right) dy = - \int_0^y \left(\frac{\partial^2 \bar{\psi}}{\partial x^2} - \bar{\omega} \right) dy - 1. \tag{3.29}$$

Equation (3.29) is one condition that we make use of. The second condition can be obtained by integrating (3.26) again with respect to y, which gives

$$\int_0^1 [\psi_y]_0^1 + \int_0^1 \left[\int_0^y \left(\frac{\partial^2 \psi}{\partial x^2} - \omega\right) dy\right] dy = 0, \tag{3.30}$$

and hence

$$\psi(1) - \psi(0) + \int_0^1 \left[\int_0^y \left(\frac{\partial^2 \psi}{\partial x^2} - \omega\right) dy\right] dy = 0. \tag{3.31}$$

Using $\psi(1) = \psi(0) = 0$ on $y = 0$, we find

$$\int_0^1 \left[\int_0^y \left(\frac{\partial^2 \psi}{\partial x^2} - \omega\right) dy\right] dy = 0. \tag{3.32}$$

Putting $\omega_{i,j} = \bar{\omega}_{i,j} + \Omega_{i,j}, \psi_{i,j} = \bar{\psi}_{i,j} + \Psi_{i,j}$ gives

$$\int_0^1 \left[\int_0^y \left(\frac{\partial^2 \Psi}{\partial x^2} - \Omega\right)\right] dy = -\int_0^1 \left[\int_0^y \left(\frac{\partial^2 \bar{\psi}}{\partial x^2} - \bar{\omega}\right) dy\right] dy. \tag{3.33}$$

From both conditions, it is obvious that we need to approximate the integrals of the form $\int h(y)dy$ at $h(y_i)$, where $h(y) = \int_0^y g(y_1)dy_1$. This can be obtained using Gaussian Quadrature with Legendre Polynomial as basis functions, such that

$$I = \int_0^1 h(y)dy = \sum_{j=1}^{N} q_j h(p_j) \tag{3.34}$$

where q_j are known weights and p_j are known points. If we let N be the degree of the approximating Chebyshev polynomial, then $h(y)$ can be written as follows

$$h(y) = \sum_{n=0}^{N} a_n T_n(z), \tag{3.35}$$

so that

$$h(y_k) = \sum_{n=0}^{N} a_n T_n(z_k),$$

where z_k are the Chebyshev collocation points in $[0, 1]$) for $k = 0, 1, 2, ..., N$. This leads to the following matrix form

$$(\mathbf{H})_{N+1\times 1} = (\mathbf{T})_{(N+1)\times(N+1)}(\mathbf{a})_{(N+1)\times 1}$$

where $\mathbf{T} = (T_{jk}) = T_k(z_j) = \cos(n\cos^{-1}(z_j)) = \cos(\frac{njp}{N})$ where $j = 0, 1, 2, ..., N$ and $\mathbf{H} = (h(y_k))$. Hence, $\mathbf{a} = a_k$ can be written as

$$\underline{\mathbf{a}} = (\mathbf{T})^{-1}\mathbf{H}.$$

To approximate the h at the quadrature points, Equation 3.35 can be used to give

$$h(p_j) = \sum_{n=0}^{N} a_n T_n(\bar{z}_j), \qquad j = 1, 2, ..., NC$$

where $\bar{z}_j = j/NC$ where $j = 0, 1, 2, ..., NC$. Hence, the vector $\underline{h} = h(p_j)$ can be given as

$$\underline{\mathbf{h}} = (\underline{\mathbf{B}})_{NC+1\times(N+1)} \begin{pmatrix} a_0 \\ \vdots \\ a_n \end{pmatrix} \tag{3.36}$$

where $\underline{\mathbf{B}}_{jn} = T_n(\bar{z}_j)$. Substituting $\underline{a}$ in (3.36) gives

$$\underline{\mathbf{h}} = \left(\underline{\mathbf{B}}(\underline{\mathbf{T}})^{-1}\right)\underline{\mathbf{H}}.$$

Therefore, $\mathbf{I}$ can be given by

$$\mathbf{I} = \underline{\mathbf{q}}.\underline{\mathbf{h}} = \underline{\mathbf{q}}.\left(\underline{\mathbf{B}}(\mathbf{T})^{-1}\right)\underline{\mathbf{H}}.$$

The above discussion is the same as in Azzam (2003). By the same token, the other boundary conditions integrals can be derived by integrating the first equation of (3.4) system with respect to x.

3.3.2 Numerical Results for Lid-Driven Cavity Flow

In this section, numerical results are discussed for the square-driven cavity. As already described, the problem was discretized using the spectral collocation method in both directions, x and y, and then solved directly using MATLAB. The upper moving wall boundary condition has been modified to $\psi_y = 1 - e^{500x(1-x)}$ to avoid the difficulty of a singularity at the corner. Without this modification and solving for the cavity problem we could not generate results at high Reynolds number as the code fails to converge. Figures (3.6,3.7) show the u-velocity profiles along the vertical lines passing the geometry center of the cavity; $x = 1/2$. Moreover, the Figure (3.8) shows the v-velocity profiles along the horizontal lines, passing the geometric center of the cavity; $y = 1/2$ on a 121×121 grid at $5000 \leq Re \leq 12500$. The high Re profiles of u-velocity show a sharp twist near $y = 1$, which can be observed clearly when $Re \geq 5000$ in Figure 3.7. A similar behavior can be observed in the profiles of v-velocity when x is close to 1. Ghia *et al.* (1982) have reported the same behavior and mentioned that the kink move towards the upper wall as Re increases, as noted in Figure 3.7. The u-velocity and v-velocity profiles in Figures (3.6-3.8) show a good agreement with the well-known Ghia *et al.* (1982) study. Furthermore, good agreement is

observed with Erturk *et al.* (2005) results for $Re \leq 12500$. For $Re \geq 15000$, one can note the deviation between the present results and those of Erturk *et al.* (2005) as Re increases, see Figure 3.7. We believe that the present work results are more accurate for two reasons. Firstly, Erturk *et al.* (2005) generated the results using the finite difference method, while in the present work we use a spectral method in both directions. Secondly, Tables (3.4-3.8) show an agreement with Azzam (2003) results where a Chebyshev collocation discretization has been used in one direction and finite difference in the other direction. However, there is some disagreement with Azzam (2003) in some precise features for high Reynolds numbers $Re \geq 15000$ which will be mentioned later. The Figure (3.9) shows a good agreement of vorticity quantity along the moving wall of the cavity, with the results tabulated by Ghia *et al.* (1982) at various Re. An often compared quantity is the tabulating of u-velocity values along the horizontal line passing through the geometry center and, similarly, tabulating the v-velocity values along the vertical line passing through the geometry center. A difficulty is faced when we want to tabulate these values to be compared with some reference results. That is, previous investigators have worked on uniform grids unlike the present work which is carried out on non-uniform grids. Therefore, the possibility of finding common points is low and, hence, the present results had to be approximated on a uniform grid. For this purpose, approximation of the present results are calculated on uniform grid. We know that a smooth function $f(x)$ can be approximated using Chebyshev polynomials, as explained in Chapter 2, as follows

$$f(x) = \sum_{k=0}^{N} a_k T_k(x), \tag{3.37}$$

where N is the number of nodes and a_k will be explained shortly. Consider that the data of u-velocity along the horizontal line passing through the cavity center on x_j points is expressed in vector $u(x)$, where

$$x_j = \cos\frac{j\pi}{N} \qquad j = 0, ..., N.$$

According to 3.37, a data of $u(x)$ can be approximated using Chebyshev polynomials as follows

$$u(x_j) = \sum_{k=0}^{N} a_k T_k(x_j). \tag{3.38}$$

For simplicity of notation, let $u(x_j) = u_j$. In matrix form Equation 3.38 can be written as

$$\underline{\mathrm{u}} = \begin{pmatrix} u_0 \\ u_1 \\ \vdots \\ \vdots \\ u_N \end{pmatrix} = \begin{pmatrix} \\ \underline{\mathbf{T}} \\ \\ \end{pmatrix} \begin{pmatrix} a_0 \\ a_1 \\ \vdots \\ \vdots \\ a_N \end{pmatrix}, \tag{3.39}$$

where $\underline{\mathrm{T}} = T_{jk} = T_k(x_j) = \cos(k\cos^{-1}(x_j))$. From (3.39), the coefficient vector a can be written as follows

$$\mathbf{a} = \mathbf{T}^{-1}\mathbf{u} \qquad k = 0, 1, ..., N. \tag{3.40}$$

Now, we want the value of $u(x_j)$ on the uniform spacing points. In other words, we want the value of $u(\bar{x_j})$, where

$$\bar{x_j} = \frac{j}{p} \qquad j = 0, 1, ..., p.$$

Here p, is the number of points. From 3.37, the approximation at the equi-spaced points can be written as follows

$$u(\bar{x_j}) = \sum_{k=0}^{N} a_k T_k(\bar{x_j}), \tag{3.41}$$

which leads the matrix form as

$$\underline{\mathrm{u}} = \begin{pmatrix} u(\bar{x_0}) \\ u(\bar{x_1}) \\ \vdots \\ \vdots \\ u(\bar{x_p}) \end{pmatrix}_{(p+1\times 1)} = \begin{pmatrix} & & \\ & \bar{\underline{\mathbf{T}}} & \\ & & \end{pmatrix}_{p+1\times N+1} \begin{pmatrix} a_0 \\ a_1 \\ \vdots \\ \vdots \\ a_N \end{pmatrix}_{(N+1\times 1)}, \tag{3.42}$$

where $\bar{\underline{\mathbf{T}}} = (\bar{T}_{jk}) = (\bar{T}_k(\bar{x}_j)) = \cos(k \arccos(\bar{x}_j))$. Putting $\mathbf{a} = \mathbf{T}^{-1}\mathbf{u}$ provides the desired value at equi-spaced points

$$\underline{\mathrm{u}} = \begin{pmatrix} u(\bar{x_0}) \\ u(\bar{x_1}) \\ \vdots \\ \vdots \\ u(\bar{x_p}) \end{pmatrix} = \begin{pmatrix} & & \\ & \bar{\underline{\mathbf{T}}} & \\ & & \end{pmatrix} \begin{pmatrix} & & \\ & \underline{\mathbf{T}}^{-1} & \\ & & \end{pmatrix} \begin{pmatrix} u(x_0) \\ u(x_1) \\ \vdots \\ \vdots \\ u(x_N) \end{pmatrix}. \tag{3.43}$$

Having the u,v-velocity at $Re = 1000$ approximated on the uniform grid, Tables (3.2) and (3.3) show excellent agreement with Ghia *et al.* (1982) and Botella & Peyret (1998). The opposite sign in reference Botella & Peyret (1998) is due to the opposite direction of the driven wall movement. Excellent agreement is observed mostly for the fourth digit, with results tabulated by Botella & Peyret (1998).

Figures (3.9-3.10) show a comparison of the vorticity along the moving wall ($y = 1$) with Ghia *et al.* (1982) results at $Re = 100, 400, 1000, 3200, 5000, 7500$ and at $Re = 10000$. The comparison shows good agreement, but one can observe some oscillations in our results. These oscillations increases when Re is increased, as it is clear at $Re = 10000$. However, using finer grid size decreases the oscillations as we tried to to generate the values of vorticity along the moving wall on a grid coarser than 120×120, and the oscillations appeared at $Re < 3200$.

Figures (3.11-3.22) show the streamlines and vorticity contour levels for $100 \leq Re \leq 25000$. These figures show the primary vortices accompanied by secondary and tertiary vortices in the corner. It is clear that the center of the primary vortex commences near the top right corner at $Re = 100$, and moves towards the center as Re increases. Its location remains stable at the center for $Re \geq 5000$, as observed by Ghia *et al.* (1982). The primary vortex size is sensitive to the grid size, as it is obvious when the size of primary vortex at $Re = 2000$ on 51×51 is compared with the size of the primary vortex at the same Re on 65×65 grid. It is clearly observed at $Re = 5000$ where the primary vortex occupies nearly the half of the domain on the coarse grid 65×65, whereas, it looks much smaller on the fine grid 130×130. Secondary eddies appear near the bottom left corner and bottom right corner as Re is increased. Also, they appear near the top of the left wall. Moffatt (1964) mentioned a sequence of eddies near the bottom corners is observed up to tertiary eddies, see Figures (3.23), (3.24) and 3.25. The size of these eddies decreases as we get closer to the corner. The tertiary eddies start appearing in the bottom right for $Re \geq 5000$, while they appear in the bottom left for $Re \geq 15000$. Barragy & Carey (1997) have reported the secondary top left vortex encloses tertiary vortex appears at $10500 \leq Re \leq 11000$, and mentioned

that this tertiary has not been reported previously. The present work shows the secondary top left vortex encloses the tertiary third vortex at $Re > 10000$ and still appear at $Re > 11000$. This is clear in Figures (3.23), (3.24) and (3.25), which show the corners and top left eddies at $Re = 20000, 22000$ and 25000. New results at high Re are reported in this work, and results at Re up to 25000 are generated using Chebychev collocation in each direction. Streamlines and vorticity contours levels are plotted in Figures (3.20-3.22) for $Re = 23000, 24000$ and 25000 on a 131×131 grid. Secondary vortices are zoomed in and plotted in figures (3.23), (3.24) and 3.25 with notation T, B, L and R, which denote respectively top, bottom, left and right. The subscript numbers denote the hierarchy of the secondary vortices. However, it is worth mentioning that these new high Reynolds number results especially for $Re \geq 20000$ need to be resolved on finer grids as more oscillations are very clear in these vorticity contours near the corners and in the middle of the contour. This suggests finer grid are needed to obtain more accurate results.

Tables (3.4-3.8) provide a comprehensive comparison of the primary and secondary vortices properties. The present work shows an agreement with Ghia *et al.* (1982) and Azzam (2003) for $Re \leq 10000$, and with Azzam (2003) at $Re = 15000$ except in TL2, BL3 and BR3 properties, where one can see the differences in the vorticity values. At $Re = 20000$, there is a slight difference, which is 10^{-1}, in the value of minimum of the streamfunction in the primary vortex. For TL2, BL3 and BR3 properties at $Re = 20000$, the same comment of $Re = 15000$ is applied here. However, the present work may be more accurate than Azzam (2003) due to the use of spectral discretization in both directions, rather than one direction as in Azzam (2003). Moreover, in Azzam's work, the high order differencing reduces

in order at the boundaries, which is not the case with our use of spectral methods. For higher Re, Table (3.9) shows the properties of primary and secondary vortices at Re values $21000, 23000$ and 25000. For $Re > 20000$, the maximum streamfunction values of the primary vortices increases as the Reynolds number is increased as it can be observed in table (3.9) where again a finer grid is suggested to obtain more accurate results.

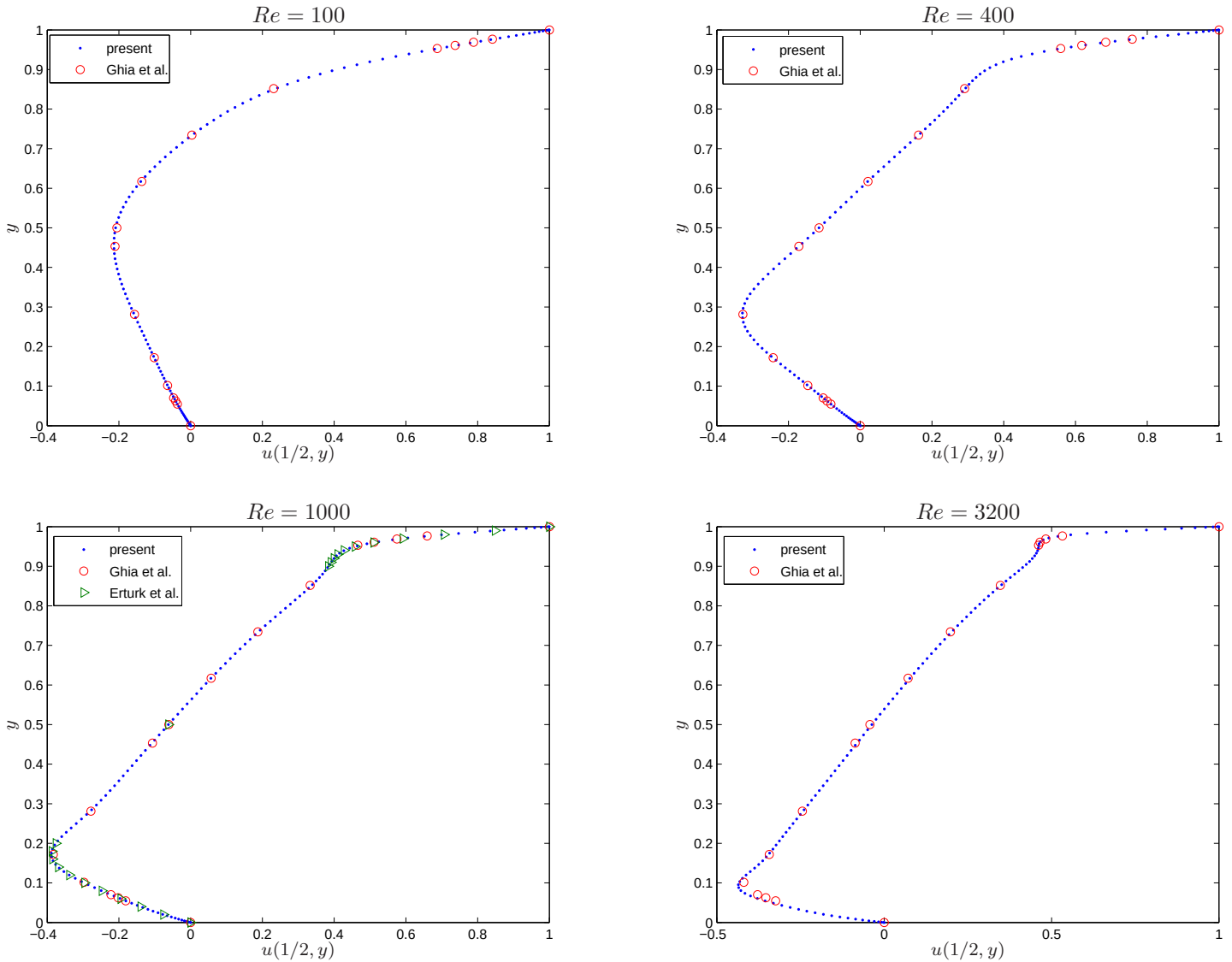

Figure 3.6: Comparison of u-velocity profiles along a vertical line passing through the geometry centre at various Reynolds numbers using $N = M = 120$ solution.

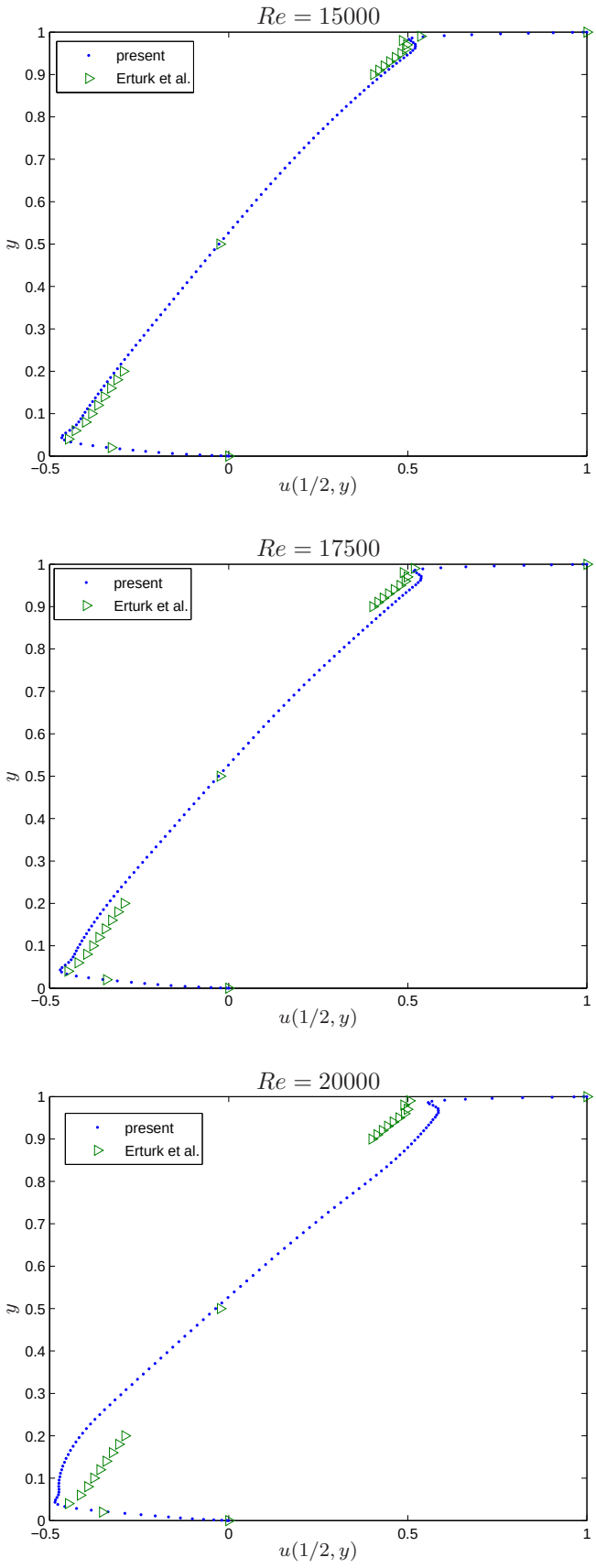

Figure 3.7: Comparison of u-velocity profiles along a vertical line passing through the geometry centre at various Reynolds numbers using $N = M = 120$ solution.

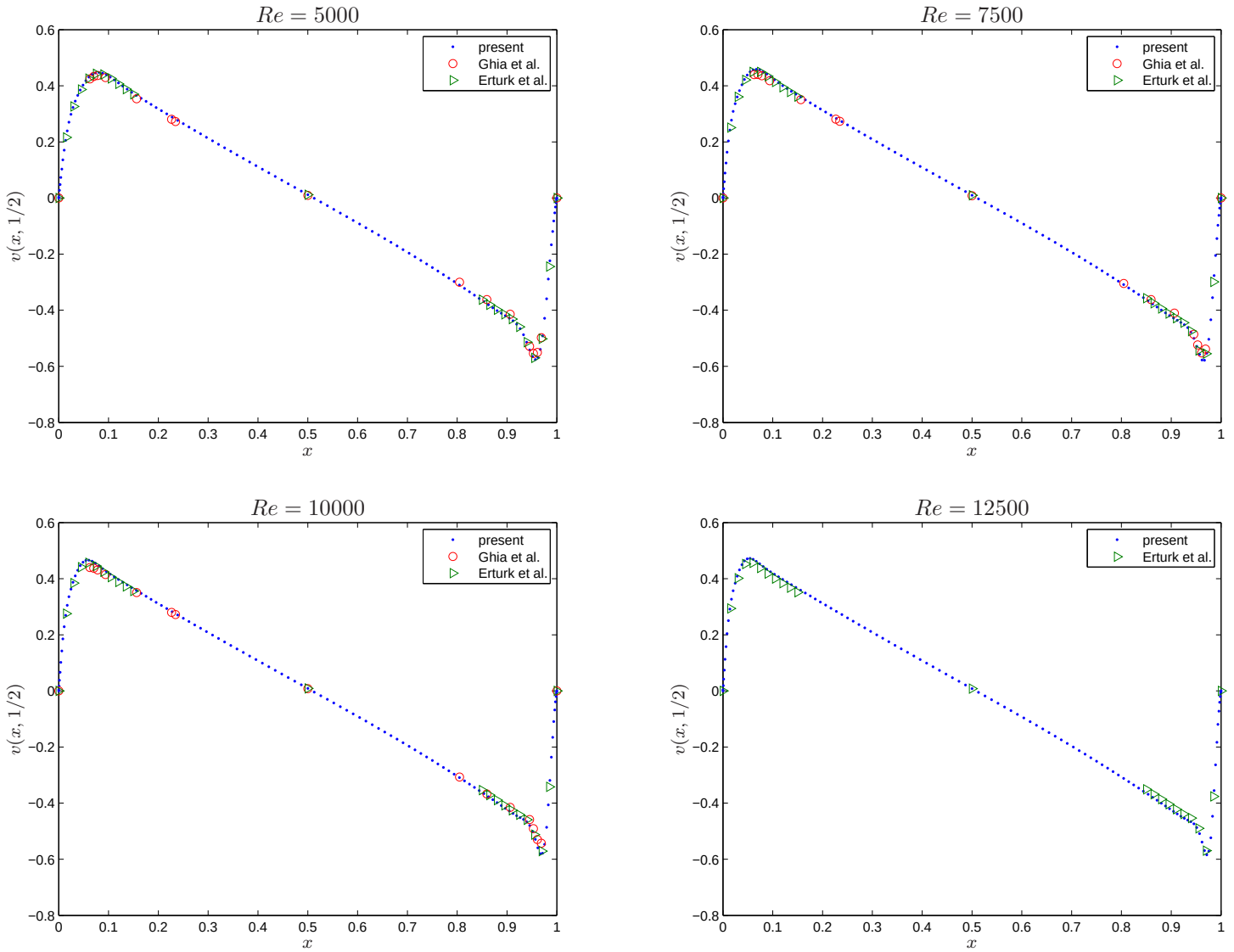

Figure 3.8: Comparison of v-velocity profiles along a horizontal line passing through the geometry centre at various Reynolds numbers using $N = M = 120$ solution.

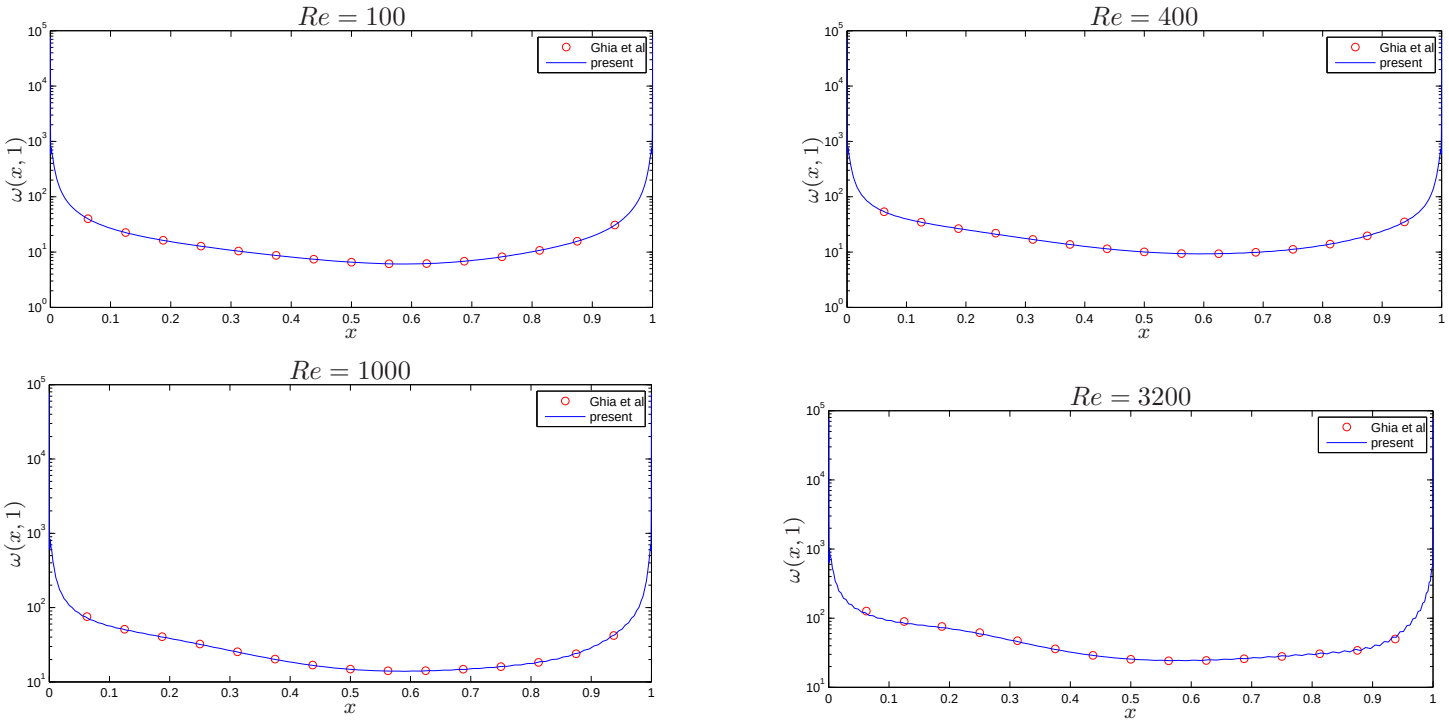

Figure 3.9: Comparison of the vorticity along moving wall ($y = 1$) with Ghia et al. results at $Re = 100$, $Re = 400$, $Re = 1000$ and $Re = 3200$ using $N = M = 120$.

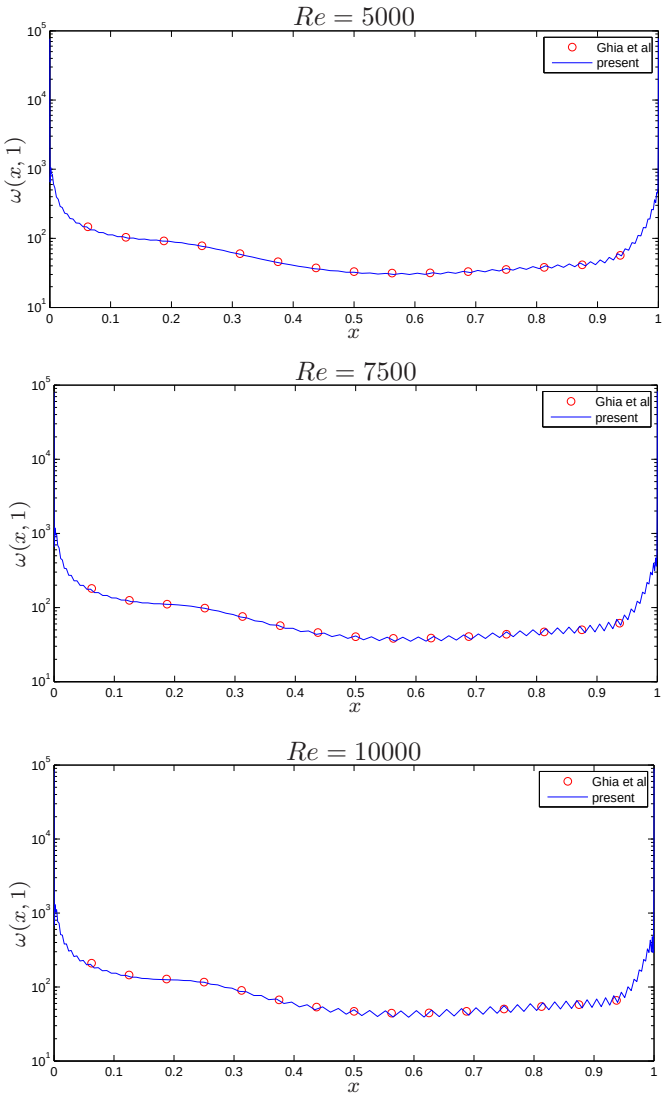

Figure 3.10: Comparison of the vorticity along moving wall ($y = 1$) with Ghia et al. results at $Re = 5000$, $Re = 7500$ and $Re = 10000$ using $N = M = 120$.

y	u,Ref. Ghia *et al.* (1982)	u,Ref.Botella & Peyret (1998)	u,present
1.0000	1.00000	-1.0000000	1.0000000
0.9766	0.65928	-0.6644227	0.6639700
0.9688	0.57492	-0.5808359	0.5803324
0.9609	0.51117	-0.5169277	0.5171793
0.9531	0.46604	-0.4723329	0.4724223
0.8516	0.33304	-0.3372212	0.3371788
0.7344	0.18719	-0.1886747	0.1886466
0.6172	0.05702	-0.0570178	0.0570070
0.5000	-0.06080	0.0620561	-0.0620530
0.4531	-0.10648	0.1081999	-0.1081721
0.2813	-0.27805	0.2803696	-0.2804342
0.1719	-0.38289	0.3885691	-0.3885725
0.1016	-0.29730	0.3004561	-0.3003726
0.0703	-0.22220	0.2228955	-0.2229314
0.0625	-0.20196	0.2023300	-0.2023288
0.0547	-0.18109	0.1812881	-0.1812581
0.0000	-0.00000	0.0000000	-0.0000000

Table 3.2: Horizontal velocity u along the vertical line through the geometric center of cavity, at $Re = 1000$ with $N = M = 80$.

x	u,Ref. Ghia *et al.* (1982)	u,Ref.Botella & Peyret (1998)	u,present
1.0000	0.00000	0.0000000	0.0000000
0.9688	-0.21388	-0.2279225	-0.2283338
0.9609	-0.27669	-0.2936869	-0.2933988
0.9531	-0.33714	-0.3553213	-0.3551266
0.9453	-0.39188	-0.4103754	-0.4103109
0.9063	-0.51550	-0.5264392	-0.5264190
0.8594	-0.42665	-0.4264545	-0.4263811
0.8047	-0.31966	-0.3202137	-0.3201946
0.5000	0.02526	0.0257995	0.0257981
0.2344	0.32235	0.3253592	0.3253755
0.2266	0.33075	0.3339924	0.3340338
0.1563	0.37095	0.3769189	0.3769373
0.0938	0.32627	0.3330442	0.3329679
0.0781	0.30353	0.3099097	0.3099698
0.0703	0.29012	0.2962703	0.2962728
0.0625	0.27485	0.2807056	0.2806893
0.0000	0.00000	0.0000000	0.0000000

Table 3.3: Vertical velocity v along the horizontal line through the geometric center of cavity, at $Re = 1000$ with $N = M = 80$.

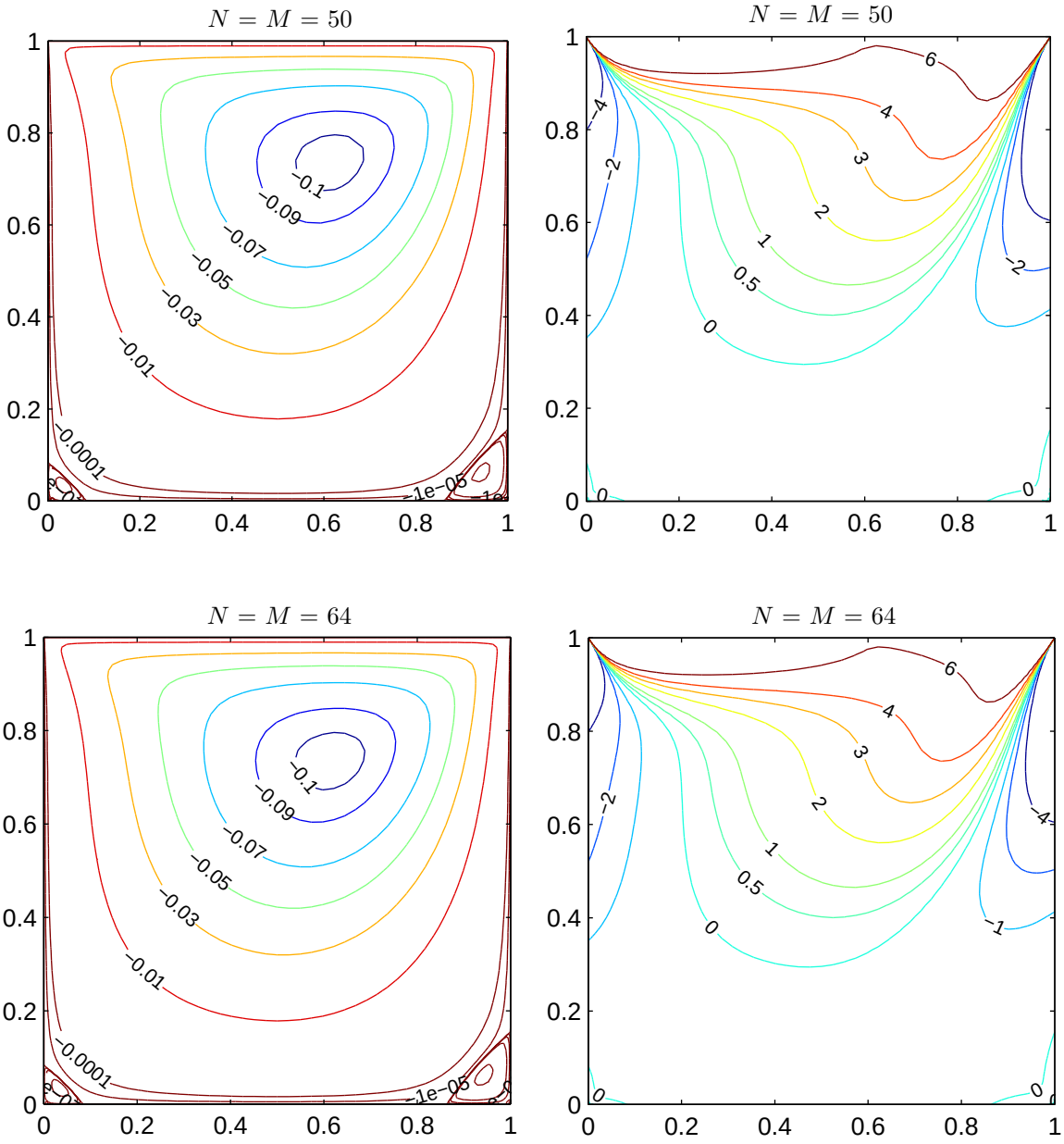

Figure 3.11: Streamline and vorticity contours plot at $Re = 100$ on 51×51 and 65×65 grid.

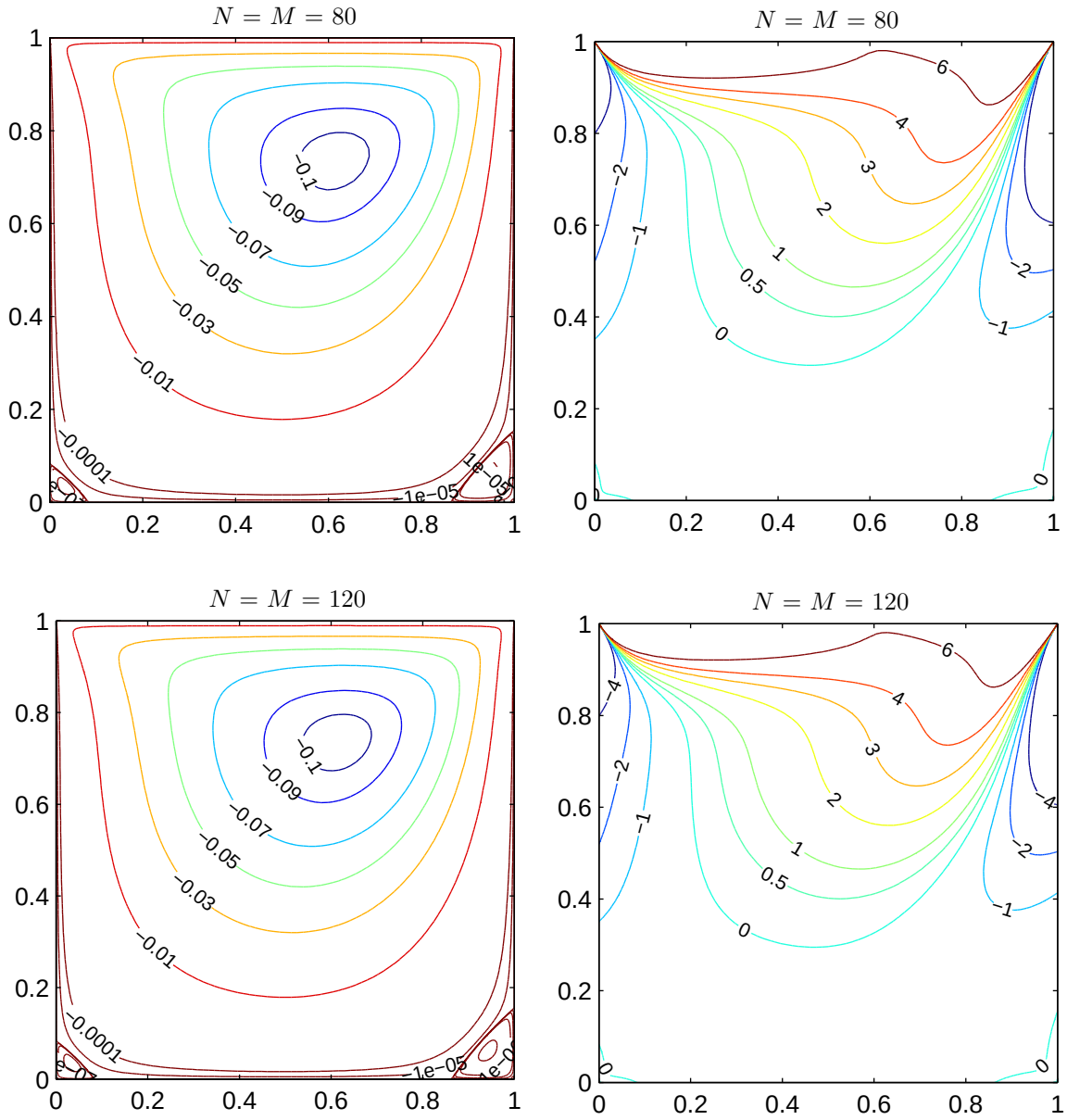

Figure 3.12: Streamline and vorticity contours plot at $Re = 100$ on 81×81 and 121×121 grid.

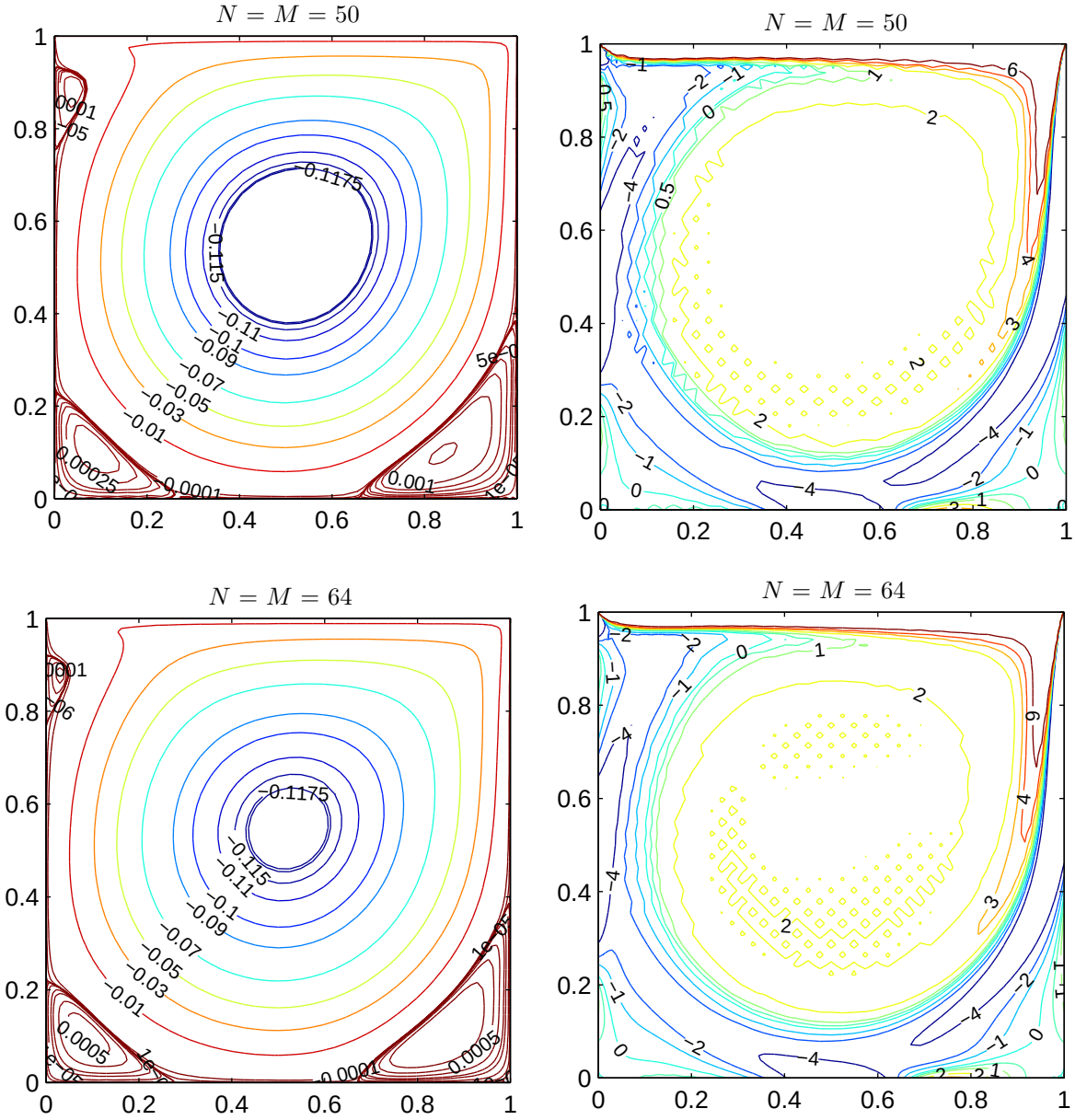

Figure 3.13: Streamline and vorticity contours plot at $Re = 2000$ on 51×51 and 65×65 grid.

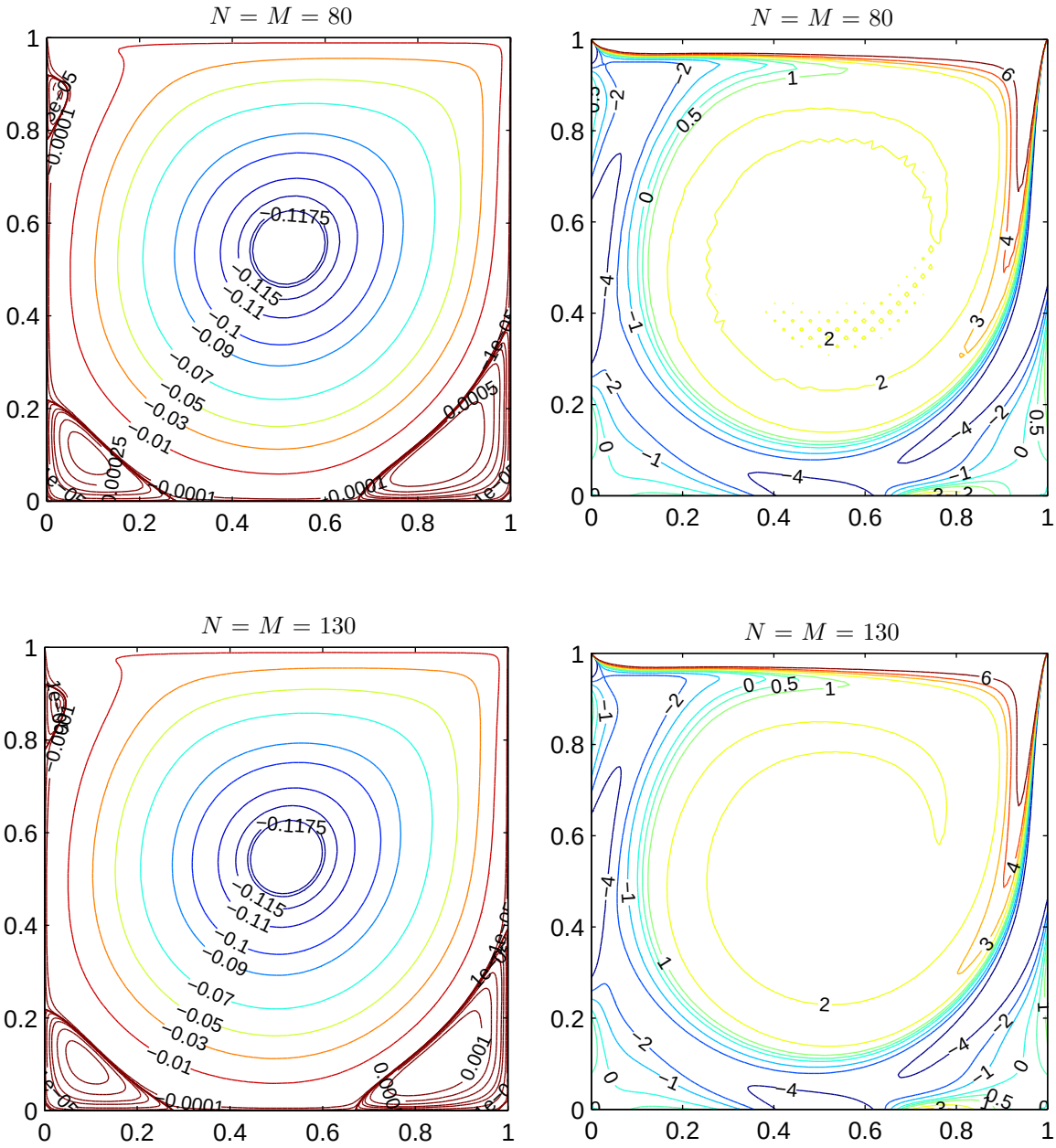

Figure 3.14: Streamline and vorticity contours plot at $Re = 2000$ on a 81×81 and 131×131 grid.

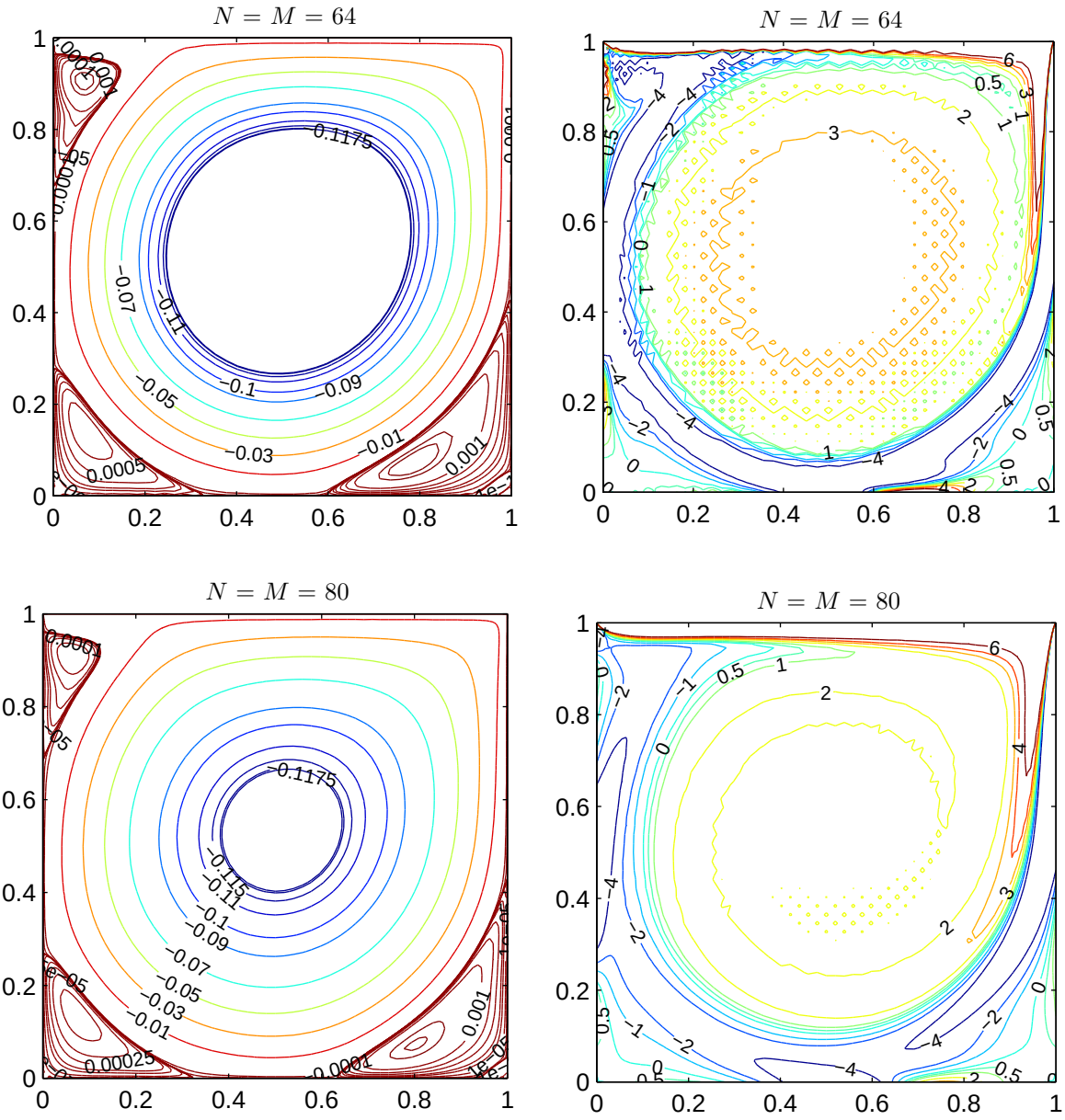

Figure 3.15: Streamline and vorticity contours plot at $Re = 5000$ on 65×65 and 81×81 grid.

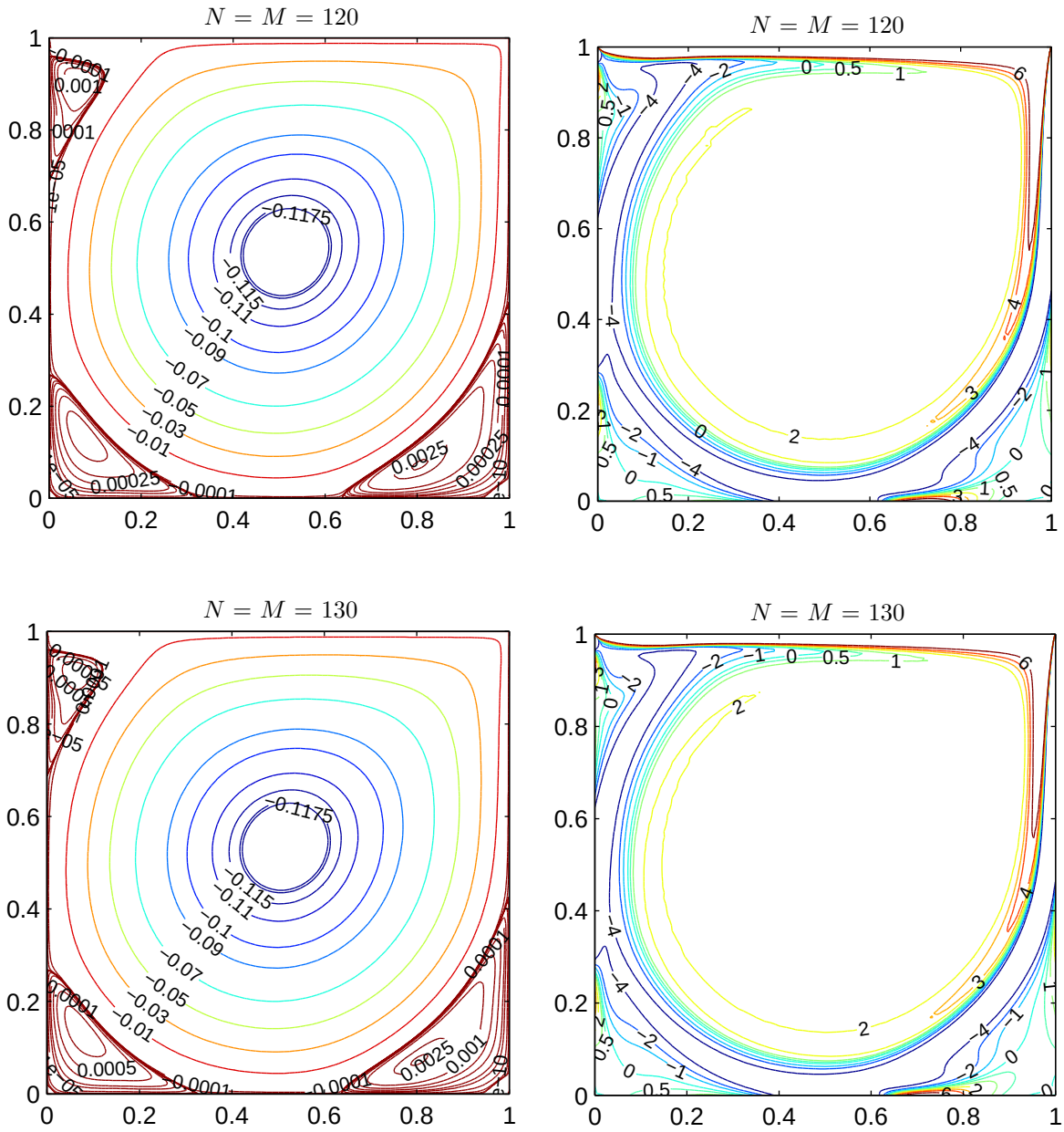

Figure 3.16: Streamline and vorticity contours plot at $Re = 5000$ on a 121×121 and 131×131 grid.

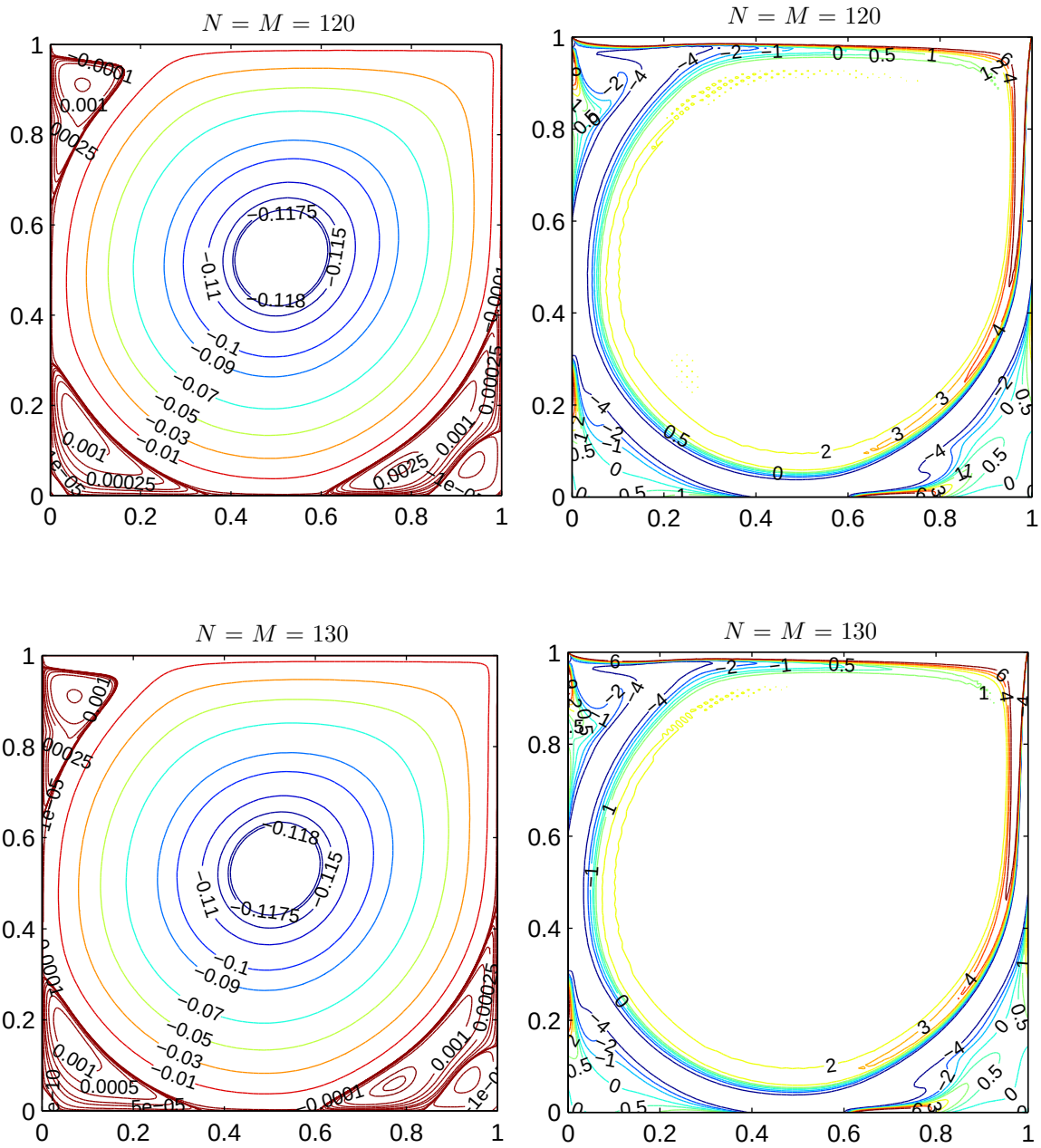

Figure 3.17: Streamline and vorticity contours plot at $Re = 10000$ on a 121×121 and 131×131 grid.

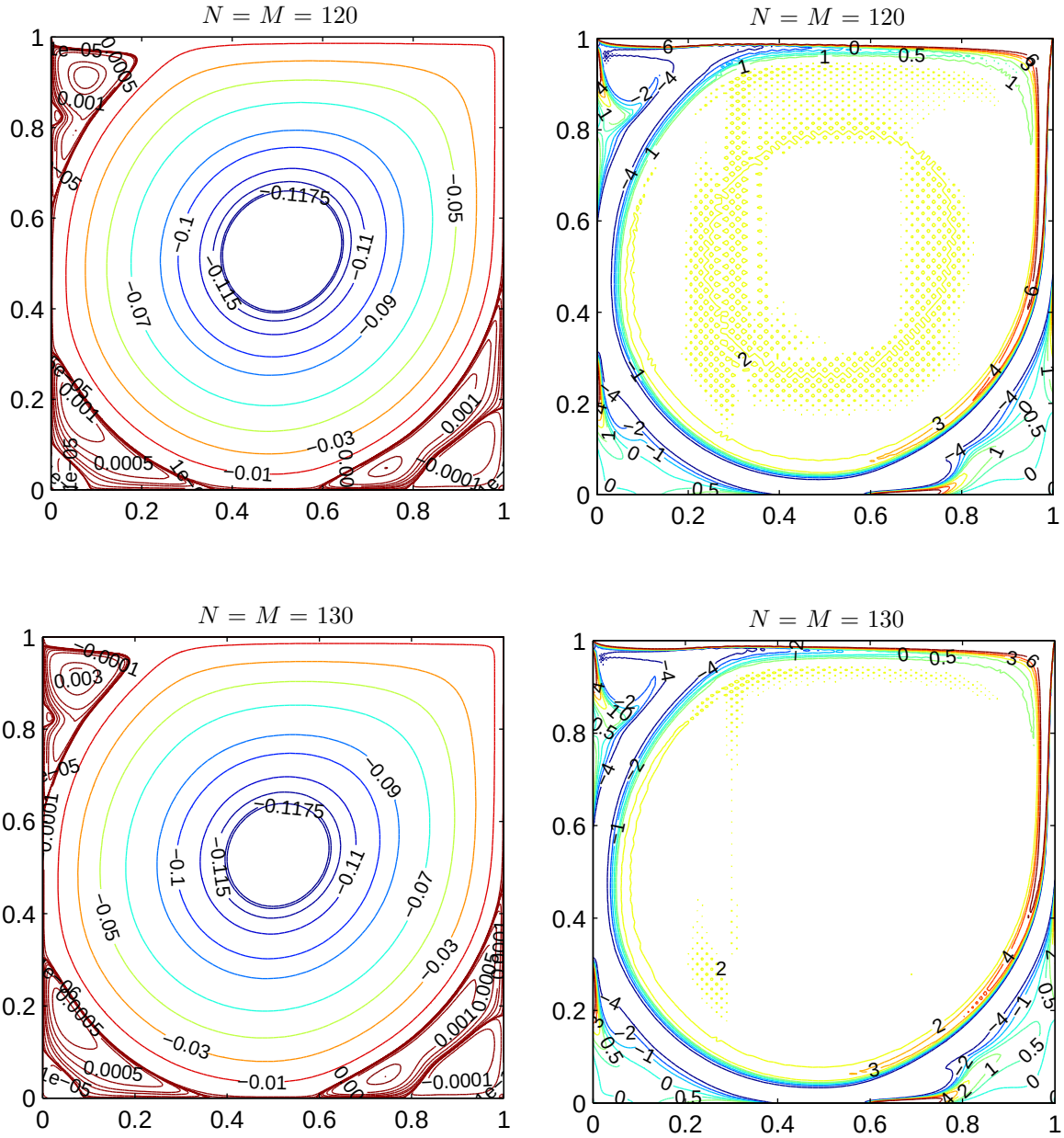

Figure 3.18: Streamline and vorticity contours plot at $Re = 15000$ on a 121×121 and 131×131 grid.

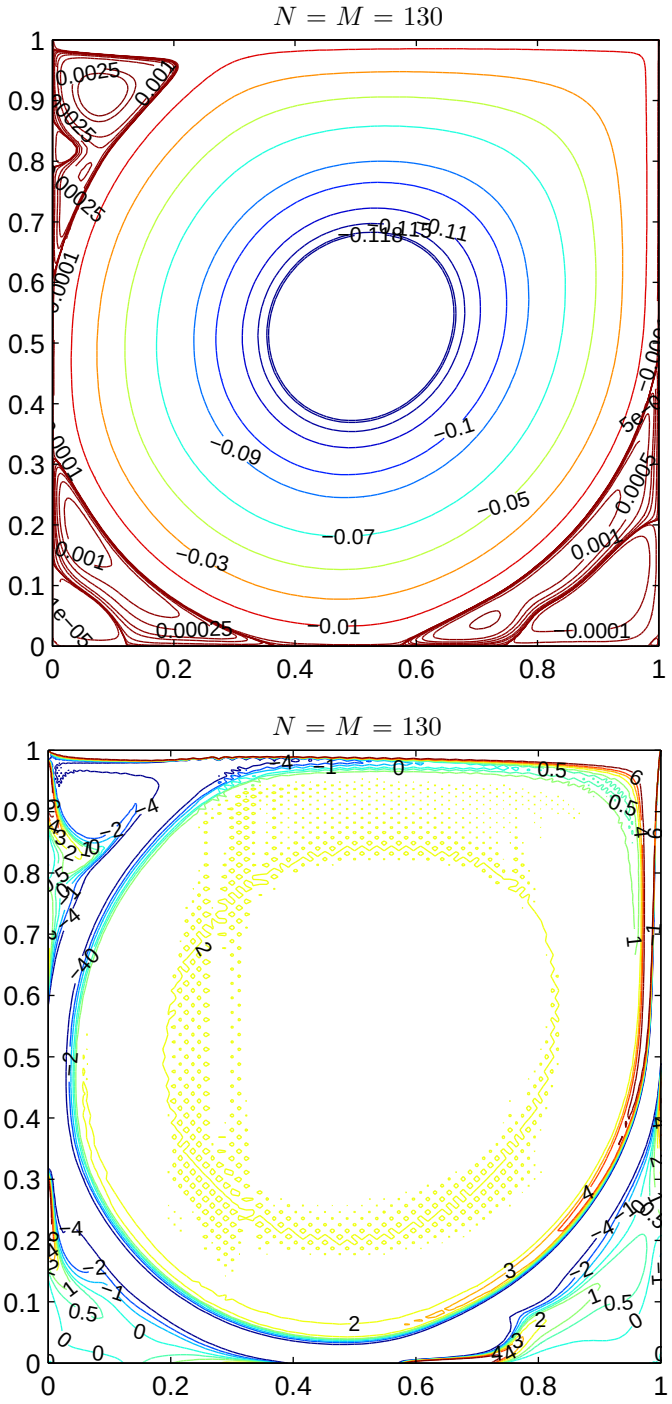

Figure 3.19: Streamline and vorticity contours plot at $Re = 20000$ on a 121×121 and 131×131 grid.

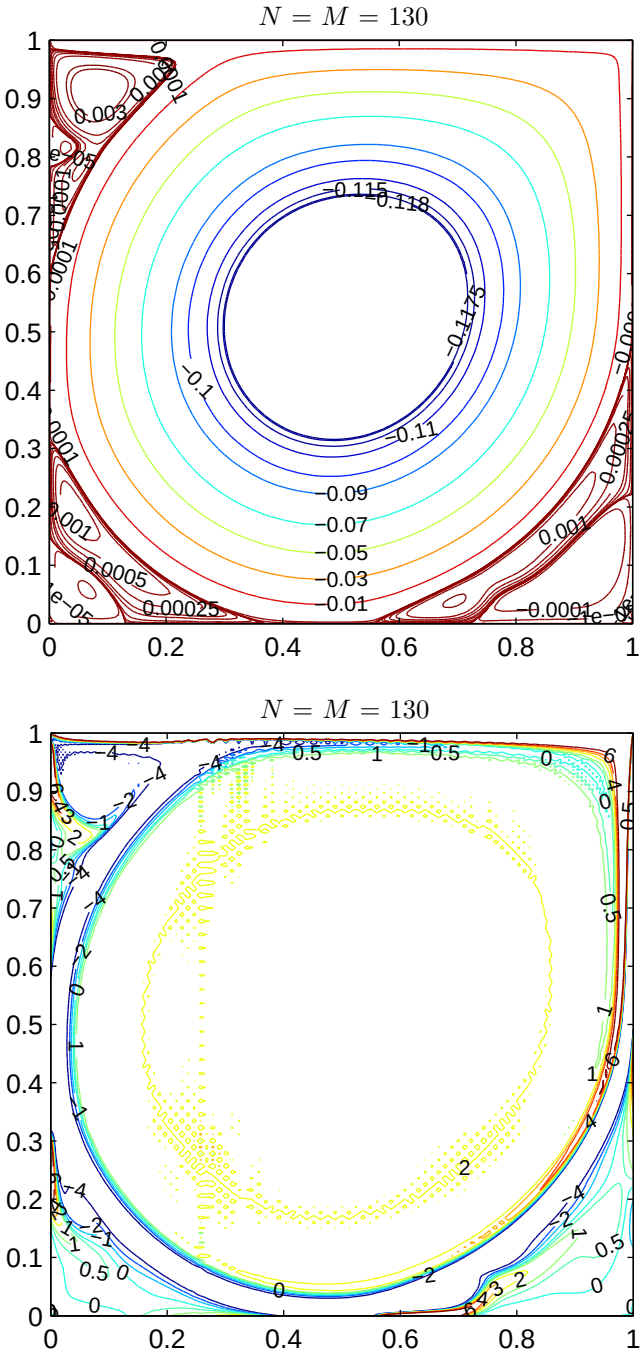

Figure 3.20: Streamline and vorticity contours plot at $Re = 23000$ on a 131×131 grid.

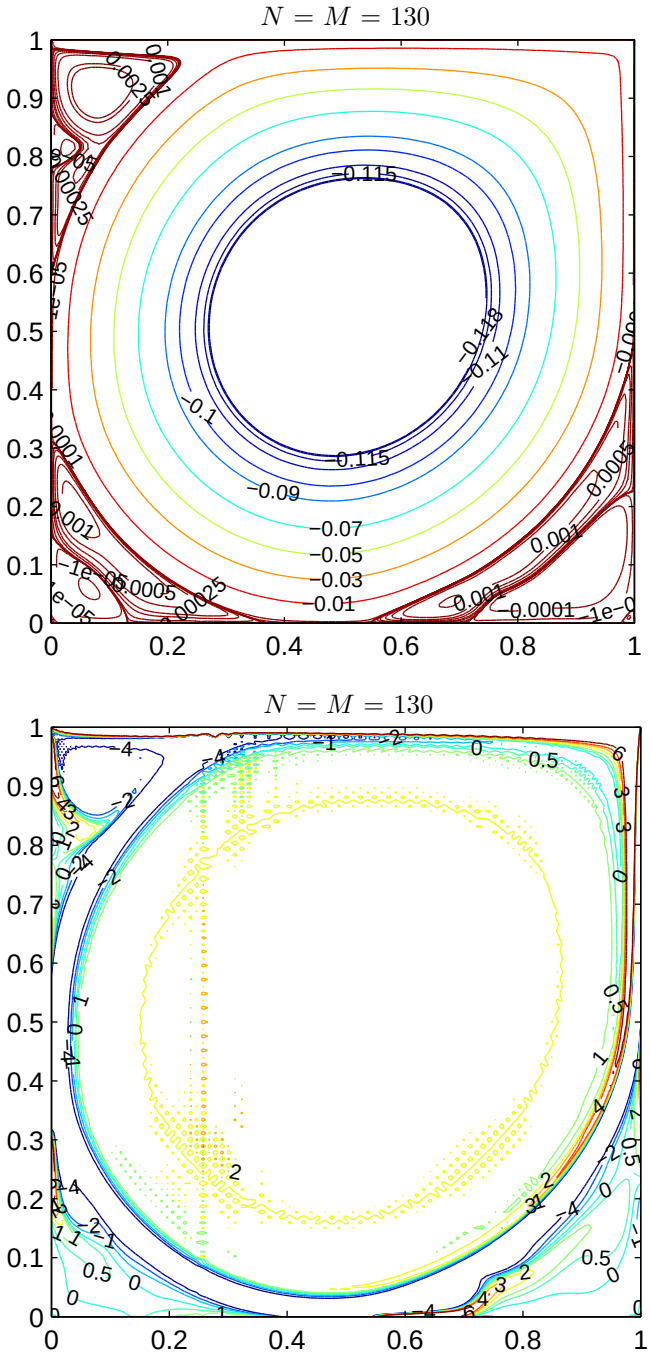

Figure 3.21: Streamline and vorticity contours plot at $Re = 24000$ on a 131×131 grid.

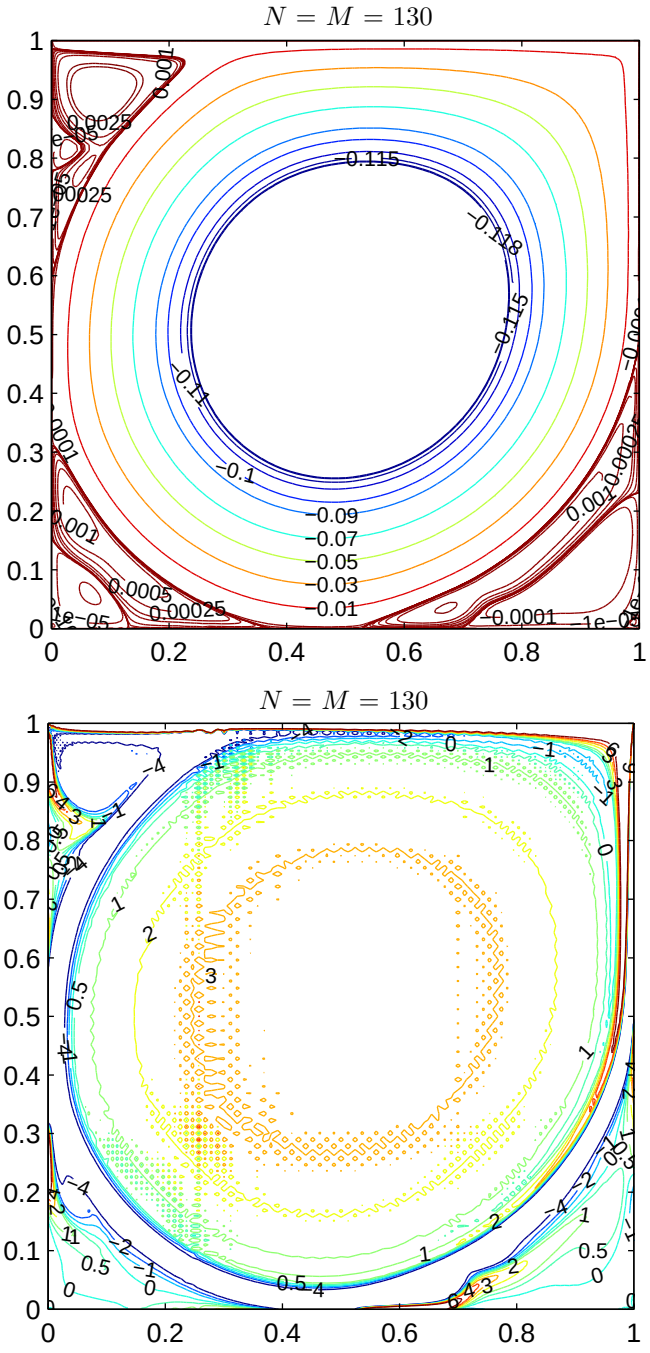

Figure 3.22: Streamline and vorticity contours plot at $Re = 25000$ on a 131×131 grid.

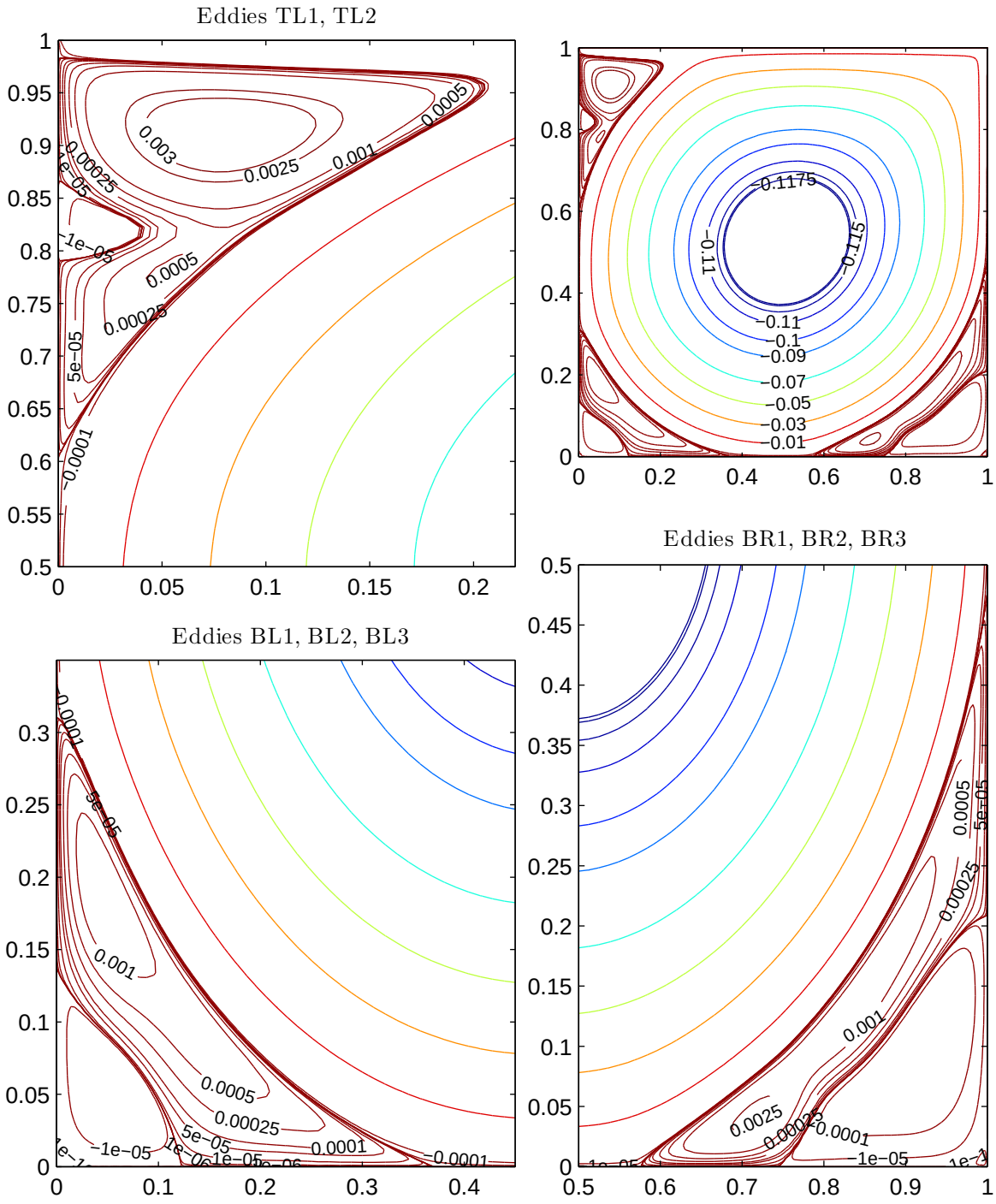

Figure 3.23: Streamline contours of primary and secondary vortices at $Re = 20000$ on a 131×131 grid.

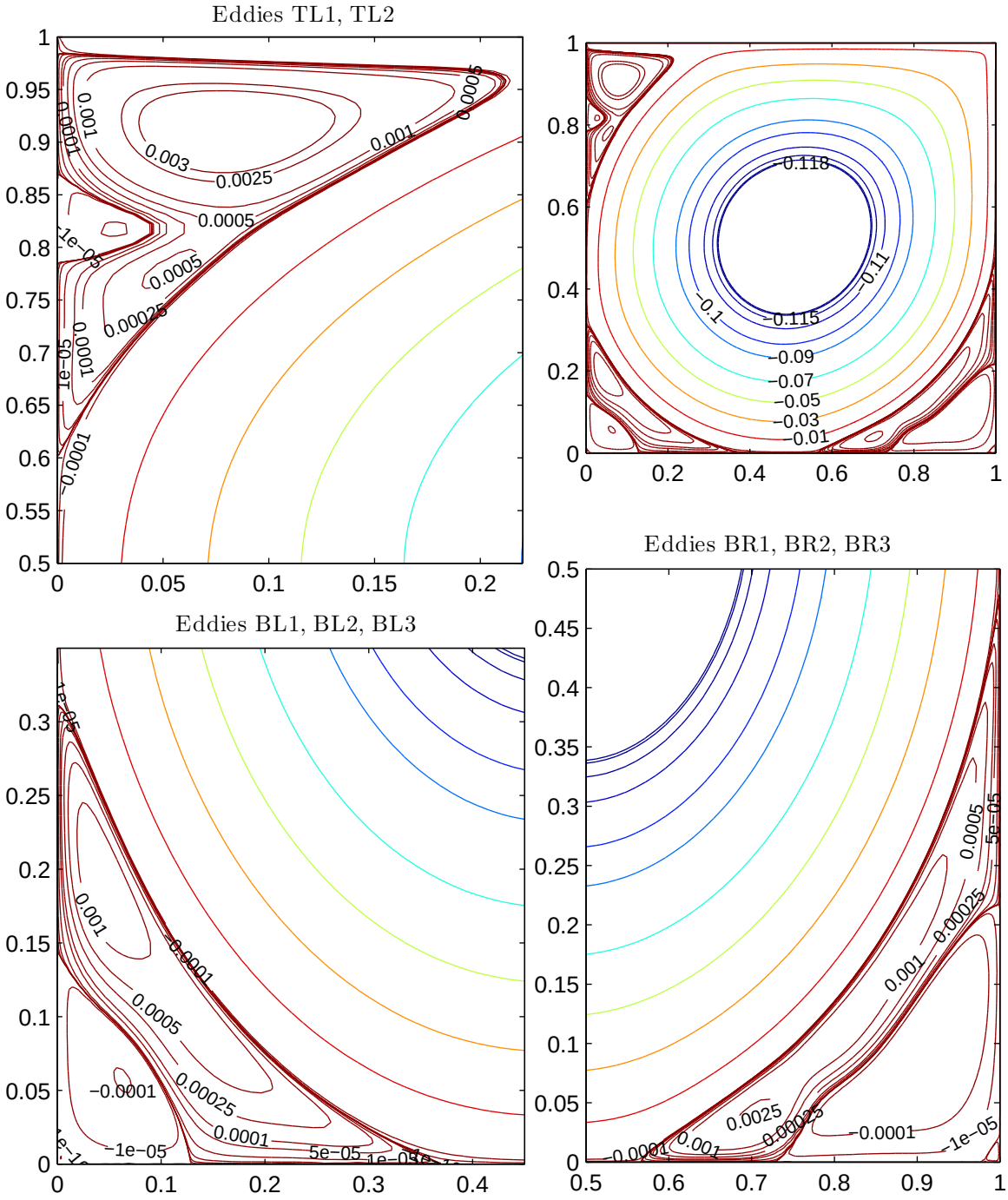

Figure 3.24: Streamline contours of primary and secondary vortices at $Re = 22000$ on a 131×131 grid.

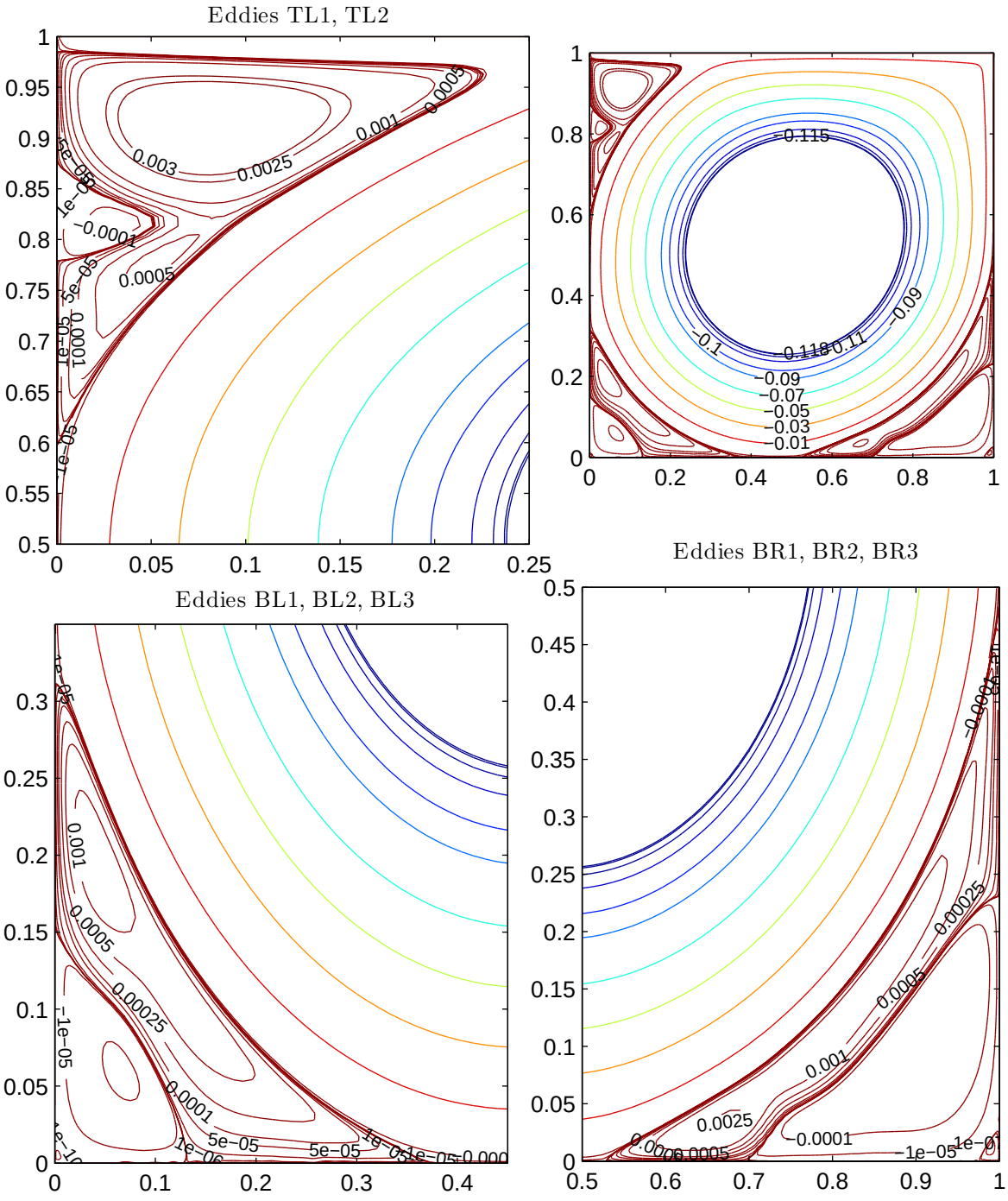

Figure 3.25: Streamline contours of primary and secondary vortices at $Re = 25000$ on a 131×131 grid.

Re=1000		Present	Ghia et al.	Azzam C/4D
Primary	$\psi_{\min}$	-0.118923	-0.117929	-0.1189188
	ω	2.06757	2.04968	2.06745
	(x, y)	(0.5261,0.5625)	(0.5313,0.5625)	(0.5325,0.5664)
TL1	$\psi_{\max}$	-	-	-
	ω	-	-	-
	(x, y)	-	-	-
BL1	$\psi_{\max}$	2.32912E-4	2.31129E-4	2.33132E-4
	ω	-0.35557	-0.36175	-0.34481
	(x, y)	(0.0806,0.0806)	(0.0859,0.0781)	(0.0820,0.0781)
BR1	$\psi_{\max}$	0.17293E-2	0.175102E-2	0.172836E-2
	ω	-1.12499	-1.15465	-1.138799
	(x, y)	(0.8626,0.1114)	(0.8594,0.1094)	(0.8633,0.1133)
BL2	$\psi_{\min}$	-0.57390E-8	-	-
	ω	-0.001824	-	-
	(x, y)	(0.0042,0.0042)	-	-
BR2	$\psi_{\min}$	-4.69177E-8	-9.31929E-8	-5.201598E-8
	ω	0.67911E-2	0.852782E-2	0.88759E-2
	(x, y)	(0.9916,0.0061)	(0.9922,0.0078)	(0.9922,0.0078)

Table 3.4: Comparison of the properties of primary and secondary vortices, streamfunction and vortices values and their (x, y) locations at $Re = 1000$.

Re=5000		Present	Ghia et al.	Azzam C/4D
Primary	$\psi_{\min}$	-0.12224	-0.118966	-0.12074
	ω	1.941951	1.86016	2.06745
	(x, y)	(0.5130,0.5392)	(0.5117,0.5373)	(0.5156,0.5352)
TL1	$\psi_{\max}$	1.44389E-3	1.45641E-3	1.43321E-3
	ω	-2.18732	-2.08843	-2.11204
	(x, y)	(0.0605,0.9120)	(0.0625,0.9102)	(0.0625,0.9102)
BL1	$\psi_{\max}$	1.37613E-3	1.36119E-3	1.36325E-3
	ω	-1.5322	-1.53055	-1.520253
	(x, y)	(0.0736,0.1373)	(0.0703,0.1367)	(0.0742,0.1328)
BR1	$\psi_{\max}$	3.07276E-3	3.08358E-2	3.06056E-2
	ω	-2.75494	-2.66354	-2.72155
	(x, y)	(0.8043,0.0736)	(0.8086,0.0742)	(0.8047,0.0742)
BL2	$\psi_{\min}$	-6.25204E-8	-7.08860E-8	-2.8058E-7
	ω	1.25017E-2	1.88395E-2	7.3275E-2
	(x, y)	(0.0083,0.0083)	(0.0117,0.0078)	(0.0117,0.0039)
BR2	$\psi_{\min}$	-1.43384E-6	-1.43226E-6	-1.3767E-6
	ω	3.75573E-2	3.19311E-2	3.1956E-2
	(x, y)	(0.9794,0.0205)	(0.9805,0.0195)	(0.9805,0.0195)

Table 3.5: Comparison of the properties of primary and secondary vortices, streamfunction and vortices values and their (x, y) locations at $Re = 5000$.

Re=10000		Present	Ghia et al.	Azzam C/4D
Primary	$\psi_{\min}$	-0.12317	-0.119731	-0.12111
	ω	1.93769	1.88082	1.90129
	(x, y)	(0.5130,0.5262)	(0.5117,0.5333)	(0.5117,0.5313)
TL1	$\psi_{\max}$	2.64642E-3	2.42103E-3	2.536148E-3
	ω	-2.29556	-2.18276	-2.281775
	(x, y)	(0.0736,0.9120)	(0.0703,0.9141)	(0.0703,0.9102)
BL1	$\psi_{\max}$	1.61248E-3	1.51829E-3	1.57731E-3
	ω	-2.00736	-2.08560	-2.080154
	(x, y)	(0.0605,0.1558)	(0.0586,0.1641)	(0.0586,0.1602)
BR1	$\psi_{\max}$	3.18780E-3	3.41831E-3	3.16998E-3
	ω	-3.74926	-4.0531	-3.7049
	(x, y)	(0.7723,0.0605)	(0.7656,0.0586)	(0.7734,0.0586)
BL2	$\psi_{\min}$	-1.12515E-6	-7.75652E-7	-1.102966E-6
	ω	3.22502E-3	2.75450E-2	3.8301E-2
	(x, y)	(0.0170,0.0205)	(0.0156,0.0195)	(0.0195,0.0156)
BR2	$\psi_{\min}$	-1.41586E-4	-1.31321E-4	-1.22176E-4
	ω	3.13280E-1	3.11258E-1	2.871E-1
	(x, y)	(0.9330,0.0669)	(0.9336,0.0625)	(0.9375,0.0641)
BR3	$\psi_{\max}$	1.46075E-8	5.6683E-9	3.6614E-7
	ω	-4.24431E-3	-	7.48227E-2
	(x, y)	(0.9957,0.0043)	(0.9961,0.0039)	(0.9922,0.0039)

Table 3.6: Comparison of the properties of primary and secondary vortices, streamfunction and vortices values and their (x, y) locations at $Re = 10000$.

Re=15000		Present	Azzam C/4D
Primary	$\psi_{\min}$	-0.12673	-0.122200
	ω	2.00973	1.90905
	(x, y)	(0.5130,0.5261)	(0.5097,0.5273)
TL1	$\psi_{\max}$	3.40013E-3	3.22545E-3
	ω	-2.50687	-2.39719
	(x, y)	(0.0806,0.9121)	(0.07813,0.9121)
BL1	$\psi_{\max}$	1.67192E-3	1.67566E-3
	ω	-2.44086	-2.42273
	(x, y)	(0.0545,0.1654)	(0.0546,0.1680)
BR1	$\psi_{\max}$	3.01257E-3	2.99777E-3
	ω	-5.04029	-4.94016
	(x, y)	(0.7386,0.0487)	(0.7460,0.0508)
BL2	$\psi_{\min}$	-2.31104E-5	-2.64342E-5
	ω	1.47342E-1	1.48847E-1
	(x, y)	(0.0381,0.0432)	(0.041,0.0391)
BR2	$\psi_{\min}$	-3.48190E-4	-3.40445E-4
	ω	4.57611E-1	4.58477E-1
	(x, y)	(0.9263,0.0879)	(0.925,0.0879)
TL2	$\psi_{\min}$	-2.01457E-5	-2.27687E-5
	ω	6.37882E-1	1.248599
	(x, y)	(0.0170,0.8247)	(0.0078,0.838)
BL3	$\psi_{\max}$	1.14225E-8	2.54121E-5
	ω	-0.71198E-2	-11.63082E-3
	(x, y)	(0.0027,0.0042)	(0.0059,0.0020)
BR3	$\psi_{\max}$	3.15661E-8	3.31309E-6
	ω	-5.21837E-3	-3.15454
	(x, y)	(0.9938,0.0043)	(0.9985,0.0020)

Table 3.7: Comparison of the properties of primary and secondary vortices, streamfunction and vortices values and their (x, y) locations at $Re = 15000$.

Re=20000		Present	Azzam C/4D
Primary	$\psi_{\min}$	-0.13019	-0.121658
	ω	2.08645	1.89997
	(x, y)	(0.5120,0.5242)	(0.5125,0.5275)
TL1	$\psi_{\max}$	3.90472E-3	3.61239E-3
	ω	-2.59977	-2.36545
	(x, y)	(0.0818,0.9115)	(0.0825,0.9125)
BL1	$\psi_{\max}$	1.62200E-3	1.59644E-3
	ω	-2.97556	-2.95067
	(x, y)	(0.0466,0.1869)	(0.0475,0.1825)
BR1	$\psi_{\max}$	2.80950E-3	2.81006E-3
	ω	-6.38771	-6.08323
	(x, y)	(0.7216,0.0466)	(0.7225,0.0425)
BL2	$\psi_{\min}$	-8.18552E-5	-8.16565E-5
	ω	2.61159E-1	2.43271E-1
	(x, y)	(0.0573,0.0573)	(0.599,0.5249)
BR2	$\psi_{\min}$	-4.75360E-4	-4.514639E-4
	ω	6.03230E-1	5.26751E-1
	(x, y)	(0.9310,0.1102)	(0.927,0.0999)
TL2	$\psi_{\min}$	-8.05661E-5	-2.49534E-3
	ω	9.63705E-1	11.32008
	(x, y)	(0.0244,0.8224)	(0.0999,0.8000)
BL3	$\psi_{\max}$	9.43090E-9	2.42359E-5
	ω	-2.90919E-3	-5.819478
	(x, y)	(0.0036,0.0036)	(0.0075,0.0025)
BR3	$\psi_{\max}$	4.36311E-8	4.14697E-6
	ω	-6.73959E-3	-2.03357
	(x, y)	(0.9929,0.0071)	(0.9975,0.0025)

Table 3.8: Comparison of the properties of primary and secondary vortices, streamfunction and vortices values and their (x, y) locations at $Re = 20000$.

	Property	Re=21000	Re=23000	Re=25000
Primary	$\psi_{\min}$	-0.13322	-0.14430	-0.17500
	ω	2.15589	2.41084	3.10862
	(x, y)	(0.5121,0.5242)	(0.5120,0.5242)	(0.5121,0.5242)
TL1	$\psi_{\max}$	4.02840E-3	4.32375E-3	4.79308E-3
	ω	-2.63865	-2.74545	-2.95676
	(x, y)	(0.0818,0.9115)	(0.0818,0.9115)	(0.0818,0.9115)
BL1	$\psi_{\max}$	1.60699E-3	1.56161E-3	1.46495E-3
	ω	-3.029370	-3.12863	-3.08656
	(x, y)	(0.0466,0.1869)	(0.0466,0.1869)	(0.0466,0.1869)
BR1	$\psi_{\max}$	2.79890E-3	2.73167E-3	2.70124E-3
	ω	-6.68934	-7.42837	-8.73758
	(x, y)	(0.7107,0.0416)	(0.6997,0.0416)	(0.6773,0.0369)
BL2	$\psi_{\min}$	-9.32248E-5	-1.12438E-5	-1.17195E-4
	ω	2.88126E-1	2.72187E-1	2.97771E-1
	(x, y)	(0.0630,0.0573)	(0.0630,0.0573)	(0.0690,0.0573)
BR2	$\psi_{\min}$	-9.41920E-4	-5.60733E-4	-6.21799E-4
	ω	-17.52558	0.63354	6.24940E-1
	(x, y)	(0.8224,0.1595)	(0.9310,0.1178)	(0.9310,0.1178)
TL2	$\psi_{\min}$	-9.32947E-5	-1.32626E-5	-1.80051E-4
	ω	0.94105	1.32382	1.43207
	(x, y)	(0.0245,0.8224)	(0.0283,0.8131)	(0.0283,0.8131)
BL3	$\psi_{\max}$	1.00350E-8	1.21528E-8	1.85370E-8
	ω	-2.81117E-3	-4.83697E-3	-5.24281E-3
	(x, y)	(0.0036,0.0036)	(0.0036,0.0052)	(0.0036,0.0052)
BR3	$\psi_{\max}$	5.24296E-8	8.65752E-8	1.59207E-7
	ω	-5.94051E-3	-9.31028E-3	-9.61675E-3
	(x, y)	(0.9929,0.0071)	(0.9907,0.0093)	(0.9907,0.0118)

Table 3.9: Properties of primary and secondary vortices, streamfunction and vortices values and their (x, y) locations at various Re.

Chapter 4

Steady Separated Corner Flow

In this chapter, we study the steady separated flow in a corner, and solve the full Navier-Stokes equations for high Reynolds numbers. The two-dimensional stream function-vorticity formulation is used to be discretized using the Chebyshev collocation method in both directions, x and y. The problem will be solved using Newton linearisation with a direct solver in MATLAB. The problem is solved on various domains and at various high Reynolds numbers. We aim to give a description of the flow and show the independence of the solution from the variation of Reynolds number and X_∞, which will be described shortly.

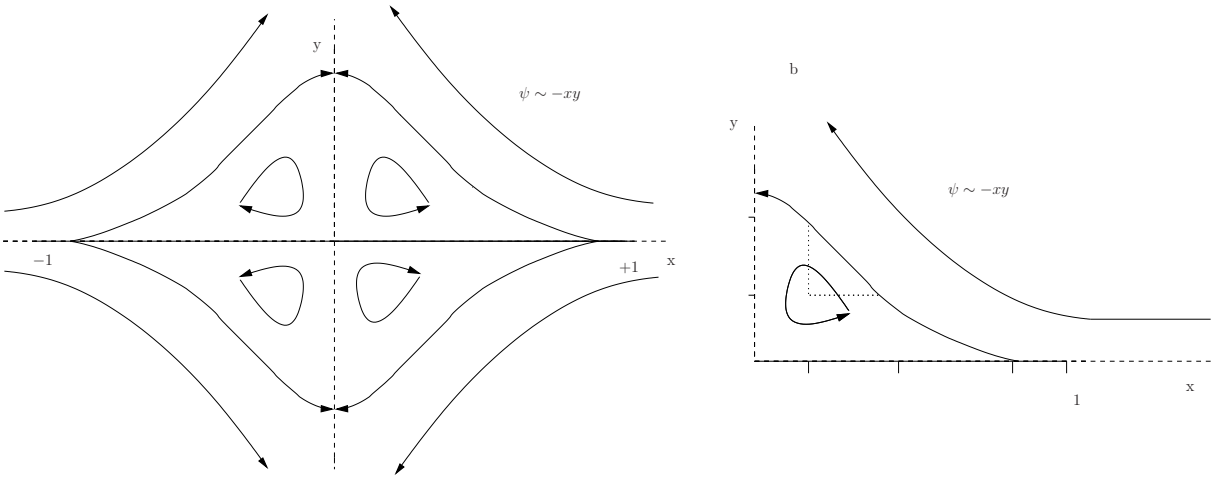

Figure 4.1: Corner flow geometry : (a) entire flow geometry, (b) local geometry .

4.1 Problem Formulation

We consider a two-dimensional problem, which describes the steady separated corner flow. A sketch of the flow problem is shown in Figure (4.1) where the left sketch is the entire plane, while the right is the local geometry that we solve. The problem is specified by the flat plate which is placed in $-1 \leq x \leq 1$ on the x axis and the line of y axis. At far distance from the flat plate, the stream function is given by $\psi = -xy$. The steady incompressible flow is described by the full Navier-Stokes equations in streamfunction-vorticity formulation, which are given by

$$\begin{aligned} \nabla^2\psi &= \omega \\ \text{and} \quad \psi_y\omega_x - \psi_x\omega_y &= \frac{1}{Re}\nabla^2\omega, \end{aligned} \tag{4.1}$$

where Re is the Reynolds number. In this formulation, the vorticity ω relates to the streamfunction ψ by $u = \psi_y$, $v = -\psi_x$, and the vorticity can be defined as $\omega = v_x - u_y$. Leal (1973) transformed the domain from (x, y) coordinates to elliptical coordinates with the relations $x = \cosh\xi\cos\eta$, $y = \sinh\xi\sin\eta$. Consequently, the equations (4.1) become

$$\nabla^2\psi = -J(\xi,\eta)\omega \tag{4.2}$$

$$\text{and} \quad \psi_y\omega_x - \psi_x\omega_y = \frac{1}{Re}\nabla^2\omega, \tag{4.3}$$

where $J(\xi,\eta) = \frac{1}{2}(\cosh(2\xi) - \cos(2\eta))$ is the Jacobian of the transformation. The new domain to be solved is where $x \geq 0$ and $y \geq 0$ map to the semi-infinite rectangular domain so that $0 \leq \eta \leq \frac{1}{2}\pi$ with the flat plate at $0 \leq x \leq 1$ transformed to the η-axis ($0 \leq \eta \leq \frac{\pi}{2}, \xi = 0$). This system is associated with the boundary conditions as follows

$$\begin{cases} \psi = 0 \quad \text{and} \quad \psi_y = 0 \quad \text{for,} & \xi = 0, \quad 0 \leq \eta \leq \frac{1}{2}\pi, \\ \psi = -xy = -\frac{1}{4}\sinh 2\xi \sin 2\eta \quad \text{and} \quad \omega = 0 \quad \text{for,} & \xi \to \infty, \quad 0 \leq \eta \leq \frac{1}{2}\pi, \\ \psi = 0 \quad \text{and} \quad \omega = 0 \quad \text{for,} & \eta = 0, \quad 0 \leq \xi \to \infty, \\ \psi = 0 \quad \text{and} \quad \omega = 0 \quad \text{for,} & \eta = \frac{1}{2}\pi, \quad 0 \leq \xi \to \infty. \end{cases} \tag{4.4}$$

The problem can be discretized and linearized in the same manner as the lid-driven cavity problem detailed in the previous chapter.

Value of (ξ) in computational domain	Value of X_∞ in physical domain
$\xi = 1$	$X_\infty = 1.543$
$\xi = 1.5$	$X_\infty = 2.354$
$\xi = 2$	$X_\infty = 3.762$
$\xi = 2.5$	$X_\infty = 6.132$
$\xi = 3$	$X_\infty = 10.067$
$\xi = 4$	$X_\infty = 27.308$

Table 4.1: The various values of X_∞ corresponding to ξ value.

4.2 Numerical Results

As in the lid-driven cavity problem, a direct solver has been used to solve the linearized system form (4.3) and the steady separated corner flow boundary conditions (4.4) in order to obtain the numerical solution of the streamfunction ψ and the vorticity ω. The code combines the Newton iteration with the MATLAB backslash operator as a direct solver to obtain the solution corrected by correction terms, as explained in the lid-cavity problem. The convergence criteria for Newton iteration are the same as the lid-driven convergence criteria, see section 3.2.4.

The aim of this work, as mentioned, is to provide an accurate description of the steady corner flow, and show the independence of the solution from the variation of Re and X_∞ where $X_\infty = \cosh \xi_\infty$. In other words, X_∞ is $X_\infty = \cosh \xi \cos \eta$ when $\eta = 0$, which is the value of x on the x-axis when $\xi \to \infty$. The code is run on various grid sizes, namely, on 51×51, 81×81, 101×101, and on a fine grid 121×121. Moreover, we run the code on various semi-infinite domains. The results are generated for different values of X_∞, as shown in the Table (4.1). We have obtained solutions of the problem for Re up to 14000 when $X_\infty = 1.543$, which is a much higher Re compared with the previous reported results by Leal

(1973), Suh & Liu (1990) and Mclachlan (1991). Table 4.2 shows the highest Re obtained for various X_∞ on the fine grid 121×121. We start at $Re = 100$ in each domain (different value of X_∞), and use the solution at each Reynolds number as an initial value at the next higher Re.

Figures (4.2-4.3) present the streamfunction and vorticity profiles along the horizontal line passing through the geometry center for various values of X_∞ at several Re. It is observed that the streamfunction profiles are identical for various X_∞. From the graphs in Figures (4.2-4.3), one can see that the streamfunction profiles start from around zero at various values of Re, and maintain the same profile at different values of Re and X_∞, which indicate the independence of the solution from the variation of Re and X_∞. This can be observed clearly in Figure 4.2 at $Re = 250$ and $Re = 1000$. The same behavior is observed for the computed vorticity along a horizontal line passing through the transformed geometry center ($x(\xi, \eta = \frac{\pi}{4}) = \cosh\xi \cos\frac{\pi}{4}$) for various values of X_∞ at several Re in Figures (4.4-4.5). In these figures we zoomed in to show the clear behavior of the vorticity on the x-axis between approximately 0.5 and 1.2 where the actions of separation and circulations occur. In the same Figures, when we increase the value of X_∞, the vorticity along the horizontal line passing the geometry center, which is at a large distance from the separation point, remains almost constant and near zero. Figures (4.6-4.17) show the streamline and vorticity contour plots at various Re on various grid sizes for different values of X_∞. The contour levels plotted for the streamlines are $(-0.9, -0.7, -0.5, -0.1, -0.2, -0.3, -0.001, 0.001, 0.004, 0.008, 0.012, 0.016, 0.02, 0.024, 0.028, 0.032)$ and $(-1, -2, 1, 2, 4, 6, 8, 10)$ for the vorticity contour levels.

Value of X_∞ in physical domain	The highest Re obtained
$X_\infty = 1.543$	14000
$X_\infty = 2.354$	11000
$X_\infty = 3.762$	9500
$X_\infty = 6.132$	7500
$X_\infty = 10.067$	5000
$X_\infty = 27.308$	1500

Table 4.2: The various values of X_∞ corresponding to ξ value.

The streamline and vorticity contours conform with the Mclachlan (1991) contour levels plots at the common levels and common Reynolds numbers. From the contour plots, it is obvious that, for large Reynolds number, the solutions are dependent on the mesh size, and finer grids provide more accurate solution. As mentioned, the code succeeded in generating the solution at $Re = 14000$ for $X_\infty = 1.543$ on the grid 121×121, whereas it fails to do so on the 101×101 grid size. The presence of the oscillations in Figure (4.17) clearly indicates the dependency of the solution on the grid size, and the vorticity plot is not fully resolved. The same comment can be said for the dependency of the value of X_∞ on the grid size. As the value of X_∞ increases, we need to use a finer grid to obtain the solution at high Re. For $X_\infty = 27.308$, which is the largest value of X_∞ in the present work, the code fails to obtain the solution at Re higher than 1500 on the grid 121×121, as highlighted in Table (4.2).

It is worth mentioning that, in Figure (4.11), one can see the effect of the fine grid 121×121 in obtaining the solution of the vorticity at $Re = 5000$, and the difference from the solution of the vorticity on the grid 81×81 at the same value of Re and X_∞. It is evident that the circles (bubbles) around the separation points are not physical and are due to the coarse grid 81×81 as they disappear on the fine grid 121×121 solution. Moreover, this indicates that the circles in

the contour plots of the vorticity in Figures (4.15), (4.16) and (4.17) are not physical. Table 4.3 shows the comparison of the vorticity values at the center of Richardson-extrapolated eddy, with Mclachlan (1991), at the common Reynolds numbers. From this table, it is observed that the center of the corner eddy moves first left and then moves down as we increase Re, and remains almost fixed for high $Re \geq 3000$. The same observation has been reported by Mclachlan (1991) without reporting the positions (x, y) of the center of Richardson-extrapolated eddy as we have in Table 4.3. Mclachlan (1991) mentioned in his paper that the separated region remains of size $O(1)$ as Reynolds number is increased. This is confirmed by the present results for various Reynolds numbers. One can observe the separated region for $x_\infty = 1.543$ from low to high Reynolds number throughout the listed figures.

Figures (4.18-4.20) show the behavior of vorticity on $y = 0$ at various Re for several X_∞. Mclachlan (1991) mentioned that the separation point occurs at the point where $\omega = 0$ and moves to the right as the Reynolds number increases. We observe the same behavior movement of the separation point for $x_\infty = 1.543$, as is clear in Figure(4.18). The same behavior is observed for various X_∞. However, one can observe oscillations in Figures (4.18) and (4.19) for some Reynolds numbers. The oscillations increase as the Reynolds number increases or as X_∞ increases, as demonstrated in Figure (4.19) at $Re = 7000$ for $X_\infty = 6.132$. These oscillations suggest that a finer grid is required to resolve some features.

Each plot in Figures (4.21) and (4.22) shows the vorticity profile on $y = 0$ at fixed Re for various X_∞. These plots confirm that more resolution is required as the X_∞ increases, as is very clear in Figure(4.22).

Re	Value of ω at the center (present)	$(x, y)_{\text{phy}}$ (present)	Mclachlan (1991)
1000	1.66923	(0.1429,0.2738)	1.583
2000	1.81680	(0.1662,0.2378)	1.777
3000	1.93989	(0.1658,0.2266)	1.912
4000	2.02886	(0.1787,0.2261)	2.014
5000	2.09864	(0.1787,0.2261)	2.105

Table 4.3: The values of ω at the center of Richardson-extrapolated eddy compared with Mclachlan (1991).

To conclude, the simplicity of the problem domain and the ability of using the conformal mapping makes this an attractive problem to solve at high Reynolds number. This problem is full of rich flow features of interest, such as separation, circulations and eddies. A solution at high Reynolds number on a domain of $X_\infty = 1.543$, in addition to solutions at high Reynolds number for various X_∞, are obtained. As the Reynolds number increases the separated region remains of size $O(1)$ and the separation point moves to the right. More resolution is required as we increase either the Reynolds number or the value of X_∞. More work is required to investigate the oscillations. It may be that the oscillations also arise because of the boundary conditions for large X_∞. In our work, we have used $\psi = xy$, but a more accurate asymptotic condition valid for large x and y may be needed. The results we have obtained are at much higher Reynolds numbers in comparison with previous researchers. Figures and tables are presented for future comparisons.

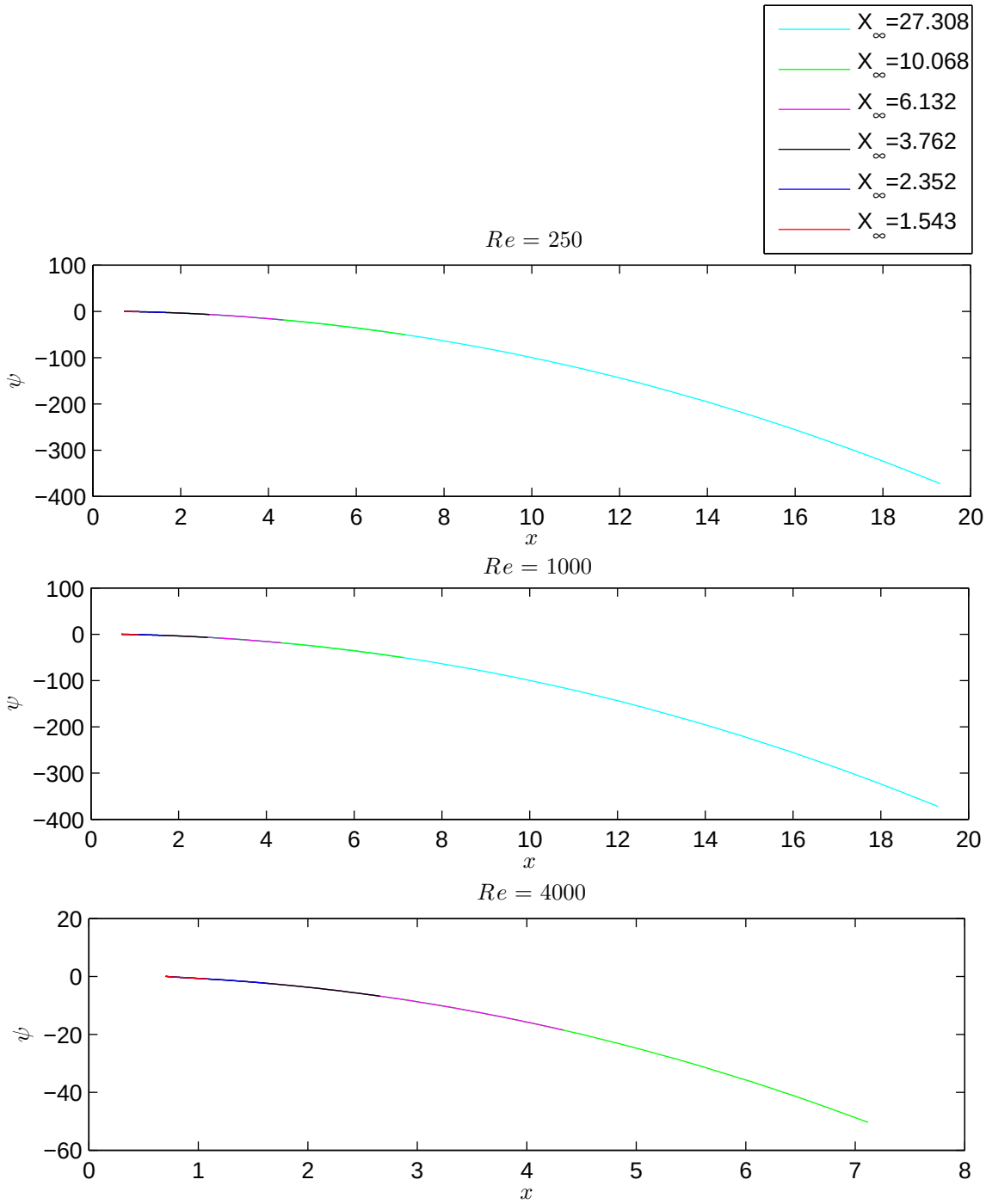

Figure 4.2: Computed streamfunction along a horizontal line passing through the transformed geometry center ($x(\xi, \eta = \frac{\pi}{4}) = \cosh\xi \cos\frac{\pi}{4}$) of each X_∞ at various $Re = 250, 1000$ and 4000.

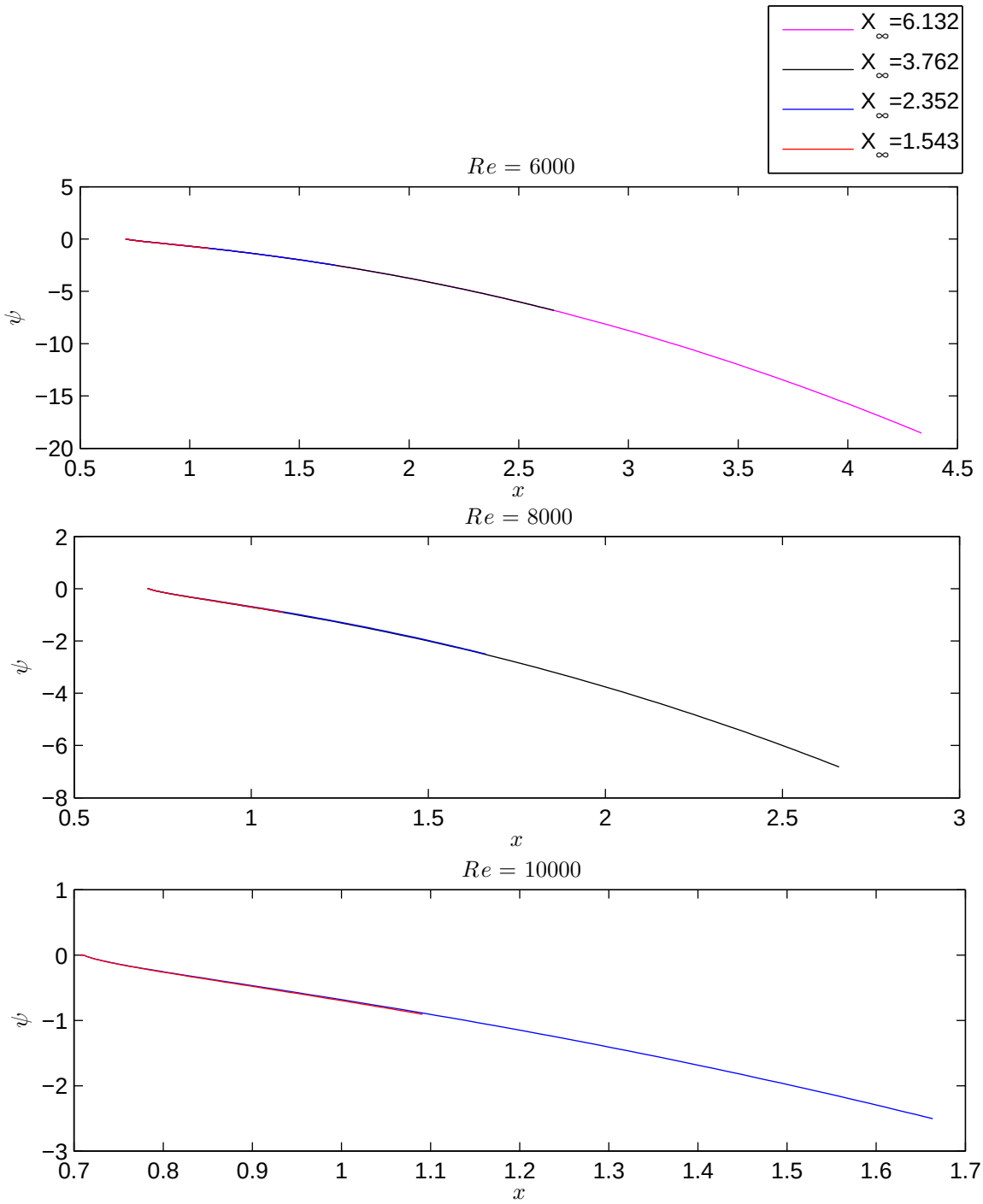

Figure 4.3: Computed streamfunction along a horizontal line passing through the transformed geometry center ($x(\xi, \eta = \frac{\pi}{4}) = \cosh\xi \cos\frac{\pi}{4}$) of each X_∞ at various $Re = 6000, 8000$ and 10000.

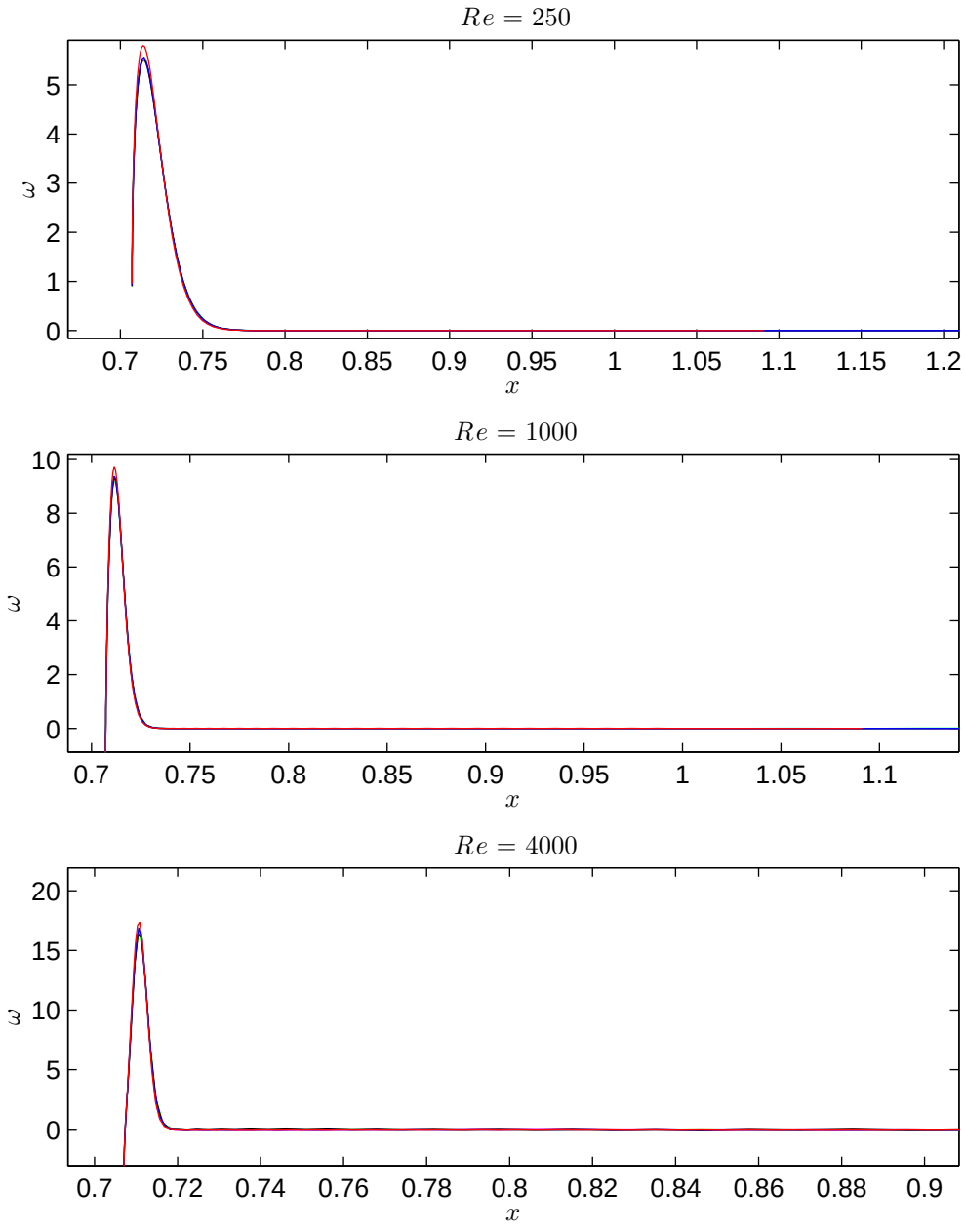

Figure 4.4: Computed vorticity along a horizontal line passing through the transformed geometry center ($x(\xi, \eta = \frac{\pi}{4}) = \cosh\xi \cos\frac{\pi}{4}$) of each X_∞ at various $Re = 250, 1000$ and 4000.

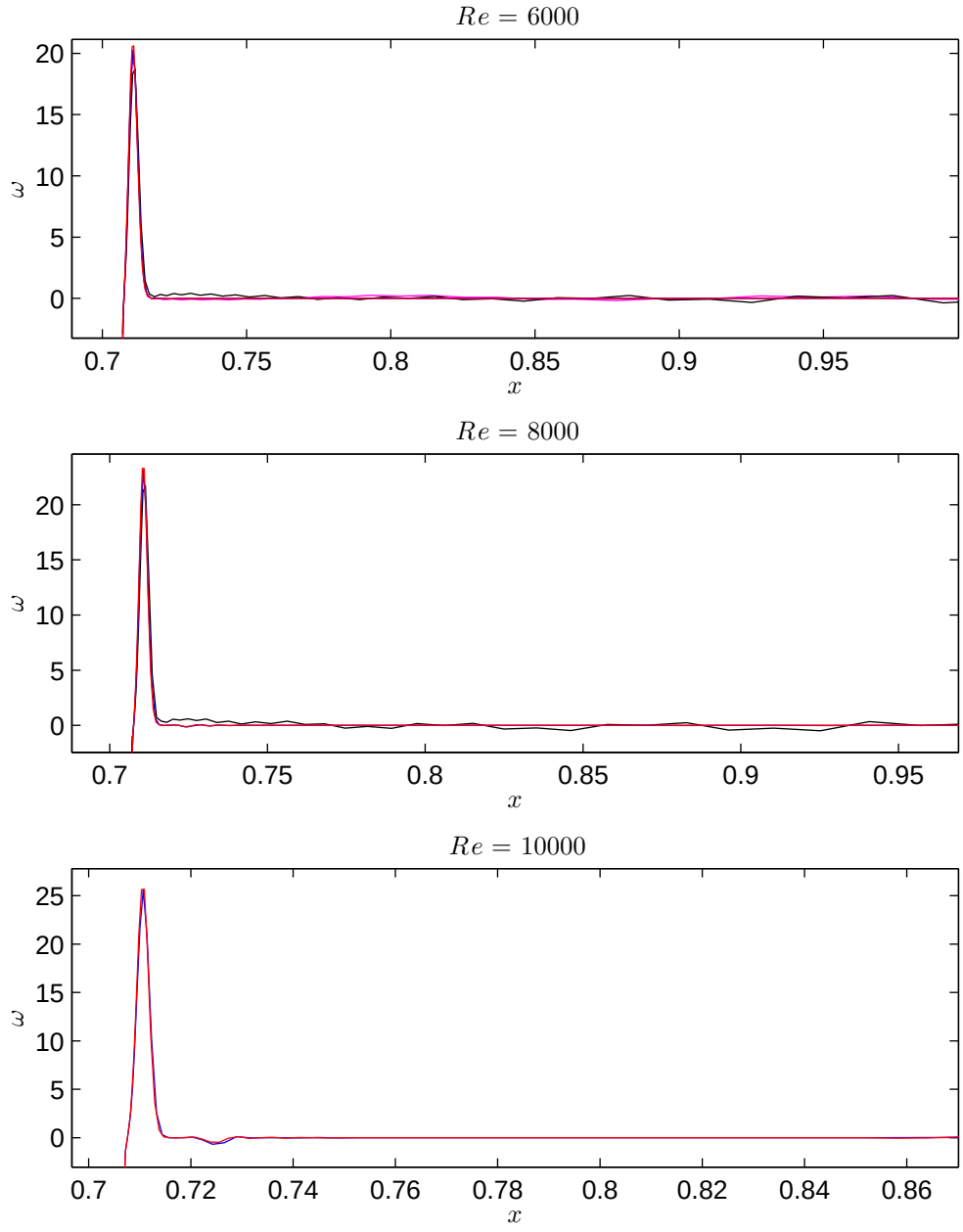

Figure 4.5: Computed vorticity along a horizontal line passing through the transformed geometry center ($x(\xi, \eta = \frac{\pi}{4}) = \cosh\xi \cos\frac{\pi}{4}$) of each X_∞ at various $Re = 6000, 8000$ and 10000.

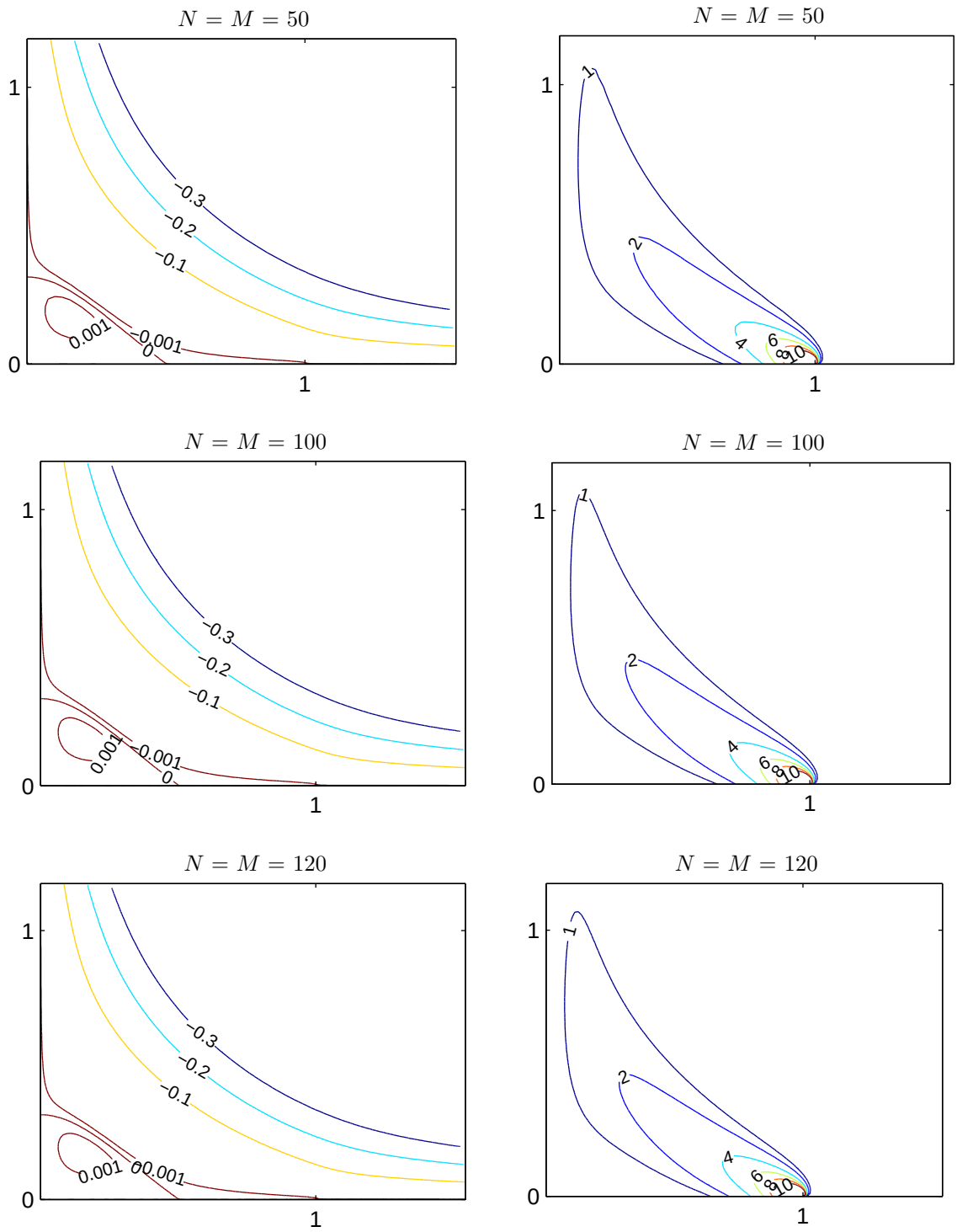

Figure 4.6: Streamline (left) and vorticity (right) contours plot at $Re = 100$ on various grids for $X_\infty = 1.543$.

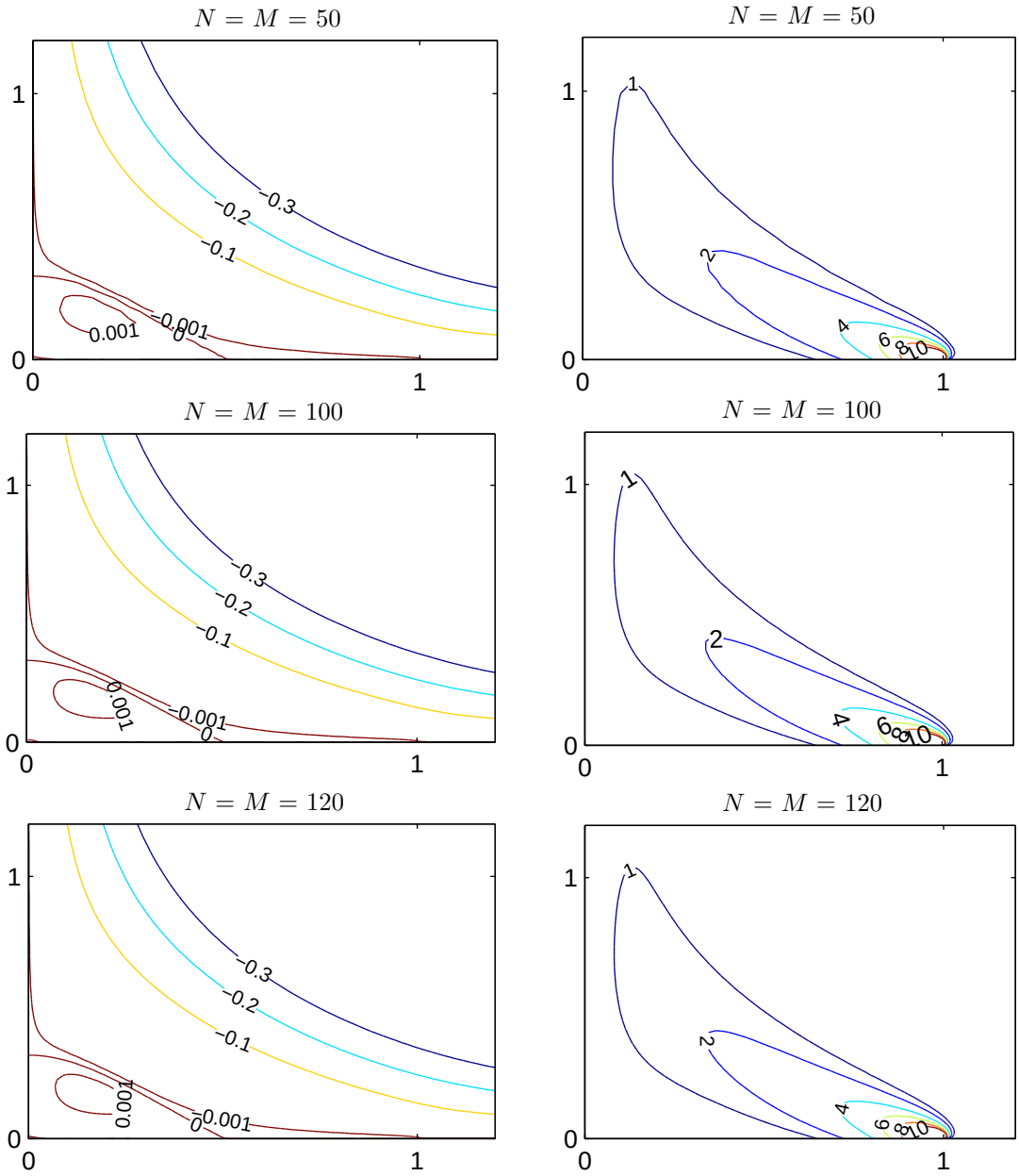

Figure 4.7: Streamline (left) and vorticity (right) contours plot at $Re = 100$ on various grids for $X_\infty = 10.067$.

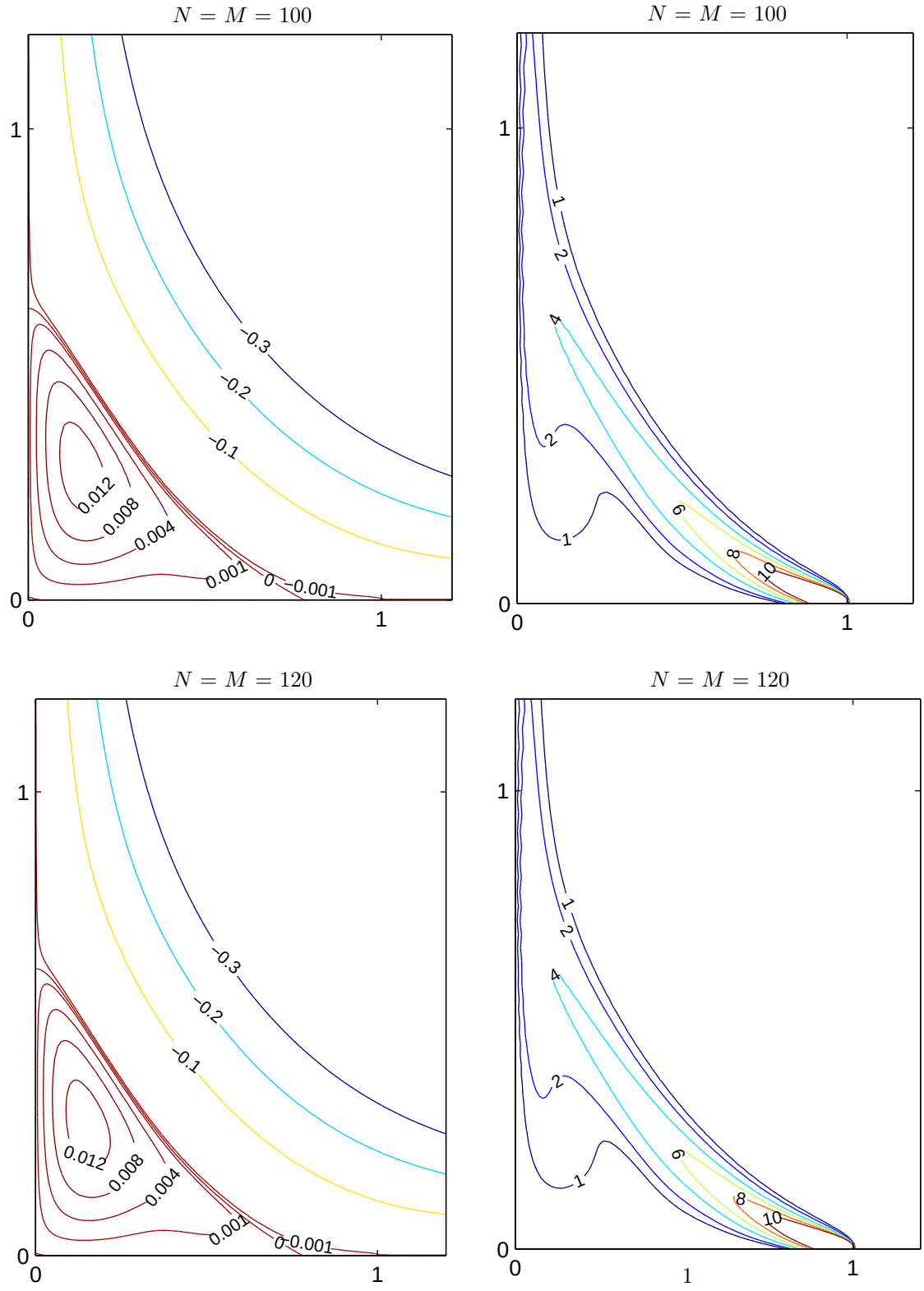

Figure 4.8: Streamline (left) and vorticity (right) contours plot at $Re = 1000$ on various grids for $X_\infty = 3.762$.

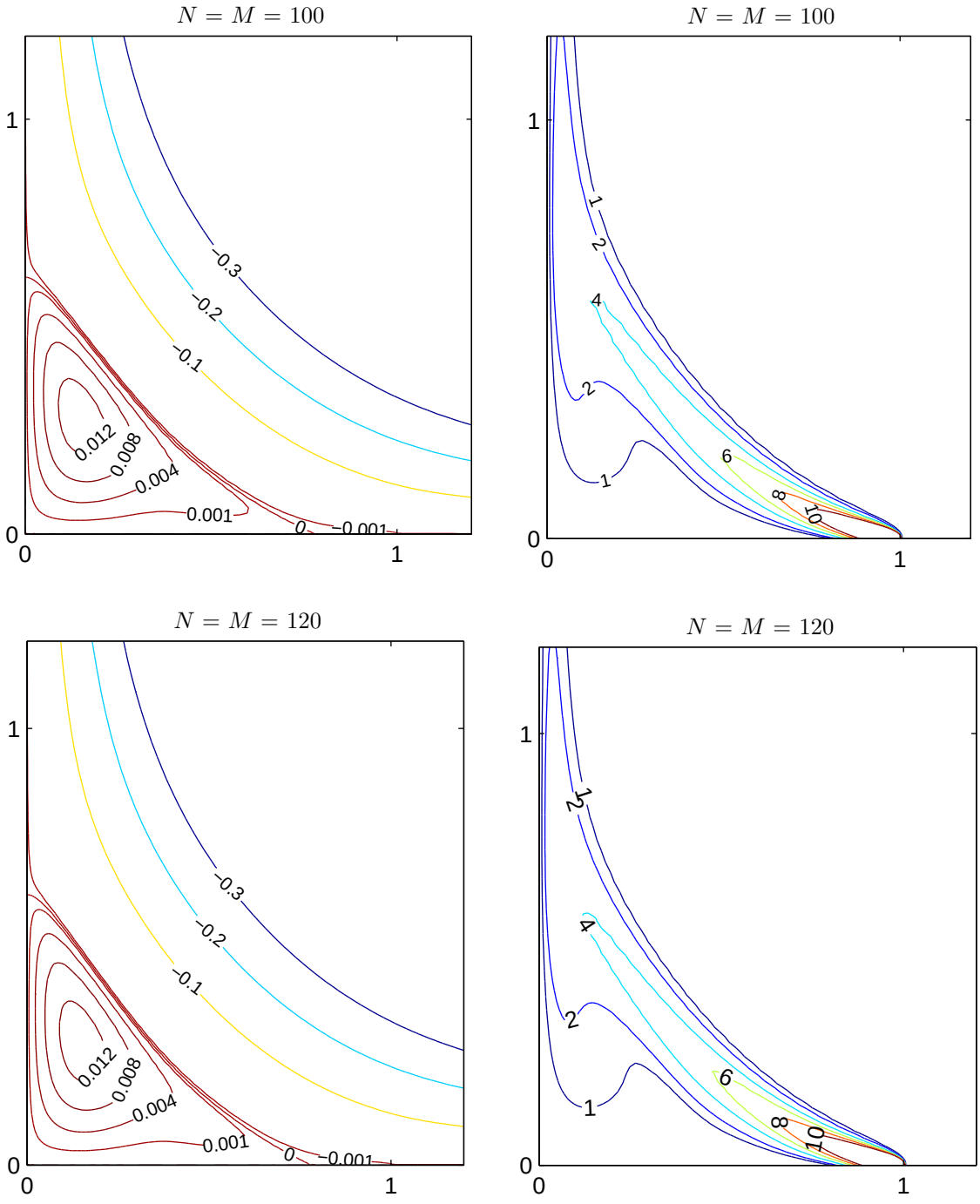

Figure 4.9: Streamline (left) and vorticity (right) contours plot at $Re = 1000$ on various grids for $X_\infty = 27.308$.

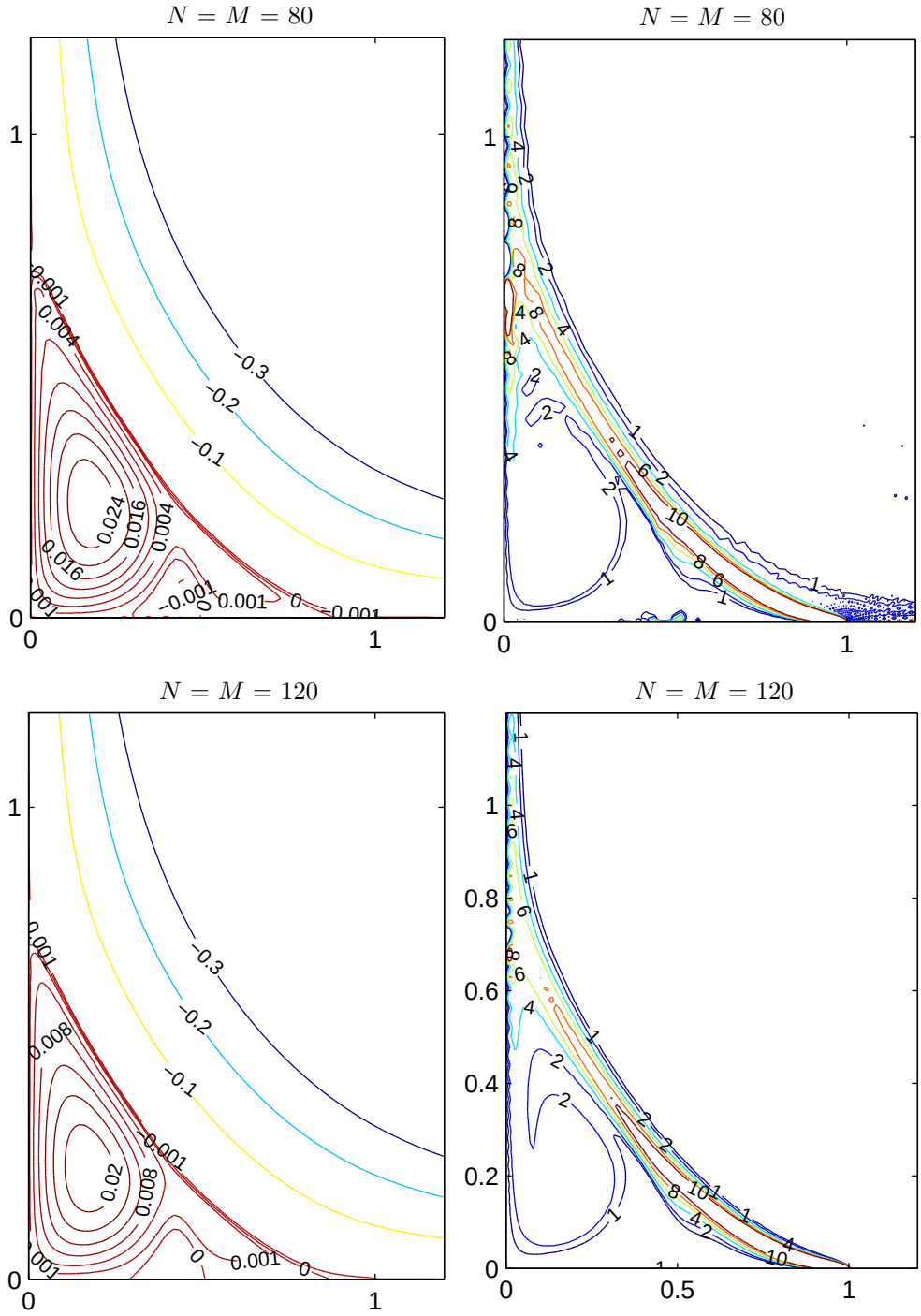

Figure 4.10: Streamline (left) and vorticity (right) contours plot at $Re = 5000$ on various grids for $X_\infty = 2.352$.

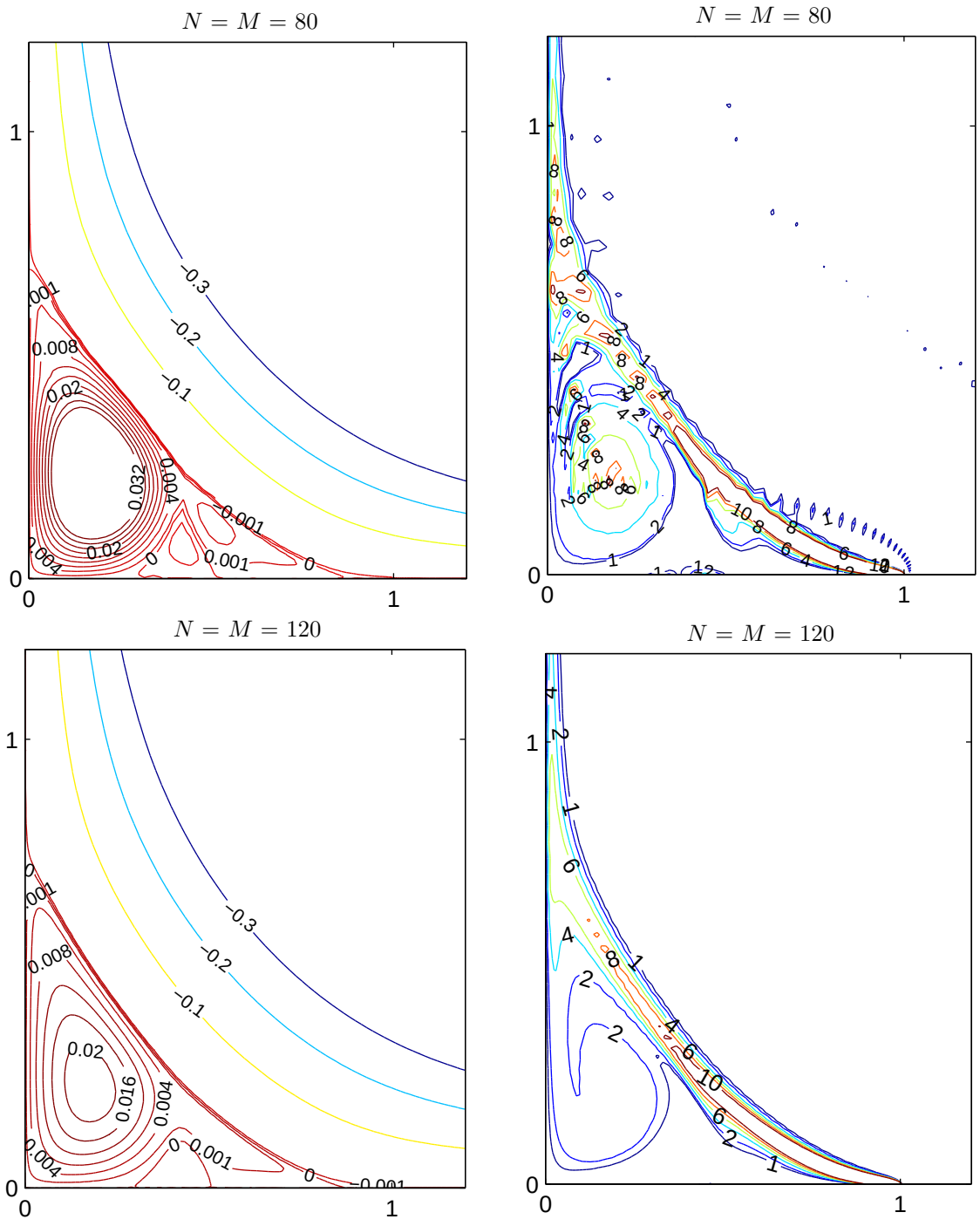

Figure 4.11: Streamline (left) and vorticity (right) contours plot at $Re = 5000$ on various grids for $X_\infty = 6.132$.

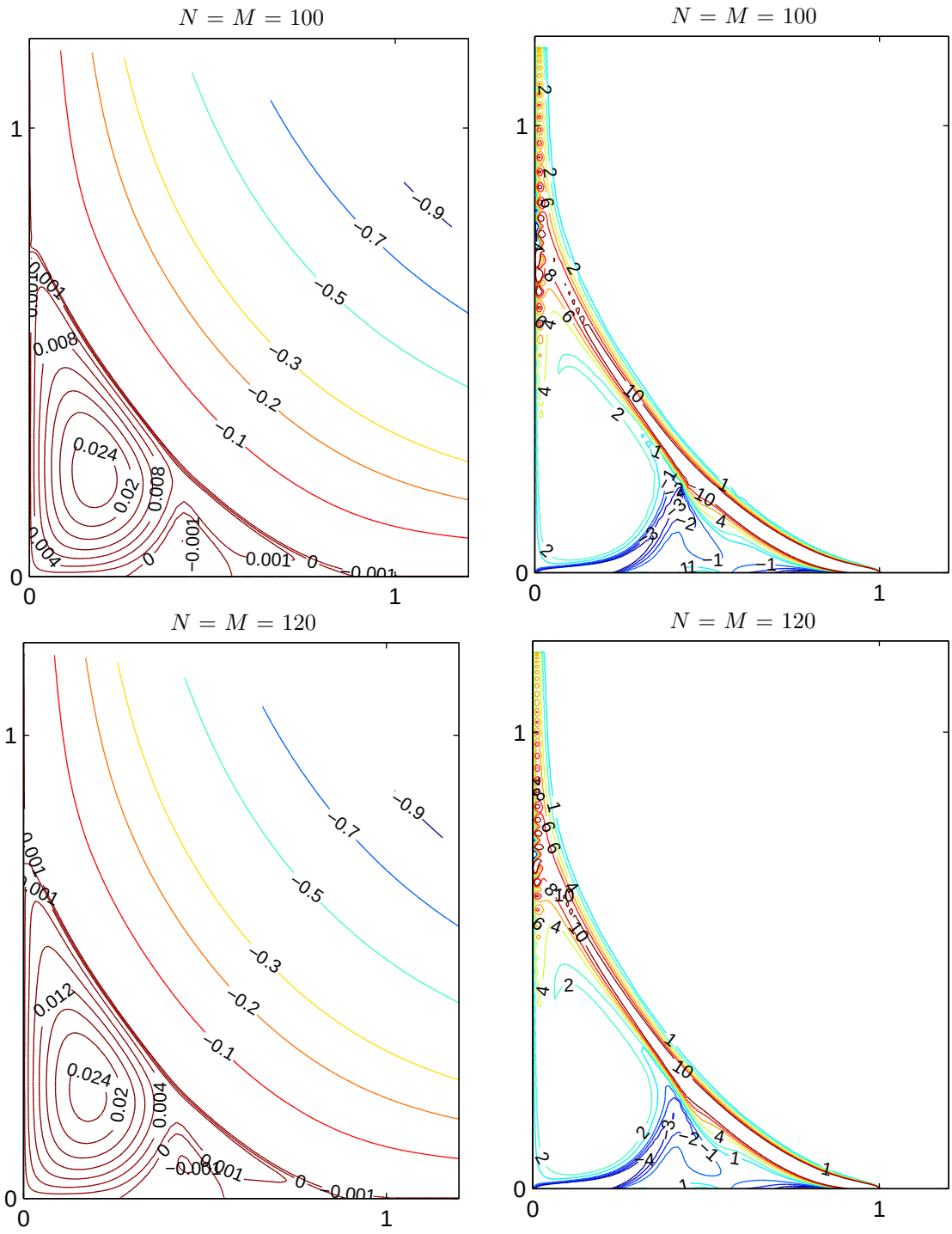

Figure 4.12: Streamline (left) and vorticity (right) contours plot at $Re = 8000$ on various grids for $X_\infty = 1.543$.

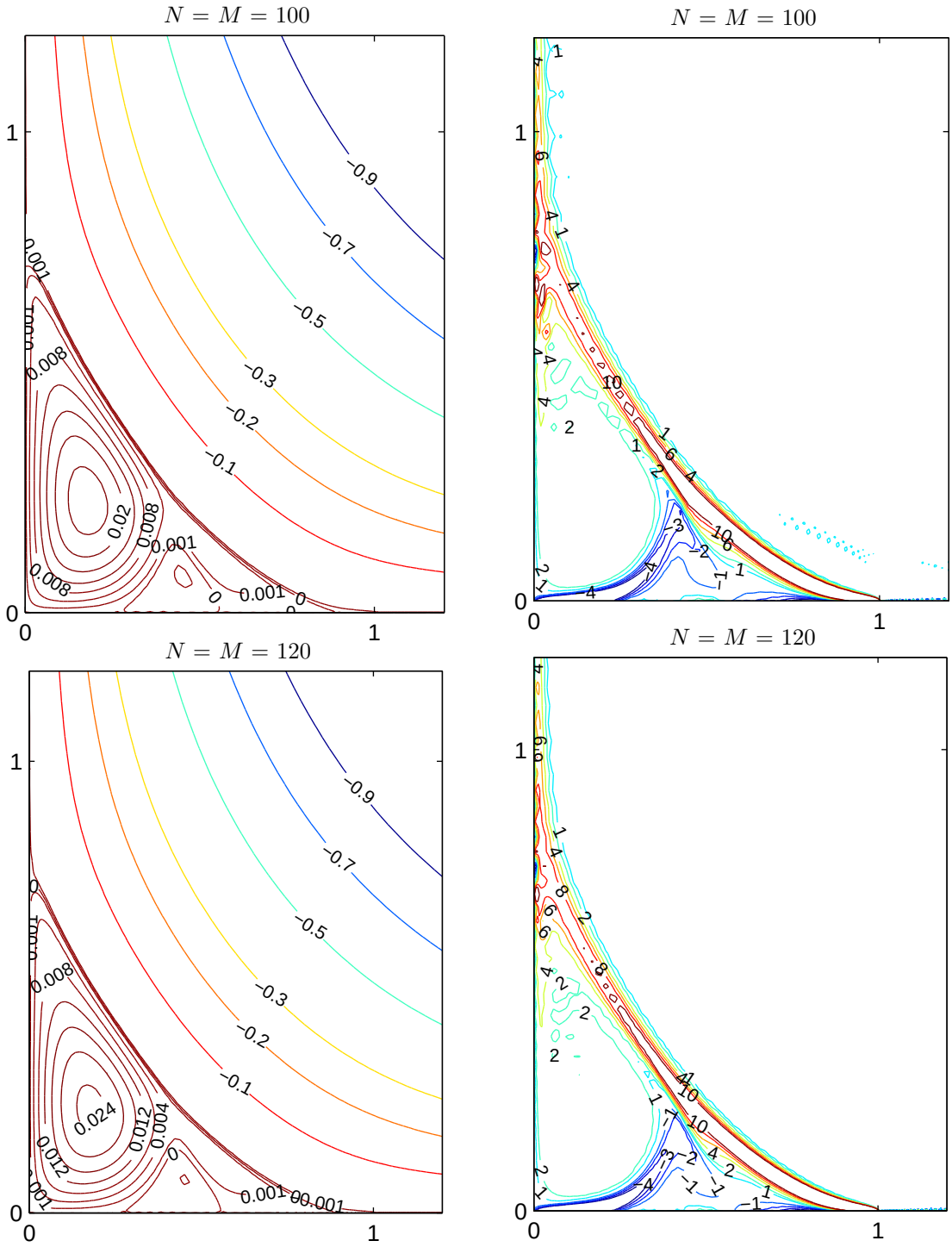

Figure 4.13: Streamline (left) and vorticity (right) contours plot at $Re = 8000$ on various grids for $X_\infty = 3.762$.

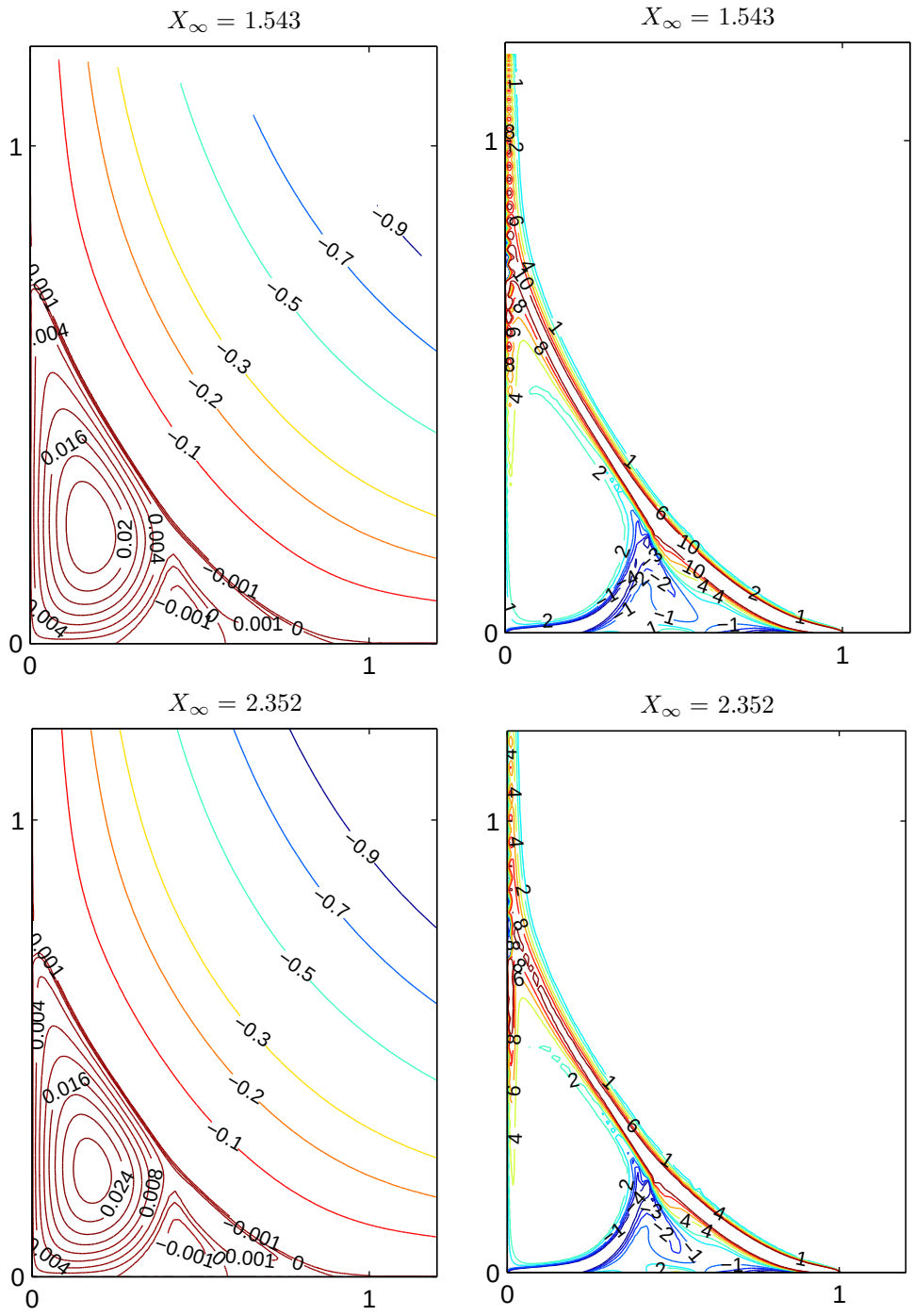

Figure 4.14: Streamline (left) and vorticity (right) contours plot at $Re = 10000$ on 121×121 grid for $X_\infty = 1.543$ and $X_\infty = 3.762$.

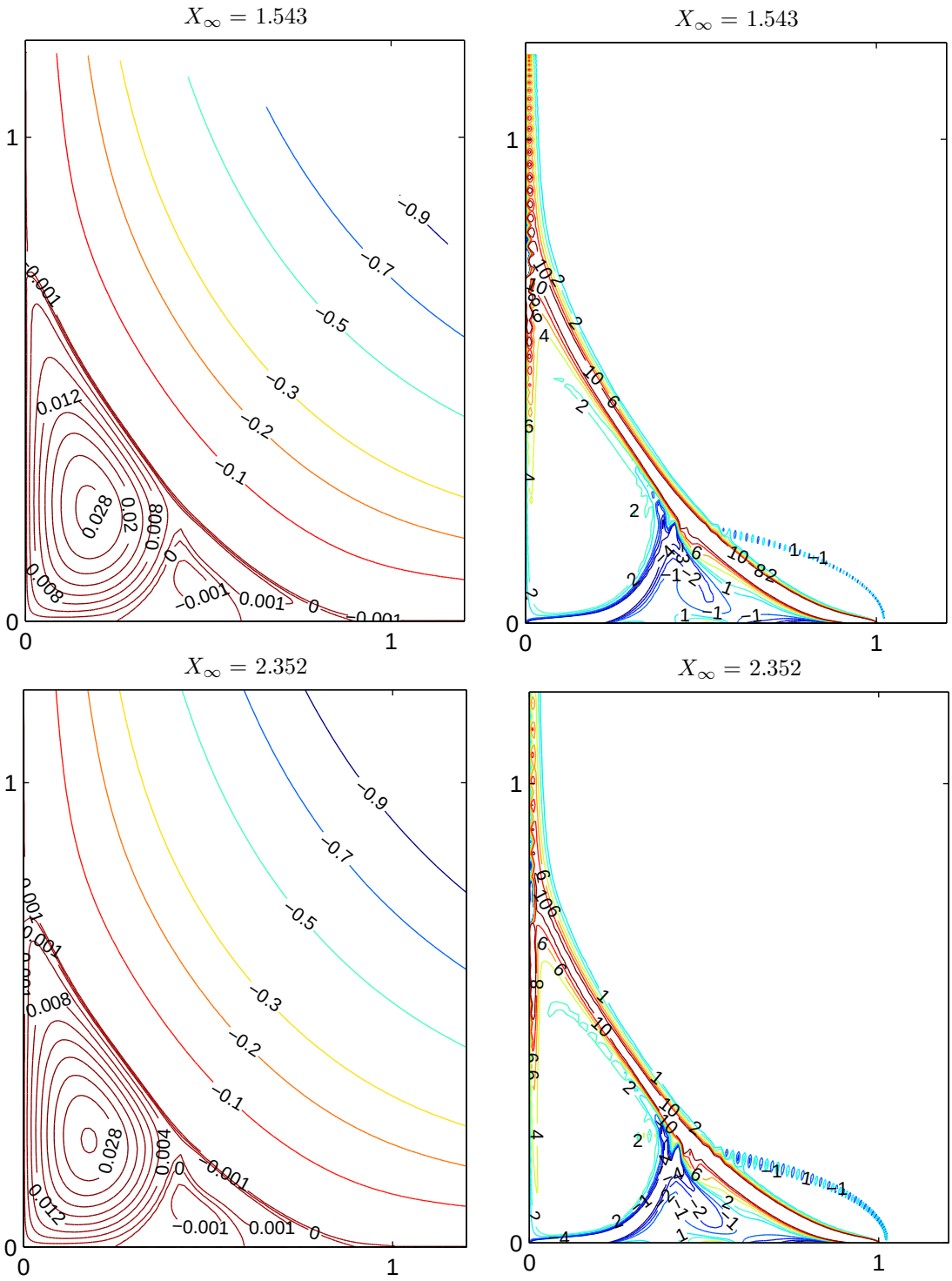

Figure 4.15: Streamline (left) and vorticity (right) contours plot at $Re = 11000$ on 121×121 grid for $X_\infty = 1.543$ and $X_\infty = 2.352$.

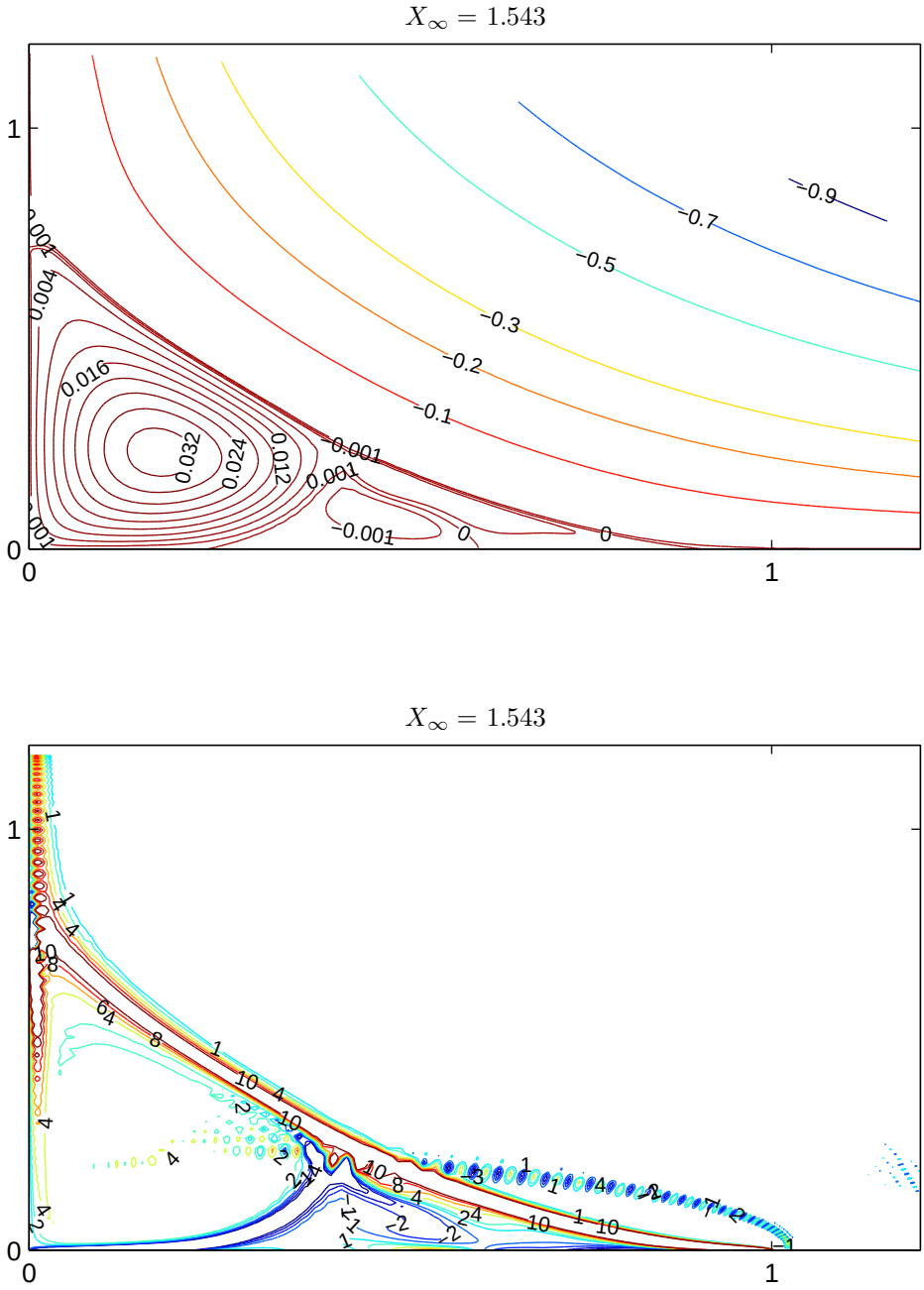

Figure 4.16: Streamline (left) and vorticity (right) contours plot at $Re = 13000$ on 121×121 grid for $X_\infty = 1.543$.

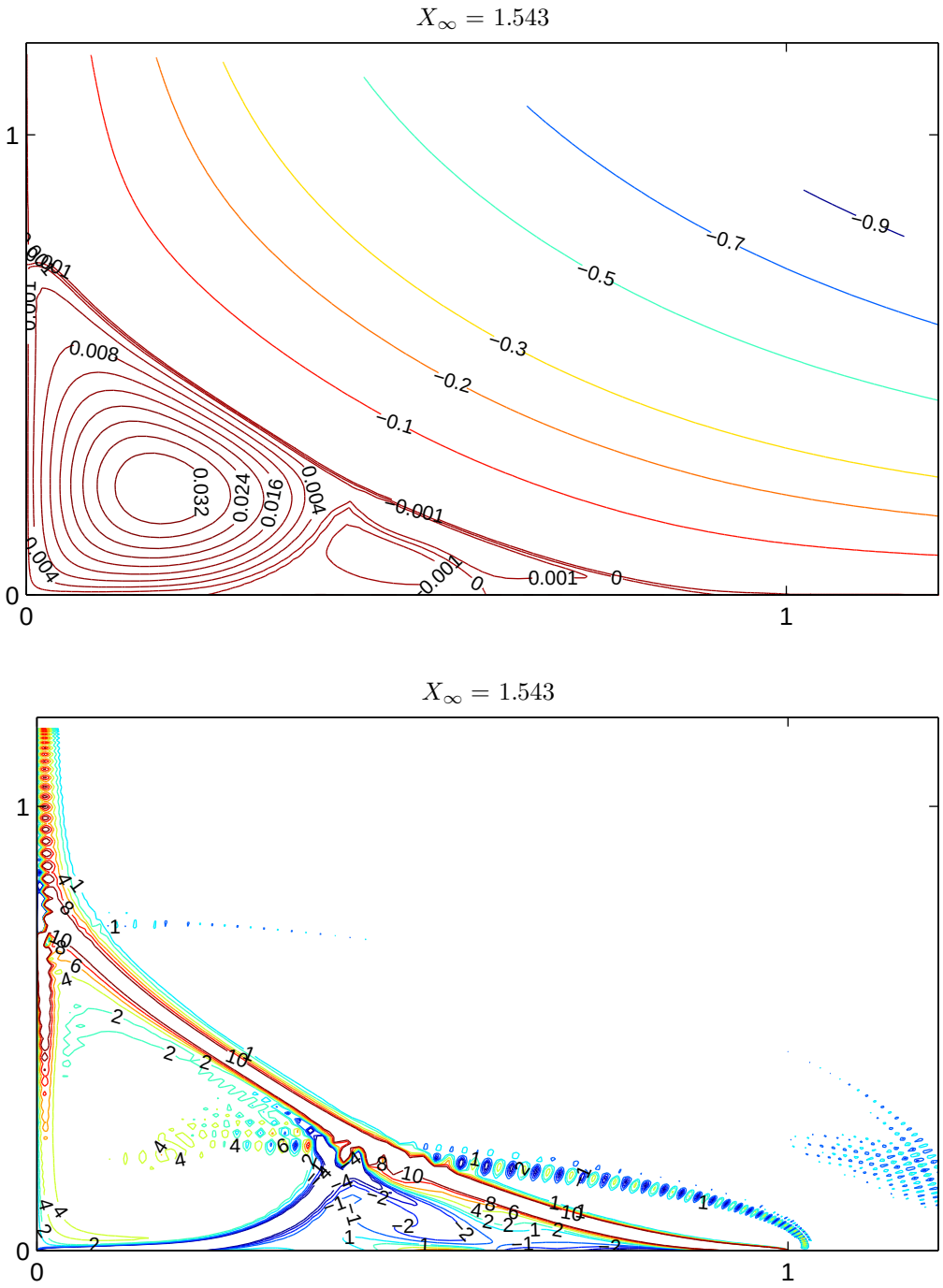

Figure 4.17: Streamline (left) and vorticity (right) contours plot at $Re = 14000$ on 121×121 grid for $X_\infty = 1.543$.

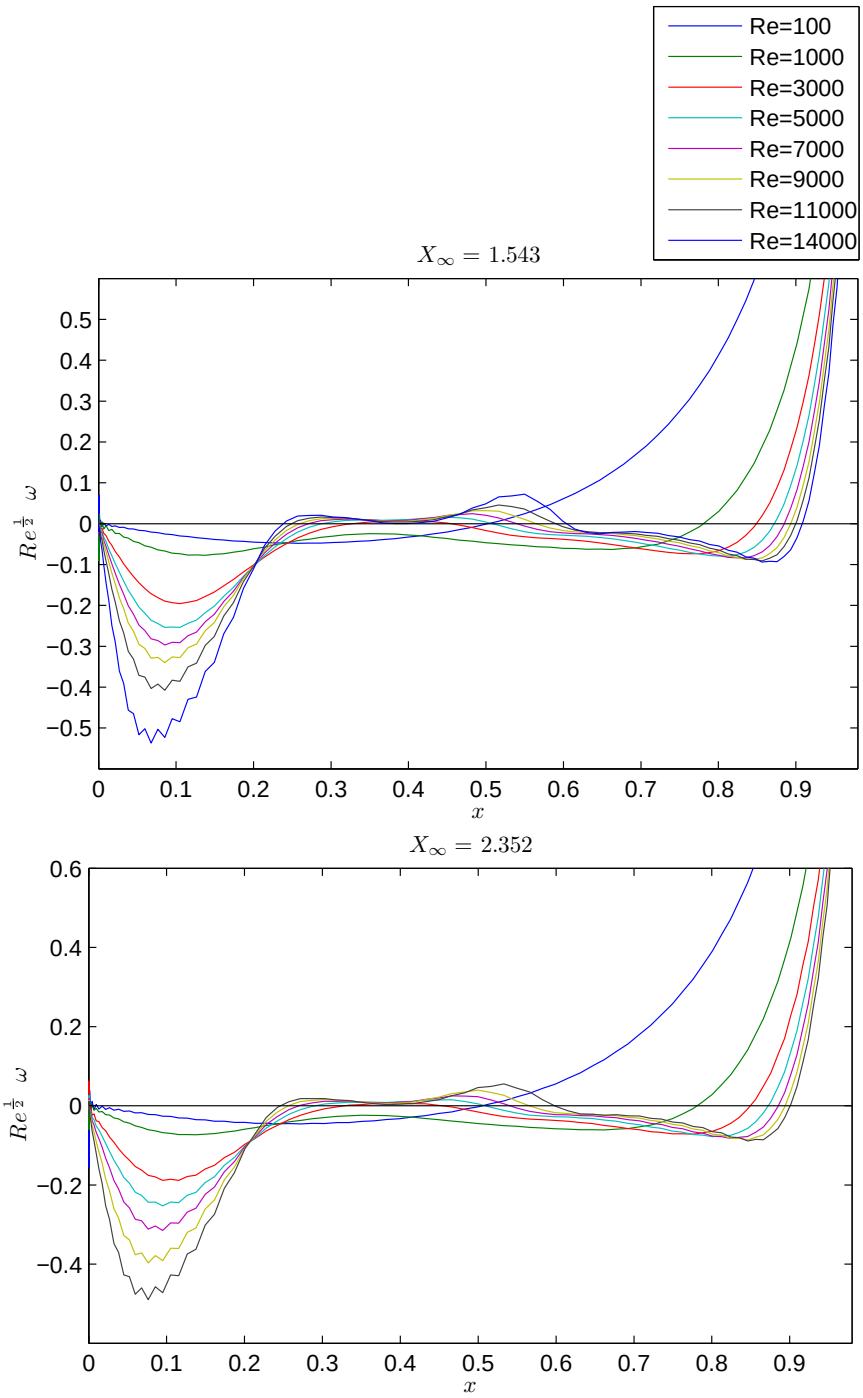

Figure 4.18: The vorticity profile on $y = 0$ at various Re for $X_\infty = 1.543$ (top) and $X_\infty = 2.352$ (bottom).

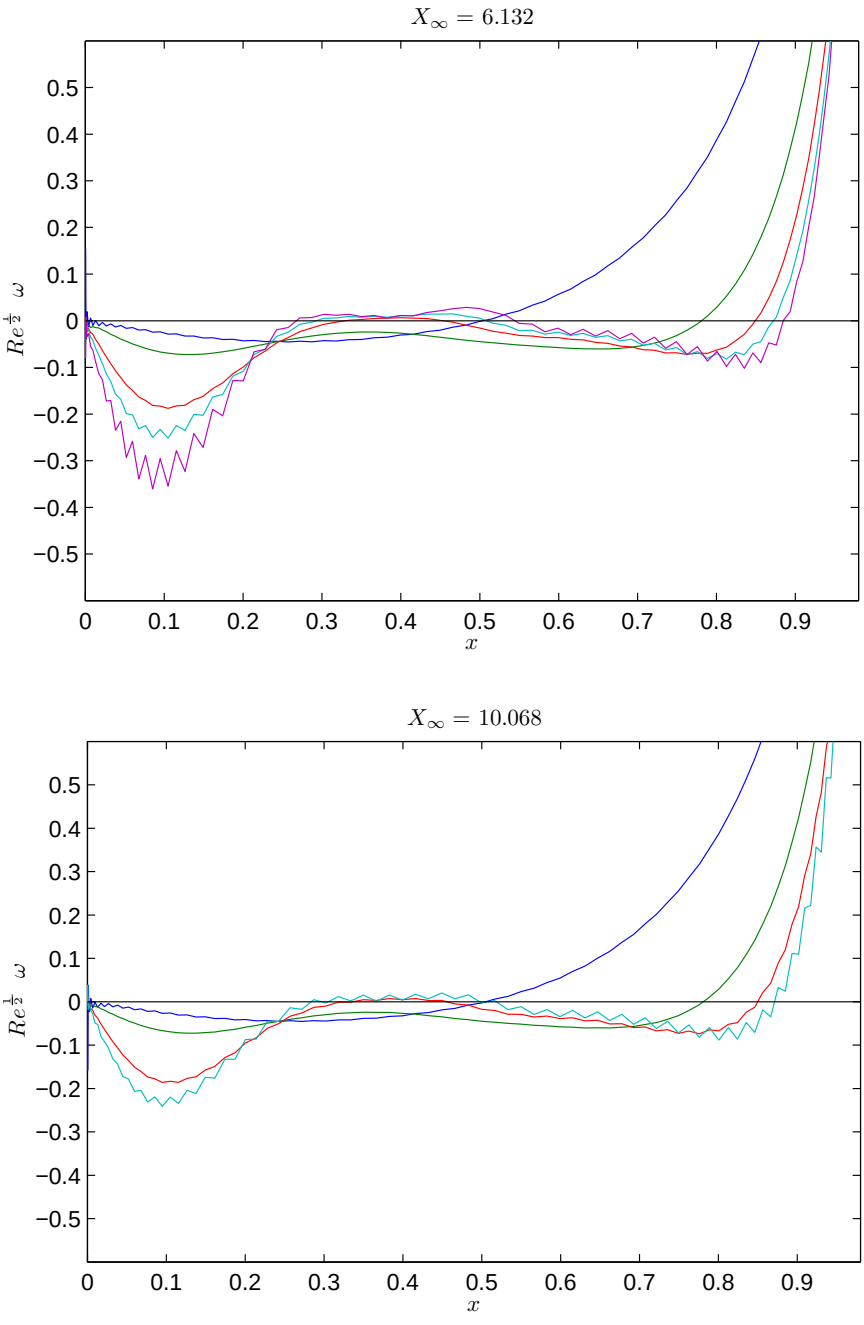

Figure 4.19: The vorticity profile on $y = 0$ at various Re for $X_\infty = 6.132$ (top) and $X_\infty = 10.068$ (bottom).

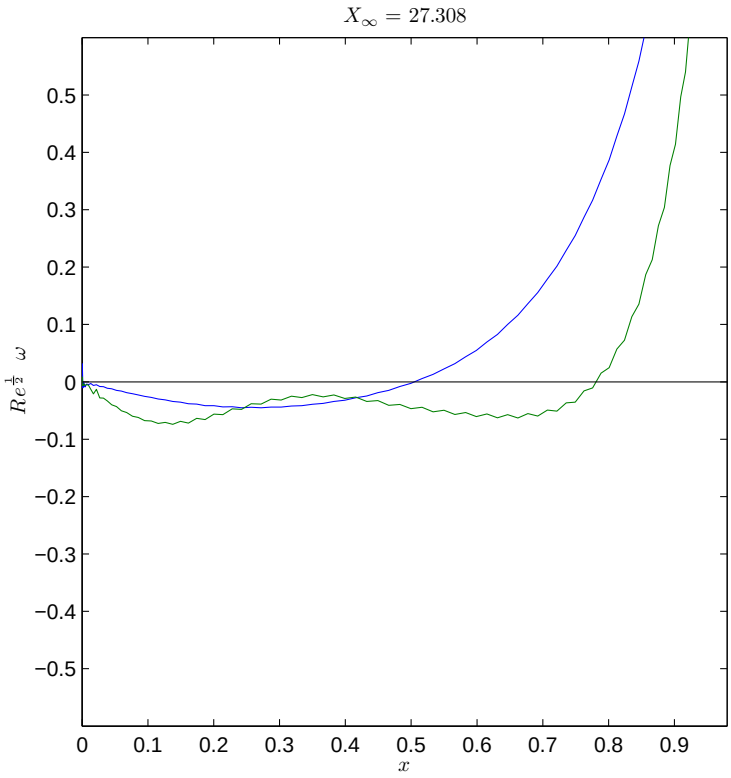

Figure 4.20: The vorticity profile on $y = 0$ at various Re for $X_\infty = 27.308$.

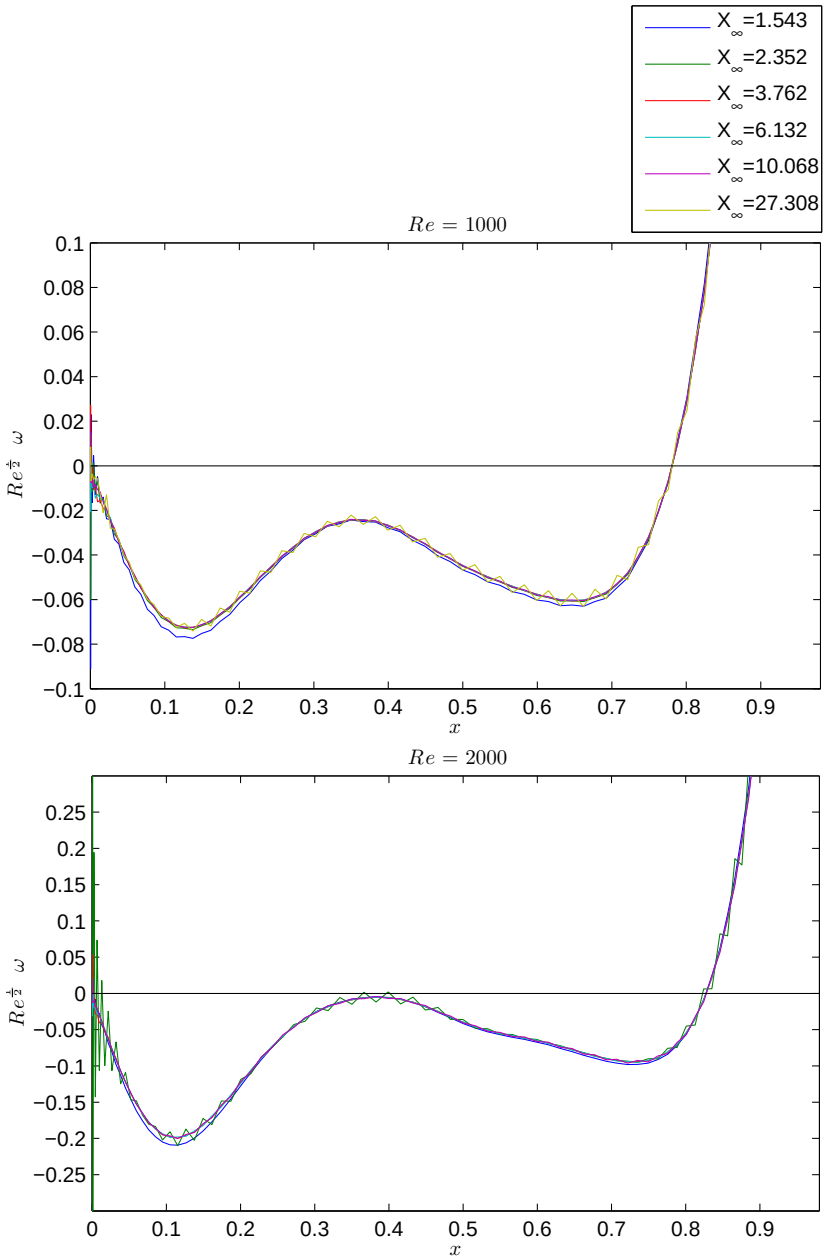

Figure 4.21: The vorticity profile on $y = 0$ at $Re = 1000$ for various X_∞ (top) and at $Re = 2000$ for various X_∞ (bottom).

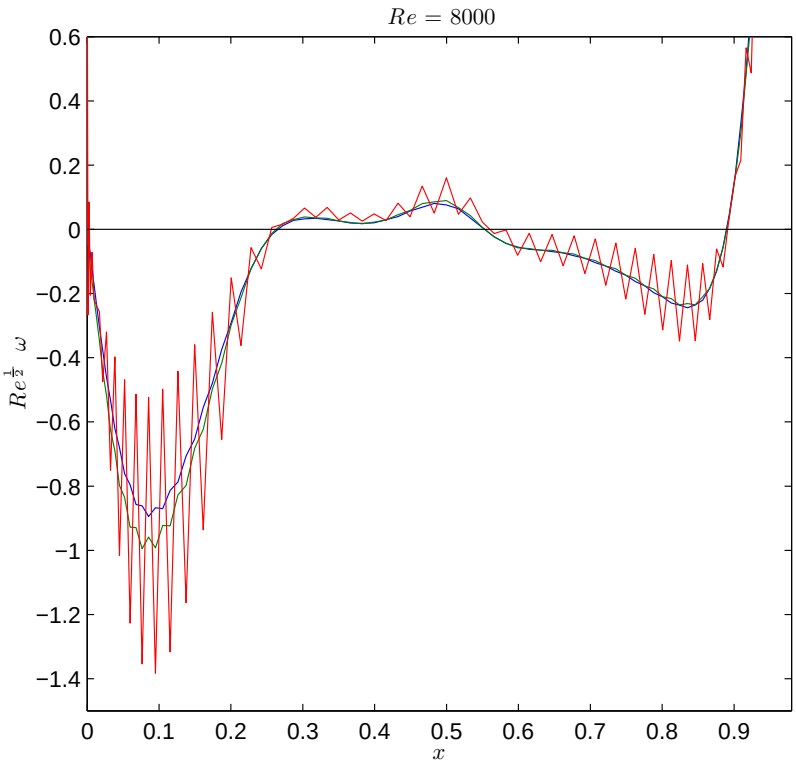

Figure 4.22: The vorticity profile on $y = 0$ at $Re = 8000$ for various X_∞.

Chapter 5

Solution to 3-D Navier Stokes Equations

5.1 Introduction

In this chapter, we consider the solution of the steady flow in a three-dimensional lid-driven cavity using numerical methods. The three-dimensional velocity-vorticity formulation, used by Davies & Carpenter (2001), is considered. A test problem with a known exact solution is solved; hence, we can compare the numerical solution with the exact solution. Then, the cubical lid-driven cavity problem is solved. The problem is discretized using the Chebyshev discretization in the y and z directions, and fourth-order finite differences are used for the discretization in the x direction. Newton linearization is used to linearize the problem and a direct solver is devoted to solve the problem. The problem has been coded in both the MATLAB and FORTRAN environments.

5.2 Problem Formulation

In the present work, we use the velocity-vorticity formulation of the Navier-Stokes equations, which has been used by Davies & Carpenter (2001). "The advantage of the formulation is that there are only three governing equations to be solved for three dependent unknowns", Davies & Carpenter (2001).

The momentum equation for steady incompressible flows with the continuity equation can be written as

$$(\mathbf{q}.\nabla)\mathbf{q} = -\nabla P + \frac{1}{Re}\nabla^2\mathbf{q} \tag{5.1}$$

$$\nabla.\mathbf{q} = 0. \tag{5.2}$$

For the three-dimensional lid-driven cavity problem, the boundary conditions are as follows, see Figure(5.1):

$$\begin{cases} u = v = w = 0 \quad \text{for,} & x = 0, 1 \\ u = v = w = 0 \quad \text{for,} & y = 0, 1 \\ u = v = w = 0 \quad \text{for,} & z = 0 \\ u = 1, v = 0, w = 0 \quad \text{for,} & z = 1. \end{cases} \tag{5.3}$$

Let the velocity $\mathbf{q} = (u, v, w)$, $\mathbf{w} = (\omega_x, \omega_y, \omega_z)$ and introduce the definition of vorticity $\mathbf{w}$ as follows

$$\mathbf{w} = \nabla \times \mathbf{q}. \tag{5.4}$$

Taking the curl of the momentum equation leads to the vorticity transport equation, which can be written in conservative form as:

$$\frac{1}{Re}\nabla^2\mathbf{w} = \nabla \times (\mathbf{w} \times \mathbf{q}). \tag{5.5}$$

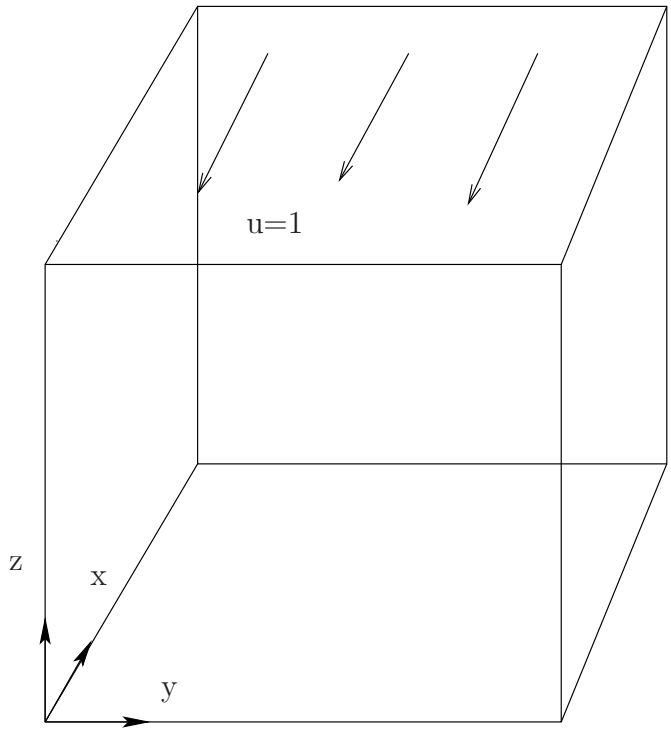

Figure 5.1: Sketch of the three-dimensional lid-driven cavity geometry.

Let

$$N = \nabla \times (\mathbf{w} \times \mathbf{q}) = (N_x, N_y, N_z). \tag{5.6}$$

To find N, we find $(\mathbf{w} \times \mathbf{q})$ and then take the curl of it, as follows

$$\mathbf{w} \times \mathbf{q} = \begin{vmatrix} i & j & k \\ \omega_x & \omega_y & \omega_z \\ u & v & w \end{vmatrix} = (w\omega_y - v\omega_z, u\omega_z - w\omega_x, v\omega_x - u\omega_y). \tag{5.7}$$

Then

$$N_x = \frac{\partial}{\partial y}[v\omega_x - u\omega_y] - \frac{\partial}{\partial z}[u\omega_z - w\omega_x], \tag{5.8}$$

$$N_y = \frac{\partial}{\partial z}[w\omega_y - v\omega_z] - \frac{\partial}{\partial x}[v\omega_x - u\omega_y], \tag{5.9}$$

$$N_z = \frac{\partial}{\partial x}[u\omega_z - w\omega_x] - \frac{\partial}{\partial y}[w\omega_y - v\omega_z]. \tag{5.10}$$

N_x can be rewritten as

$$\begin{aligned}
N_x &= \frac{\partial}{\partial y}[v\omega_x - u\omega_y] - \frac{\partial}{\partial z}[u\omega_z - w\omega_x]. \qquad (5.11)\\
&= v\frac{\partial \omega_x}{\partial y} - u\frac{\partial \omega_y}{\partial y} + \omega_x\frac{\partial v}{\partial y} - \omega_y\frac{\partial u}{\partial y}\\
&- u\frac{\partial \omega_z}{\partial z} + w\frac{\partial \omega_x}{\partial z} - \omega_z\frac{\partial u}{\partial z} + \omega_x\frac{\partial w}{\partial z}.\\
&= -u\left(\frac{\partial \omega_y}{\partial y} + \frac{\partial \omega_z}{\partial z}\right) + v\frac{\partial \omega_x}{\partial y} + w\frac{\partial \omega_x}{\partial z}\\
&+ \omega_x\left(\frac{\partial v}{\partial y} + \frac{\partial w}{\partial z}\right) - \omega_y\frac{\partial u}{\partial y} - \omega_z\frac{\partial u}{\partial z}.\\
N_x &= u\frac{\partial \omega_x}{\partial x} + v\frac{\partial \omega_x}{\partial y} + w\frac{\partial \omega_x}{\partial z}\\
&- \left(\omega_x\frac{\partial u}{\partial x} + \omega_y\frac{\partial u}{\partial y} + \omega_z\frac{\partial u}{\partial z}\right).\\
&= \mathbf{q}\cdot\nabla\omega_x - \mathbf{w}\cdot\nabla u.
\end{aligned}$$

In the same manner, N_y can be rewritten as

$$\begin{aligned}
N_y &= \frac{\partial}{\partial z}[w\omega_y - v\omega_z] - \frac{\partial}{\partial x}[v\omega_x - u\omega_y] \qquad (5.12)\\
&= w\frac{\partial \omega_y}{\partial z} - v\frac{\partial \omega_z}{\partial z} + \omega_y\frac{\partial w}{\partial z} - \omega_z\frac{\partial v}{\partial z}\\
&- v\frac{\partial \omega_x}{\partial x} + u\frac{\partial \omega_y}{\partial x} - \omega_x\frac{\partial v}{\partial x} + \omega_y\frac{\partial u}{\partial x}.\\
&= u\frac{\partial \omega_y}{\partial x} - v\left(\frac{\partial \omega_z}{\partial z} + \frac{\partial \omega_x}{\partial x}\right) + w\frac{\partial \omega_y}{\partial z}\\
&- \omega_x\frac{\partial v}{\partial x} + \omega_y\left(\frac{\partial v}{\partial x} + \frac{\partial w}{\partial z}\right) - \omega_z\frac{\partial v}{\partial z}.\\
N_y &= u\frac{\partial \omega_y}{\partial x} + v\frac{\partial \omega_y}{\partial y} + w\frac{\partial \omega_y}{\partial z}\\
&- \left(\omega_x\frac{\partial v}{\partial x} + \omega_y\frac{\partial v}{\partial y} + \omega_z\frac{\partial v}{\partial z}\right).\\
&= \mathbf{q}\cdot\nabla\omega_y - \mathbf{w}\cdot\nabla v.
\end{aligned}$$

Similarly, N_z can be written in the same manner

$$\begin{aligned} N_z &= \frac{\partial}{\partial x}[u\omega_z - w\omega_x] - \frac{\partial}{\partial y}[w\omega_y - v\omega_z] \\ &= u\frac{\partial \omega_z}{\partial x} - w\frac{\partial \omega_x}{\partial x} + \omega_z\frac{\partial u}{\partial x} - \omega_x\frac{\partial w}{\partial x} \\ &- w\frac{\partial \omega_y}{\partial y} + v\frac{\partial \omega_z}{\partial y} - \omega_y\frac{\partial w}{\partial y} + \omega_z\frac{\partial v}{\partial y}. \\ &= u\frac{\partial \omega_z}{\partial x} + v\frac{\partial \omega_z}{\partial y} - w\left(\frac{\partial \omega_x}{\partial x} + \frac{\partial \omega_y}{\partial y}\right) \\ &- \left(\omega_x\frac{\partial w}{\partial x} + \omega_y\frac{\partial w}{\partial y} + \omega_z\frac{\partial w}{\partial z}\right). \\ N_z &= u\frac{\partial \omega_z}{\partial x} + v\frac{\partial \omega_z}{\partial y} + w\frac{\partial \omega_z}{\partial z} \\ &- \left(\omega_x\frac{\partial w}{\partial x} + \omega_y\frac{\partial w}{\partial y} + \omega_z\frac{\partial w}{\partial z}\right). \\ &= \mathbf{q}\cdot\nabla\omega_z - \mathbf{w}\cdot\nabla w. \end{aligned} \tag{5.13}$$

Following the Davies & Carpenter (2001) study, the components of the velocity $\mathbf{q}$ and vorticity $\mathbf{w}$ fields can be divided into two categories. The components (ω_x, ω_y, w) are considered to be primary variables. The second category is that the components (u, v, ω_z) are considered to be secondary variables. These variables can be defined in terms of the primary variables and so-called secondary variables which are follows

$$u = \int_0^z \left(\omega_y + \frac{\partial w}{\partial x}\right) dz \tag{5.14}$$

$$v = \int_0^z \left(-\omega_x + \frac{\partial w}{\partial y}\right) dz \tag{5.15}$$

$$\omega_z = -\int_0^z \left(\frac{\partial \omega_x}{\partial x} + \frac{\partial \omega_y}{\partial y}\right) dz. \tag{5.16}$$

The expression for u and v can be obtained by integrating the appropriate component of the vorticity definition (5.4) with respect to z. ω_z can then be obtained

by integrating the condition that the vorticity is solenoidal $\nabla.\omega = 0$ and using the boundary conditions on u and v shows that ω_z is zero when $z = 0$, see Davies & Carpenter (2001).

5.3 Test Problem

In this section, we consider a three-dimensional test problem that has a known exact solution for the six variables $(u, v, w, \omega_x, \omega_y \quad \text{and} \quad \omega_z)$. The test problem has been chosen such that in the absence of certain forcing functions, the equation reduced the novel velocity-vorticity formulation. We solve the test problem for the three primary variables (ω_x, ω_y, w) by solving the following three equations

$$\begin{aligned} &\frac{1}{Re}\nabla^2\omega_x - u\frac{\partial\omega_x}{\partial x} - v\frac{\partial\omega_x}{\partial y} - w\frac{\partial\omega_x}{\partial z} \\ &+\omega_x\frac{\partial u}{\partial x} + \omega_y\frac{\partial u}{\partial y} + \omega_z\frac{\partial u}{\partial z} = F_1. \end{aligned}$$

$$\begin{aligned} &\frac{1}{Re}\nabla^2\omega_y - u\frac{\partial\omega_y}{\partial x} - v\frac{\partial\omega_y}{\partial y} - w\frac{\partial\omega_y}{\partial z} \\ &+\omega_x\frac{\partial v}{\partial x} + \omega_y\frac{\partial v}{\partial y} + \omega_z\frac{\partial v}{\partial y} = F_2. \end{aligned} \tag{5.17}$$

$$\frac{1}{Re}\nabla^2 w + \frac{\partial\omega_y}{\partial x} - \frac{\partial\omega_x}{\partial y} = F_3.$$

Here, the forcing functions F_1, F_2 and F_3, are as follows

$$F_1 = 3\pi^3 \cos(\pi z)[\sin(\pi x)\sin(\pi y) - \cos(\pi(x+y))] +$$
$$\{z + \sin(\pi x)\sin(\pi y)\sin(\pi z)\}\{\pi^2 \cos(\pi z)[\sin(\pi(x+y)) + \cos(\pi x)\sin(\pi y)]\} +$$
$$\{\sin(\pi x)\sin(\pi y)\sin(\pi z)\}\{\pi^2 \cos(\pi z)[\sin(\pi(x+y)) + \sin(\pi x)\sin(\pi y)]\} +$$
$$\{\cos(\pi z)\sin(\pi(x+y))\}\{\pi^2 \sin(\pi z)[\cos(\pi(x+y)) - \sin(\pi x)\sin(\pi y)]\} +$$
$$\{\pi \cos(\pi z)[\cos(\pi(x+y)) - \sin(\pi x)\sin(\pi y)]\}\{\pi \cos(\pi x)\sin(\pi y)\sin(\pi z)\} +$$
$$\{1 + \pi \cos(\pi z)[\sin(\pi x)\sin(\pi y) - \cos(\pi(x+y))]\}\{\pi \sin(\pi x)\cos(\pi y)\sin(\pi z)\} +$$
$$\{\pi \sin(\pi z)[\cos(\pi x)\sin(\pi y) - \sin(\pi x)\cos(\pi y)]\}\{1 + \pi \sin(\pi x)\sin(\pi y)\cos(\pi z)\},$$

$$F_2 = 3\pi^3 \cos(\pi z)[\cos(\pi(x+y)) - \sin(\pi x)\sin(\pi y)] -$$
$$\{z + \sin(\pi x)\sin(\pi y)\sin(\pi z)\}\{\pi^2 \cos(\pi z)[\sin(\pi(x+y)) + \cos(\pi x)\sin(\pi y)]\} -$$
$$\{\sin(\pi x)\sin(\pi y)\sin(\pi z)\}\{\pi^2 \cos(\pi z)[\sin(\pi(x+y)) + \sin(\pi x)\sin(\pi y)]\} +$$
$$\{\cos(\pi z)\sin(\pi(x+y))\}\{\pi^2 \sin(\pi z)[\sin(\pi x)\sin(\pi y) - \cos(\pi(x+y))]\} +$$
$$\{\pi \cos(\pi z)[\cos(\pi(x+y)) - \sin(\pi x)\sin(\pi y)]\}\{\pi \cos(\pi x)\sin(\pi y)\sin(\pi z)\} +$$
$$\{1 + \pi \cos(\pi z)[\sin(\pi x)\sin(\pi y) - \cos(\pi(x+y))]\}\{\pi \sin(\pi x)\cos(\pi y)\sin(\pi z)\} +$$
$$\{\pi \sin(\pi z)[\cos(\pi x)\sin(\pi y) - \sin(\pi x)\cos(\pi y)]\}\{\pi \sin(\pi x)\sin(\pi y)\cos(\pi z)\},$$

$$F_3 = 3\pi^2 \cos(\pi z)\sin(\pi(x+y)) + \pi^2 \cos(\pi z)[\cos(\pi x)\sin(\pi y) + \sin(\pi(x+y))]$$
$$\pi^2 \cos(\pi z)[\sin(\pi x)\cos(\pi y) + \sin(\pi(x+y))].$$

The problem is solved in a cubical domain for $0 \leq x, y, z \leq 1$ with the following boundary conditions

$$\omega_x = \pi \cos(\pi z)[\cos(\pi(x+y)) - \sin(\pi x)\sin(\pi y)] \qquad \text{for}, x = 0, 1, \quad (5.18a)$$

$$\omega_x - \frac{\partial w}{\partial y} = 0 \qquad \text{for}, y = 0, 1, \quad (5.18b)$$

$$\int_0^1 \left(\omega_x - \frac{\partial w}{\partial y}\right) dz = 0 \qquad \text{for}, z = 1, \quad (5.18c)$$

$$\omega_x - \frac{\partial w}{\partial y} = -\pi \cos(\pi z)\sin(\pi x)\sin(\pi y) \qquad \text{for}, z = 0, \quad (5.18d)$$

$$\omega_y + \frac{\partial w}{\partial x} = 0 \qquad \text{for}, x = 0, 1, \quad (5.18e)$$

$$\omega_y = 1 + \pi \cos(\pi z)[\sin(\pi x)\sin(\pi y) - \cos(\pi(x+y))] \qquad \text{for}, y = 0, 1, \quad (5.18f)$$

$$\int_0^1 \left(\omega_y + \frac{\partial w}{\partial x}\right) dz = 1 \qquad \text{for}, z = 1, \quad (5.18g)$$

$$\omega_y + \frac{\partial w}{\partial x} = 1 + \pi \cos(\pi z)\sin(\pi x)\sin(\pi y) \qquad \text{for}, z = 0, \quad (5.18h)$$

$$w = \cos(\pi z)\sin(\pi(x+y)) \qquad \text{for}, x = 0, 1, \quad (5.18i)$$

$$w = \cos(\pi z)\sin(\pi(x+y)) \qquad \text{for}, y = 0, 1, \quad (5.18j)$$

$$w = \cos(\pi z)\sin(\pi(x+y)) \qquad \text{for}, z = 0, 1. \quad (5.18k)$$

In the above, the relation $\omega_x - \frac{\partial w}{\partial y} = 0$ in (5.18b) can be obtained from the definition of the vorticity $\mathbf{w} = \nabla \times \mathbf{q}$ as follow. Since

$$\omega_x = \frac{\partial w}{\partial y} - \frac{\partial v}{\partial z}, \quad (5.19)$$

the conditions in (5.18b) follow after using the boundary conditions on v and w on $y = 0, 1$. The boundary condition $\int_0^1 \left(\omega_x - \frac{\partial w}{\partial y}\right) dz = 0$ in (5.18c) can be

obtained by integrating (5.19) with respect to z, and this leads to

$$v = -\int_0^z \left(\omega_x - \frac{\partial w}{\partial y}\right) dz,$$

and then setting $z = 1$. In solving the three-dimensional lid driven cavity we set $\frac{\partial v}{\partial z} = 0$ on $y = 0, 1$ which is the same as the boundary condition in our test problem. Similarly, we set $v = 0$ on $z = 1$ which leads to the same as the test problem boundary condition on $z = 1$. Similarly, the relation in (5.18e) $\omega_y + \frac{\partial w}{\partial x} = 0$ can be obtained from the definition of the vorticity $\mathbf{w} = \nabla \times \mathbf{q}$, where

$$\omega_y = \frac{\partial u}{\partial z} - \frac{\partial w}{\partial x}, \tag{5.20}$$

and using the condition that $u = 0$ on $x = 0, 1$. The boundary condition $\int_0^1 \left(\omega_y + \frac{\partial w}{\partial y}\right) dz = 0$ can be obtained by integrating (5.20) with respect to z, and this leads to

$$u = \int_0^z \left(\omega_y + \frac{\partial w}{\partial x}\right) dz,$$

and then setting $z = 1$. In solving the three-dimensional lid driven cavity we set $\frac{\partial u}{\partial z} = 0$ on $x = 0, 1$ which is the same as the boundary condition in our test problem. Similarly, we set $u = 1$ on $z = 1$ which leads to the same as the test problem boundary condition on $z = 1$. It can be noticed that the boundary conditions of our test problem has been chosen to be as close to the three-dimensional lid driven cavity as possible.

The system of equations (5.18) and (**??**) has the following exact solution

$$\begin{aligned}
u &= z + \sin(\pi x)\sin(\pi y)\sin(\pi z). \\
v &= \sin(\pi x)\sin(\pi y)\sin(\pi z). \\
w &= \cos(\pi z)\sin(\pi(x+y)). \\
\omega_x &= \pi\cos(\pi z)[\cos(\pi(x+y)) - \sin(\pi x)\sin(\pi y)] \\
\omega_y &= 1 + \pi\cos(\pi z)[\sin(\pi x)\sin(\pi y) - \cos(\pi(x+y))] \\
\omega_z &= \frac{\partial v}{\partial x} - \frac{\partial u}{\partial y} \\
&= \pi\sin(\pi z)[\cos(\pi x)\sin(\pi y) - \sin(\pi x)\cos(\pi y)].
\end{aligned} \tag{5.21}$$

The forcing functions in the boundary conditions above are just the values of the velocities and vorticities at the boundaries. The flow in the lid-driven cavity is identical to the test problem above, but with these forcing functions all set to zero.

5.3.1 Discretization

Finite differences are used to discretize the x direction, and Chebyshev collocation is employed to discretize y and z directions. The mapping $y \in (0,1) \rightarrow z \in (-1,1)$ in Chebyshev space is used so that the collocation points are given by

$$\bar{z} = \bar{z}_j = \cos(\frac{j\pi}{N}), \qquad j = 0, 1, ..., N \tag{5.22}$$

and

$$y = y(\bar{z}_i) = y_i = \frac{1}{2}(\bar{z}_i + 1), \qquad i = 0, 1, ..., N. \tag{5.23}$$

In a similar way, the mapping can be used for the z direction

$$z = z(\bar{z}_j) = z_j = \frac{1}{2}(\bar{z}_j + 1), \qquad j = 0, 1, ..., M. \tag{5.24}$$

For the x direction, the finite difference points are given by

$$x = x_p = x_{min} + (p-1)\Delta x \qquad p = 1, 2, ..., R$$

where

$$\Delta x = \frac{1}{R-1}.$$

The derivatives in y and z can be written as follows

$$\left(\frac{\partial \psi}{\partial y}\right)_{p,i,j} = 2\sum_{k=0}^{N} D1_{i,k}\psi_{k,j,p}, \tag{5.25}$$

$$\left(\frac{\partial \psi}{\partial z}\right)_{p,i,j} = 2\sum_{k=0}^{M} D2_{j,k}\psi_{i,k,p}. \tag{5.26}$$

$D1$ and $D2$ are the Chebychev differentiation matrices described previously, and N,M are the number of points in the y and z directions respectively. Here, R is the number of points in the x direction. The second derivative can be obtained simply by squaring the differentiation matrix. Notice that we define $\psi_{p,i,j} = \psi(x = x_p, y = y_i, z = z_j)$.

For the x direction, the usual fourth order central difference approximation of the variable ω_x, say, at the point (x, y, z), is given by

$$(\frac{\partial \psi}{\partial x})_p = \frac{\omega_{x_{p-2}} - 8\omega_{x_{p-1}} + 8\omega_{x_{p+1}} - \omega_{x_{p+2}}}{12\Delta x}, \tag{5.27}$$

and

$$(\frac{\partial^2 \omega_x}{\partial x^2})_p = \frac{-\omega_{x_{p-2}} + 16\omega_{x_{p-1}} - 30\omega_{x_p} + 16\omega_{x_{p+1}} - \omega_{x_{p+2}}}{12(\Delta x)^2}. \tag{5.28}$$

The approximation is obtained by replacing all derivatives in (5.17-5.18) with Chebychev approximation and fourth-order finite difference approximation.

First Equation The equation (5.17) can be disretized as follows:

$$\begin{aligned}
&\frac{-\omega_{x_{p-2,i,j}} + 16\omega_{x_{p-1,i,j}} - 30\omega_{x_{p,i,j}} + 16\omega_{x_{p+1,i,j}} - \omega_{x_{p+2,i,j}}}{12{h_x}^2} \\
&+ \sum_{k=0}^{N} D^2_{i,k}\omega_{x_{pkj}} + \sum_{k=0}^{M} D^2_{j,k}\omega_{x_{pik}} \\
&- u_{pij}\left(\frac{\omega_{x_{p-2,i,j}} - 8\omega_{x_{p-1,i,j}} + 8\omega_{x_{p+1,i,j}} - \omega_{x_{p+2,i,j}}}{12h_x}\right) \\
&- v_{p,i,j}\sum_{k=0}^{N} D_{i,k}\omega_{x_{pkj}} - w_{p,i,j}\sum_{k=0}^{M} D_{j,k}\omega_{x_{pik}} \\
&+ \omega_{x_{pij}}\left(\frac{u_{p-2,i,j} - 8u_{p-1,i,j} + 8u_{p+1,i,j} - u_{p+2,i,j}}{12h_x}\right) \\
&+ \omega_{y_{pij}}\sum_{k=0}^{N} D_{i,k}u_{pkj} = (F_1)_{p,i,j}.
\end{aligned} \tag{5.29}$$

Second Equation In the same manner, the Equation (5.17) can be discretized

as follows:

$$
\begin{aligned}
&\frac{-\omega_{y_{p-2,i,j}} + 16\omega_{y_{p-1,i,j}} - 30\omega_{y_{p,i,j}} + 16\omega_{y_{p+1,i,j}} - \omega_{y_{p+2,i,j}}}{12{h_x}^2} \\
&+ \sum_{k=0}^{N} D^2_{i,k}\omega_{y_{pkj}} + \sum_{k=0}^{M} D^2_{j,k}\omega_{y_{pik}} \\
&- u_{pij}\left(\frac{\omega_{y_{p-2,i,j}} - 8\omega_{y_{p-1,i,j}} + 8\omega_{y_{p+1,i,j}} - \omega_{y_{p+2,i,j}}}{12h_x}\right) \\
&- v_{p,i,j}\sum_{k=0}^{N} D_{i,k}\omega_{y_{pkj}} - w_{p,i,j}\sum_{k=0}^{M} D_{j,k}\omega_{y_{pik}} \\
&+ \omega_{y_{pij}}\left(\frac{v_{p-2,i,j} - 8u_{p-1,i,j} + 8v_{p+1,i,j} - v_{p+2,i,j}}{12h_x}\right) \\
&+ \omega_{y_{pij}}\sum_{k=0}^{N} D_{i,k}v_{pkj} = (F_2)_{p,i,j}.
\end{aligned}
\tag{5.30}
$$

Third Equation Also, and in the same manner, the Equation (5.18) can be discretized as follows:

$$\begin{aligned}
&\frac{-w_{p-2,i,j} + 16w_{p-1,i,j} - 30w_{p,i,j} + 16w_{p+1,i,j} - w_{p+2,i,j}}{12{h_x}^2} \\
&+ \sum_{k=0}^{N} D^2_{i,k} w_{pkj} + \sum_{k=0}^{M} D^2_{j,k} w_{pik} \\
&+ \left(\frac{\omega_{y_{p-2,i,j}} - 8\omega_{y_{p-1,i,j}} + 8\omega_{y_{p+1,i,j}} - \omega_{y_{p+2,i,j}}}{12h_x} \right) \\
&- \sum_{k=0}^{N} D_{i,k} \omega_{x_{pkj}} = (F_3)_{p,i,j}.
\end{aligned} \tag{5.31}$$

5.3.2 Linearization

One difficulty with the system (5.29), (5.30) and (5.31) is the non-linearity. The non-linearity can be overcome by using a Newton-Raphson linearization and working in terms of correction terms. Let $\tilde{\omega_x}$, $\tilde{\omega_y}$, $\tilde{\omega_z}$, $\tilde{u}$, $\tilde{v}$ and $\tilde{w}$ be the correction terms where

$$\begin{aligned}
\omega_{x_{p,i,j}} &= \bar{\omega}_{x_{p,i,j}} + \tilde{\omega}_{x_{p,i,j}}, \\
\omega_{y_{p,i,j}} &= \bar{\omega}_{y_{p,i,j}} + \tilde{\omega}_{y_{p,i,j}}, \\
\omega_{z_{p,i,j}} &= \bar{\omega}_{z_{p,i,j}} + \tilde{\omega}_{z_{p,i,j}}, \\
u_{p,i,j} &= \bar{u}_{p,i,j} + \tilde{u}_{p,i,j}, \\
v_{p,i,j} &= \bar{v}_{p,i,j} + \tilde{v}_{p,i,j}, \\
w_{p,i,j} &= \bar{w}_{p,i,j} + \tilde{w}_{p,i,j},
\end{aligned} \tag{5.32}$$

and where $\bar{\omega_x}$, $\bar{\omega_y}$, $\bar{\omega_z}$, $\bar{u}$, $\bar{v}$ and $\bar{w}$ are the initial approximations. Given this, the system becomes

$$\frac{1}{Re}\nabla^2(\bar{\omega_x}_{p,i,j} + \tilde{\omega_x}_{p,i,j}) - (\bar{u}_{p,i,j} + \tilde{u}_{p,i,j})\frac{\partial(\bar{\omega_x}_{p,i,j} + \tilde{\omega_x}_{p,i,j})}{\partial x} - (\bar{v}_{p,i,j} + \tilde{v}_{p,i,j})\frac{\partial(\bar{\omega_x} + \tilde{\omega_x})}{\partial y}$$
$$-(\bar{w}_{p,i,j} + \tilde{w}_{p,i,j})\frac{\partial(\bar{\omega_x}_{p,i,j} + \tilde{\omega_x}_{p,i,j})}{\partial z} + (\bar{\omega_x}_{p,i,j} + \tilde{\omega_x}_{p,i,j})\frac{\partial(\bar{u}_{p,i,j} + \tilde{u}_{p,i,j})}{\partial x} + \tag{5.33}$$
$$(\bar{\omega_y}_{p,i,j} + \tilde{\omega_y}_{p,i,j})\frac{\partial(\bar{u}_{p,i,j} + \tilde{u}_{p,i,j})}{\partial y} + (\bar{\omega_z}_{p,i,j} + \tilde{\omega_z}_{p,i,j})\frac{\partial(\bar{u}_{p,i,j} + \tilde{u}_{p,i,j})}{\partial z} = F1_{p,i,j} + Rh1_{p,i,j}.$$

$$\frac{1}{Re}\nabla^2(\bar{\omega_y}_{p,i,j} + \tilde{\omega_y}_{p,i,j}) - (\bar{u}_{p,i,j} + \tilde{u}_{p,i,j})\frac{\partial(\bar{\omega_y}_{p,i,j} + \tilde{\omega_y}_{p,i,j})}{\partial x} - (\bar{v}_{p,i,j} + \tilde{v}_{p,i,j})\frac{\partial(\bar{\omega_y}_{p,i,j} + \tilde{\omega_y}_{p,i,j})}{\partial y}$$
$$-(\bar{w}_{p,i,j} + \tilde{w}_{p,i,j})\frac{\partial(\bar{\omega_y}_{p,i,j} + \tilde{\omega_y}_{p,i,j})}{\partial z} + (\bar{\omega_x}_{p,i,j} + \tilde{\omega_x}_{p,i,j})\frac{\partial(\bar{v}_{p,i,j} + \tilde{v}_{p,i,j})}{\partial x} + \tag{5.34}$$
$$(\bar{\omega_y}_{p,i,j} + \tilde{\omega_y}_{p,i,j})\frac{\partial(\bar{v}_{p,i,j} + \tilde{v}_{p,i,j})}{\partial y} + (\bar{\omega_z}_{p,i,j} + \tilde{\omega_z}_{p,i,j})\frac{\partial(\bar{v}_{p,i,j} + \tilde{v}_{p,i,j})}{\partial z}_{p,i,j} = F2_{p,i,j} + Rh2_{p,i,j}.$$

$$\nabla^2(\bar{w}_{p,i,j} + \tilde{w}_{p,i,j}) + \frac{\partial(\bar{\omega_y}_{p,i,j} + \tilde{\omega_y}_{p,i,j})}{\partial x} - \frac{\partial(\bar{\omega_x}_{p,i,j} + \tilde{\omega_x}_{p,i,j})}{\partial y} = F3_{p,i,j} + Rh3_{p,i,j}. \tag{5.35}$$

$Rh1$ is

$$\begin{aligned} Rh1_{p,i,j} = \quad & -\frac{1}{Re}\left(\frac{-\bar{\omega}_{x_{p-2,i,j}} + 16\bar{\omega}_{x_{p-1,i,j}} - 30\bar{\omega}_{x_{p,i,j}} + 16\bar{\omega}_{x_{p+1,i,j}} - \bar{\omega}_{x_{p+2,i,j}}}{12{h_x}^2}\right) \\ & -\frac{1}{Re}\sum_{k=0}^{N} D^2_{i,k}\bar{\omega}_{x_{pkj}} - \frac{1}{Re}\sum_{k=0}^{M} D^2_{j,k}\bar{\omega}_{x_{pik}} \\ & +\bar{u}_{pij}\left(\frac{\bar{\omega}_{x_{p-2,i,j}} - 8\bar{\omega}_{x_{p-1,i,j}} + 8\bar{\omega}_{x_{p+1,i,j}} - \bar{\omega}_{x_{p+2,i,j}}}{12h_x}\right) \\ & +\bar{v}_{p,i,j}\sum_{k=0}^{N} D_{i,k}\bar{\omega}_{x_{pkj}} + \bar{w}_{p,i,j}\sum_{k=0}^{M} D_{j,k}\bar{\omega}_{x_{pik}} \\ & -\bar{\omega}_{x_{pij}}\left(\frac{\bar{u}_{p-2,i,j} - 8\bar{u}_{p-1,i,j} + 8\bar{u}_{p+1,i,j} - \bar{u}_{p+2,i,j}}{12h_x}\right) \\ & -\bar{\omega}_{y_{pij}}\sum_{k=0}^{N} D_{i,k}\bar{u}_{pkj} - \omega_{z_{pij}}\sum_{k=0}^{M} D_{j,k}\bar{u}_{pik}, \end{aligned} \tag{5.36}$$

$Rh2$ is

$$\begin{aligned} Rh2_{p,i,j} = & -\frac{1}{Re}\left(\frac{-\bar{\omega}_{y_{p-2,i,j}} + 16\bar{\omega}_{y_{p-1,i,j}} - 30\bar{\omega}_{y_{p,i,j}} + 16\bar{\omega}_{y_{p+1,i,j}} - \bar{\omega}_{y_{p+2,i,j}}}{12{h_x}^2}\right) \\ & -\frac{1}{Re}\sum_{k=0}^{N} D^2_{i,k}\bar{\omega}_{y_{pkj}} - \frac{1}{Re}\sum_{k=0}^{M} D^2_{j,k}\bar{\omega}_{y_{pik}} + \bar{u}_{pij}\left(\frac{\bar{\omega}_{y_{p-2,i,j}} - 8\bar{\omega}_{y_{p-1,i,j}} + 8\bar{\omega}_{y_{p+1,i,j}} - \bar{\omega}_{y_{p+2,i,j}}}{12h_x}\right) \\ & +\bar{v}_{p,i,j}\sum_{k=0}^{N} D_{i,k}\bar{\omega}_{y_{pkj}} + \bar{w}_{p,i,j}\sum_{k=0}^{M} D_{j,k}\bar{\omega}_{y_{pik}} - \bar{\omega}_{x_{pij}}\left(\frac{\bar{v}_{p-2,i,j} - 8\bar{v}_{p-1,i,j} + 8\bar{v}_{p+1,i,j} - \bar{v}_{p+2,i,j}}{12h_x}\right) \\ & -\bar{\omega}_{y_{pij}}\sum_{k=0}^{N} D_{i,k}\bar{v}_{pkj} - \omega_{z_{pij}}\sum_{k=0}^{M} D_{j,k}\bar{u}_{pik}, \end{aligned} \tag{5.37}$$

and $Rh3$ is

$$\begin{aligned} Rh3_{p,i,j} \quad &= -\left(\frac{-\bar{w}_{p-2,i,j} + 16\bar{w}_{p-1,i,j} - 30\bar{w}_{p,i,j} + 16\bar{w}_{p+1,i,j} - \bar{w}_{p+2,i,j}}{12{h_x}^2}\right) \\ &- \sum_{k=0}^{N} D^2_{i,k}\bar{w}_{pkj} - \sum_{k=0}^{M} D^2_{j,k}\bar{w}_{pik} - \left(\frac{\bar{\omega}_{y_{p-2,i,j}} - 8\bar{\omega}_{y_{p-1,i,j}} + 8\bar{\omega}_{y_{p+1,i,j}} - \tilde{\omega}_{y_{p+2,i,j}}}{12h_x}\right) \\ &+ \sum_{k=0}^{N} D_{i,k}\bar{\omega}_{x_{pkj}}. \end{aligned} \tag{5.38}$$

Rearranging the linearized system (5.33-5.35) and using the relations

$$\tilde{u} = \int_0^1 \left(\tilde{\omega_y} + \frac{\partial\tilde{w}}{\partial x}\right) dz \tag{5.39}$$

$$\tilde{v} = \int_0^1 \left(-\tilde{\omega_x} + \frac{\partial\tilde{w}}{\partial y}\right) dz \tag{5.40}$$

$$\tilde{\omega_z} = -\int_0^1 \left(\frac{\partial\tilde{\omega_x}}{\partial x} + \frac{\partial\tilde{\omega_y}}{\partial y}\right) dz, \tag{5.41}$$

Equation (5.33) can be rewritten as follows

$$\begin{aligned} &A11_{p,i,j}\tilde{\omega}_{x_{p-2,i,j}} + B11_{p,i,j}\tilde{\omega}_{x_{p-1,i,j}} + C11_{p,i,j}\tilde{\omega}_{x_{p,i,j}} + D11_{p,i,j}\tilde{\omega}_{x_{p+1,i,j}} + E11_{p,i,j}\tilde{\omega}_{x_{p+2,i,j}} \\ &+A12_{p,i,j}\tilde{\omega}_{y_{p-2,i,j}} + B12_{p,i,j}\tilde{\omega}_{y_{p-1,i,j}}C12_{p,i,j}\tilde{\omega}_{y_{p,i,j}} + D12_{p,i,j}\tilde{\omega}_{y_{p+1,i,j}} + E12_{p,i,j}\tilde{\omega}_{y_{p+2,i,j}} \\ &+A13_{p,i,j}\tilde{w}_{p-2,i,j} + B13_{p,i,j}\tilde{w}_{p-1,i,j} + C13_{p,i,j}\tilde{w}_{p,i,j} + D13_{p,i,j}\tilde{w}_{p+1,i,j} + E13_{p,i,j}\tilde{w}_{p+2,i,j} \\ &= F1_{p,i,j} + Rh1_{p,i,j}, \end{aligned} \tag{5.42}$$

where

$$A11_{p,i,j} = \frac{-1}{Re12h_x^2} - \frac{1}{12h_x}\bar{u}_{p,i,j} - \frac{1}{12h_x}\sum_{k=0}^{M} D2_{j,k}\bar{u}_{p,i,k}\sum_{k=0}^{M} H_{j,k}$$

$$B11_{p,i,j} = \frac{16}{Re12h_x^2} + \frac{8}{12h_x}u_{p,i,j} + \frac{8}{12h_x}\sum_{k=0}^{M} D2_{j,k}\bar{u}_{p,i,k}\sum_{k=0}^{M} H_{j,k}$$

$$C11_{p,i,j} = \frac{-30}{Re12{h_x}^2} + \frac{1}{Re}\sum_{k=0}^{N} D1_{i,k}^2 + \frac{1}{Re}\sum_{k=0}^{M} D2_{j,k}^2 - \bar{v}_{p,i,j}\sum_{k=0}^{N} D1_{i,k} - \bar{w}_{p,i,j}\sum_{k=0}^{M} D2_{j,k}$$
$$+ \sum_{k=0}^{N} D1_{i,k}\bar{\omega}_{x_{p,k,j}}\sum_{k=0}^{M} H_{j,k} + \frac{\bar{u}_{p-2,i,j} - 8\bar{u}_{p-1,i,j} + 8\bar{u}_{p+1,i,j} - \bar{u}_{p+2,i,j}}{12h_x}$$

$$D11_{p,i,j} = \frac{16}{Re12h_x^2} - \frac{8}{12h_x}u_{p,i,j} - \frac{8}{12h_x}\sum_{k=0}^{M} D2_{j,k}\bar{u}_{p,i,k}\sum_{k=0}^{M} H_{j,k}$$

$$E11_{p,i,j} = \frac{-1}{Re12h_x^2} + \frac{1}{12h_x}u_{p,i,j} + \frac{1}{12h_x}\sum_{k=0}^{M} D2_{j,k}\bar{u}_{p,i,k}\sum_{k=0}^{M} H_{j,k}$$

$$A12_{p,i,j} = \frac{1}{12h_x}\bar{\omega}_{x_{p,i,j}}\sum_{k=0}^{M} H_{j,k}$$

$$B12_{p,i,j} = \frac{-8}{12h_x}\bar{\omega}_{x_{p,i,j}}\sum_{k=0}^{M} H_{j,k}$$

$$C12_{p,i,j} = -\left(\frac{\bar{\omega}_{x_{p-2,i,j}} - 8\bar{\omega}_{x_{p-1,i,j}} + 8\bar{\omega}_{x_{p+1,i,j}} - \bar{\omega}_{x_{p+2,i,j}}}{12h_x}\right)\sum_{k=0}^{M} H_{j,k}$$
$$+ \sum_{k=0}^{N} D1_{i,k}\bar{u}_{p,i,j} + \bar{\omega}_{y_{p,i,j}}\sum_{k=0}^{N} D1_{i,k}\sum_{k=0}^{M} H_{j,k} + \bar{\omega}_{z_{p,i,j}}\sum_{k=0}^{M} D2_{j,k}\bar{u}_{p,i,k}\sum_{k=0}^{M} H_{j,k}\sum_{k=0}^{N} D1_{i,k}$$

$$D12_{p,i,j} = \frac{8}{12h_x}\bar{\omega}_{x_{p,i,j}}\sum_{k=0}^{M} H_{j,k}$$

$$E12_{p,i,j} = \frac{-1}{12h_x}\bar{\omega}_{x_{p,i,j}}\sum_{k=0}^{M} H_{j,k}$$

$$A13_{p,i,j} = \frac{-1}{12h_x}\left(\frac{\bar{\omega}_{x_{p-2,i,j}} - 8\bar{\omega}_{x_{p-1,i,j}} + 8\bar{\omega}_{x_{p+1,i,j}} - \bar{\omega}_{x_{p+2,i,j}}}{12h_x}\right)\sum_{k=0}^{M} H_{j,k} - \frac{1}{12h_x^2}\bar{\omega}_{x_{p,i,j}}\sum_{k=0}^{M} H_{j,k}$$
$$+\frac{1}{12h_x}\bar{\omega}_{y_{p,i,j}}\sum_{k=0}^{M} H_{j,k}\sum_{k=0}^{N} D_{i,k} + \frac{1}{12h_x}\bar{\omega}_{z_{p,i,j}}$$
$$B13_{p,i,j} = \frac{8}{12h_x}\left(\frac{\bar{\omega}_{x_{p-2,i,j}} - 8\bar{\omega}_{x_{p-1,i,j}} + 8\bar{\omega}_{x_{p+1,i,j}} - \bar{\omega}_{x_{p+2,i,j}}}{12h_x}\right)\sum_{k=0}^{M} H_{j,k} + \frac{16}{12h_x^2}\bar{\omega}_{x_{p,i,j}}\sum_{k=0}^{M} H_{j,k}$$
$$-\frac{8}{12h_x}\bar{\omega}_{y_{p,i,j}}\sum_{k=0}^{M} H_{j,k}\sum_{k=0}^{N} D_{i,k} - \frac{8}{12h_x}\bar{\omega}_{z_{p,i,j}}$$
$$C13_{p,i,j} = -\sum_{k=0}^{M} D_{j,k}\bar{\omega}_{x_{p,i,j}} - \sum_{k=0}^{N} D_{i,k}\bar{\omega}_{x_{p,i,j}}\sum_{k=0}^{M} H_{j,k}\sum_{k=0}^{N} D_{i,k} - \frac{30}{12h_x^2}\sum_{k=0}^{M} H_{j,k}\bar{\omega}_{x_{p,i,k}}$$
$$+\sum_{k=0}^{N} D_{i,k}\bar{u}_{p,i,j} + \bar{\omega}_{y_{p,i,j}}\sum_{k=0}^{N} D_{i,k}\sum_{k=0}^{M} H_{j,k} + \bar{\omega}_{z_{p,i,j}}\sum_{k=0}^{M} D_{j,k}\bar{u}_{p,i,k}\sum_{k=0}^{M} H_{j,k}\sum_{k=0}^{N} D_{i,k}$$
$$D13_{p,i,j} = \frac{-8}{12h_x}\left(\frac{\bar{\omega}_{x_{p-2,i,j}} - 8\bar{\omega}_{x_{p-1,i,j}} + 8\bar{\omega}_{x_{p+1,i,j}} - \bar{\omega}_{x_{p+2,i,j}}}{12h_x}\right)\sum_{k=0}^{M} H_{j,k} + \frac{16}{12h_x^2}\bar{\omega}_{x_{p,i,j}}\sum_{k=0}^{M} H_{j,k}$$
$$+\frac{8}{12h_x}\bar{\omega}_{y_{p,i,j}}\sum_{k=0}^{M} H_{j,k}\sum_{k=0}^{N} D_{i,k} + \frac{8}{12h_x}\bar{\omega}_{z_{p,i,j}}$$
$$E13_{p,i,j} = \frac{1}{12h_x}\left(\frac{\bar{\omega}_{x_{p-2,i,j}} - 8\bar{\omega}_{x_{p-1,i,j}} + 8\bar{\omega}_{x_{p+1,i,j}} - \bar{\omega}_{x_{p+2,i,j}}}{12h_x}\right)\sum_{k=0}^{M} H_{j,k} - \frac{1}{12h_x^2}\bar{\omega}_{x_{p,i,j}}\sum_{k=0}^{M} H_{j,k}$$
$$-\frac{1}{12h_x}\bar{\omega}_{y_{p,i,j}}\sum_{k=0}^{M} H_{j,k}\sum_{k=0}^{N} D_{i,k} - \frac{1}{12h_x}\bar{\omega}_{z_{p,i,j}}.$$

By the same token, Equation (5.34) can be rewritten as follows

$$\begin{aligned}
&A21_{p,i,j}\tilde{\omega}_{x_{p-2,i,j}} + B21_{p,i,j}\tilde{\omega}_{x_{p-1,i,j}} + C21_{p,i,j}\tilde{\omega}_{x_{p,i,j}} + D21_{p,i,j}\tilde{\omega}_{x_{p+1,i,j}} + E21_{p,i,j}\tilde{\omega}_{x_{p+2,i,j}} \\
&+A22_{p,i,j}\tilde{\omega}_{y_{p-2,i,j}} + B22_{p,i,j}\tilde{\omega}_{y_{p-1,i,j}} + C22_{p,i,j}\tilde{\omega}_{y_{p,i,j}} + D22_{p,i,j}\tilde{\omega}_{y_{p+1,i,j}} + E22_{p,i,j}\tilde{\omega}_{y_{p+2,i,j}} \\
&+A23_{p,i,j}\tilde{w}_{p-2,i,j} + B23_{p,i,j}\tilde{w}_{p-1,i,j} + C23_{p,i,j}\tilde{w}_{p,i,j} + D23_{p,i,j}\tilde{w}_{p+1,i,j} + E23_{p,i,j}\tilde{w}_{p+2,i,j} \\
&= F2_{p,i,j} + Rh2_{p,i,j}.
\end{aligned} \tag{5.43}$$

where

$$A21_{p,i,j} = \frac{-1}{12h_x}\bar{\omega}_{x_{p,k,j}} \sum_{k=0}^{M} H_{j,k} - \frac{1}{12h_x} \sum_{k=0}^{M} D_{j,k}\bar{v}_{p,i,k} \sum_{k=0}^{M} H_{j,k}$$

$$B21_{p,i,j} = \frac{8}{12h_x}\bar{\omega}_{x_{p,k,j}} \sum_{k=0}^{M} H_{j,k} + \frac{8}{12h_x} \sum_{k=0}^{M} D2_{j,k}\bar{v}_{p,i,k} \sum_{k=0}^{M} H_{j,k}$$

$$C21_{p,i,j} = \sum_{k=0}^{N} D1_{i,k}\bar{\omega}_{y_{p,k,j}} \sum_{k=0}^{M} H_{j,k} + \frac{\bar{v}_{p-2,i,j} - 8\bar{v}_{p-1,i,j} + 8\bar{v}_{p+1,i,j} - \bar{v}_{p+2,i,j}}{12h_x}$$

$$-\bar{\omega}_{y_{p,k,j}} \sum_{k=0}^{N} D1_{i,k} \sum_{k=0}^{M} H_{j,k} - \bar{\omega}_{z_{p,k,j}}$$

$$D21_{p,i,j} = \frac{-8}{12h_x}\bar{\omega}_{x_{p,k,j}} \sum_{k=0}^{M} H_{j,k} - \frac{8}{12h_x} \sum_{k=0}^{M} D2_{j,k}\bar{v}_{p,i,k} \sum_{k=0}^{M} H_{j,k}$$

$$E21_{p,i,j} = \frac{1}{12h_x}\bar{\omega}_{x_{p,k,j}} \sum_{k=0}^{M} H_{j,k} + \frac{1}{12h_x} \sum_{k=0}^{M} D2_{j,k}\bar{v}_{p,i,k} \sum_{k=0}^{M} H_{j,k}$$

$$A22_{p,i,j} = \frac{-1}{Re12h_x^2} - \frac{1}{12h_x}\bar{u}_{p,i,j}$$

$$B22_{p,i,j} = \frac{16}{Re12h_x^2} + \frac{8}{12h_x}\bar{u}_{p,i,j}$$

$$C22_{p,i,j} = \frac{-30}{Re12{h_x}^2} + \frac{1}{Re}\sum_{k=0}^{N} D1_{i,k}^2 + \frac{1}{Re}\sum_{k=0}^{M} D2_{j,k}^2 - \bar{v}_{p,i,j}\sum_{k=0}^{N} D1_{i,k} - \bar{w}_{p,i,j}\sum_{k=0}^{M} D2_{j,k}$$

$$+\sum_{k=0}^{N} D1_{i,k}\bar{v}_{p,i,j} - \sum_{k=0}^{M} D2_{j,k}\bar{v} \sum_{k=0}^{M} H_{j,k} \sum_{k=0}^{N} D1_{i,k}$$

$$-\left(\frac{\bar{\omega}_{x_{p-2,i,j}} - 8\bar{\omega}_{x_{p-1,i,j}} + 8\bar{\omega}_{x_{p+1,i,j}} - \bar{\omega}_{x_{p+2,i,j}}}{12h_x}\right) \sum_{k=0}^{M} H_{j,k}$$

$$D22_{p,i,j} = \frac{16}{Re12h_x^2} - \frac{8}{12h_x}\bar{u}_{p,i,j}$$

$$E22_{p,i,j} = \frac{-1}{Re12h_x^2} + \frac{1}{12h_x}\bar{u}_{p,i,j}$$

$$A23_{p,i,j} = \frac{-1}{12h_x}\left(\frac{\bar{\omega}_{y_{p-2,i,j}} - 8\bar{\omega}_{y_{p-1,i,j}} + 8\bar{\omega}_{y_{p+1,i,j}} - \bar{\omega}_{y_{p+2,i,j}}}{12h_x}\right)\sum_{k=0}^{M} H_{j,k}$$

$$+\frac{1}{12h_x}\bar{\omega}_{x_{p,i,j}}\sum_{k=0}^{M} H_{j,k}\sum_{k=0}^{N} D1_{i,k}$$

$$B23_{p,i,j} = \frac{8}{12h_x}\left(\frac{\bar{\omega}_{y_{p-2,i,j}} - 8\bar{\omega}_{y_{p-1,i,j}} + 8\bar{\omega}_{y_{p+1,i,j}} - \bar{\omega}_{y_{p+2,i,j}}}{12h_x}\right)\sum_{k=0}^{M} H_{j,k}$$

$$-\frac{8}{12h_x}\bar{\omega}_{y_{p,i,j}}\sum_{k=0}^{M} H_{j,k}\sum_{k=0}^{N} D1_{i,k}$$

$$C23_{p,i,j} = -\sum_{k=0}^{N} D1_{i,k}\bar{\omega}_{y_{p,i,j}}\sum_{k=0}^{M} H_{j,k}\sum_{k=0}^{N} D1_{i,k} - \sum_{k=0}^{M} D2_{j,k}\bar{\omega}_{y_{p,i,j}} + \bar{\omega}_{y_{p,i,j}}\sum_{k=0}^{M} H_{j,k}\sum_{k=0}^{N} D1_{i,k}^2$$

$$+\bar{\omega}_{z_{p,i,k}}\sum_{k=0}^{N} D1_{i,k}$$

$$D23_{p,i,j} = \frac{-8}{12h_x}\left(\frac{\bar{\omega}_{y_{p-2,i,j}} - 8\bar{\omega}_{y_{p-1,i,j}} + 8\bar{\omega}_{y_{p+1,i,j}} - \bar{\omega}_{y_{p+2,i,j}}}{12h_x}\right)\sum_{k=0}^{M} H_{j,k}$$

$$+\frac{8}{12h_x}\bar{\omega}_{x_{p,i,j}}\sum_{k=0}^{M} H_{j,k}\sum_{k=0}^{N} D1_{i,k}$$

$$E23_{p,i,j} = \frac{1}{12h_x}\left(\frac{\bar{\omega}_{y_{p-2,i,j}} - 8\bar{\omega}_{y_{p-1,i,j}} + 8\bar{\omega}_{y_{p+1,i,j}} - \bar{\omega}_{y_{p+2,i,j}}}{12h_x}\right)\sum_{k=0}^{M} H_{j,k}$$

$$-\frac{1}{12h_x}\bar{\omega}_{x_{p,i,j}}\sum_{k=0}^{M} H_{j,k}\sum_{k=0}^{N} D1_{i,k}.$$

For completion, Equation (5.35) can be rewritten as follows

$$A31_{p,i,j}\tilde{\omega}_{x_{p-2,i,j}} + B31_{p,i,j}\tilde{\omega}_{x_{p-1,i,j}} + C31_{p,i,j}\tilde{\omega}_{x_{p,i,j}} + D31_{p,i,j}\tilde{\omega}_{x_{p+1,i,j}} + E31_{p,i,j}\tilde{\omega}_{x_{p+2,i,j}}$$

$$+A32_{p,i,j}\tilde{\omega}_{y_{p-2,i,j}} + B32_{p,i,j}\tilde{\omega}_{y_{p-1,i,j}} + C32_{p,i,j}\tilde{\omega}_{y_{p,i,j}} + D32_{p,i,j}\tilde{\omega}_{y_{p+1,i,j}} + E32_{p,i,j}\tilde{\omega}_{y_{p+2,i,j}}$$

$$+A33_{p,i,j}\tilde{w}_{p-2,i,j} + B33_{p,i,j}\tilde{w}_{p-1,i,j} + C33_{p,i,j}\tilde{w}_{p,i,j} + D33_{p,i,j}\tilde{w}_{p+1,i,j} + E33_{p,i,j}\tilde{w}_{p+2,i,j}$$

$$= F3_{p,i,j} + Rh3_{p,i,j}, \tag{5.44}$$

where

$$A31_{p,i,j} = 0, \qquad B31_{p,i,j} = 0, \qquad C31_{p,i,j} = \sum_{k=0}^{N} D1_{i,k} \qquad D31_{p,i,j} = 0, \qquad E31_{p,i,j} = 0$$

$$A32_{p,i,j} = \frac{1}{12h_x}, \qquad B32_{p,i,j} = \frac{-8}{12h_x}, \qquad C32_{p,i,j} = 0, \qquad D32_{p,i,j} = \frac{8}{12h_x},$$

$$E32_{p,i,j} = \frac{-1}{12h_x}, \qquad A33_{p,i,j} = \frac{-1}{12h_x^2}, \qquad B33_{p,i,j} = \frac{16}{12h_x^2},$$

$$C33_{p,i,j} = \frac{-30}{12{h_x}^2} + \sum_{k=0}^{N} D1_{i,k}^2 + \sum_{k=0}^{M} D2_{j,k}^2 + \bar{\omega}_{z_{p,i,k}} \sum_{k=0}^{N} D1_{i,k}, \qquad D33_{p,i,j} = \frac{16}{12h_x^2},$$

$$E33_{p,i,j} = \frac{-1}{12h_x^2}.$$

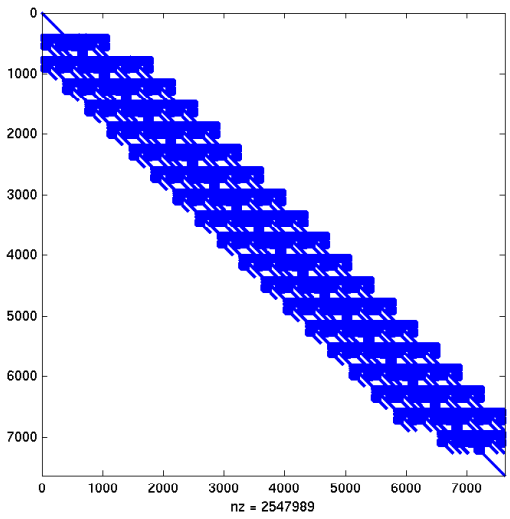

Figure 5.2: The coefficient matrix form of three-dimensional problem for $N = M = 10$ and $R = 20$.

Collecting from the discrete equations together provide a system that takes the block pentadiagonal form, as in Figure (5.2). In the matrix form, the system can be written as follows

$$L\Phi = RI \tag{5.45}$$

where

$$L = \begin{pmatrix} CC_0 & DD_0 & EE_0 & & & & & \\ BB_1 & CC_1 & DD_1 & E_1 & & & & \\ AA_2 & BB_2 & CC_2 & DD_2 & EE_3 & & & \\ & AA_3 & BB_3 & CC_3 & DD_3 & EE_3 & & \\ & & \ddots & \ddots & \ddots & \ddots & \ddots & \\ & & & AA_{R-2} & BB_{R-2} & CC_{R-2} & DD_{R-2} & EE_{R-2} \\ & & & & AA_{R-1} & BB_{R-1} & CC_{R-1} & DD_{R-1} \\ & & & & & AA_R & BB_R & CC_R \end{pmatrix}$$

and the blocks AA, BB, CC, DD, EE are of size $3(N+1)(M+1)\times 3(N+1)(M+1)$. The suffix notation corresponds to the x direction points, where $x = x_p, \quad p = 0, 1, ..., R$. The blocks AA, BB, CC, DD, EE consist of the following

$$AA_p = \begin{pmatrix} A11_p & A12_p & A13_p \\ A21_p & A22_p & A23_p \\ A31_p & A32_p & A33_p \end{pmatrix}$$

$$BB_p = \begin{pmatrix} B11_p & B12_p & B13_p \\ B21_p & B22_p & B23_p \\ B31_p & B32_p & B33_p \end{pmatrix}$$

$$CC_p = \begin{pmatrix} C11_p & C12_p & C13_p \\ C21_p & C22_p & C23_p \\ C31_p & C32_p & C33_p \end{pmatrix}$$

$$DD_p = \begin{pmatrix} D11_p & D12_p & D13_p \\ D21_p & D22_p & D23_p \\ D31_p & D32_p & D33_p \end{pmatrix}$$

$$EE_p = \begin{pmatrix} E11_p & E12_p & E13_p \\ E21_p & E22_p & E23_p \\ E31_p & E32_p & E33_p \end{pmatrix}.$$

The unknown array is ordered in the following way :

$$\Phi = \begin{pmatrix} \Phi_0 \\ \Phi_1 \\ \Phi_2 \\ \vdots \\ \Phi_R \end{pmatrix}$$

where

$$\Phi_p = [\tilde{\omega}_{x_{pij}}, \tilde{\omega}_{y_{pij}}, \tilde{w}_{pij}], \quad i = 0, 1, ..., N. \quad j = 0, 1, ..., M \quad p = 0, 1, ..., R$$

and

$$\tilde{\omega}_{x_{pij}} = \begin{pmatrix} \tilde{\omega}_{x_{p00}} \\ \tilde{\omega}_{x_{p10}} \\ \tilde{\omega}_{x_{p20}} \\ \vdots \\ \tilde{\omega}_{x_{pN0}} \\ \tilde{\omega}_{x_{p01}} \\ \tilde{\omega}_{x_{p11}} \\ \tilde{\omega}_{x_{p21}} \\ \vdots \\ \tilde{\omega}_{x_{pNM}} \end{pmatrix}.$$

The right-hand side of the system (5.45) can be expressed in the same way as the unknowns array; hence, $RI = [RI_0, RI_1, RI_2, ..., RI_R]^T$ where $RI_p =$

$[Rh1_{pij}, Rh2_{pij}, Rh3_{pij}]$. The boundary conditions (**??**) can be linearized to give

$$\begin{cases} \tilde{\omega_x} = -\bar{\omega}_x + \pi\cos(\pi z)[\cos(\pi(x+y)) - \sin(\pi x)\sin(\pi y)] \quad \text{for,} & x = 0,1 \\ \tilde{\omega_x} - \frac{\partial\tilde{w}}{\partial y} = -\bar{\omega_x} + \frac{\partial\bar{w}}{\partial y} \quad \text{for,} & y = 0,1 \\ \int_0^1 \left(\tilde{\omega_x} - \frac{\partial\tilde{w}}{\partial y}\right) dz = \int_0^1 \left(-\bar{\omega_x} + \frac{\partial\bar{w}}{\partial y}\right) dz \quad \text{for,} & z = 1 \\ \tilde{\omega_x} - \frac{\partial\tilde{w}}{\partial y} = -\bar{\omega_x} + \frac{\partial\bar{w}}{\partial y} - \pi\cos(\pi z)\sin(\pi x)\sin(\pi y) \quad \text{for,} & z = 0 \\ \tilde{\omega_y} + \frac{\partial\tilde{w}}{\partial x} = -\bar{\omega_y} - \frac{\partial\bar{w}}{\partial x} \quad \text{for,} & x = 0,1 \\ \tilde{\omega_y} = \bar{\omega_y} + 1 + \pi\cos(\pi z)[\sin(\pi x)\sin(\pi y) - \cos(\pi(x+y))] \quad \text{for,} & y = 0,1 \\ \int_0^1 \left(\tilde{\omega_y} + \frac{\partial\tilde{w}}{\partial x}\right) dz = 1 - \int_0^1 \left(\bar{\omega_y} + \frac{\partial\bar{w}}{\partial x}\right) dz \quad \text{for,} & z = 1 \\ \tilde{\omega_y} + \frac{\partial\tilde{w}}{\partial x} = -\bar{\omega_y} - \frac{\partial\bar{w}}{\partial x} + 1 + \pi\cos(\pi z)\sin(\pi x)\sin(\pi y) \quad \text{for,} & z = 0 \\ \tilde{w} = -\bar{w} + \cos(\pi z)\sin(\pi(x+y)) \quad \text{for,} & x = 0,1 \\ \tilde{w} = -\bar{w} + \cos(\pi z)\sin(\pi(x+y)) \quad \text{for,} & y = 0,1 \\ \tilde{w} = -\bar{w} + \cos(\pi z)\sin(\pi(x+y)) \quad \text{for,} & z = 0,1. \end{cases} \tag{5.46}$$

Note that the integration involved in the system and the boundary condition can be treated as the two-dimensional lid-driven cavity detailed in Chapter 3.

5.3.3 Numerical Results

This test problem has been coded in the MATLAB and FORTRAN programming environment, and Newton linearization combined with a direct solver have been used to solve the problem. The convergence stopping criteria that stop the Newton iteration when the desired corrections have been made is as follows:

$$\epsilon = \max\left(R_{\tilde{\omega_x}}, R_{\tilde{\omega_y}}, R_{\tilde{w}}\right) \leq 10^{-6} \tag{5.47}$$

where $R_{\tilde{\omega_x}}, R_{\tilde{\omega_y}}$ and $R_{\tilde{w}}$ are the infinite norm of the correction terms vectors, $\tilde{\omega_x}, \tilde{\omega_y}$ and w respectively. In other words, they can be written as $R_{\tilde{\omega_x}} = \|\tilde{\omega_x}\|_\infty$, $R_{\tilde{\omega_y}} = \|\tilde{\omega_x}\|_\infty$ and $R_{\tilde{w}} = \|\tilde{w}\|_\infty$.

Figure (5.3), we show the numerical error of ω_x given as $||\omega_{x_{exact}} - \omega_{y_{numerical}}||_\infty$ and a similar calculation is used for the error of ω_y and w. In addition the Figure (5.3) shows the numerical error of the primary variables (ω_x, ω_y, w) on the grids of $101 \times 11 \times 11$ and $151 \times 16 \times 16$. Here, the grid of size $R \times N \times M$ correspond to the number of points in the x, y, z directions respectively. It is clear that solution accuracy is dependent on the grid size, as a more accurate solution is obtained on finer grids. The numerical error increases as Re increases. Moreover, Tables (5.1) and (5.2) emphasize the dependency of the solution of the secondary variables (u, v, ω_z) on the grid size. The test problem has been solved numerically to test the method, the code and to prepare for solving the three-dimensional lid-driven cavity, which will be explained in the next section.

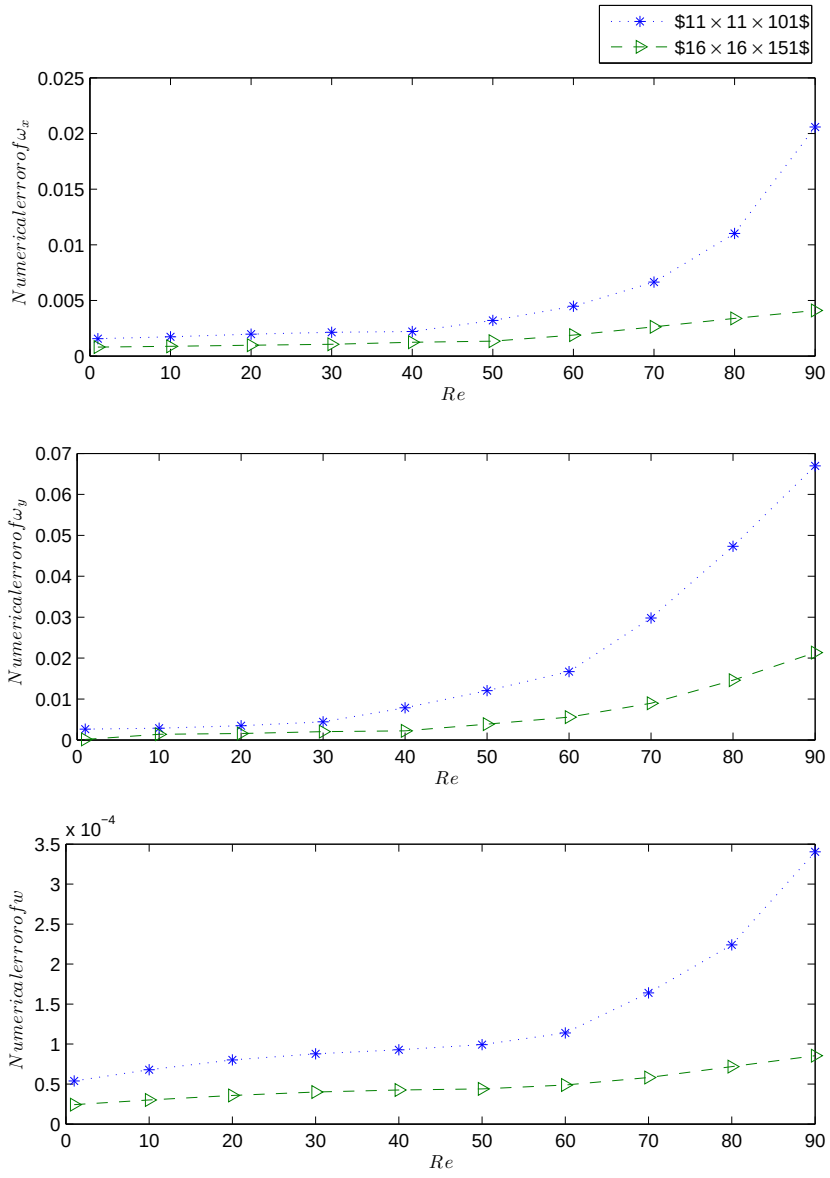

Figure 5.3: The numerical error of ω_x, ω_y and w on grids of $101 \times 11 \times 11$ and $151 \times 16 \times 16$.

Re	Numerical error of u	Numerical error of v	Numerical error of ω_z
10	4.56449E-4	9.64206E-5	1.74315E-2
30	4.65218E-4	1.45803E-4	1.79569E-2
50	4.85458E-4	2.35985E-4	1.84247E-2

Table 5.1: The numerical error of u, v and ω_z on a grid of $101 \times 11 \times 11$.

Re	Numerical error of u	Numerical error of v	Numerical error of ω_z
10	2.11363E-4	4.25220E-5	1.56942E-2
30	2.21880E-4	6.26588E-5	1.61875E-2
50	2.13851E-4	9.75225E-5	1.66563E-2

Table 5.2: The numerical error of u, v and ω_z on a grid of $151 \times 16 \times 16$.

5.4 Solution to 3-D Lid-Driven Cavity

The cubical lid-driven cavity problem is considered with an upper moving wall, see Figure (5.1). The problem is discretized using the Chebyshev discretization in the y and z directions, and fourth-order finite differences is used for the discretization in the x direction. Newton linearization is used to linearize the problem and a direct solver is devoted to solve the problem. The problem has been coded in both the MATLAB and FORTRAN programming environments. Consider the previous test problem with setting F_1, F_2, F_3, in the system (5.17) to zero. The modified system is solved with the boundary conditions similar to the test problem boundary conditions with simple modifications. These modifications are simply, to set all the forcing functions to zero, as shown in (5.48) and modified the boundary conditions on $z = 0$ as shown in (5.48). That leads to the cubical lid-driven cavity with an upper moving wall.

$$\begin{cases} \omega_x = 0 \quad \text{for}, & x = 0, 1 \\ \omega_x - \frac{\partial w}{\partial y} = 0 \quad \text{for}, & y = 0, 1 \\ \int_0^1 \left(\omega_x - \frac{\partial w}{\partial y}\right) dz = 0 \quad \text{for}, & z = 1 \\ \omega_x = -\frac{\partial v}{\partial z} \quad \text{for}, & z = 0 \\ \omega_y + \frac{\partial w}{\partial x} = 0 \quad \text{for}, & x = 0, 1 \\ \omega_y = 0 \quad \text{for}, & y = 0, 1 \\ \int_0^1 \left(\omega_y + \frac{\partial w}{\partial x}\right) dz = 1 \quad \text{for}, & z = 1 \\ \omega_y = \frac{\partial u}{\partial z} \quad \text{for}, & z = 0 \\ w = 0 \quad \text{for}, & x = 0, 1 \\ w = 0 \quad \text{for}, & y = 0, 1 \\ w = 0 \quad \text{for}, & z = 0, 1. \end{cases} \tag{5.48}$$

The boundary conditions on $z = 0$ can be obtained from the relations (5.19) and (5.20) where $\frac{\partial w}{\partial y} = \frac{\partial w}{\partial x} = 0$.

5.4.1 Numerical Results for Three-Dimensional LDC

The convergence criteria used are similar to the three-dimensional test problem. The results were generated on various grid sizes of which the finest was $251 \times 33 \times 33$ and for various Reynolds numbers. We use the solution of the previous Reynolds number as the initial guess to obtain the solution for the next larger Reynolds number.

$Re = 1$				
Grid size	u_{min}	u_{max}	w_{min}	w_{max}
$21 \times 5 \times 5$	-0.10998	1	-0.23735	0.23634
$41 \times 8 \times 8$	-0.20623	1	-0.30276	0.30026
$61 \times 10 \times 10$	-0.20722	1	-0.32534	0.32234
$Re = 50$				
Grid size	u_{min}	u_{max}	w_{min}	w_{max}
$21 \times 5 \times 5$	-0.13413	1	-0.22015	0.20638
$41 \times 8 \times 8$	-0.26654	1	-0.34878	0.24255
$61 \times 10 \times 10$	-0.26769	1	-0.38709	0.25980

Table 5.3: Minimum and maximum of u-velocity component is evaluated along the vertical centerline, and the minimum and maximum of w-velocity component is evaluated along the horizontal centerline at the symmetry plane $y = \frac{1}{2}$ for $Re = 1, 50$.

Table (5.3) shows that the minimum and maximum values of the u-velocity component are evaluated along the vertical centerline, and the minimum and maximum values of the w-velocity component are evaluated along the horizontal centerline at the symmetry plane $y = \frac{1}{2}$. It can be observed that how the use of finer grids gives values which are convergent because of the increased accuracy. Figures (5.4-5.7) show the u-velocity component along the vertical centerline and w-velocity component along the horizontal centerline of the symmetry plane $x - z, y = \frac{1}{2}$. The results of the u-velocity profile agree with those of Jackson (1996), Albensoeder & Kuhlmann (2005), Ku *et al.* (1987) and Dennis *et al.* (1979) and good agreement can be observed for the w-velocity profiles when we compare with the same references. It is worth mentioning that the w-velocity component corresponds to v-velocity in some references such as Jackson (1996) and Ku *et al.* (1987) due to the difference in the axes directions that have been considered. However, the small difference in $u-$ velocity profile, which is of order $(10^{(-2)})$, can be attributed to the need to use more grid points especially in the x direction where we use the finite difference method. That can be seen clearly

around the corners of contours plots of u in Figures (5.12-5.15).

Figures (5.8-5.11) show the mesh of u-velocity and v-velocity values on the plane $(\frac{1}{2}, y, z)$ for various $Re = 1, 50, 100$ and 200 using the grid of size $251 \times 33 \times 33$. It can be observed that near the boundary conditions, the values of u-velocity on the mentioned plane change significantly, especially at $y = 0, 1$ where more resolution is needed. Significant changes to v-velocity also occur near $z = 1$, where the moving wall is located. One can see that the values of the v-velocity are small because the flow velocity in the y direction is small. These values increase in tandem with the Reynolds numbers as evidenced in Figure (5.11) for $Re = 200$.

Some velocity and vorticity component contour plots are presented in Figures (5.12-5.15) for $Re = 1, 50, 100$ and 200, using the grid of size $251 \times 33 \times 33$. Generally, good agreement with Jackson (1996) is observed in the common contour plots which are $u(\frac{1}{2}, y, z)$, $u(x, y, \frac{1}{2})$, and $w(\frac{1}{2}, y, z)$. From the contours plots of u, it can be suggested that resolution is needed as some coarse small circles appear around the bottom corners. The same observation apply for w contours where the effect of the used coarse grid is obvious in the interior contours levels. at the contours plots of u at $Re = 200$ the need to use a finer grid is more obvious as the Reynold number increased, see Figure (5.15).

Figures (5.16-5.27) show the velocity component (u, v, w) on the boundaries to show that our results demonstrate that lid driven cavity boundary conditions are satisfied. It is clear that all the velocity component (u, v, w) for various Reynolds numbers are almost zero everywhere on the boundary conditions, except on $z = 1$ where $u = 1$.

To conclude, a test problem for the velocity-vorticity formulation was prepared to test the numerical methods and the code. Although good results are obtained using the novel velocity-vorticity formulation, more accurate numerical solutions can be obtained using finer grids. But finer grids could not be used because of the huge amount of memory which is required for the direct solver. With the use of parallelisation, we can overcome this obstacle. However, the novel velocity-vorticity formulation show its equivalence to the the original formulation with only solving for three primary variables. This makes this formulation promising and attractive to use rather than other formulations.

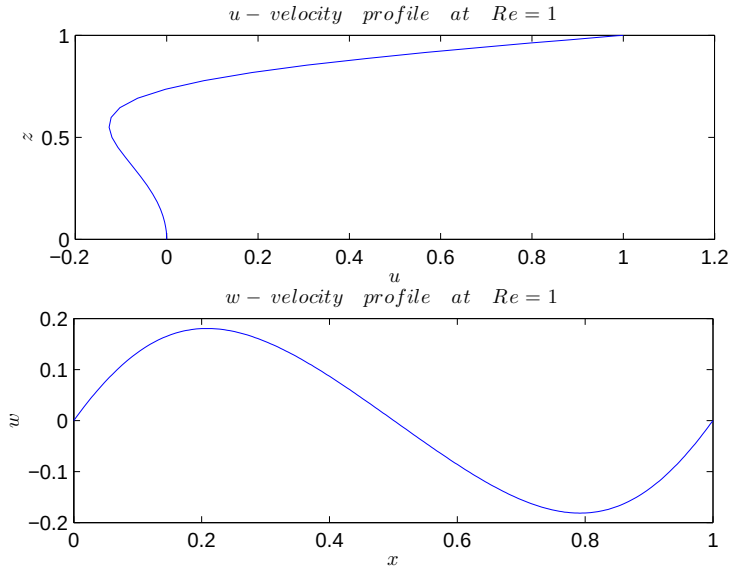

Figure 5.4: $u, w-$Velocity profiles for $Re = 1$ along the vertical and horizontal centerline of the $x - z$ symmetry plane $(x, \frac{1}{2}, z)$.

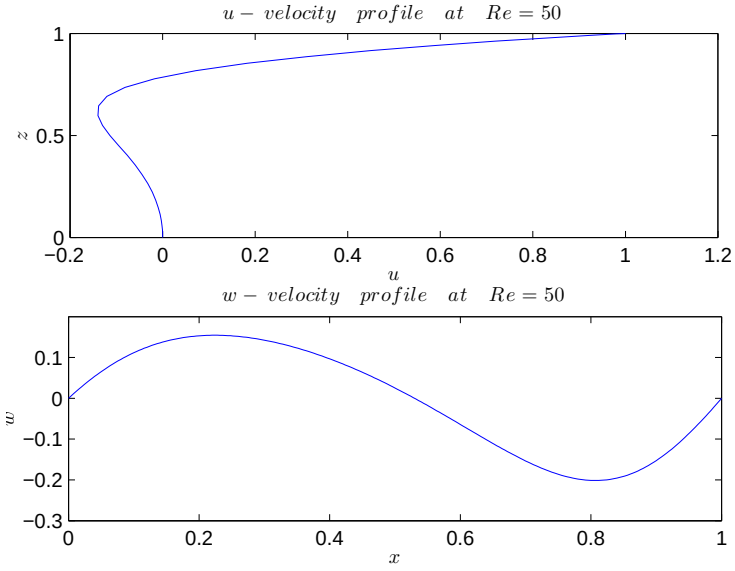

Figure 5.5: $u, w-$Velocity profiles for $Re = 50$ along the vertical and horizontal centerline of the $x - z$ symmetry plane $(x, \frac{1}{2}, z)$.

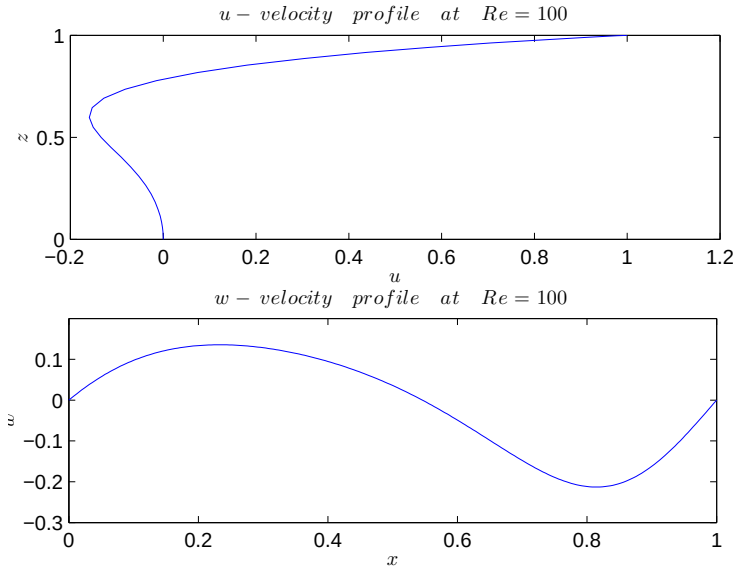

Figure 5.6: $u, w-$Velocity profiles for $Re = 100$ along the vertical and horizontal centerline of the $x - z$ symmetry plane $(x, \frac{1}{2}, z)$.

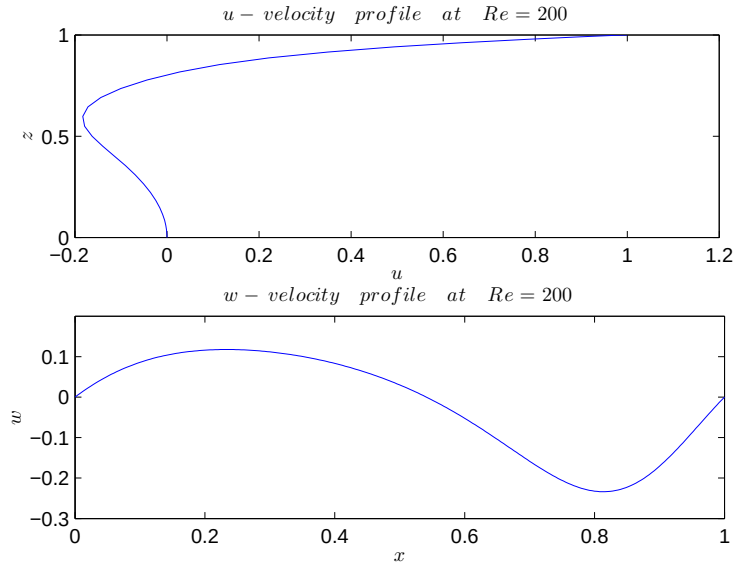

Figure 5.7: $u, w-$Velocity profiles for $Re = 200$ along the vertical and horizontal centerline of the $x - z$ symmetry plane $(x, \frac{1}{2}, z)$.

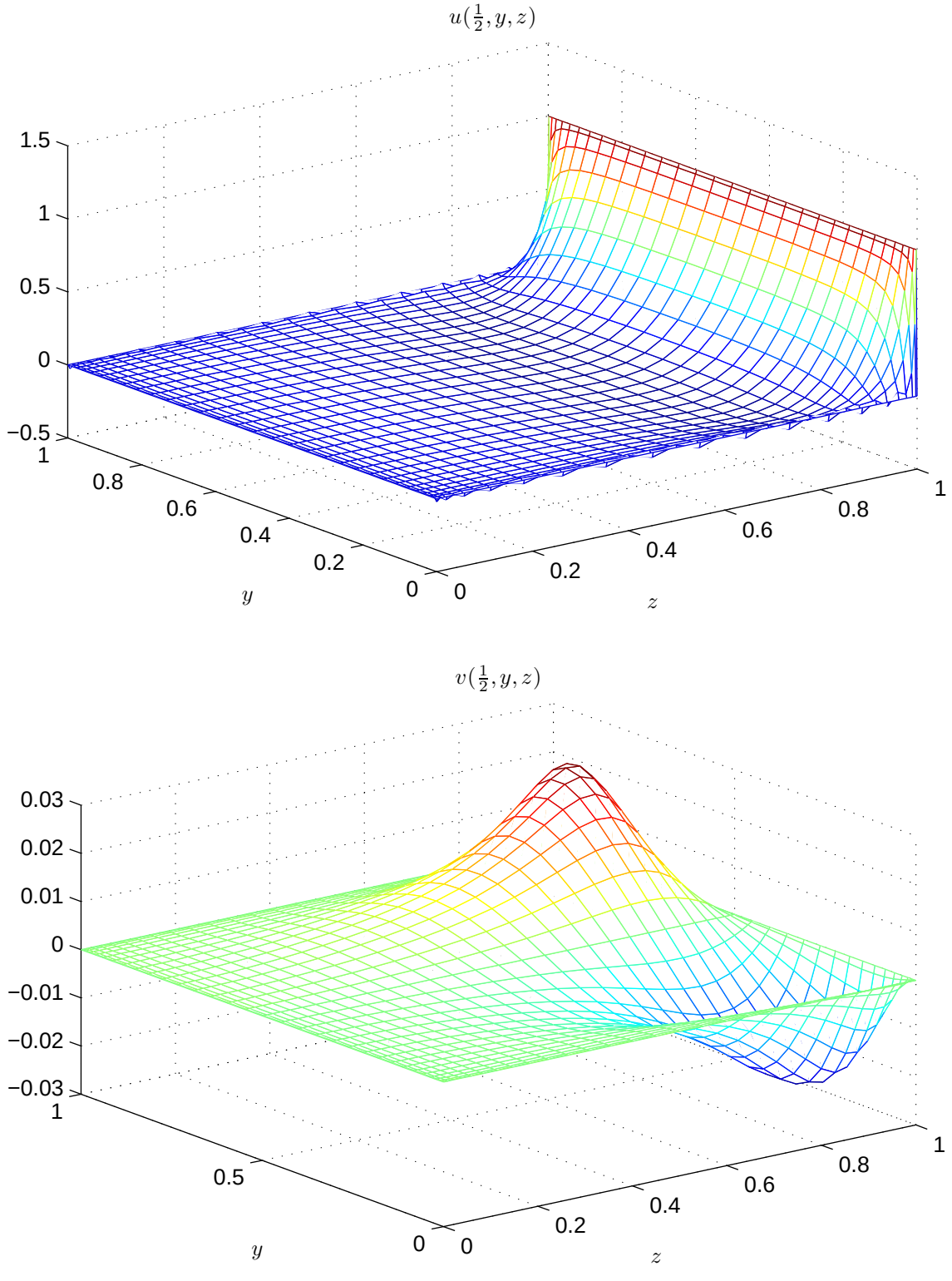

1

Figure 5.8: u, v-velocity profiles on the plane $(\frac{1}{2}, y, z)$ for $Re = 1$.

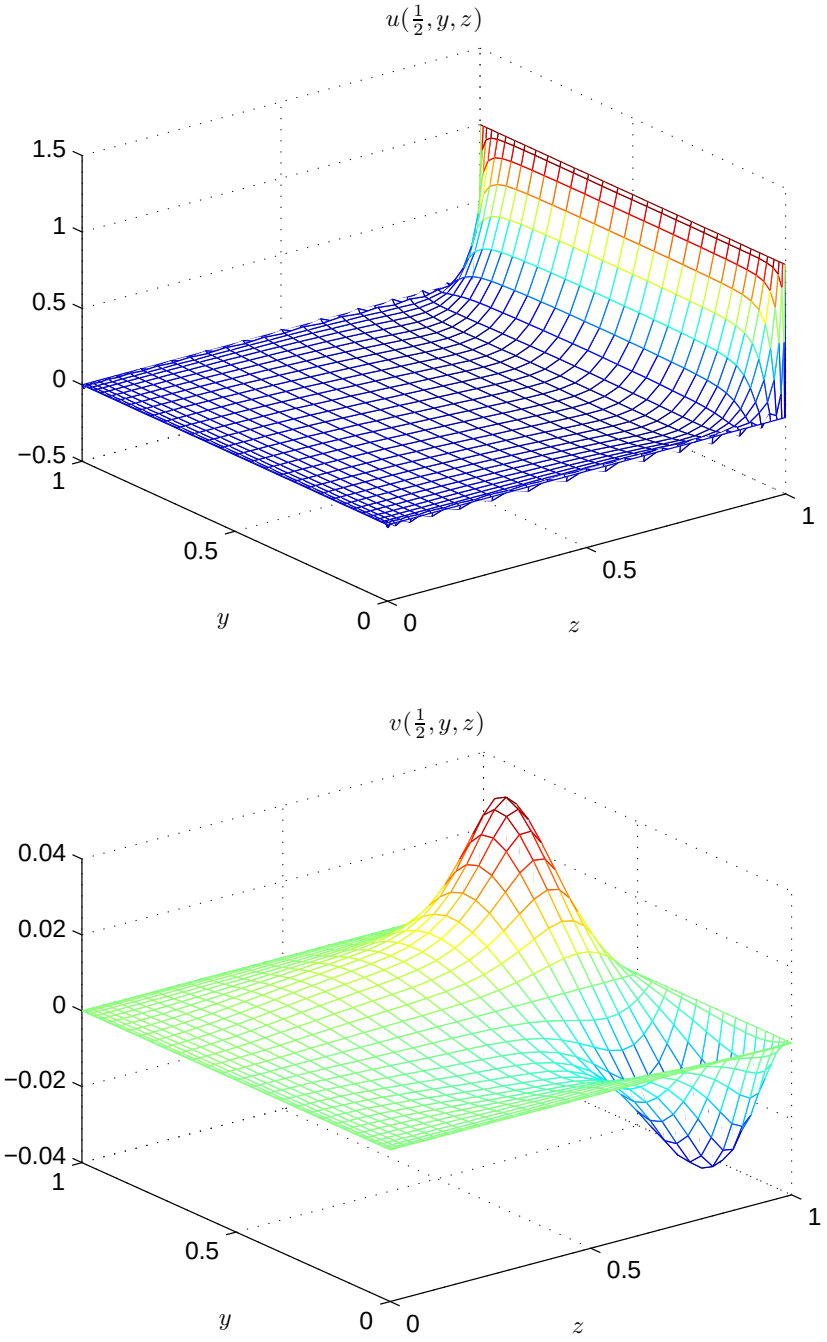

Figure 5.9: u, v-velocity profiles on the plane $(\frac{1}{2}, y, z)$ for $Re = 50$.

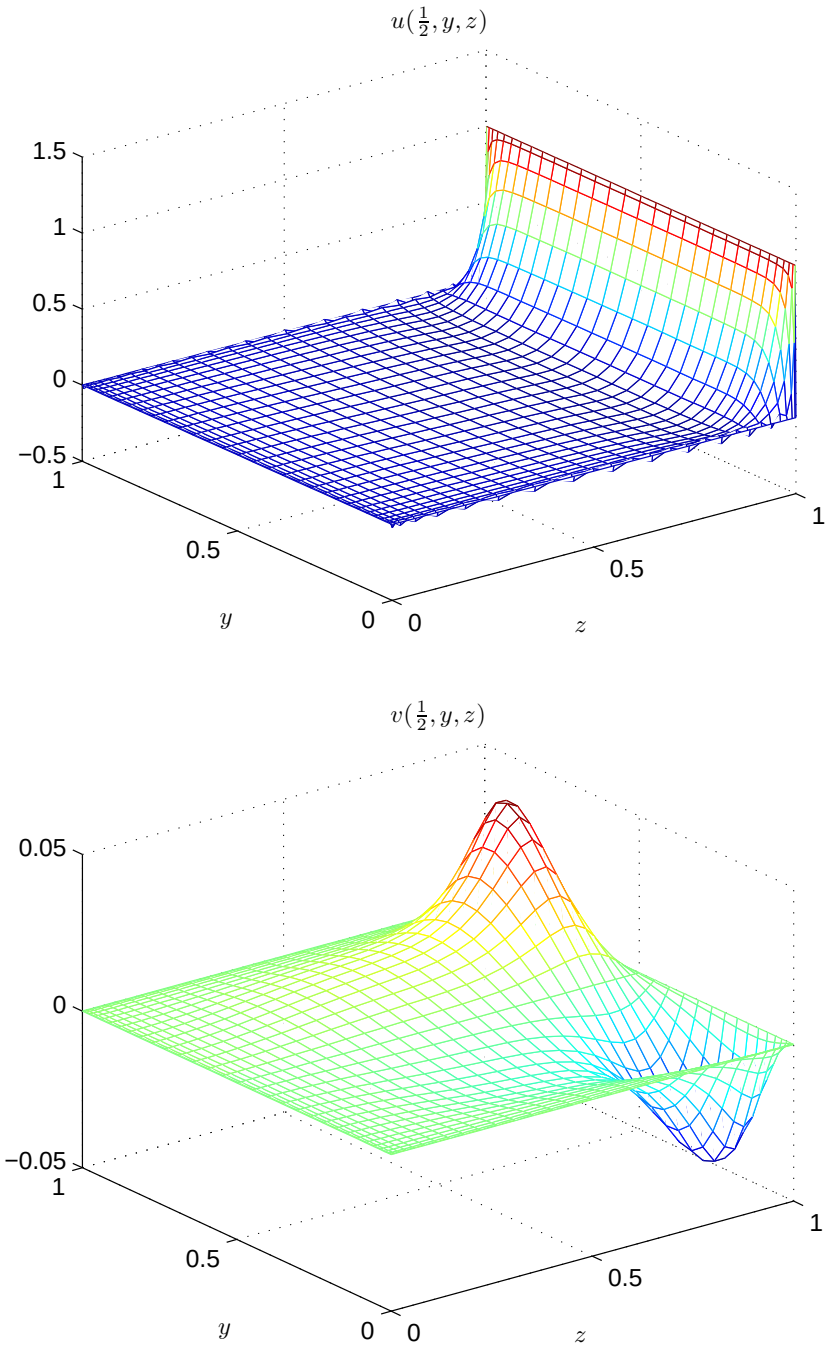

Figure 5.10: u, v-velocity profiles on the plane $(\frac{1}{2}, y, z)$ for $Re = 100$.

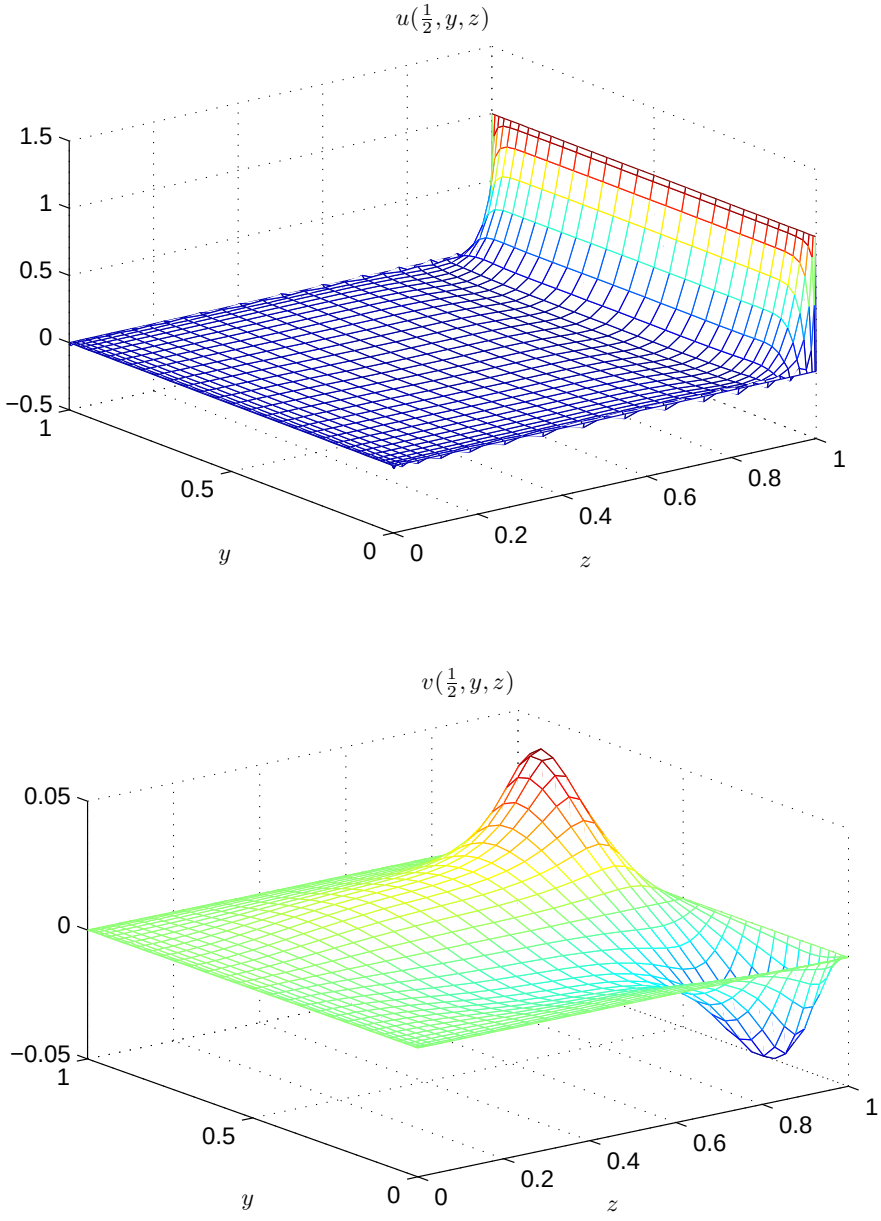

Figure 5.11: u, v-velocity profiles on the plane $(\frac{1}{2}, y, z)$ for $Re = 200$.

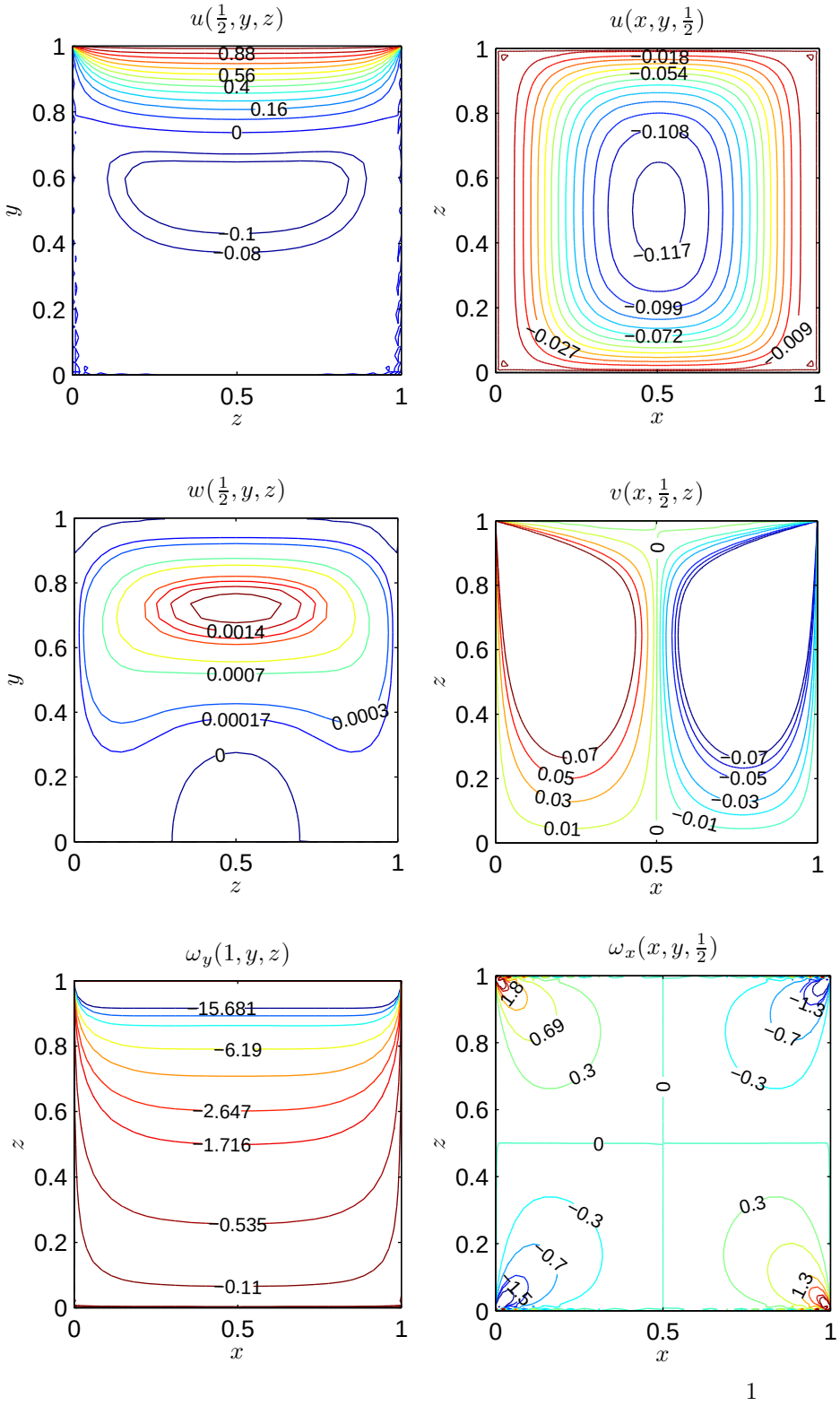

1

Figure 5.12: Contour plots for $Re = 1$ using a grid of size $251 \times 33 \times 33$.

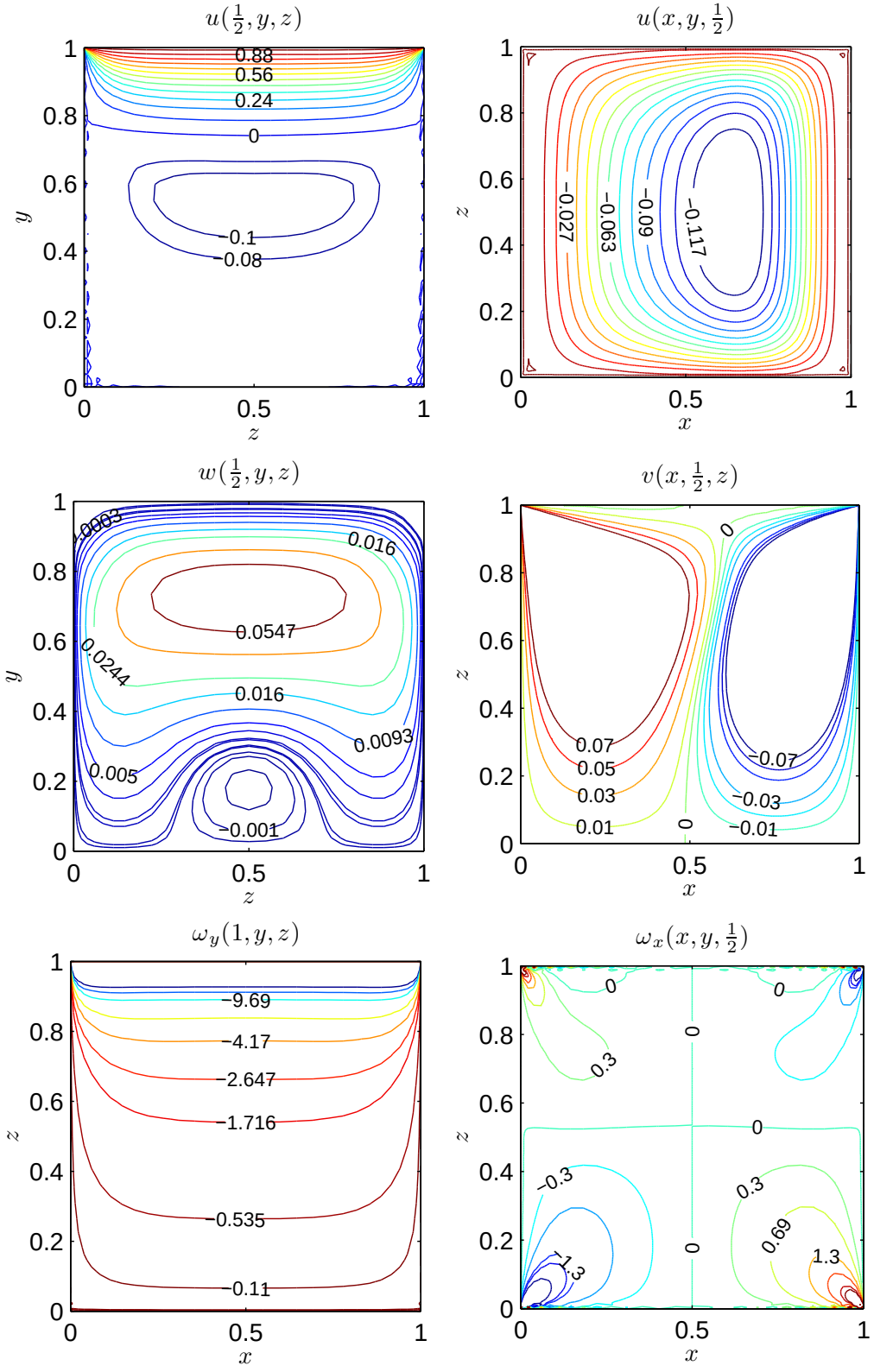

1

Figure 5.13: Contour plots for $Re = 50$ using a grid of size $251 \times 33 \times 33$.

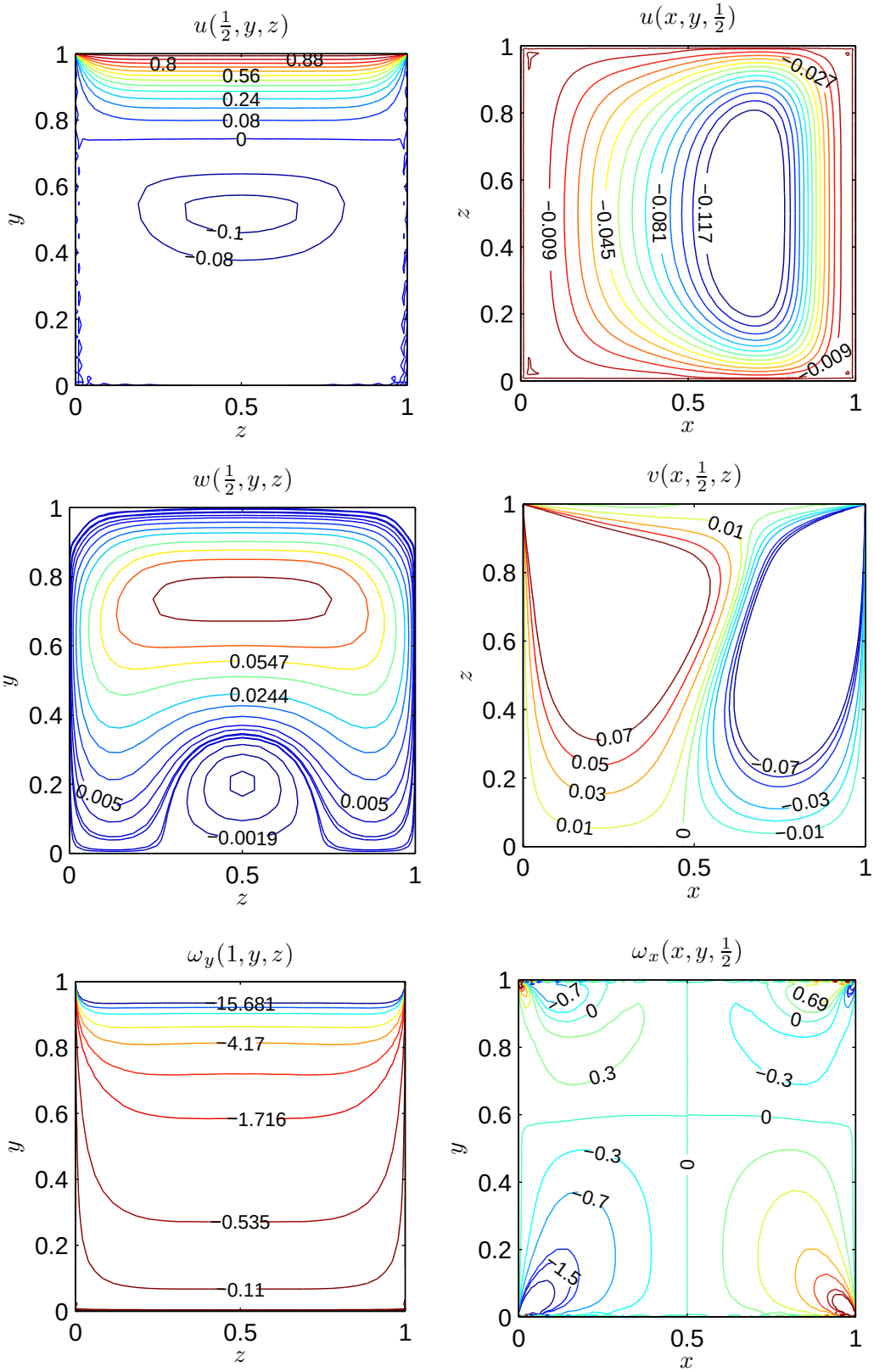

Figure 5.14: Contour plots for $Re = 100$ using a grid of size $251 \times 33 \times 33$.

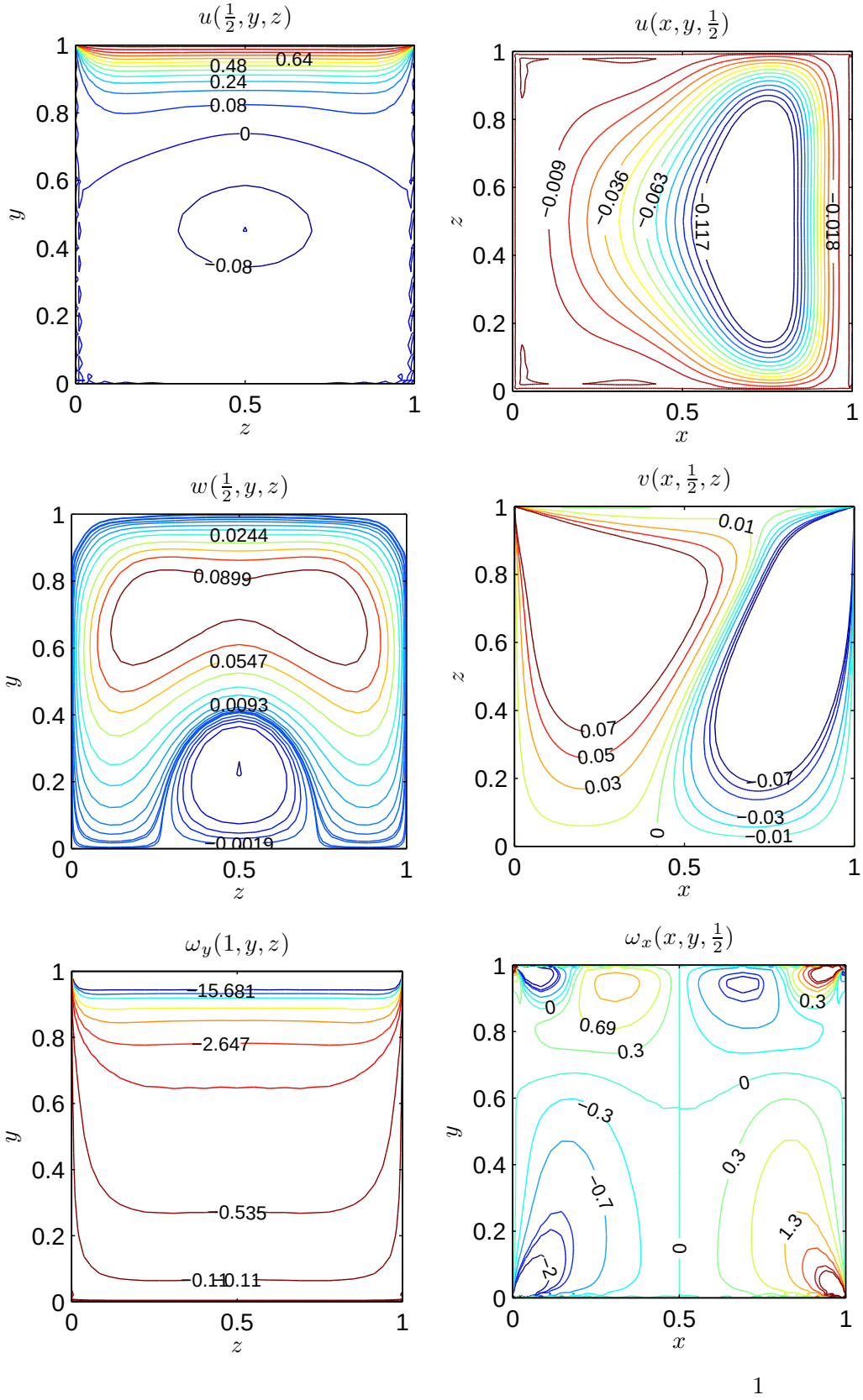

Figure 5.15: Contour plots for $Re = 200$ using a grid of size $251 \times 33 \times 33$.

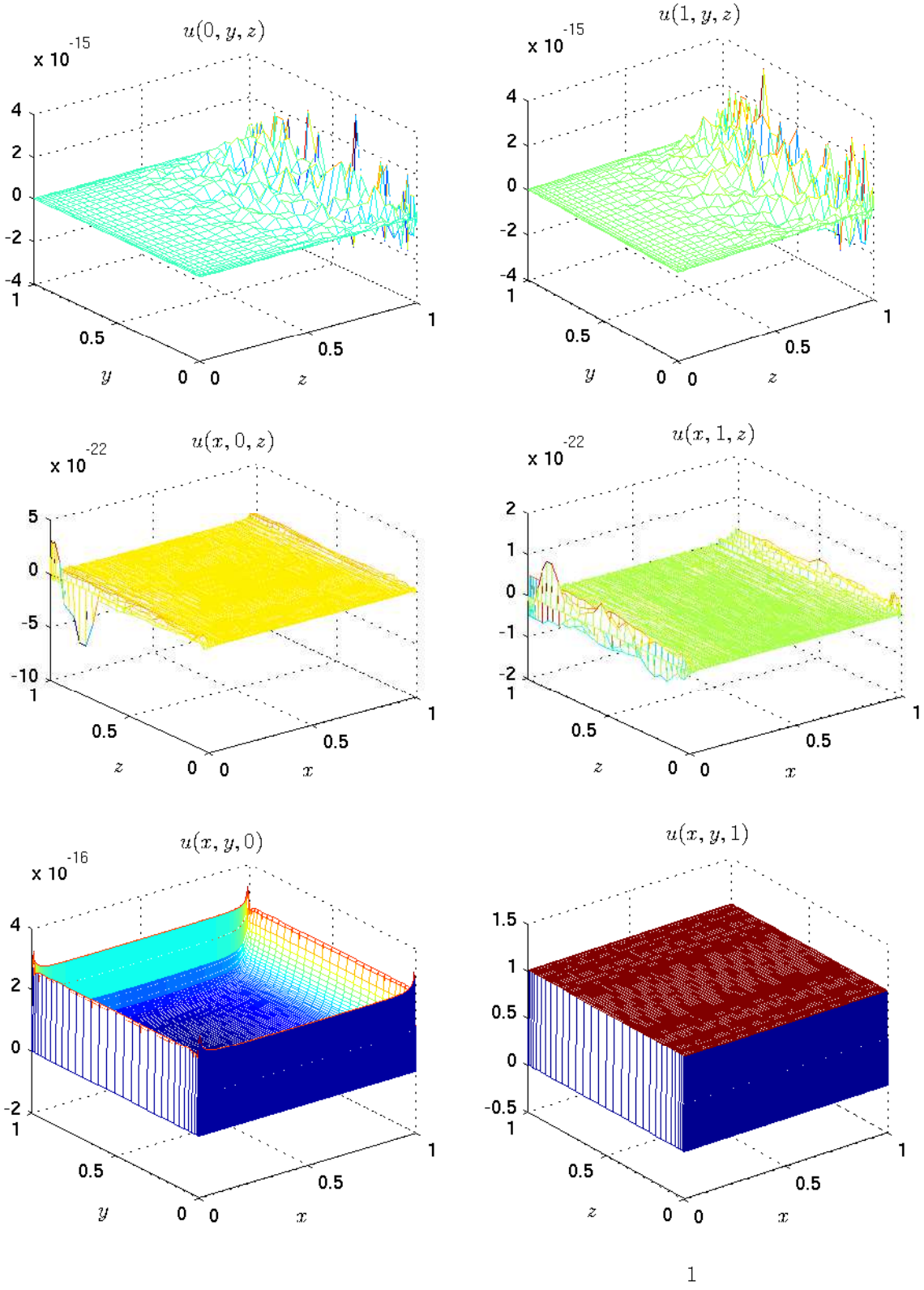

Figure 5.16: u-velocity values on the boundary conditions for $Re = 1$.

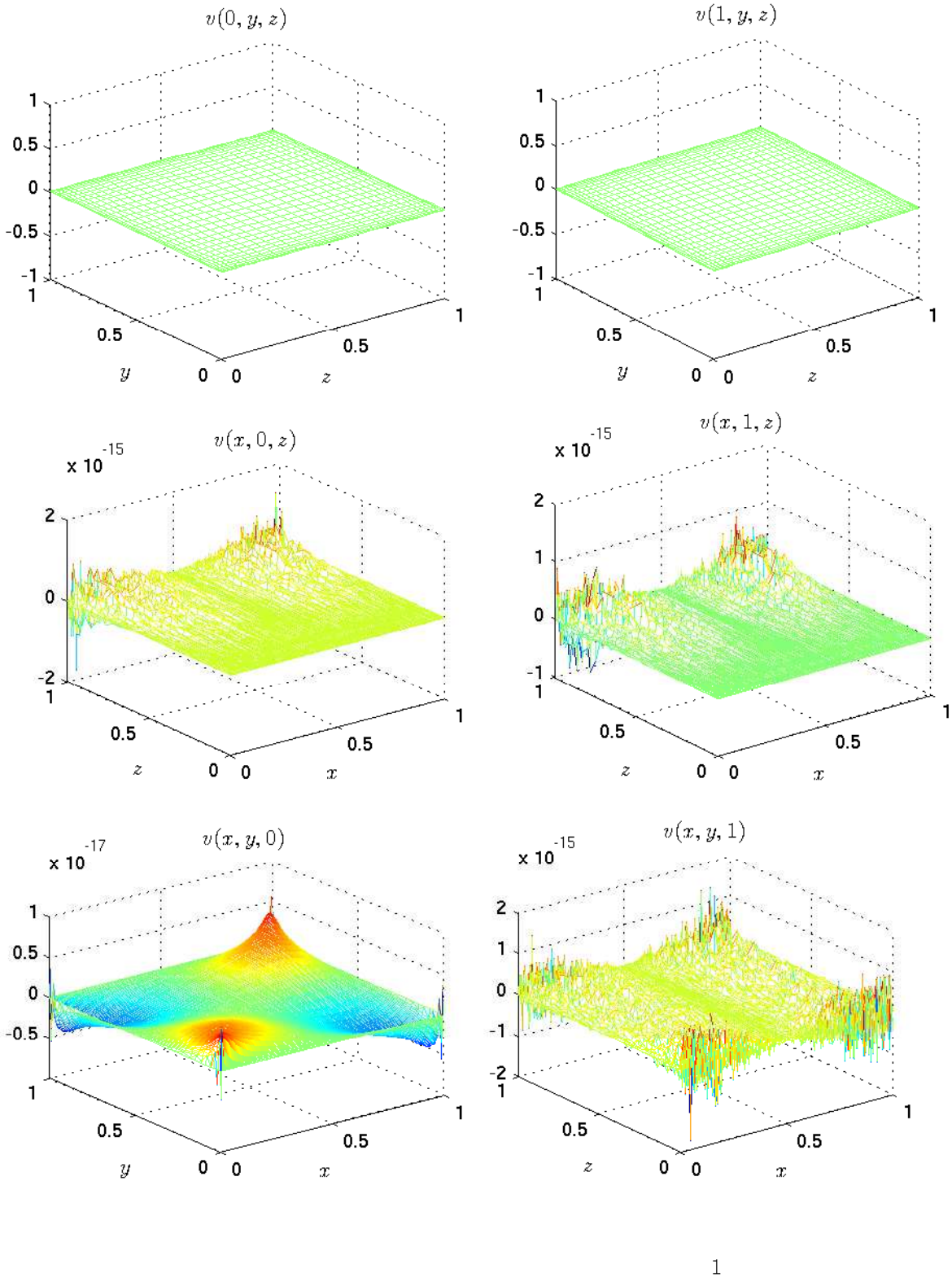

1

Figure 5.17: v-velocity values on the boundary conditions for $Re = 1$.

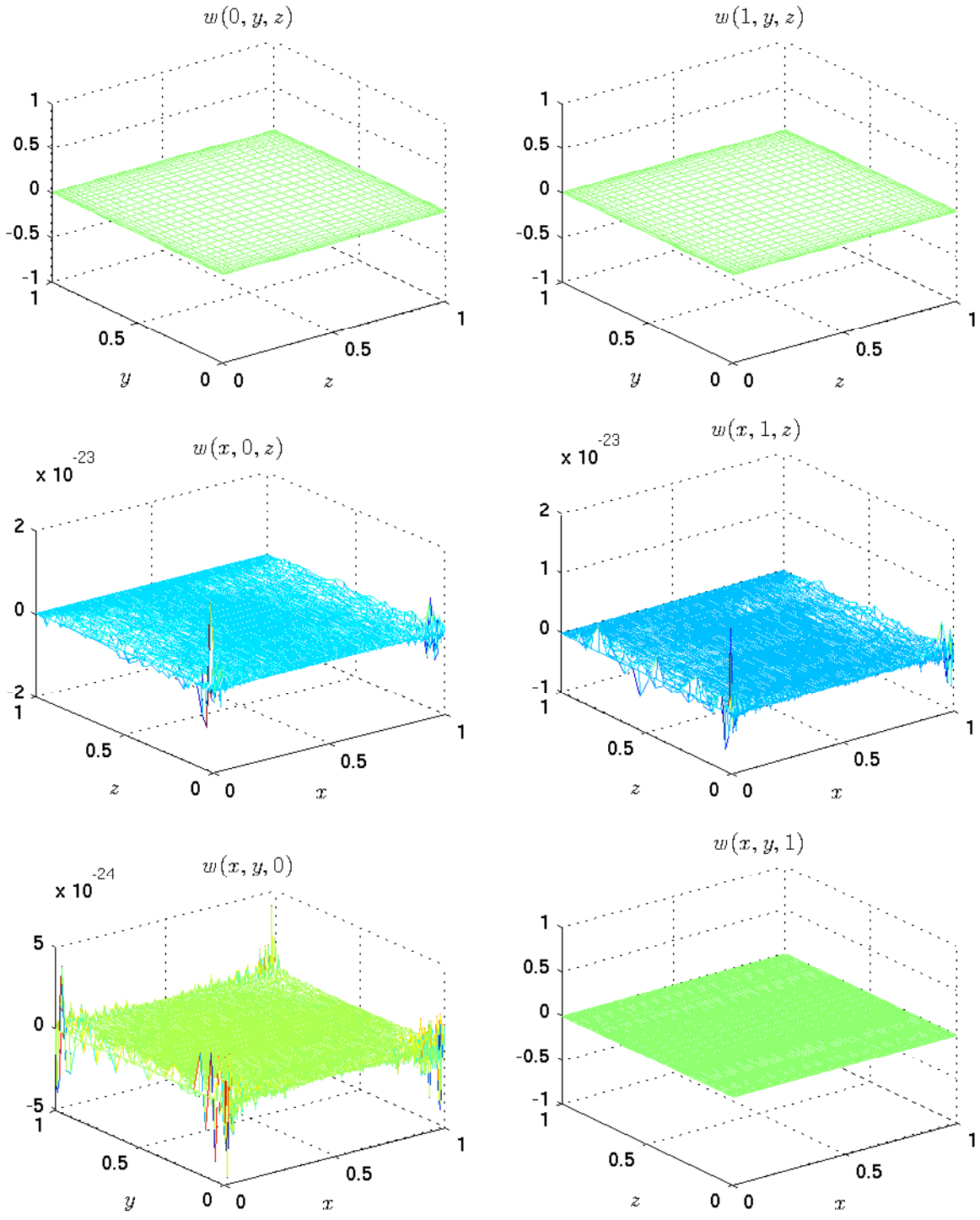

1

Figure 5.18: w-velocity values on the boundary conditions for $Re = 1$.

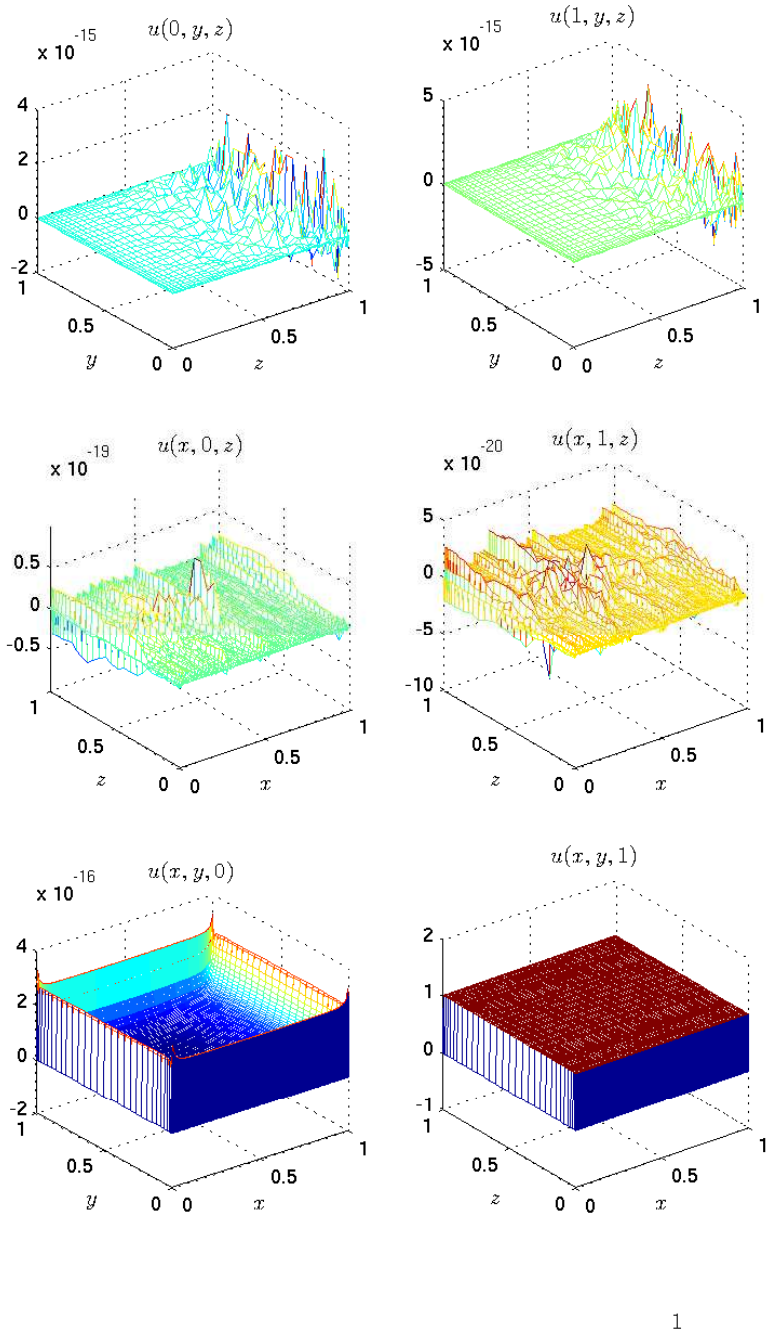

Figure 5.19: u-velocity values on the boundary conditions for $Re = 50$.

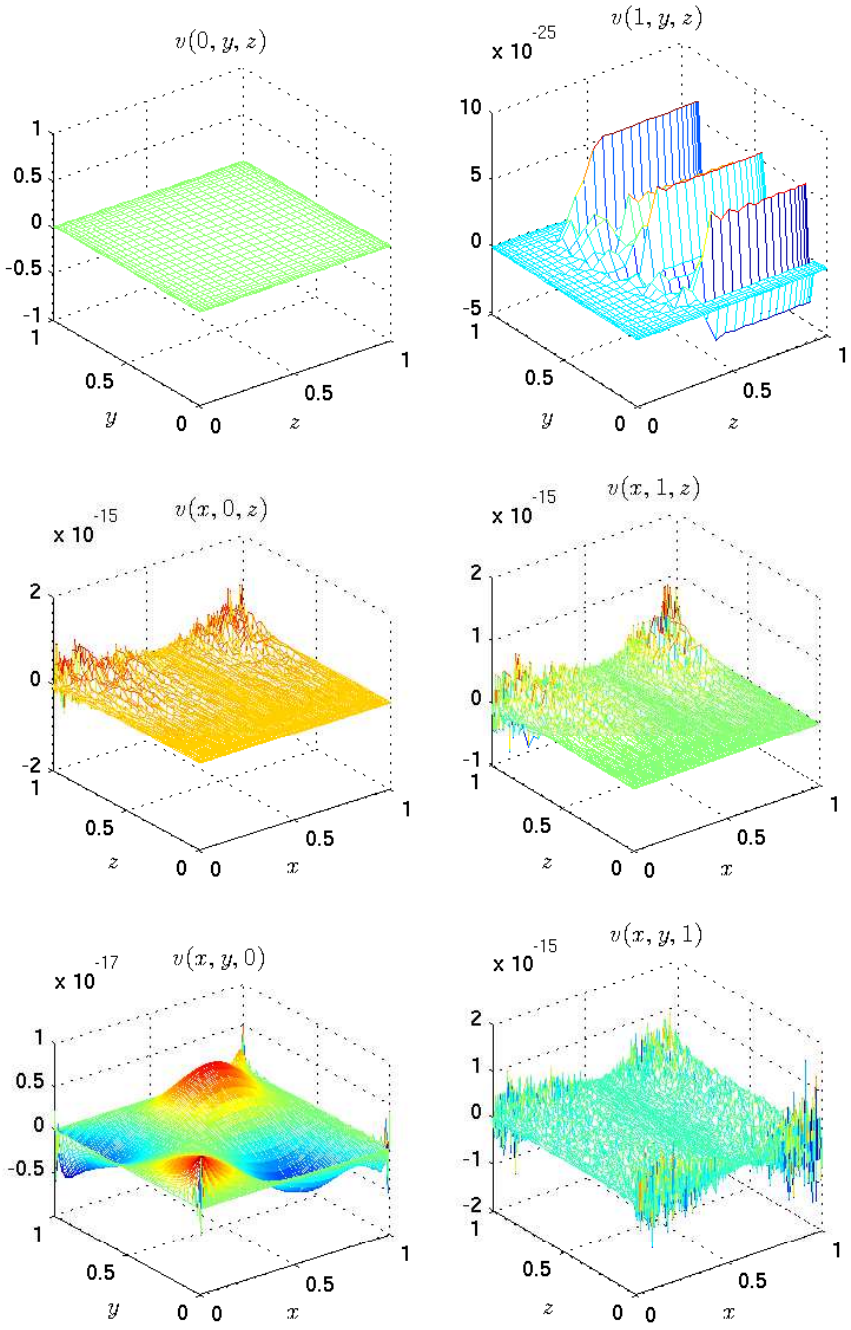

Figure 5.20: v-velocity values on the boundary conditions for $Re = 50$.

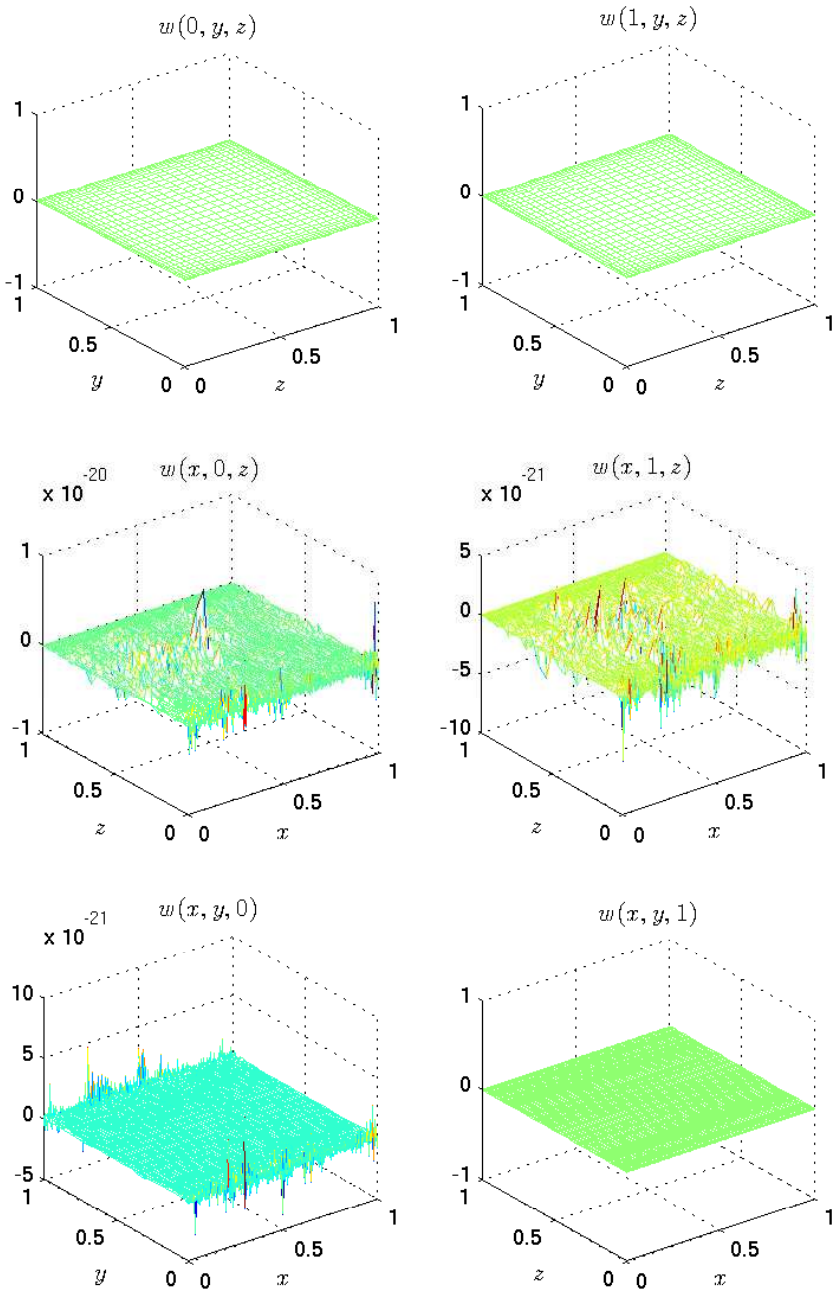

Figure 5.21: w-velocity values on the boundary conditions for $Re = 50$.

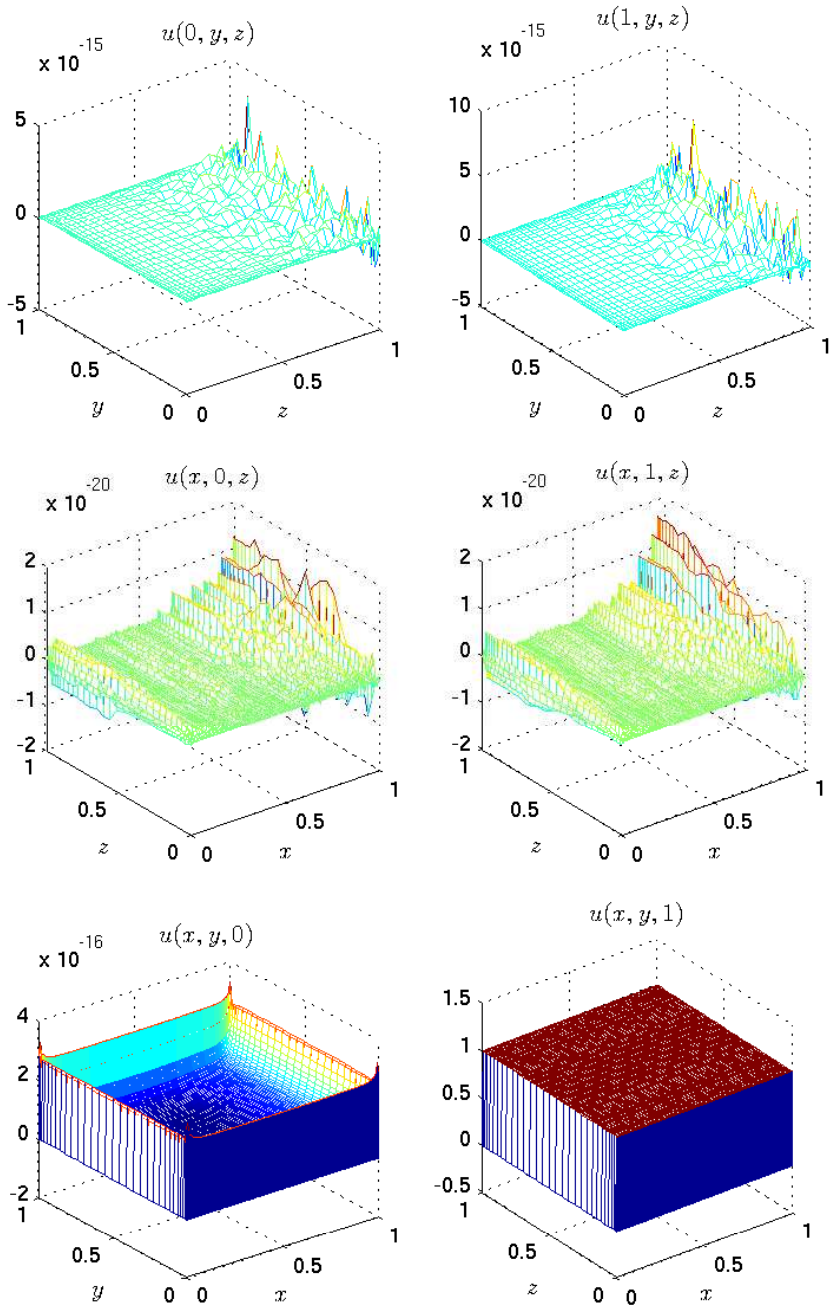

Figure 5.22: u-velocity values on the boundary conditions for $Re = 100$.

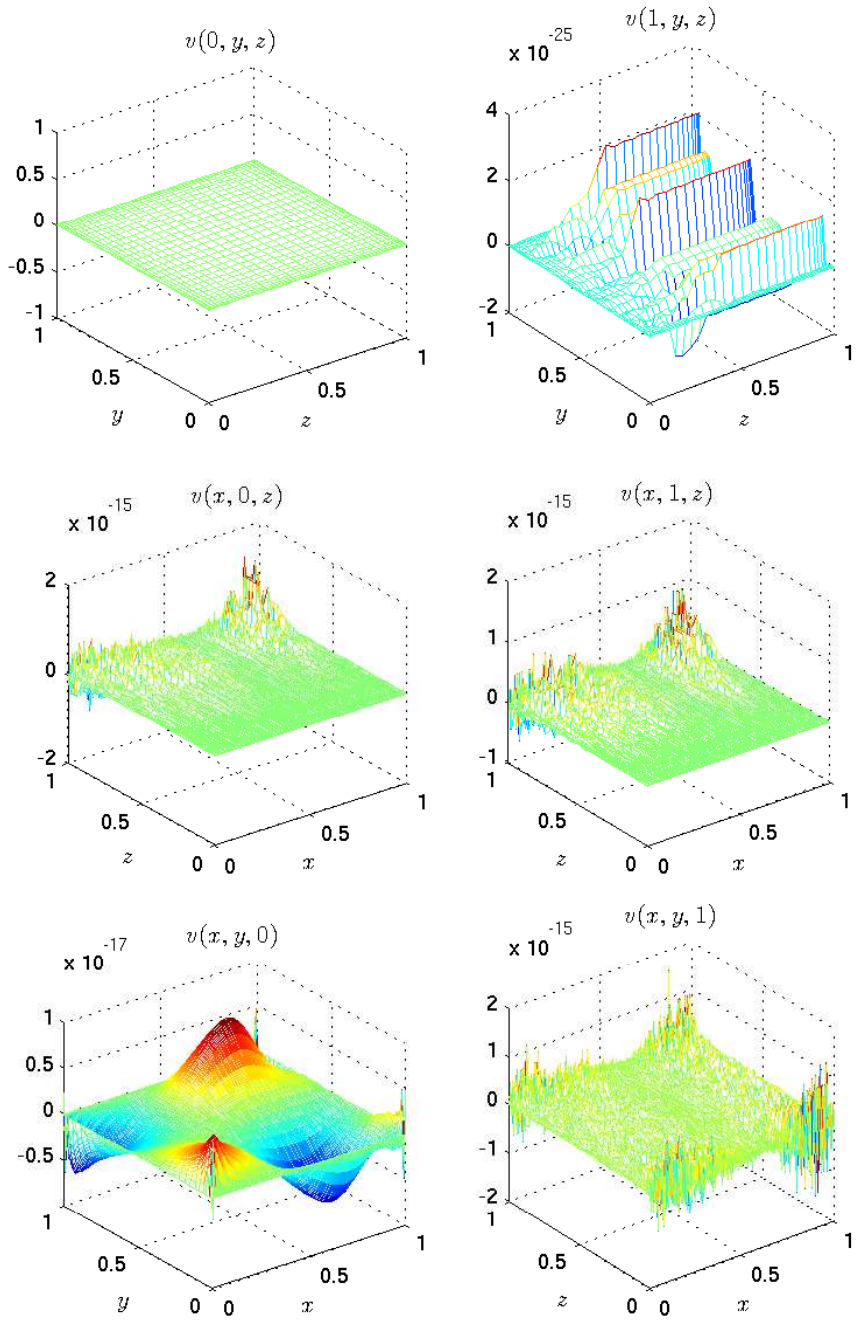

1

Figure 5.23: v-velocity values on the boundary conditions for $Re = 100$.

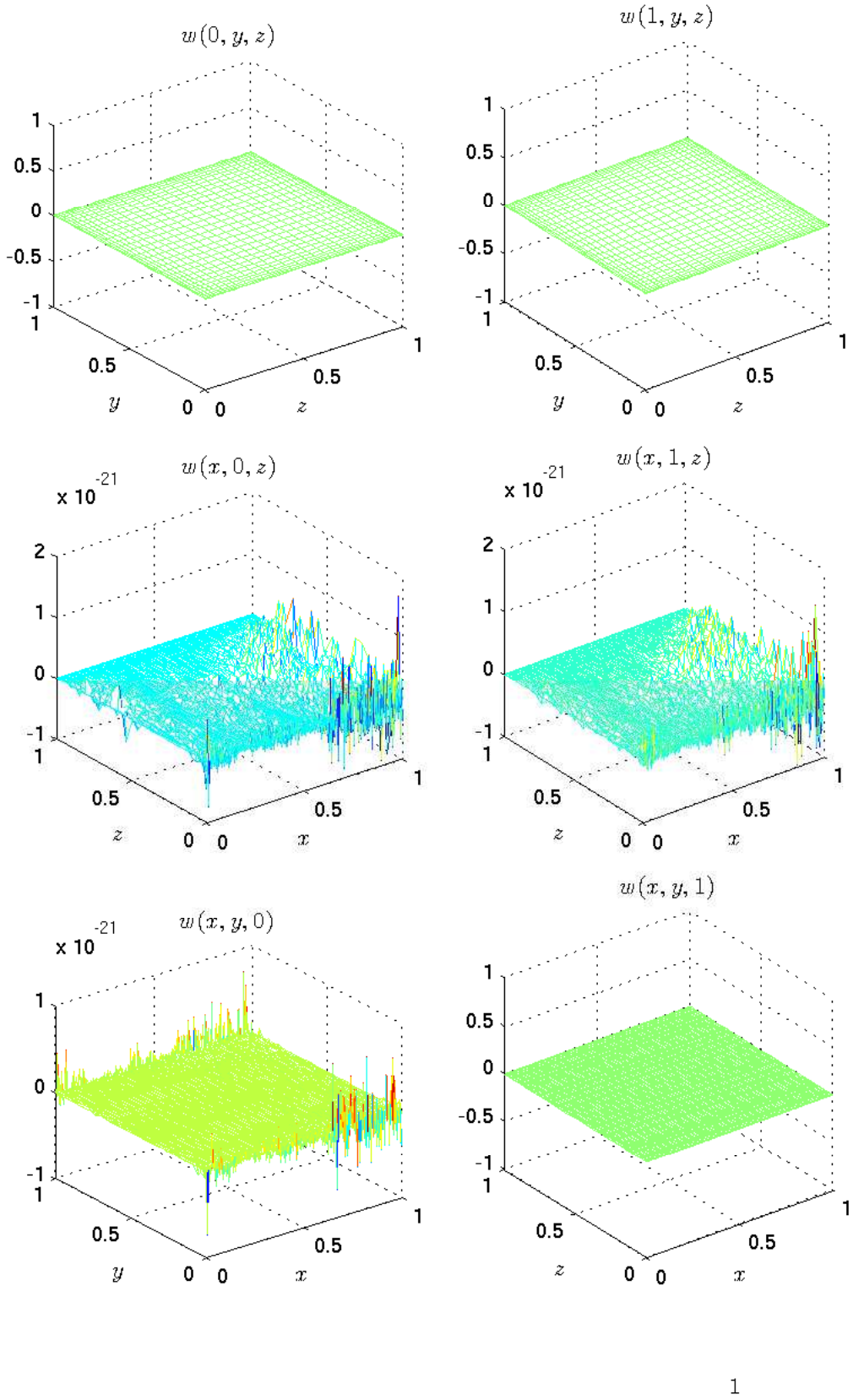

Figure 5.24: w-velocity values on the boundary conditions for $Re = 100$.

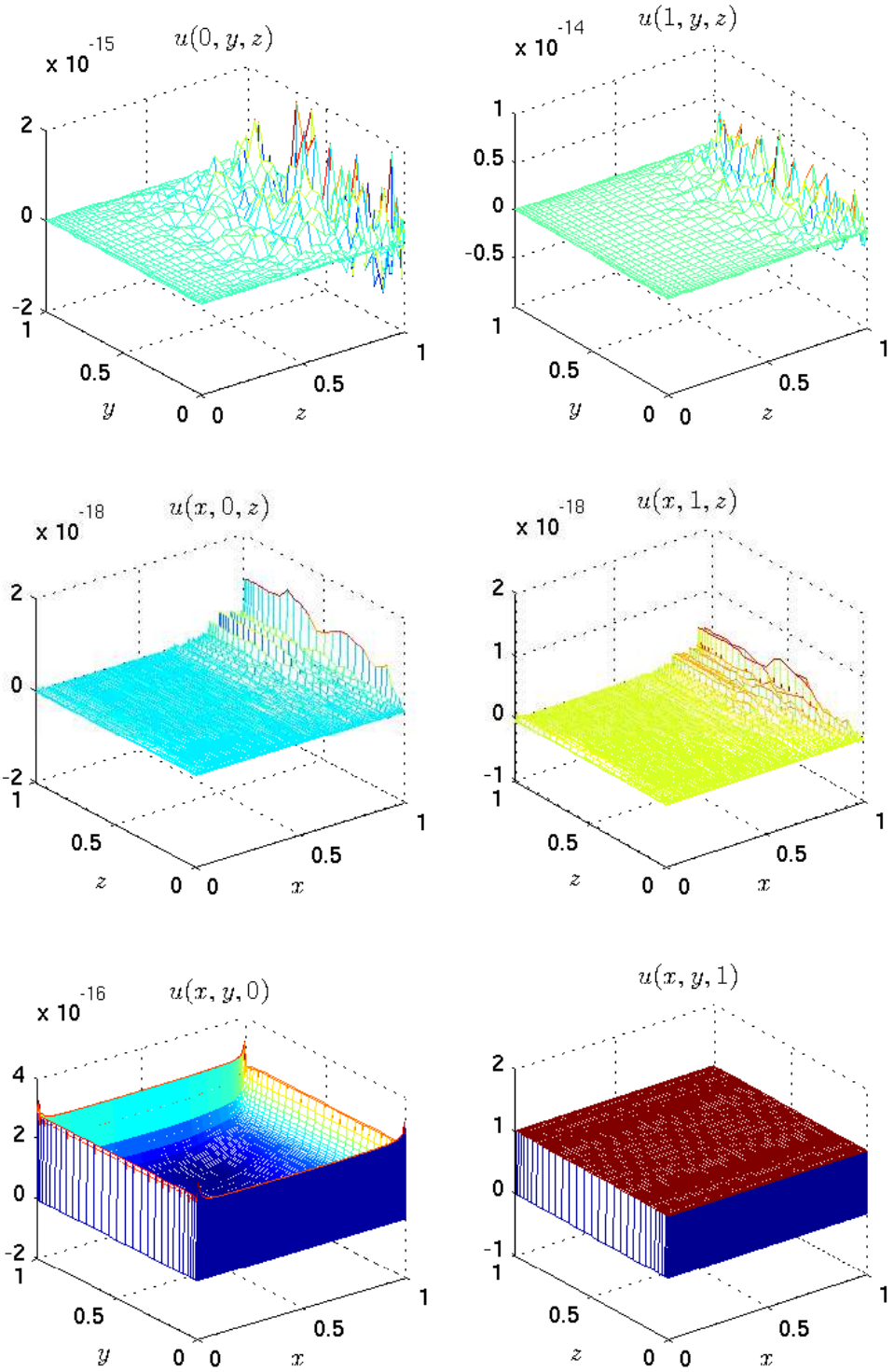

Figure 5.25: u-velocity values on the boundary conditions for $Re = 200$.

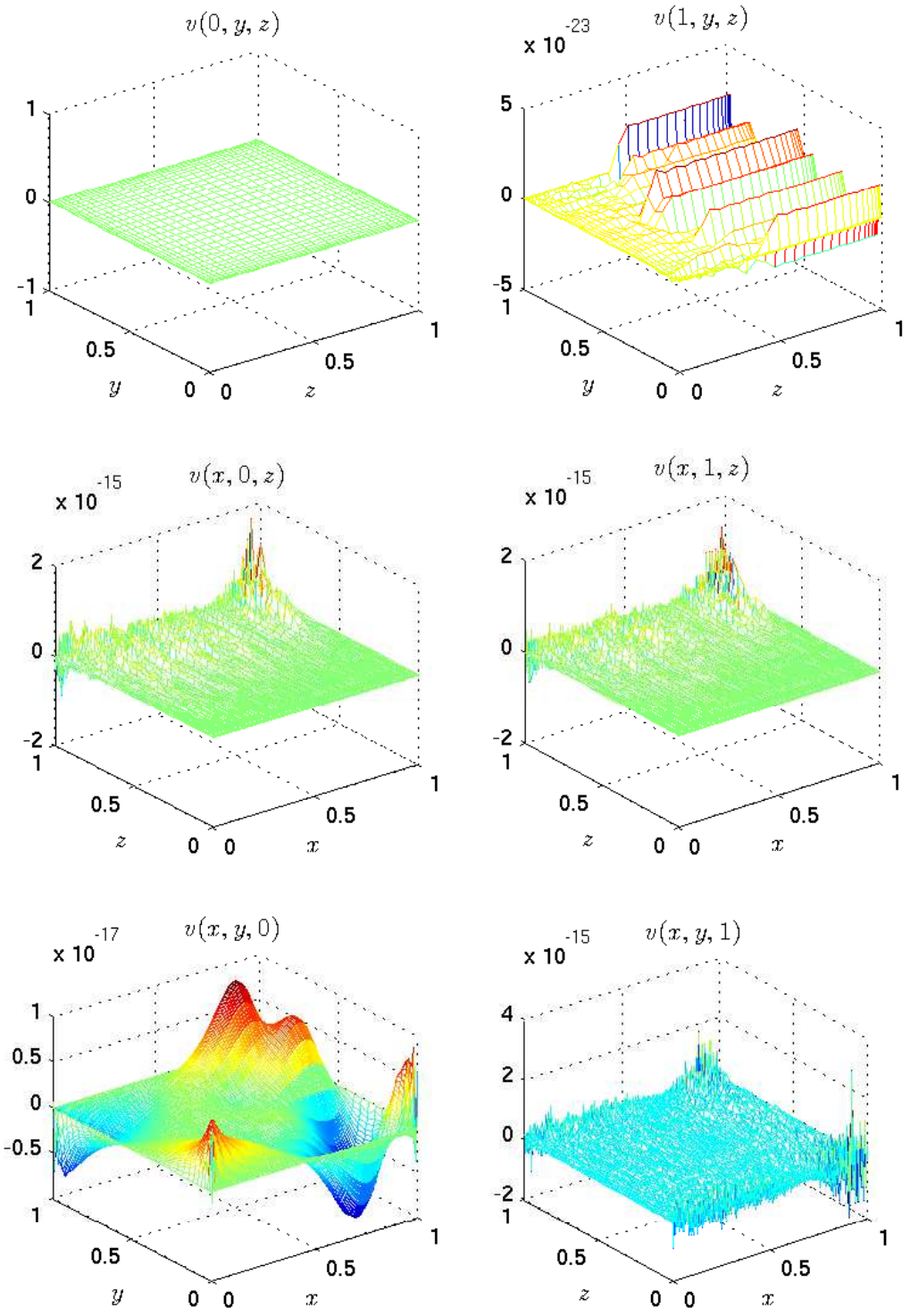

Figure 5.26: v-velocity values on the boundary conditions for $Re = 1$.

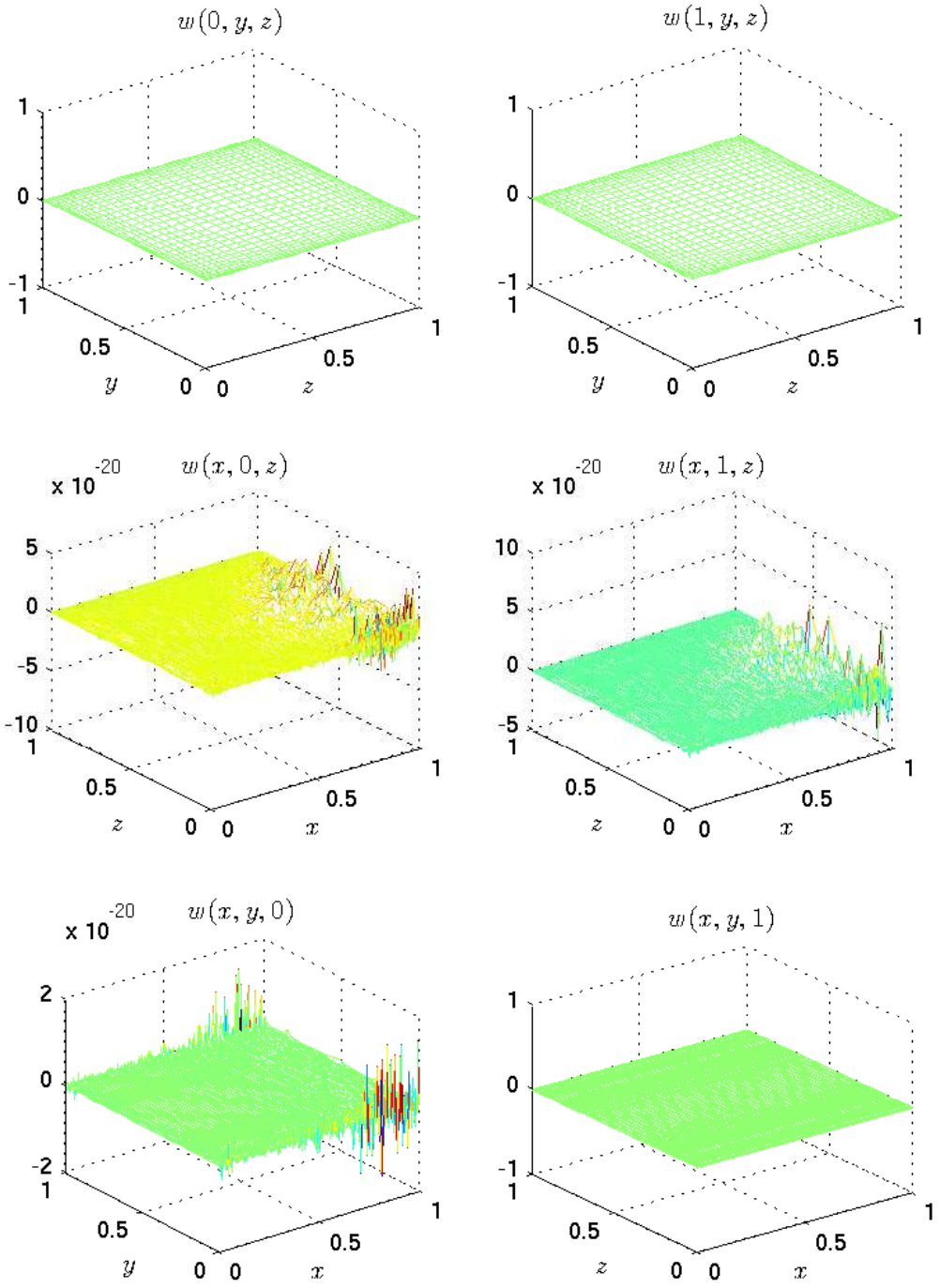

Figure 5.27: w-velocity values on the boundary conditions for $Re = 200$.

Chapter 6

Conclusions

In this project, firstly, we have investigated the solution of the two-dimensional lid-driven cavity problem by solving the steady Navier-Stokes equations. The streamfunction-vorticity formulation was used to obtain the solution for the flow in a square domain. The Chebyshev collocation method was used to discretize the equations in both the x and y directions. The Newton-Raphson technique was employed to linearize the system. A MATLAB code was developed to solve the system using a direct method to obtain the solution at high Reynolds number. The advantage of using the spectral method is the greater accuracy that it offers. Solutions have been obtained for Reynolds number, far higher than those presented previously by other researchers. Our results obtained concurred with those available in the literature. There are small differences for $Re > 10000$ in the secondary and tertiary corner eddies features, as described previously. We believe that the present results are more accurate due to the use of the spectral method in both directions, which offers a great accuracy. New results were obtained for Reynolds number values of $Re = 21000, 22000, 23000, 24000$ and 25000. Our solutions show oscillations in the vorticity contour plots near the top left corner

but it is suggested that using finer grids would resolve the area in particular, for $Re \geq 22000$.

Secondly, the same technique that has been used for the two-dimensional lid-driven cavity problem was employed to solve the steady separated corner flow. Solutions for high Reynolds number, far higher than those obtained previously by other researchers, were obtained for various grids. Streamfunction and vorticity contour plots and their profiles for various Reynolds numbers and grids were presented. They were compared with Mclachlan (1991) and agreed with his results. New results were obtained for $Re \geq 5000$ and up to $Re = 14000$ for $X_\infty = 1.543$. Some circles and oscillation near the separation point suggests that a finer grid needs to be used. A clear finding is that the separated region remains of size $O(1)$ as the Reynolds number becomes large.

Thirdly, we have investigated the solution of the three-dimensional cubical lid-driven cavity problem by solving the equations with the three-dimensional velocity-vorticity formulation. A Chebyshev collocation method was used to discretize the problem in the y and z directions and the fourth-order finite difference method was used to discretize the equations in the x direction. The Newton-Raphson technique was employed to linearize the problem. The discretization of the equations leads to a sparse block pentadiagonal matrix, which was solved directly. Some results for Reynolds numbers were presented and compared with available previous literature. Results were obtained for $Re = 1, 50, 100$ and 200 and velocity and vorticity contour plots, and their profiles were presented. The comparisons show agreements between our results and the those of others.

6.1 Future Work

In the present work, the Chebyshev collocation method has been used successfully in both directions x and y to solve the two-dimensional problems and it show its success to generate results for high Reynolds number. Thus, this approach is suitable for solving other problems and geometries for two dimensions. Moreover, one can generate more results for higher Reynolds number with finer grids. For the three-dimensional problem, the sparse block pentadiagonal matrix that arises from using the hybrid methods is attractive and makes this approach convenient for solving three-dimensional problems. Additionally, with parallel computing, there is considerable scope to solve three-dimensional problems; however, we have found that the method requires a lot of memory and CPU time. Without making use of a parallel solver, it is unlikely that the present method can be taken further.

Appendix A

Two-Dimensional Lid Driven Cavity

This appendix shows some further results for two-dimensional lid driven cavity. It shows u-velocity profiles along a vertical line passing through the geometry centre at various Reynolds numbers ($Re = 5000 - 12500$) using $N = M = 120$ grid. Similarly, v-velocity profiles along a horizontal line passing through the geometry centre at various Reynolds numbers ($Re = 100 - 20000$) using $N = M = 120$ grid has been presented. In addition, this appendix presents streamline and vorticity contours plots for various Reynolds number up to 24000 on various grids.

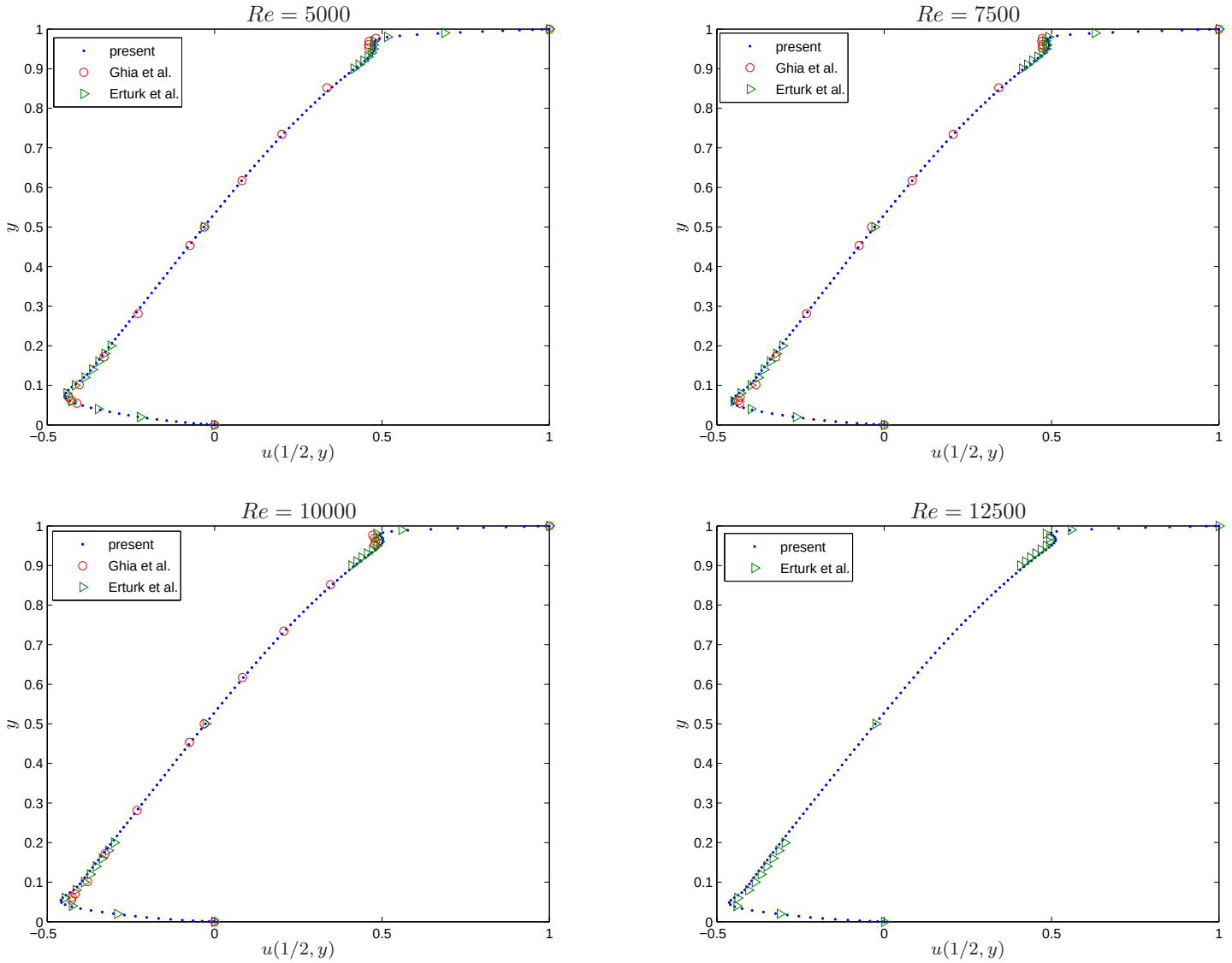

Figure A.1: Comparison of u-velocity profiles along a vertical line passing through the geometry centre at various Reynolds numbers using $N = M = 120$ solution.

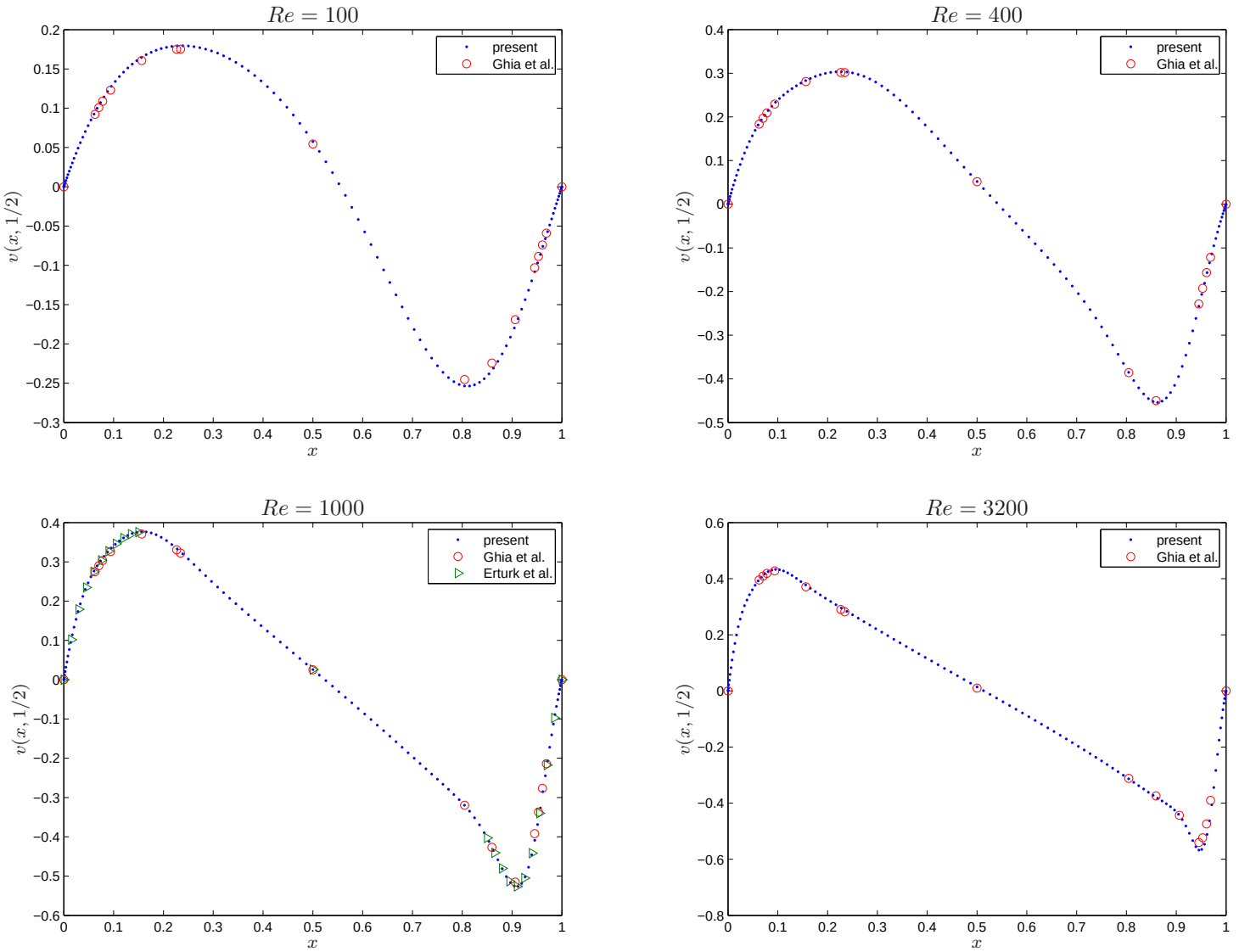

Figure A.2: Comparison of v-velocity profiles along a horizontal line passing through the geometry centre at various Reynolds numbers using $N = M = 120$ solution.

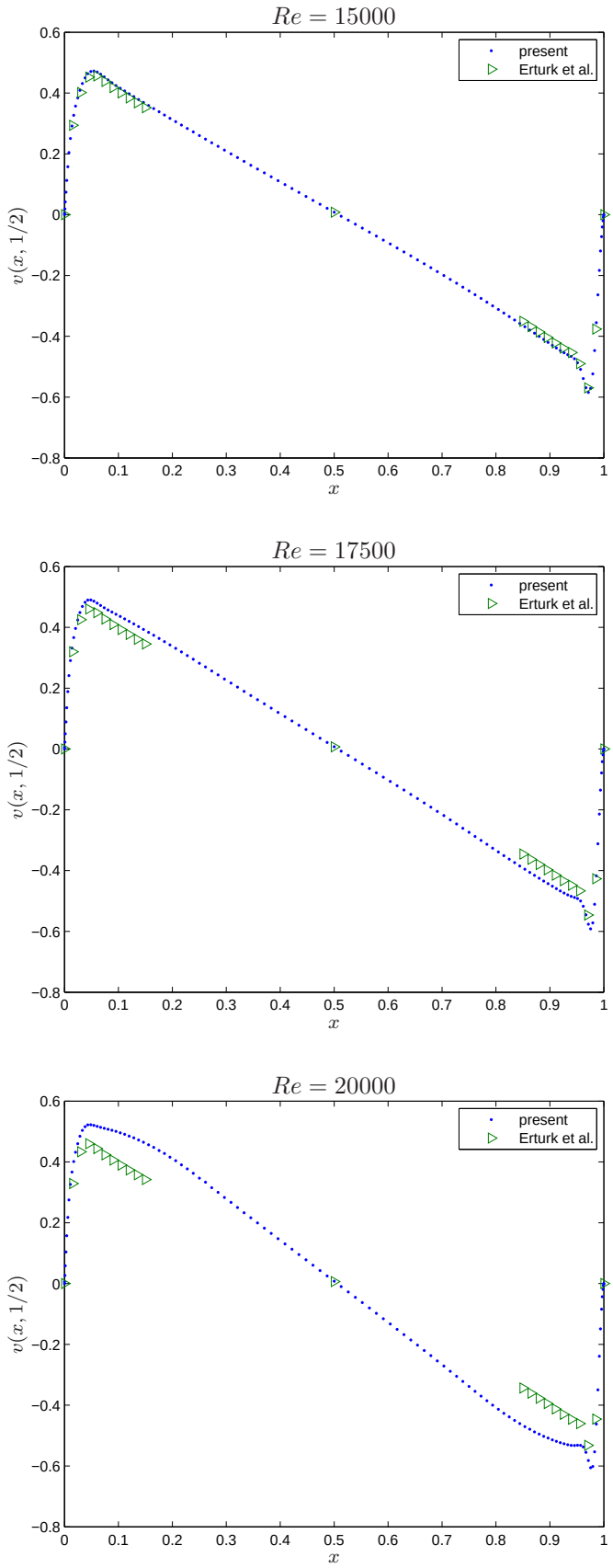

Figure A.3: Comparison of v-velocity profiles along a horizontal line passing through the geometry centre at various Reynolds numbers using $N = M = 120$ solution.

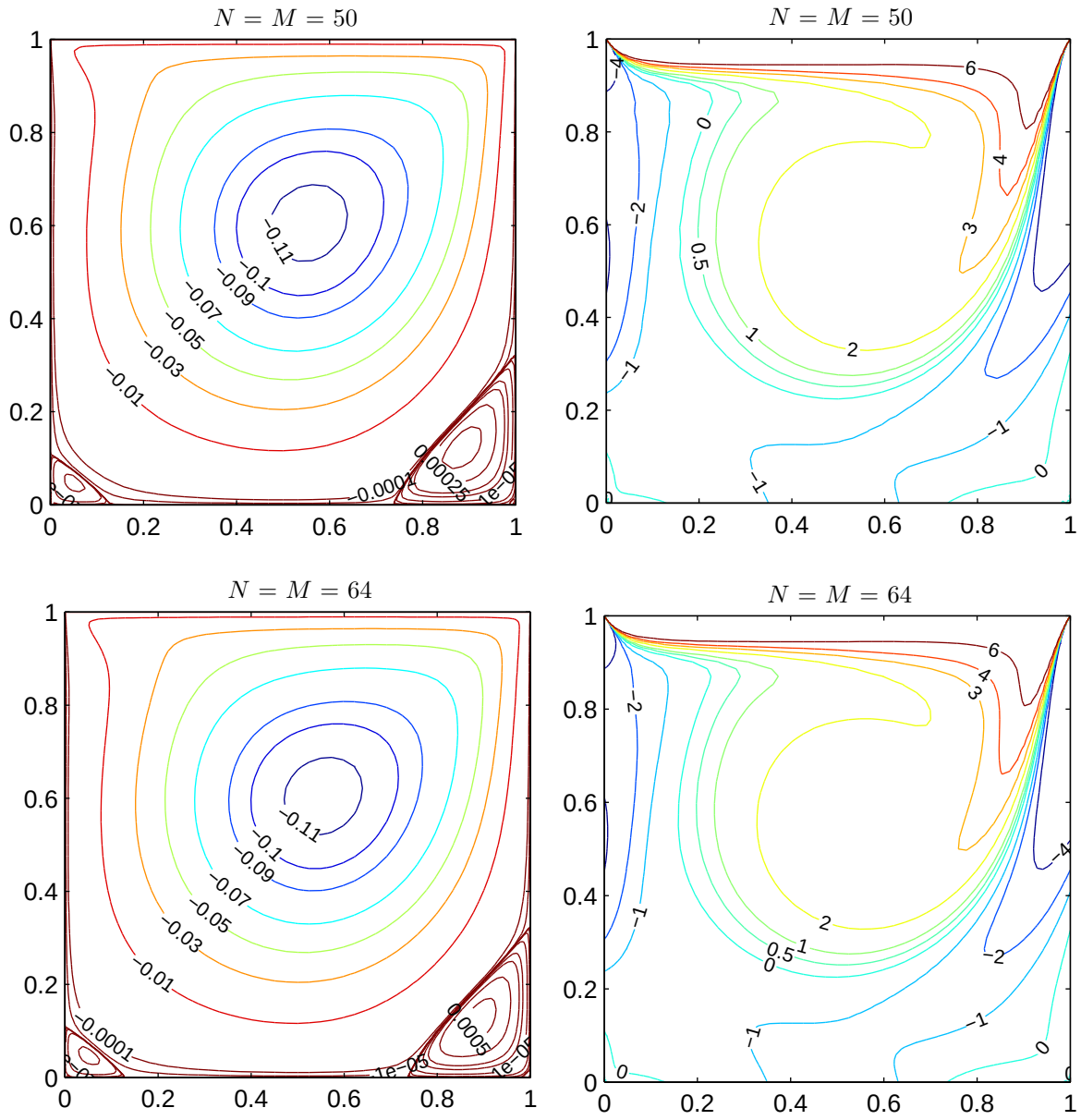

Figure A.4: Streamline and vorticity contours plot at $Re = 400$ on 51×51 and 65×65 grid.

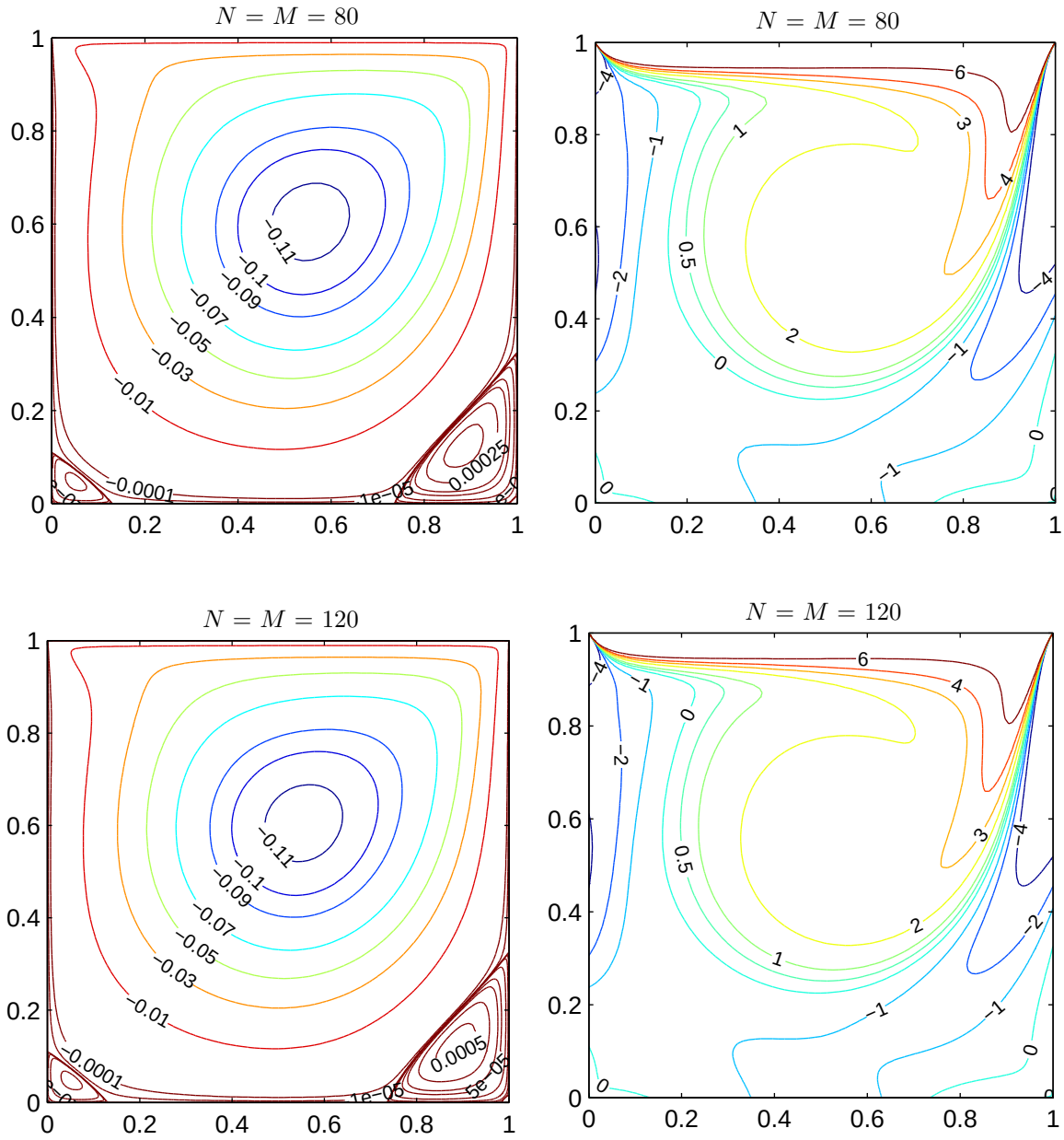

Figure A.5: Streamline and vorticity contours plot at $Re = 400$ on 81×81 and 121×121 grid.

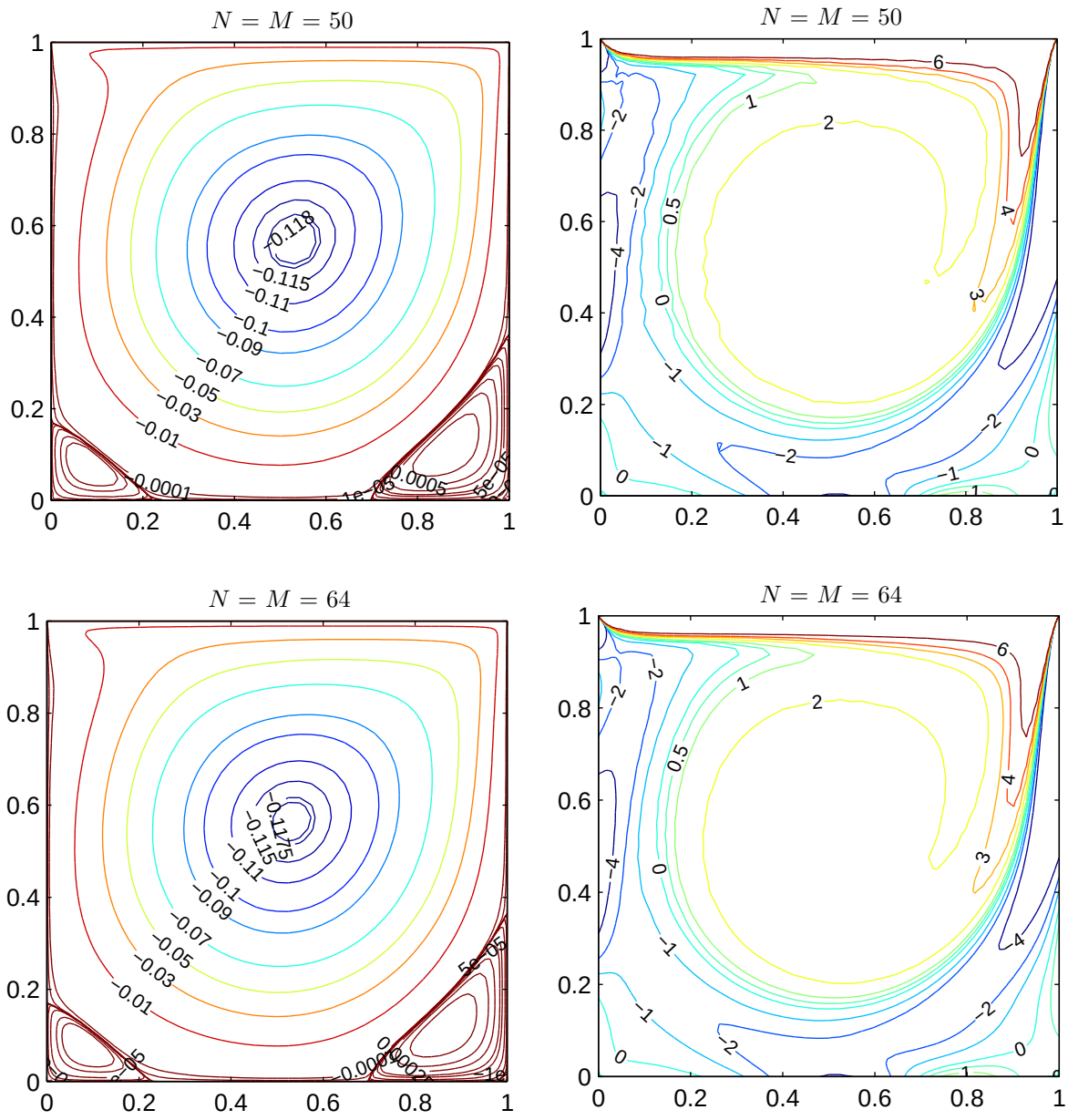

Figure A.6: Streamline and vorticity contours plot at $Re = 1000$ on 51×51 and 65×65 grid.

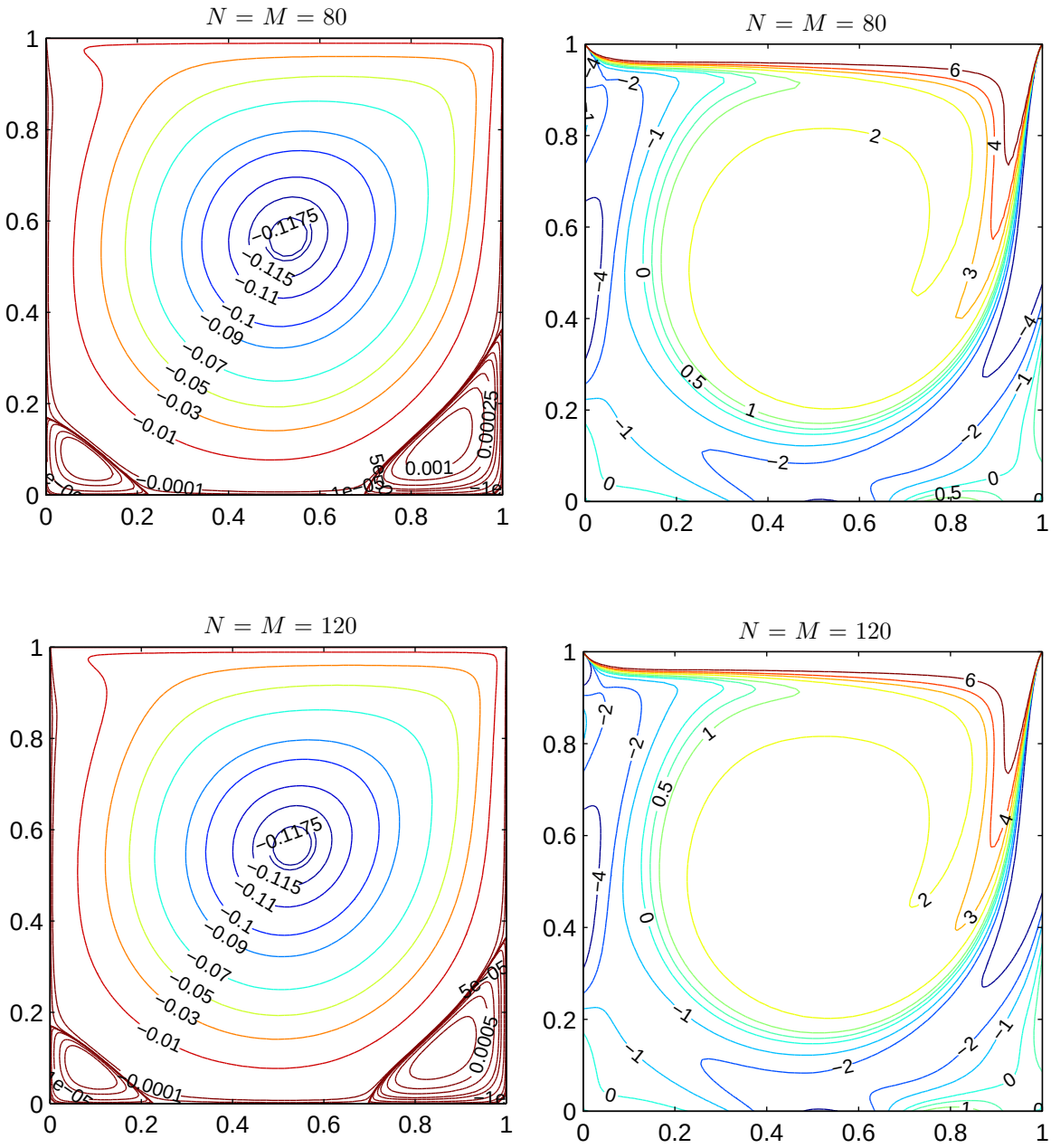

Figure A.7: Streamline and vorticity contours plot at $Re = 1000$ on 81×81 and 121×121 grid.

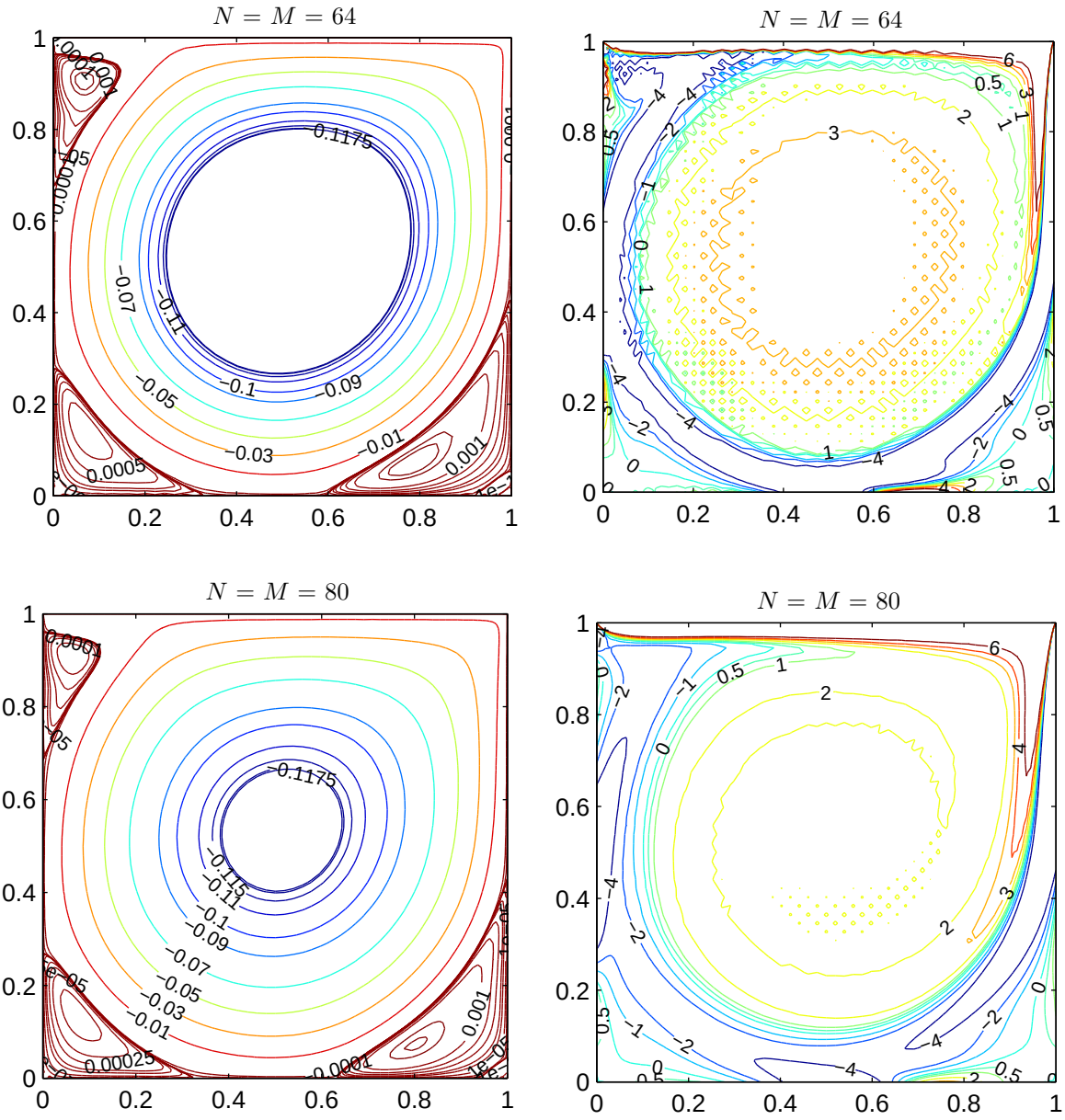

Figure A.8: Streamline and vorticity contours plot at $Re = 5000$ on 65×65 and 81×81 grid.

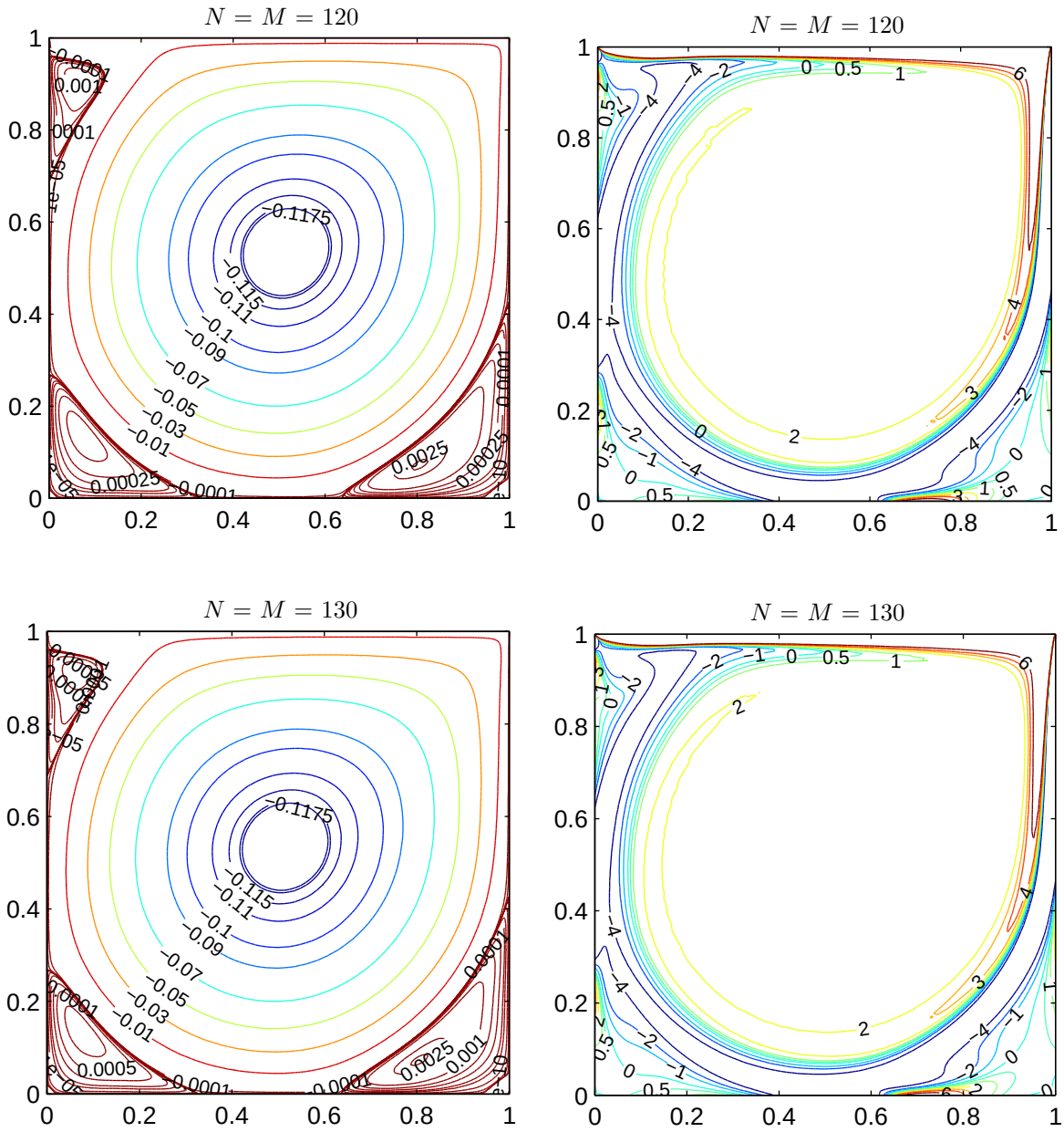

Figure A.9: Streamline and vorticity contours plot at $Re = 5000$ on a 121×121 and 131×131 grid.

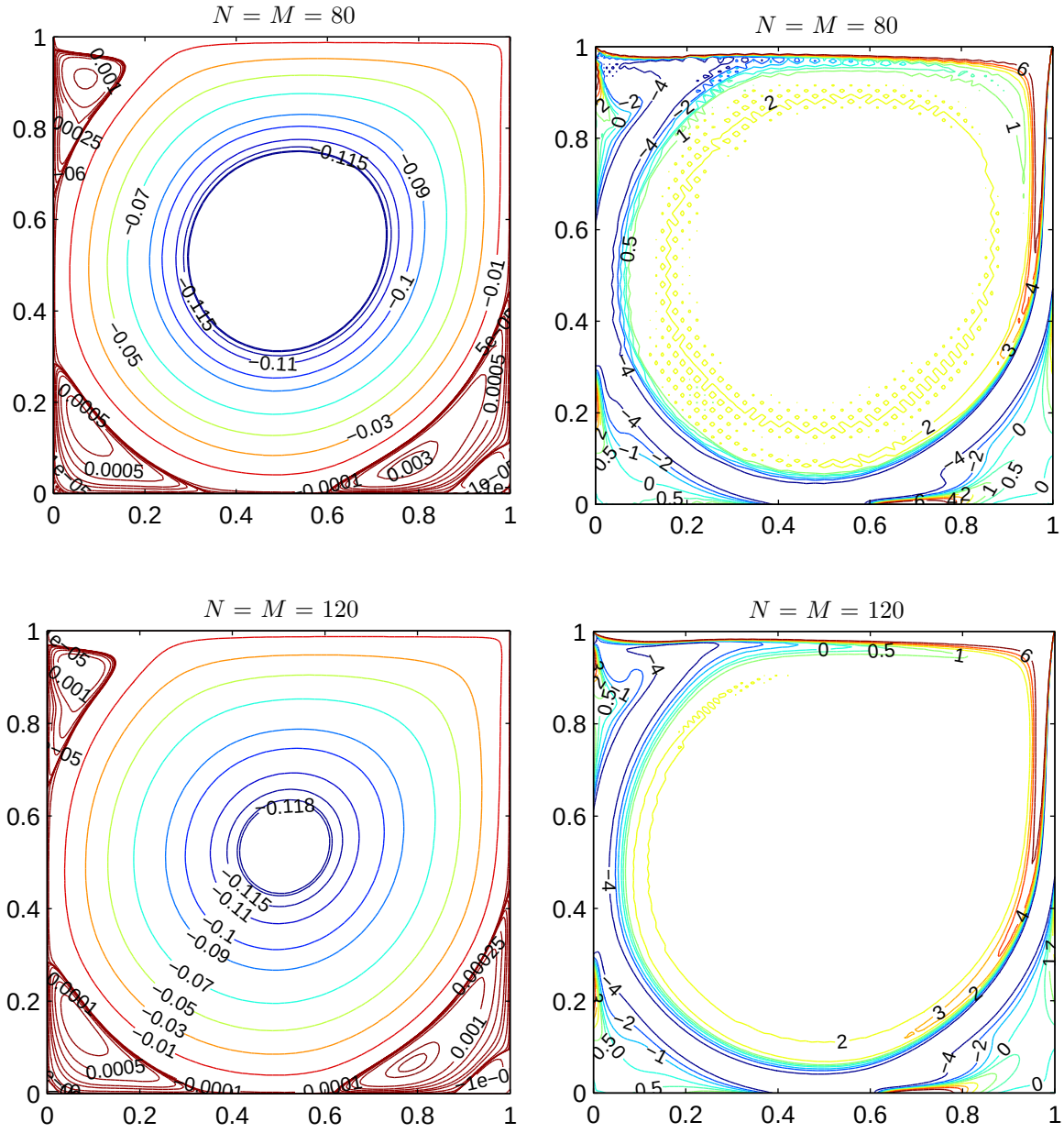

Figure A.10: Streamline and vorticity contours plot at $Re = 7500$ on 81×81 and 121×121 grid.

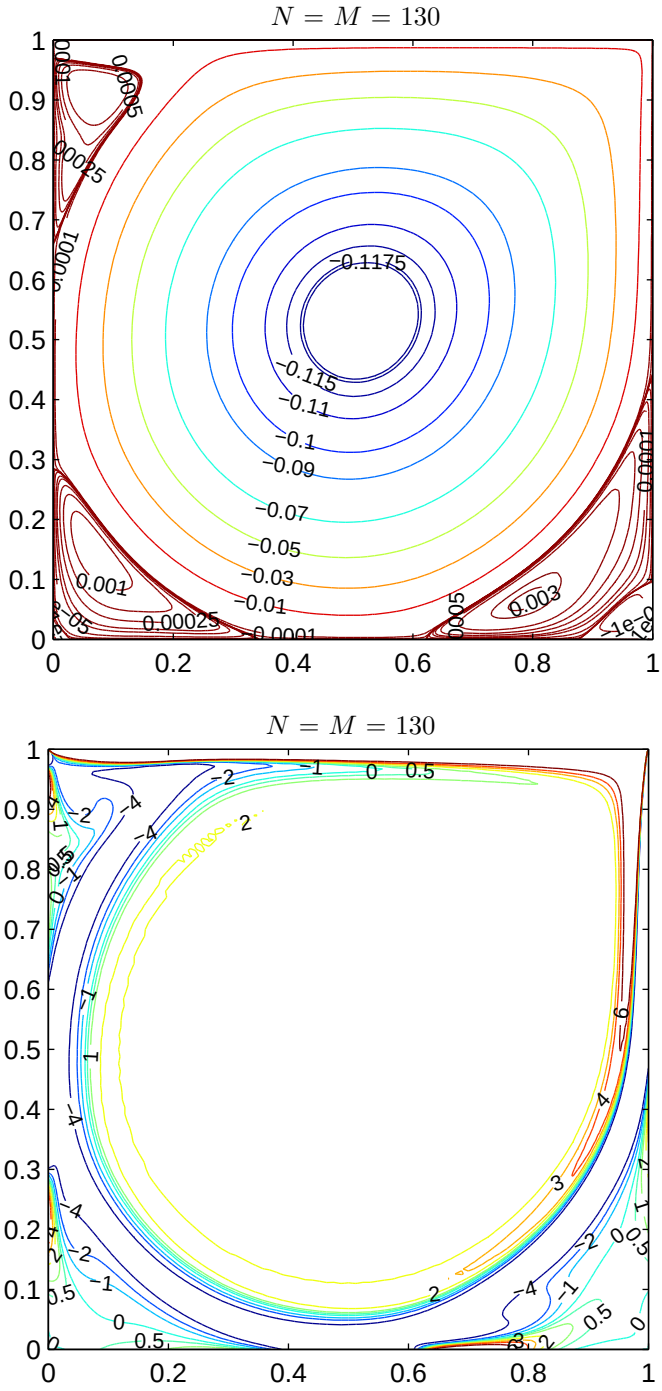

Figure A.11: Streamline and vorticity contours plot at $Re = 7500$ on 131×131 grid.

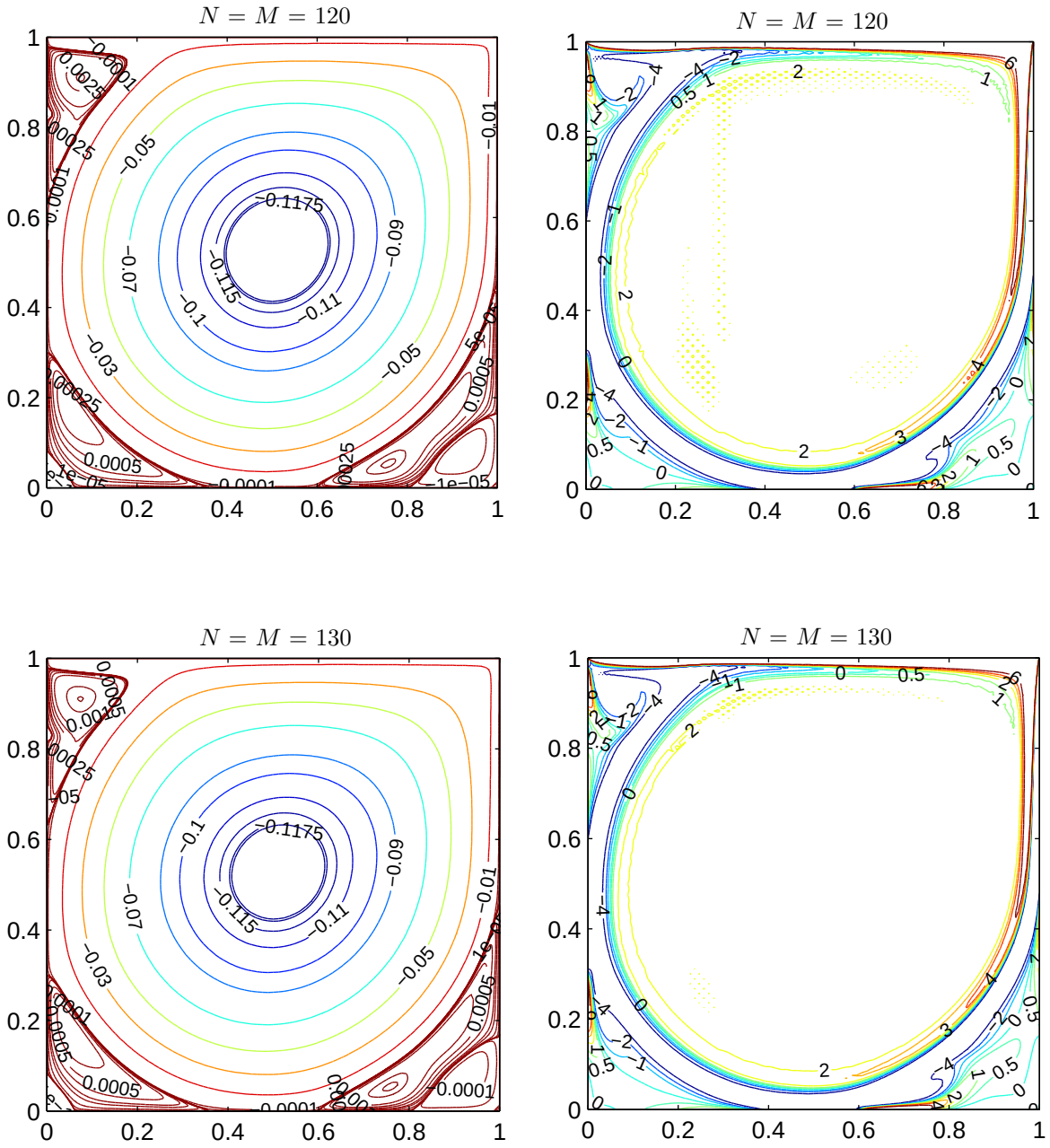

Figure A.12: Streamline and vorticity contours plot at $Re = 12500$ on a 121×121 and 131×131 grid.

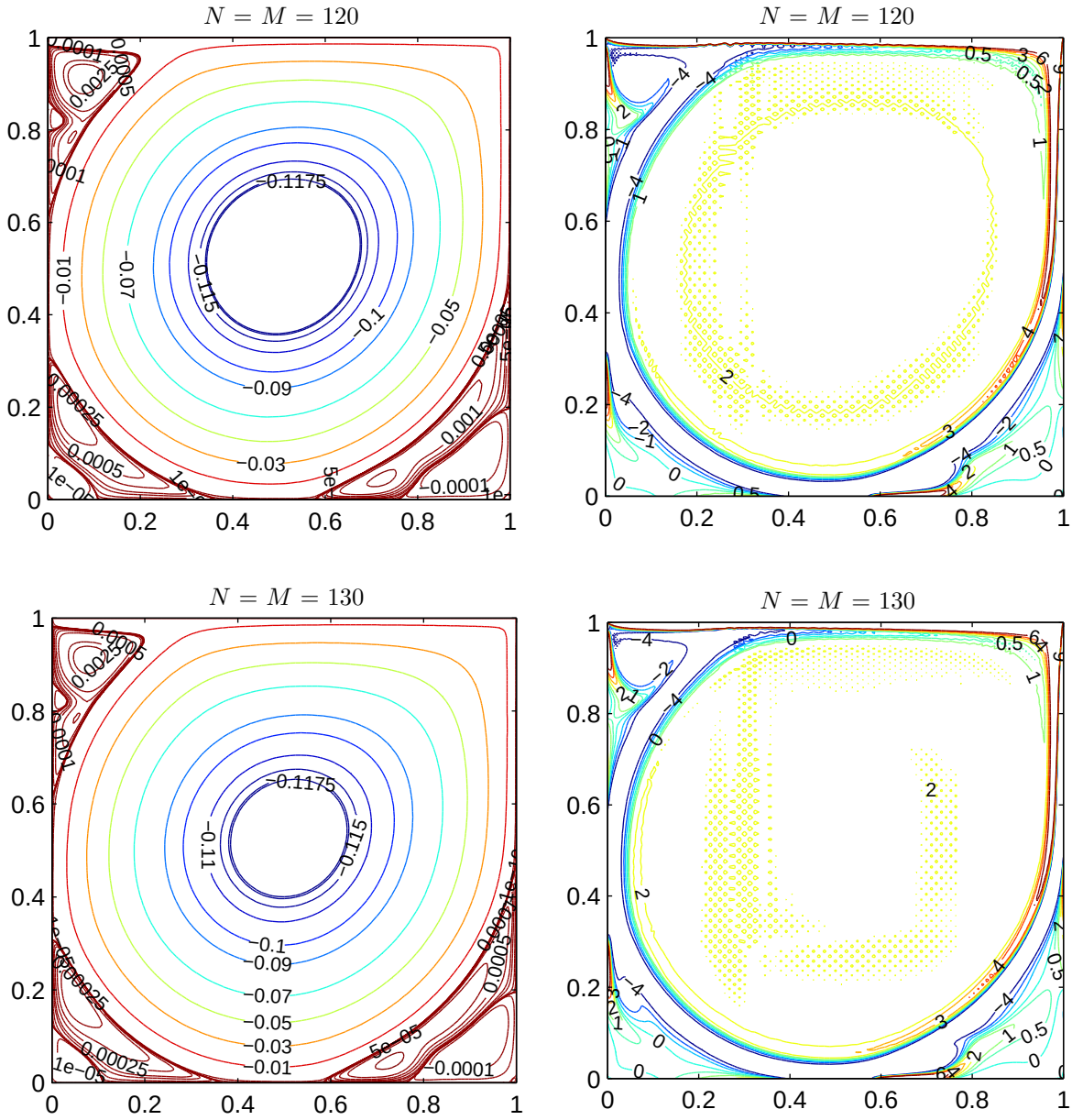

Figure A.13: Streamline and vorticity contours plot at $Re = 17500$ on a 121×121 and 131×131 grid.

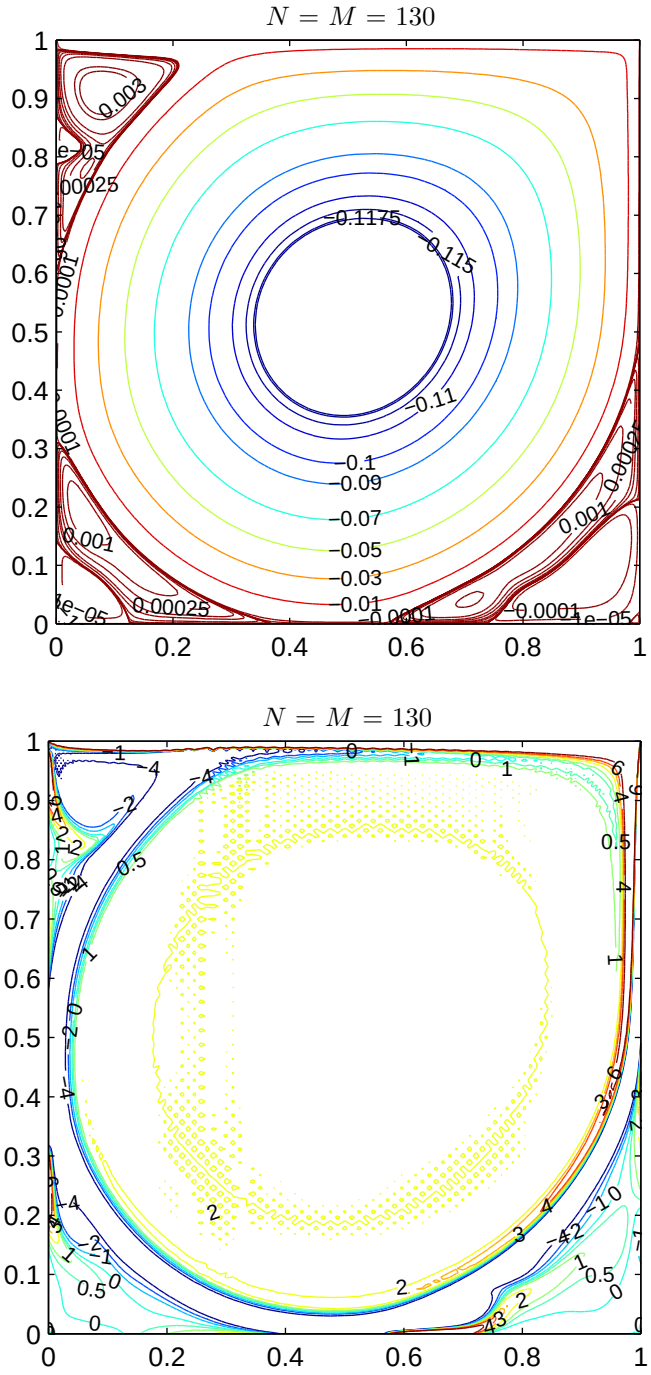

Figure A.14: Streamline and vorticity contours plot at $Re = 21000$ on a 131×131 grid.

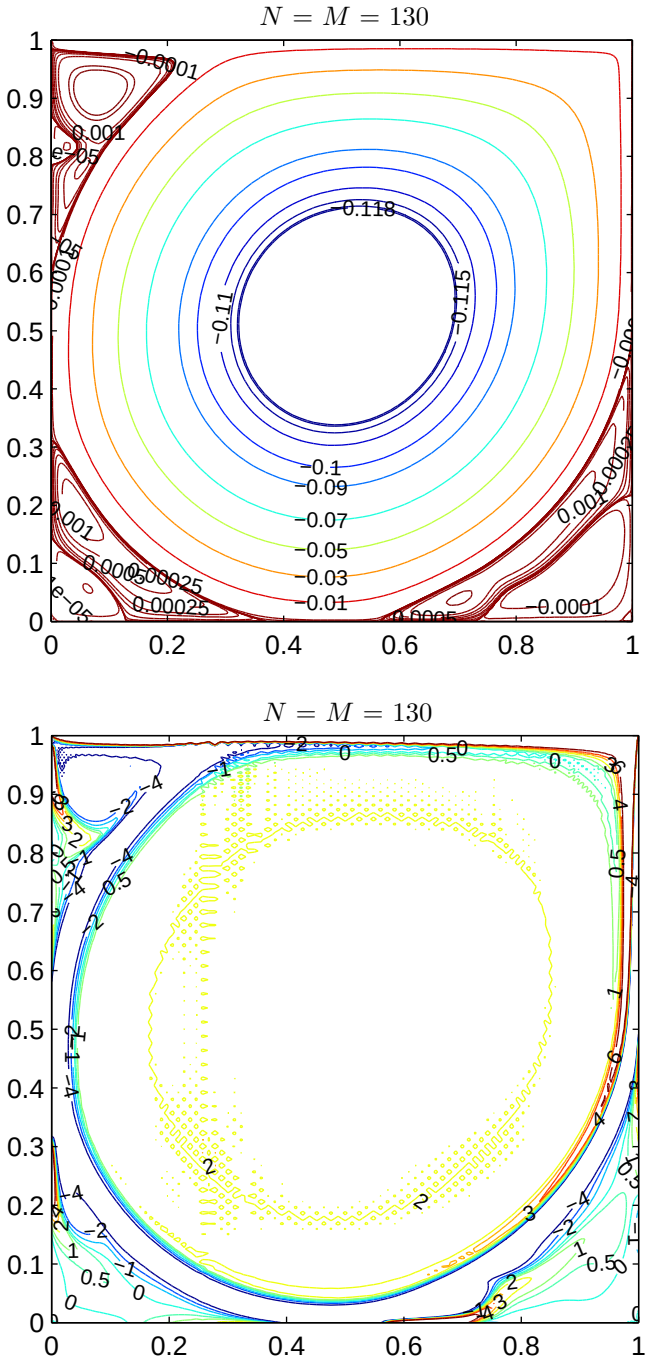

Figure A.15: Streamline and vorticity contours plot at $Re = 22000$ on a 131×131 grid.

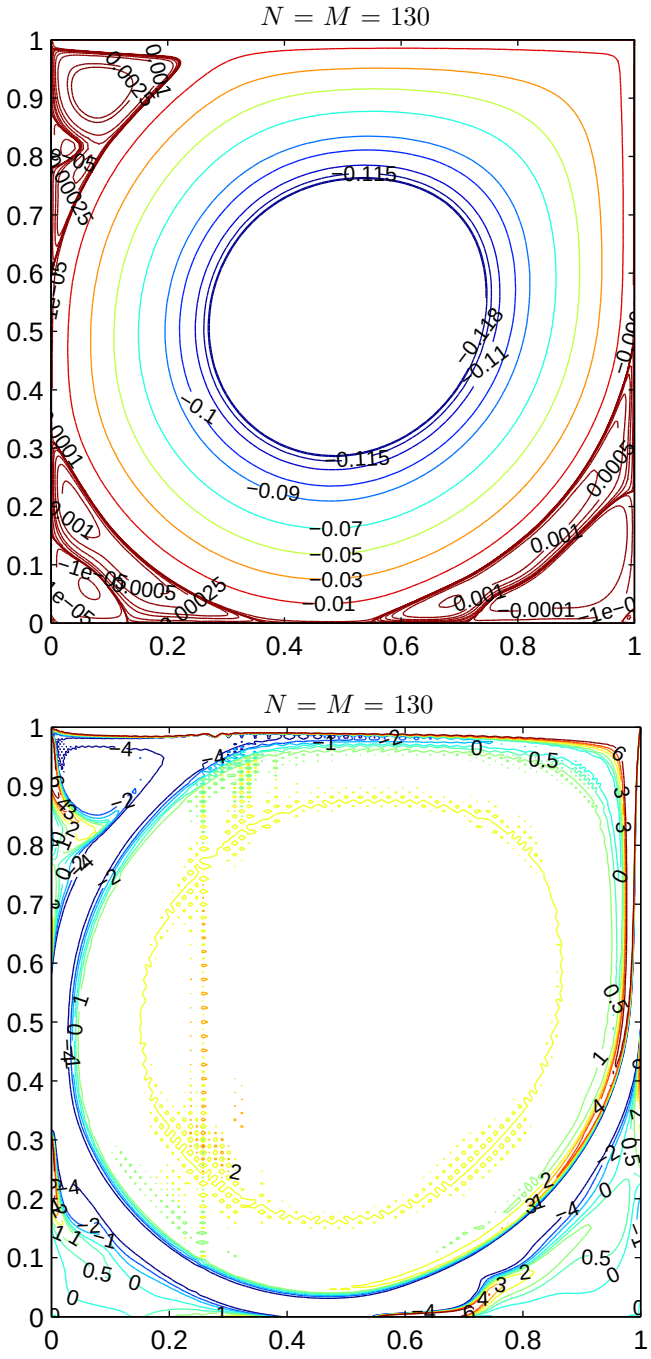

Figure A.16: Streamline and vorticity contours plot at $Re = 24000$ on a 131×131 grid.

Bibliography

Albensoeder, S. & Kuhlmann, H. C. 2005 Accurate three-dimensional lid-driven cavity flow. *Journal of Computational Physics.* **206**, 536–558.

Albensoeder, S. & Kuhlmann, H. C. 2006 Nonlinear three-dimensional flow in the lid-driven square cavity. *Journal of Fluid Mechanics.* **569**, 465–480.

Auteri, F., Parolini, N. & Quartapelle, L. 2002 Numerical investigation on the stability of singular driven cavity flow. *Journal of Computational Physics.* **183**, 1–25.

Azzam, N. A. 2003 Numerical solution of the Navier-Stokes equations for the flow in a lid driven cavity and a cylinder cascade. PhD thesis, University of Manchester, Manchester, The UK.

Barragy, E. & Carey, G. F. 1997 Stream function-vorticity driven cavity solution using p finite elements. *Computers and Fluids.* **26**, 435–468.

Boppana, V. B. L. & Gajjar, J. S. B. 2010 Global flow instability in a lid-driven cavity. *International Journal for Numerical Methods in Fluids.* **62**, 827–853.

Botella, O. & Peyret, R. 1998 Benchmark spectral result on the lid-driven cavity flow. *Computers and Fluids.* **27**, 421–433.

Bruneau, C. & Jouron, C. 1990 An efficient scheme for solving steady incompressible navier-stokes equations. *Journal of Computational Physics.* **89**, 389–413.

Bruneau, C. & Saad, M. 2004 The 2D lid-driven cavity problem revisited. *Computer and fluids* **35**, 326–348.

Burggraf, O. R. 1966 Analytical and numerical studies of the sturcture of steady seperated flows. *Journal of Fluid Mechanics.* **24**, 113–151.

Canuto, C., Hussaini, M. Y., Quarteroni, A. & Zang, T. A. 1988 *Spectral Methods in Fluid dynamics*. Springer-Verlag Berlin Heidelberg.

Chiang, T. P., Hwang, R. R. & Sheu, W. H. 1996 Finite volume analysis of spiral motion in a rectangular lid-driven cavity. *Journal of Fluid Mechanics.* **23**, 325–346.

Chiang, T. P., Sheu, W. H. & Hwang, R. 1998 Effect of Reynolds number on the eddy structure in a lid-driven cavity. *International Journal for Numerical Methods in Fluids.* **26**, 557–579.

Cortes, A. & Miller, J. 1994 Numerical solution expermints with the lid driven cavity flow problem. *Computers and Fluids.* **23**, 1005–1027.

Davies, C. & Carpenter, P. W. 1997 Numerical simulation of evolution of Tollmien-Schlichting waves over finite compliant panels. *Journal of Fluid Mechanics.* **335**, 361–392.

Davies, C. & Carpenter, P. W. 2001 A novel velocity-vorticity formulation of the Navier-Stokes equations with application to boundary layer distribution evolution. *Journal of Computational Physics.* **172**, 119–165.

Davis, G. D. V. & Mallinson, G. D. 1974 An evaluation of upwind and central difference approximations by a study of recirculating flow. *Computers and Fluids.* **4**, 29–43.

Dennis, S. C., Ingham, D. B. & Cook, R. N. 1979 Finite-difference method for calculating steady incompressible flows in three dimensions. *Journal of Computational Physics.* **33**, 325–339.

Erturk, E., Corke, T. C. & Gokcol, C. 2005 Numerical solutions of 2-d steady incompressible driven cavity flow at high Reynolds numbers. *International Journal for Numerical Mathods in Fluids.* **48**, 747–774.

Fortin, A., Jardak, M., Gervais, J. & Pierre, R. 1997 Localisation of hopf bifurcations in fluid flow problems. *International Journal for Numerical Mathods in Fluids.* **24(11)**, 1185–1210.

Freita, C. F., Street, R. L., Findikakis, A. N. & Koseff, J. R. 1985 Numerical simulation of three dimensional flow in a cavity. *Journal of Fluid Mechanics.* **5**, 561–575.

Gajjar, J. S. B. & Azzam, N. A. 2004 Numerical solution of the NavierStokes equations for the flow in a cylinder cascade. *Journal of Fluid Mechanics.* **520**, 51–82.

Gaster, M. 1967 The structure and behavior of laminar separation bubles. *Reports and Memoranda No. 3595.* .

Ghia, U., Ghia, K. N. & Shin, C. T. 1982 High-Re solutions of the navier stokes equations for incompressible flow using the Navier- Stokes equations and multigrid method. *Journal of Computational Physics.* **48**, 387411.

Goldstein, S. 1948 On laminar boundary-layer flow near a position of separation. *Quarterly Journal of Mechanics and Applied Mathematics.* **1**, 43–69.

Goodrich, J. W., Gustafson, N. & Halasi, K. 1990 Hopf bifurcation in the driven cavity. *Journal of Computational Physics.* **90**, 219–261.

Guermond, J. L., Migeon, C., Pineau, G. & quartapelle, L. 2002 Start-up flows in a three-dimensional rectangular driven cavity of aspect ratio 1:1:2 at $Re = 1000$. *Journal of Fluid Mechanics* **450**, 169–199.

Gupta, M. M., Manohar, R. P. & Noble, B. 1981 Nature of viscous flow near shape corners. *Journal of Computational Physics.* **9**, 379–388.

Gustafson, K. & Halasi, K. 1986*a* Cavity flow dynamics at higher reynolds number and higher aspect ratio. *Journal of Computational Physics.* **70**, 271283.

Gustafson, K. & Halasi, K. 1986*b* Vortex dynamics of cavity flows. *Journal of Computational Physics.* **64**, 279319.

Jackson, A. 1996 Multigrid solutions to the Navier-Stokes equations in two and three-dimensions. PhD thesis, University of Manchester, Manchester, The UK.

Koseff, J. R. & Street, R. L. 1984 On end wall effects in a lid-driven cavity flow. *Journal of Fluids Engineering.* **106**, 385–389.

Koseff, J. R., Street, R. L., Gresho, P. M., Upson, C. D., Humphrey, J. A. C. & To, W. M. 1983 A three dimensional lid-driven cavity flow: experiment and simulation. *3rd International Conference on Numerical methods in Laminar and Turbulent flow* .

Ku, H. C., Hirsh, R. S. & Taylor, T. D. 1987 A pseudospectral method for solution of the three-dimensional incompressible Navier-Stokes equations. *Journal of Computational Physics.* **70**, 439–462.

Kumar, D. S., Kumar, K. S. & Das, M. K. 2009 A fine grid solution for a lid-driven cavity flow using multigrid method. *Engineering Applications of Computational Fluid Mechanics.* **3**, 336–354.

Leal, L. G. 1973 Steady separated flow in a linearly decelerated free stream. *Journal of Fluid Mechanics* **59**, 513–535.

Logue, R. P. 2005 Numerical solution of the tow dimensional Navier-Stokes equations with a double chebyshev expansion. Master's thesis, University of Manchester, Manchester, The UK.

Mason, J. C. & Handscomb, D. C. 2002 *Chebyshev Polynomials*. Oxford University.

Mclachlan, R. 1990 Separated viscous corner via multigrid. PhD thesis, Institute of Technology, California, USA.

Mclachlan, R. 1991 A steady separated viscous corner flow. *Journal of Fluid Mechanics.* **231**, 1–34.

Miller, W. 1995 Flow in the driven calculated by lattice Boltzmann method. *Physical Review E.* **51**, 3659–3669.

Moffatt, H. K. 1964 Viscous and resistive eddies near a sharp corner. *Journal of Fluid Mechanics.* **18**, 1–18.

Pauley, L. L., Moin, P. & Reynolds, W. C. 1990 The structure of two-dimensional separation. *Journal of Fluid Engineering.* **220**, 397–411.

Perng, C. Y. & Street, R. L. 1989 Three-Dimensional unsteady flow simulations: Alternative strategies for a Volume-Averaged calculation. *International Journal for Numerical Method in Fluids.* **9**, 342–362.

Peyret, R. & Taylor, D. 1984 *Computational Method for Fluid Flow*. Springer-Verlag Berlin Heidelberg.

Poliashenko, M. & Aidun, C. K. 1995 A direct method for computation of simple bifurcation. *Journal of Computational Physics.* **121(2)**, 246–260.

Prandtl, L. 1905 Ueber fluessigkeitsbewegung bei sehr kleiner reibung. *Journal of International Mathematics.* **III**, 484491.

Saad, Y. 1998 *Iterative Method For Sparse Linear System, Second Edition*. The University of Minnesota Minneapolis.

Sahin, M. & Owens, R. G. 2003 A novel fully implicit finite volume method applied to the lid-driven cavity problem-part i: High Reynolds number flow calculations. *International Journal for Numerical Methods in Fluids.* **42**, 57–77.

Schreiber, R. & Keller, H. B. 1983 Driven cavity flows by efficient numerical techniques. *Journal of Computational Physics.* **49**, 310–333.

Shen, J. 1991 Hopf bifurcation of the steady regularized driven cavity flow. *Journal of Computational Physics.* **90**, 1–20.

Speziale, C. G. 1987 On the advantages of the Vorticity-Velocity formulation of the equations of fluid dynamics. *Journal of Computational Physics.* **73**, 476–480.

Suh, Y. K. & Liu, C. S. 1990 Study on the flow structure around a flat plate in a stagnation flow field. *Journal of Fluid Mechanics.* **214**, 469–487.

Sun, K. H., Pyle, D. L., Baines, M. J., Hall-Taylor, N. J. & Fitt, A. D. 2006 Velocity profiles and frictional pressure drop for shear thinning materials in lid-driven cavity with fully developed axial flow. *Chemical Engineering Science* **61**, 4697–4706.

Takami, H. & Kuwahara, K. 1974 Numerical study of Three-Dimensional flow within a cubic cavity. *Journal of the Physical Society of Japan.* **37(6)**, 1695–1698.

Tian, Z. H. & Yu, P. X. 2011 An efficient compact difference scheme for solving the streamfunction formulation of the incompressible Navier-Stokes equations. *Journal of Computational Physics.* **230**, 6404–6419.

Tiesinga, G., Wubs, F. & Veldman, A. 2002 Bifurcation analysis of incompressible flow in a driven cavity by the Newton-Picard method. *Journal on Applied Mathematics.* **140**, 751–772.

Trefthen, L. N. 2000 *Spectral Methods in MATLAB*. Society for Industrial and Applied Mathematics.

Yeckel, A., Smith, J. W. & Derby, J. J. 1997 Parallel finite element calculation of flow in three-dimensional lid-driven cavity using the CM-5 and T3D. *Journal of Fluid Mechanics.* **24**, 1449–1461.

Young, D. L., Lui, Y. H. & Eldho, T. I. 2000 A combined BEM-FEM model for the velocity-vorticity formulation of the Navier-Stokes equations in three-dimensions. *Journal of Fluid Mechanics.* **24**, 307–316.

Zunic, Z., Hribersek, M., Skerget, L. & Ravnik, J. 2006 3D lid driven cavity flow by mixed boundary and finite element method. *European Conference on Computational Fluid Dynamics* .